

**UCLA**

**UCLA Electronic Theses and Dissertations**

**Title**

Enhancement of Operational Flexibility in Reverse Osmosis Membrane Processes by Concentrate Recycling

**Permalink**

<https://escholarship.org/uc/item/58r3b80r>

**Author**

Lee, Tae

**Publication Date**

2019

Peer reviewed|Thesis/dissertation

UNIVERSITY OF CALIFORNIA

Los Angeles

Enhancement of Operational Flexibility  
in Reverse Osmosis Membrane Processes  
by Concentrate Recycling

A dissertation submitted in partial satisfaction of the  
requirements for the degree of Doctor of Philosophy  
in Chemical Engineering

by

Tae Lee

2019

© Copyright by

Tae Lee

2019

## ABSTRACT OF THE DISSERTATION

Enhancement of Operational Flexibility  
in Reverse Osmosis Membrane Processes  
by Concentrate Recycling

by

Tae Lee

Doctor of Philosophy in Chemical Engineering

University of California, Los Angeles, 2019

Professor Yoram Cohen, Chair

Improvements in system and process design has enabled reverse osmosis (RO) membrane technology to gain foothold in various water treatment and desalination applications. However, energy consumption and mineral scaling on membrane surfaces remain impediments to high recovery operation of RO desalination. Accordingly, research efforts have been devoted to process optimization to improve permeate water productivity, reduce energy cost, and mitigate membrane mineral scaling. In this regard, RO concentrate recycling is an effective approach for enhancing product water recovery, reducing system footprint, and lowering installation as well as operating costs of RO desalination systems and plants. Energy consumption and membrane mineral scaling propensity in RO processes are impacted primarily by the osmotic pressure magnitude and the

level of supersaturation of mineral scalants at the membrane surface, respectively, which are, in turn, governed by the operational strategy. Optimization of RO processes with concentrate recycle require fundamental models of RO processes with concentrate recycle under both steady and unsteady-state operation,

To date, only simple models have been proposed which are of limited applicability to practical systems given the use of various simplifying assumptions of complete energy recovery, neglect of the efficacy of concentrate flushing in unsteady-state semi-batch RO (SBRO), and omission of concentration polarization. Previous studies have not provided experimental data to corroborate conclusions regarding system performance based on oversimplifications. Moreover, SBRO operation was not assessed relative to steady state RO (SSRO) with partial recycle (SSRO-PR) which is also suitable for high recovery operation with a small footprint. Accordingly, in the present work a fundamental quantitative modeling framework was developed and implemented for the design and operation of SSRO-PR and SBRO. Modeling RO desalting, including at the limit of the thermodynamic restriction, was undertaken to evaluate the minimum energy consumption as a function of product water recovery. SBRO process analysis revealed a significant increase in the salinity range during the RO filtration period and a progressive rise in the initial filtration period salinity until the stable cycle-to-cycle operation is reached. SBRO performance is highly dependent on the efficacy of concentrate discharge and flushing during the SBRO flushing period. For the condition of concentrate flushing under ideal plug flow, energy consumption in SBRO was assessed to be lower than for single-pass RO (SPRO) operation at the same level of overall product water recovery. However, for the practical range of expected concentrate flushing

efficacy energy consumption in SBRO could be significantly above that which would be attained in SPRO.

Using the direct real-time membrane surface optical imaging mineral scaling was experimentally evaluated in both SBRO and SSRO-PR pilot systems, with respect to the efficacy of concentrate flushing with the undersaturated raw feed water, at given levels of supersaturation or product water recovery. The predicted RO element feed stream osmotic pressure and solution supersaturation levels (for the target mineral scalant) at the membrane surface, for a given product water recovery, were higher on average in SBRO relative to SSRO-PR as corroborated by experimental data. The experimental data revealed mineral scaling propensity, which was significantly higher in multi-cycle SBRO operation, relative to SSRO-PR at the same water recovery. However, the rates of crystal nucleation and growth were similar at when both systems are compared at the same level of average supersaturation, although the product water recovery was lower in SBRO compared to SSRO-PR.

The present theoretical modeling framework, validated by experimental data, provide a fundamental approach to assessing the performance of SBRO and SSRO-PR desalting systems with respect to energy consumption and mineral scaling propensity. The presented approach provides the means necessary for optimizing these low footprint technologies for high recovery RO desalination.

The dissertation of Tae Lee is approved.

Panagiotis D. Christofides

Yunfeng Lu

Deepak Rajagopal

Yoram Cohen, Committee Chair

University of California, Los Angeles

2019

To my mom and dad

Yeon-Im Ahn & Gu-Mo Lee



# Table of Contents

<b>ABSTRACT OF THE DISSERTATION.....</b>	<b>II</b>
<b>CHAPTER 1 INTRODUCTION.....</b>	<b>1</b>
1.1 BACKGROUND.....	1
1.2 PROBLEM STATEMENT .....	8
1.3 RESEARCH OBJECTIVES .....	9
1.4 DISSERTATION STRUCTURE.....	10
<b>CHAPTER 2 LITERATURE REVIEW.....</b>	<b>12</b>
2.1 REVERSE OSMOSIS DESALINATION .....	12
2.1.1 Reverse osmosis.....	12
2.1.2 Concentration polarization.....	14
2.1.3 Mineral scaling.....	16
2.1.4 Surface mineral prevention methods .....	24
2.1.5 Energy consumption in RO desalination .....	27
2.2 OPERATIONAL APPROACHES FOR RO PROCESSES.....	33
2.2.1 Steady-state RO process .....	33
2.2.2 Unsteady-state RO operation .....	38
<b>CHAPTER 3 STEADY STATE RO DESALINATION WITH PARTIAL CONCENTRATE RECYCLING FOR OPERATIONAL FLEXIBILITY .....</b>	<b>52</b>
3.1 OVERVIEW .....	52
3.2 STEADY STATE RO WITH PARTIAL RECYCLING (SSRO-PR) SYSTEM OPERATION WITH ENERGY RECOVERY AND CONCENTRATE RECYCLE .....	53
3.2.1 SSRO-PR design and operation .....	53
3.2.2 SSRO-PR energy utilization .....	57
3.2.3 Salt material balance in FLERO operation .....	60
3.3 EXPERIMENTAL .....	61
3.3.1 Materials and solutions .....	61

3.3.2	Pilot spiral-wound RO system for SSRO-PR operation .....	62
3.3.3	Concentration polarization.....	63
3.3.4	SSRO-PR desalination experiments .....	64
3.4	RESULTS AND DISCUSSION .....	66
3.4.1	Flexibility of SSRO-PR operation .....	66
3.4.2	Alternate SSRO-PR Configurations .....	72
3.5	SUMMARY .....	74
<b>CHAPTER 4 MULTI-CYCLE OPERATION OF SEMI-BATCH REVERSE OSMOSIS (SBRO) DESALINATION .....</b>		<b>76</b>
4.1	OVERVIEW .....	76
4.2	ANALYSIS.....	77
4.2.1	Water recovery in semi-batch RO (SBRO).....	77
4.2.2	Filtration period .....	81
4.2.3	Concentrate flushing period.....	85
4.2.3.1	Osmotic pressure during variation during the SBRO filtration period.....	86
4.2.4	RO concentrate osmotic pressure variation over progressive SBRO cycles .....	88
4.2.5	Specific energy consumption.....	92
4.2.5.1	Element average permeate flux.....	100
4.3	EXPERIMENTAL .....	101
4.3.1	Materials and model solution.....	101
4.3.2	Semi-batch RO desalination .....	101
4.4	RESULTS AND DISCUSSION .....	105
4.4.1	Multi cycle semi-batch RO (SBRO) operation.....	105
4.4.2	Energy consumption .....	112
4.5	SUMMARY .....	116
<b>CHAPTER 5 SCALING PROPENSITY IN RO DESALINATION WITH CONCENTRATE RECYCLING .....</b>		<b>118</b>
5.1	OVERVIEW .....	118

5.2	INTRODUCTION .....	118
5.3	EXPERIMENTAL .....	121
5.3.1	Materials and solution.....	121
5.3.2	Spiral wound RO system for SBRO and SSRO-PR operations.....	122
5.3.3	Membrane Surface Monitor .....	124
5.3.4	Gypsum scaling experiments .....	128
5.4	RESULT AND DISCUSSION .....	131
5.4.1	Operation of SBRO and SSRO with partial concentrate recycle.....	131
5.4.2	The onset and evolution of gypsum Scaling.....	136
5.4.3	Evolution of gypsum scale coverage .....	140
5.4.4	Rate of crystal growth and dissolution.....	142
5.4.4.1	Gypsum Crystal growth .....	145
5.4.4.2	Gypsum Crystal Dissolution.....	147
5.5	SUMMARY .....	148
<b>APPENDIX A. FLEXIBLE RO PILOT MEMBRANE SYSTEM PLATFORMS .....</b>		<b>150</b>
A.1	FLEXIBLE RO (FLERO) SYSTEM COMPONENTS .....	150
A.2	RO PROCESS MONITORING.....	152
A.2	IMPLEMENTATION OF RO PROCESS CONTROL .....	154
A.3	SYSTEM START-UP AND OPERATION .....	155
A.3.1	System start-up procedure.....	155
<b>APPENDIX B. FIELD EVALUATION OF FLEXIBLE RO (FLERO) SYSTEM FOR NITRATE REMOVAL FROM IMPAIRED SMALL COMMUNITY WELL WATER.....</b>		<b>157</b>
B.1	OVERVIEW.....	157
B.2	RO TREATMENT APPROACH.....	158
B.3	EXPERIMENTAL FIELD STUDIES .....	159
B.4	CHARACTERISTICS OF STUDY COMMUNITIES .....	160
B.5	RESULTS AND DISCUSSIONS .....	162

<b>APPENDIX C.    MEMBRANE SURFACE MONITOR OPERATION.....</b>	<b>165</b>
C.1 Membrane coupon preparation.....	165
C.2 Model solution preparation .....	165
C.3 System operating procedure .....	166
<b>APPENDIX D.    SYSTEM CLEANING PROCEDURE .....</b>	<b>167</b>
<b>REFERENCES.....</b>	<b>169</b>

## List of Figures

<b>Fig. 1-1.</b> Desalination technologies.....	1
<b>Fig. 1-2.</b> Reverse osmosis membrane desalination.....	2
<b>Fig. 1-3.</b> (Left) Photograph of the desalination plant at Orange County, California (Capacity of 378,000 m <sup>3</sup> /day) [18], and (Right) a small mobile RO desalination plant (capacity of 45.4 m <sup>3</sup> /day) [19, 20] . The same size membrane elements (8”) are used in both plants demonstrating the scalability of RO desalination.....	3
<b>Fig. 1-4.</b> Examples of different RO system configurations.....	4
<b>Fig. 2-1.</b> Schematic depiction of a cross section of a thin-film composite membrane illustrating dense polyamide layer (PA) skin located on top of the polysulfone (PS) support layer (adapted from [64]).....	13
<b>Fig. 2-2.</b> Schematic of a spiral-wound RO membrane element [22]......	13
<b>Fig. 2-3.</b> Cross-section of symmetrical spiral wound envelope with spacer mesh in feed channel providing structural integrity (SEM view of feed spacer adapted from [67]). .....	14
<b>Fig. 2-4.</b> Development of concentration polarization in the concentration boundary layer. As the feed flow along the membrane and water permeates across the membrane, the solute accumulates at the membrane surface. The box with a dashed line represents the control volume for the solute material balance in Eq. (2-3). .....	15
<b>Fig. 2-5.</b> (Left) photographs describing the development of gypsum crystals on a membrane surface causing (right) relative permeate flux decline (where $J_{v,0}$ is initial permeate flux from a scale-free membrane surface) [51] in a plate-and-frame RO channel. (note: The TDS of the raw feed solution was 7,990 ppm having the gypsum saturation index (SI) of 0.77, while the SI at membrane surface was 2.1. The RO system was operated at 1.72 MP with a crossflow velocity of 5.9 cm/s. ....	16
<b>Fig. 2-6.</b> Description of two nucleation pathways in a membrane system. Homogeneous nucleation occurs through bulk crystallization followed by crystal deposition onto the membrane surface, whereas in heterogeneous nucleation, a nucleus forms directly at the surface of the membrane (adapted from [79]). .....	17
<b>Fig. 2-7.</b> Variation of Gibb’s free energy with particle reduces. The critical free energy ( $\Delta G_{crit}$ ) at $r=r_c$ is required to form a stable nucleus (adapted from [89])......	19
<b>Fig. 2-8.</b> Induction period as a function of saturation index for CaCO <sub>3</sub> precipitation at 25°C (adapted from [92, 94]) with dominant nucleation pathways indicated on the figure. ....	20

**Fig. 2-9.** Gypsum scaling on the membrane surface on SEM images (note: the experiment conducted using a feed solution at  $SI_{\text{gypsum}}$  of 1.01 on a membrane system with a permeate flux of 32–50 L/m<sup>2</sup>/h at 20°C and 689 kPa using TFC-ULP polyamide membrane; adapted from[85]) 21

**Fig. 2-10.** Schematic of RO desalting system integrated with ex-situ membrane surface monitoring [99] for early detection of mineral scale (adapted from [100]). ..... 24

**Fig. 2-11.** Variation of saturation indices with pH for brackish water at TDS of 11,020 ppm (from a site in California San Joaquin Valley [110]). ..... 25

**Fig. 2-12.** Description of scaling inhibition via addition of antiscalant (adapted from [118]). .... 26

**Fig. 2-13.** Schematic of simplified RO system with a high-pressure pump, where  $q_F$ ,  $q_C$ , and  $q_P$  are the flow rates of the feed, retentate, and permeate, respectively,  $c_F$ ,  $c_C$ ,  $c_P$ , and  $c_m$  are the concentrations at the feed, retentate, permeate, and at the membrane surface, respectively, and  $P_F$ ,  $P_C$ , and  $P_P$  are the pressures of the feed, retentate, and permeate, respectively. .... 27

**Fig. 2-14.** Schematic illustration of the thermodynamic restriction for crossflow RO desalting. As the brine osmotic pressure increases toward the membrane exit, the permeate flux diminishes. At the limit of the thermodynamic restriction, the applied pressure is at a level equivalent to the osmotic pressure in the brine stream exiting the membrane element. .... 29

**Fig. 2-15.** Comparison of RO process configurations in (a) single stage, (b) 2-stage, and (c) 3-stage RO with interstage booster pumps. The minimum applied pressure (for permeate production) is indicated with dotted curve. .... 30

**Fig. 2-16.** Schematic illustration of single-stage RO system with an energy recovery device (ERD: energy recovery device). .... 31

**Fig. 2-17.** Variation of the specific energy consumption normalized by the feed osmotic pressure, at the limit of the thermodynamic restriction, with respect to the fractional water recovery in a single-stage RO evaluated with and without an energy recovery device (as per **Eq. (2-19)** and **(2-20)**, respectively) for pump efficiencies of  $\eta_P=50, 80, 100\%$ . .... 32

**Fig. 2-18.** The SEC in RO desalination of seawater (35,000 mg/L TDS) at 50% water recovery relative to the theoretical minimum energy requirement (indicated by the dashed line) [22, 144, 145, 147]. .... 33

**Fig. 2-19.** Two-stage RO configuration with one high-pressure pump before the first stage, and a booster pump before the 2<sup>nd</sup> stage (adapted from [148]). ..... 34

**Fig. 2-20.** Example of (Left) pump, and (Right) ERD efficiency trends with respect to volumetric flow rate (adapted from [152] and [140], respectively). .... 35

**Fig. 2-21.** Schematics of RO desalination with partial concentrate recycle (i.e., the remainder concentrate water is discharged from the system) where  $c$  indicates salt concentration, and  $q$  indicates the volumetric flow rates ( $O$ : raw-feed,  $R$ : concentrate recycle,  $C$ : concentrate,  $D$ : concentrate discharge,  $P$ : permeate water). ..... 36

**Fig. 2-22.** Variation of the volumetric flows with respect to the overall system recovery for a constant permeate flow ( $q_P$ ) where  $Y$  is the per-pass water recovery. .... 37

**Fig. 2-23.** Schematic of SBRO process with two external holding tanks (T1 and T2) with a booster pump (BP), high pressure pump (HPP) and a circulation pump (CP) (adapted from [156]). ..... 38

**Fig. 2-24.** Schematic of the two modes of operation in semi-batch RO process without external holding tank: (a) the filtration process, (b) the flushing process with continuous permeate production. .... 39

**Fig. 2-25.** Variation of the cumulative volume of raw-feed water ( $Q_O$ ), the permeate production ( $Q_P$ ), and the concentrate discharge ( $Q_C$ , indicated with the shaded area between the  $Q_O$  and  $Q_P$  curves) during SBRO filtration and the flushing periods. The water recovery in each operating period is indicated on the secondary vertical axis. .... 40

**Fig. 2-26.** Comparison theoretical minimum specific energy cost (normalized by the raw-feed osmotic pressure) in semi-batch RO and steady-state RO with ERD on 1, 2, and 3 stages system platforms [29]..... 41

**Fig. 2-27.** Schematic of the two modes SBRO operation with holding tank: (a) the filtration process with total concentrate recycle, (b) the flushing process with raw feed water from the holding tank, and (c) the concentrate discharge process from the holding tank (adapted from [168]). ..... 42

**Fig. 2-28.** Variation of the feed pressure during semi-batch RO operation from a pilot-scale RO system for desalting brackish well water (at the Brackish Groundwater National Desalination Research Facility in Alamogordo, New Mexico) of 5,900 ppm TDS, feed flow rate ( $q_F$ ) of 0.6 gpm, and the permeate flux of 16 gfd (adapted from [165]) using brackish water spiral wound membrane (Filmtec BW30-2540, Dow Corporation, Midland, Michigan). ..... 43

**Fig. 2-29.** Variation of (a) feed pressure and feed conductivity, and (b) permeate conductivity with respect to time during SBRO operation for desalting brackish water pf 16,049 ppm TDS with BW30 brackish water RO membrane in a plate-and-frame membrane cell for overall water recovery at  $Y=35 - 40\%$  (adapted from [49])..... 44

**Fig 3-1.** Schematic illustration of the concept of process system decomposition in flexible RO. The membrane process unit (MPU) maintains constant (optimal) flow rate of feed, concentrate and permeate streams, and per-pass water recovery ( $Y_{SP}$ ), while the concentrate-recycle unit (CRU) provides control over the overall system water recovery ( $Y$ ) by fluid regulation (in source, concentrate discharge, and concentrate recycle streams). The MPU must integrate hydraulic

components for pressure-generation and energy recovery in addition to the membrane array for water treatment..... 53

**Fig. 3-2.** SSRO-PR configuration with an energy recovery device (ERD). The raw feed water pressure is raised from  $P_o$  to  $P_{FL}$  by the feed pump and the ERD intensifies the pump outflow stream pressure from  $P_{FL}$  to  $P_{FH}$  by utilizing the hydraulic pressure of the concentrate stream from the membrane module. Note:  $q_i$  and  $c_i$  and  $P_i$  are the flow rate, salt concentration and pressure of the indicated stream  $i$ . ..... 55

**Fig. 3-3.** Schematic diagram of the SSRO-PR system showing the location and arrangement of actuated valves, membrane module, energy recovery device (ERD), and pumps. Streams S1 and S2 are the raw feed streams before and after filtration pretreatment, respectively, and S3 and S4 represent the RO element feed and concentrate streams, respectively. Streams S6 and S7 are those of the concentrate recycle and discharge, respectively, and S8 and S9 are the recycled and discharged portions of the total concentrate stream, S6, respectively, during SSRO-PR operation ..... 62

**Fig. 3-4.** Variation of the volumetric flow rates normalized with respect to the permeate flow rate ( $q_P$ ) for a RO unit with a single spiral-wound element for operation with a constant  $Y_{SP}$  of 9.3%. The data for the RO unit were generated, for feed solutions of salinity in the range of 860 – 37,000 ppm, by varying the raw-feed and concentrate recycle flow rates to maintain a constant membrane element feed and permeate flow rates..... 66

**Fig. 3-5.** Variation of specific energy consumption ( $SEC$ ), normalized with respect to the osmotic pressure of the raw feed solution ( $\pi_o$ ), for operation up to the thermodynamic restriction and ideal membrane (i.e., 100% salt rejection), with respect to overall water recovery ( $Y$ ) and ERD efficiency ( $\eta_{ER}$ ) for: (a) SSRO-PR with single-pass water recovery of  $Y_{SP}=10\%$  (recycle ratio varied with overall recovery as per Eq. (3-2), and (b) conventional single-pass RO (SPRO) with an ERD (Eq. 3-12)..... 67

**Fig. 3-6.** Comparison of the  $SEC$  of SSRO-PR with single pass RO (SPRO, i.e., without concentrate recycle) for operation up to at the crossflow thermodynamic restriction (Section 2.2 for ideal membranes (i.e., 100% salt rejection) and for the case of as in Fig. 3, with respect to ERD efficiency for different levels of overall product water recovery ( $Y$ ). The single pass recovery was set as (a) 10% and (b) 50%. ..... 68

**Fig. 3-7.** (a) Variation of the RO module feed pressure ( $P_{FH}$ ) with respect to overall water recovery ( $Y$ ) for desalination of raw-feed water at various salinities ( $C_o$ ) at a constant membrane feed ( $q_F$ ) and permeate ( $q_P$ ) flow rates of 10.9 L/min and 1.0 L/min, respectively, for a SSRO-PR system utilizing a single 2.5-inch RO element (single-pass recovery of  $9.3\pm 0.3\%$ ) and observed salt rejection of  $97\pm 1\%$ . (b) RO feed pump outlet pressure required to achieve the RO module feed pressure for attaining the overall recoveries at the pressures indicated in Fig. 3-7(a). ..... 69

**Fig. 3-8.** Variation of the hydraulic pressure in each fluid stream involved in SSRO-PR system



described in described in **Fig. 3-3** with the membrane process unit (MPU) indicated with the shaded area (for treatment of 11,000 ppm *NaCl* source water at the target water recovery (*Y*) of 45% in test run#3.2, **Table 3-1**). ..... 70

**Fig. 3-9.** RO element specific energy consumption as experimentally determined (based on element feed pressure and normalized with respect to the raw-feed water osmotic pressure) compared with theoretical predictions (**Eq. 3-9**) as a function of overall water recovery (*Y*) for a range of raw-feed water salinities (**Table 3-1**). (Note: the SEC in units of kWh/m<sup>3</sup> can be obtained from  $SEC = A \cdot SEC^* \pi_o$  where the osmotic pressure  $\pi_o$  is given in bar and A=0.0278 is a proportionality constant). ..... 71

**Fig. 3-10.** A SSRO-PR configuration with a membrane array (MA) and an energy recovery device (ERD) installed in parallel with the feed pump (P1) and requiring a booster pump (P2). The recycled concentrate flow is adjusted with a flow regulator (FR). (Notation: *O*-raw feed, *C*-concentrate, *P*-permeate, *D*-discharge, *R*-recycled concentrate, *FL1*-combined raw feed (*O*) and recycle (*R*) streams, *FL2*-inlet flow to pump P1, *FL3*-split flow from *FL1* to ERD, *FL4*- feed from ERD to pump P2, *FH1* and *FH2* - pumps P1 and P2 outflows, respectively, and *FH3*-membrane feed into MA. .... 72

**Fig. 3-11.** An example of a RO configuration with an energy recovery device (ERD) installed as an interstage pressure booster between membrane stages 1 (MA1) and 2 (MA2). A flow regulator (FR) regulates the fraction of the concentrate that is recycled to the feed (*R*). Streams: *O*-raw feed, *R*-recycled concentrate, *F*- combined raw feed (*O*) and concentrate recycle (*R*), *D*-brine discharge, *FH1* – pump 1 outlet flow as feed into MA1, *FH2* – ERD outlet of MA1 Concentrate (*C1*) as feed to MA2, *C2* - concentrate from MA2, *C*- MA2 concentrate after ERD, *P1* - permeate from MA1, *P2* - permeate from MA2, and *P* – combined MA1 and MA2 permeate..... 73

**Fig. 4-1.** Semi-batch RO (SBRO) process showing the operational configurations of (a) filtration period (the control volume for salt balance in **Eq. (4-6)** is indicated by the dotted line), and (b) flushing period with continued permeate production. (MA - membrane array;  $C_i$  and  $q_i$  are the salt concentration and flow rate, respectively, where the subscript *i* denotes one of the following: *O*-raw feed, *F*- RO element feed, *P*- permeate, and *C*- concentrate. .... 78

**Fig. 4-2.** Overall SBRO system water recovery (*Y*) dependence on RO filtration time-flushing time ratio (i.e.,  $t_{FT}/t_{FL}$ ) and single-pass water recovery of  $Y_{SP} = 0.1, 0.3, 0.5$ , as per **Eq. (4-5)**..... 80

**Fig. 4-3.** Observed salt rejection ( $R_S$ ) for the present CSM RE2540-BE membrane ( $R_S=0.993\pm0.003$ ) and data for DOW XLE2540 membrane based on the data from [190]) ( $R_S=0.97\pm0.01$ ) demonstrating reasonable invariance of  $R_S$  with feed water salinity. .... 84

**Fig. 4-4.** Filtration and flushing periods time profiles of the normalized concentrate osmotic pressure at the RO element exit,  $\pi_c^* = \pi_c/\pi_o$ . SBRO operation is illustrated schematically over multiple cycles as per **Eqs. (4-11)** and **(4-18)** at fixed flushing efficacy of  $F(\Theta_{FL})=0.5, 0.7$  and  $1.0$ ,

flushing period of  $\Theta_{FL}=1$  and overall water recovery of 50% at a fixed single pass recovery of 10% and complete salt rejection (i.e.,  $R_S=1$ ). Note: the RO feed osmotic pressure for each cycle is related to the exit element osmotic pressure as described in **Section 4.2.2**..... 89

**Fig. 4-5.** Variation of the concentrate osmotic pressure at the beginning of each successive filtration period  $n$ ,  $(\pi_C^*)_{i,FT}^{(n)}$ , normalized by the raw-feed water osmotic pressure  $((\pi_C^*)_{i,FT}^{(n)} = (\pi_C)_{i,FT}^{(n)} / \pi_O)$  as per **Eq. (4-18)** at various level of flushing efficacy ( $F(\Theta_{FL})$ , **Eq. (4-14)**) of 0.5, 0.7, 0.8, 0.9, and 1.0 for a given flushing period of  $\Theta_{FL}=1$  for overall system recovery target of 50% (i.e.,  $Y=0.5$ ) with complete salt rejection ( $R_S=1$ ) and fixed single pass water recovery of 10% (i.e.,  $Y_{SP}=0.1$ ). (Note: element inlet osmotic pressure is determined as per the relation in **Section 4.2.2**). ..... 89

**Fig. 4-6.** The concentrate osmotic pressure at the RO element exit (i.e.,  $(\pi_C^*)_{i,FT}$ ) for the case in which the SBRO operation has reached its stable condition (i.e.,  $n \rightarrow \infty$ ) with respect to the overall water recovery,  $Y$  (as per **Eq. (4-22)**) at the flushing efficacy in the range of  $F(\Theta_{FL})= 0.5 - 1$  for a flushing period equal to the system convective residence time (i.e.,  $\Theta_{FL}=1$ ) for a membrane of 100% salt rejection, and fixed single pass water recovery of 10% (i.e.  $Y_{SP}=0.1$ ). ..... 91

**Fig. 4-7.** Specific energy consumption (SEC) in SBRO dependence on overall system recovery ( $Y$ ) and flushing effectiveness ( $F$ ) of duration  $\Theta_{FL}=1$ , at the thermodynamic restriction relative to ideal SBRO (i.e., complete concentrate flushing),  $(SEC_{SBRO,TR})_{ideal}$ , as per **Eqs. (4-31), (4-32)** and **(4-33)** for salt rejection ( $R_S$ ) of 100% and single-pass water recovery ( $Y_{SP}$ ) of 10%. The dashed curve represents the SEC at the thermodynamic limit for SPRO relative to ideal SBRO. .... 98

**Fig. 4-8.** Variation of the permeate flux at the membrane exit ( $J_{v,exit}$ ) relative to the average permeate flux ( $\bar{J}_v$ ), as per **Eq. (4-28)** at various level of normalized average permeate flux,  $\bar{J}_v^* = \bar{J}_v / (L_p \cdot \pi_O) = 1, 2, \text{ and } 10$  with respect single pass water recovery ( $Y_{SP}$ ) for ideal membrane (i.e., 100% salt rejection). The  $\bar{J}_v^*$  for the RO system utilized for the present study was 12.5 as indicated on the figure. .... 100

**Fig. 4-9.** Experimental setup for SBRO operation with a RO stage consisting of a single element (MA) where  $C_i$ , and  $q_i$  indicate salt concentration and flow rate of stream  $i$  (note: subscript  $i$  denotes one of the following:  $O$ -raw feed,  $F$ -RO element feed,  $C$ -RO concentrate,  $P$ -permeate, and  $D$ -brine discharge stream). ..... 102

**Fig. 4-10.** Temporal profiles of SBRO concentrate stream salinity (mg/L TDS) at the RO element exit for cyclic SBRO at overall water recovery ( $Y$ ) of 79% (Runs #2d, 3d, and 4d; **Table 4-1**) for a fixed permeate ( $q_P$ ) and RO element feed ( $q_F$ ) flow rates (**Table 4-1**) and for flushing duration of  $\Theta_{FL}=1, 2.2 \text{ and } 4.4$ . The dashed lines represent the element exit concentrate salinity at the beginning and end of each filtration cycle. Note: the RO element feed salinity is related to the exit

element salinity as per  $C_F/C_C = (1 - Y_{SP}) / (1 - (1 - R_S)Y_{SP})$  (Section 4.2.2). ..... 105

**Fig. 4-11.** Predictions (solid lines) and experimental data (filled circles) of salinity profile (as per Eq. (4-11)) during a filtration period for multiple cycles for Test Run #2d (Table 1) for SBRO operation at overall recovery of 79% and raw feed salinity of 1,000 mg/L TDS. .... 106

**Fig. 4-12.** SBRO concentrate salinity (mg/L, TDS) at the RO element exit for stable cycle-to-cycle SBRO operation for overall water recovery of 46%-79% and flushing period of  $\Theta_{FL} = 1$  (Runs 2a, 2b, and 2d, Table 4-1). The dashed lines indicate as a reference the salinity at the SBRO element exit at the filtration period beginning ( $(C_C)_{i,FT}^{n=1}$ ) and end ( $(C_C)_{f,FT}^{n=1}$ ). ..... 108

**Fig. 4-13.** Salinity of the concentrate exiting the RO unit ( $C_C$ ) in stable cycle-to-cycle SBRO operation for water recovery of 46 % and flushing durations of (a)  $\Theta_{FL} = 1.0$ , (b)  $\Theta_{FL} = 2.2$ , and (c)  $\Theta_{FL} = 4.4$ . ..... 108

**Fig. 4-14.** Salinity of the concentrate exiting the RO unit ( $C_C$ ) in stable cycle-to-cycle SBRO operation for water recovery ( $Y$ ) of 62 % for flushing durations of (a)  $\Theta_{FL} = 1.0$ , (b)  $\Theta_{FL} = 2.2$ , and (c)  $\Theta_{FL} = 4.4$ . ..... 109

**Fig. 4-15.** Salinity of the concentrate exiting the RO unit ( $C_C$ ) in stable cycle-to-cycle SBRO operation for water recovery ( $Y$ ) range of 74% for flushing durations of (a)  $\Theta_{FL} = 1.0$ , (b)  $\Theta_{FL} = 2.2$ , and (c)  $\Theta_{FL} = 4.4$ . ..... 109

**Fig. 4-16.** Salinity of the salinity of the concentrate exiting the RO unit ( $C_C$ ) in stable cycle-to-cycle SBRO operation for water recovery ( $Y$ ) of 79 % for flushing durations of (a)  $\Theta_{FL} = 1.0$ , (b)  $\Theta_{FL} = 2.2$ , and (c)  $\Theta_{FL} = 4.4$ . ..... 110

**Fig. 4-17.** Variation of the flushing efficacy  $F(\Theta_{FL})$  (Eq. (4-35), Section 4.2.3) with flushing time ( $\Theta = t/\tau$ , where  $t$  and  $\tau$  are the time and the convective residence time) in response to a change in SBRO operation from total concentrate recycle to a single-pass RO operation (i.e., SPRO) for raw feed salinity of 1,000 mg/L TDS. Note:  $F(\Theta_{FL})$  is shown for the cases of concentrate salinity at the SBRO element exit at the end of the filtration periods (i.e., prior to flushing) of 5,578 and 16,770 mg/L TDS. .... 111

**Fig. 4-18.** Cumulative RTD function (Section 2.3) for spiral wound RO elements based on data reported in [44, 45] for 2.5” bench-scale (BW2530, FILMTEC) spiral wound RO elements in [44] and for 8” industrial module (SWC1, Hydronautics) in new and worn condition in [45] at cross flow velocity of about 4, 7, and 10 cm/s, respectively. .... 112

**Fig. 4-19.** The range of SBRO membrane element inlet applied feed pressure ( $\Delta P_f$ ) at different

levels of overall water recovery ( $Y$ ) for flushing durations ( $\Theta_{FL}$ ) of (a) 1.0 (Run #1), (b) 2.2 (Run#2), and (c) 4.4 (Run #4) where the range of  $F(\Theta_{FL})$  values are provided in **Table 4-1**. The upper solid curve and horizontal solid line represent the applied pressure for ideal SBRO operation at the beginning,  $(\Delta P_f)_{min}$ , and end,  $(\Delta P_f)_{max}$ , of the filtration period, respectively; Note, ideal SBRO operation refers to complete flushing (i.e.,  $F(\Theta_{FL})=1.0$  as; **Eqs. (4-11), (4-25), and (4-28)**). Note: the upper horizontal axis provides the filtration time ( $\Theta_{FT}$ ) scale based on **Eq. (4-5)** for the indicated flushing duration. ....113

**Fig. 4-20.** RO element specific energy consumption (SEC) experimentally determined as per **Eq. (4-23)** (based on element feed pressure and normalized with respect to the raw-feed water osmotic pressure) as a function of overall water recovery ( $Y$ ) compared with theoretical predictions as per **Eq. (4-29)** at  $\Theta_{FL}=1.0, 2.2,$  and  $4.4$  with fixed salt rejection  $R_S=99.7\%$  and single pass water recovery  $Y_{SP}=9.2\%$ . The results were compared with theoretical predictions in **Eq. (4-33)** for single-pass RO (SPRO; [190]) as well as SBRO operation with ideal flushing of duration equal to the convective residence time (i.e.,  $F(\Theta_{FL})=1$  and where  $\Theta_{FL}=1.0$ ). .....115

**Fig. 5-1.** Schematic of the experimental setup, for the RO system and the membrane scaling tests that utilized a membrane surface monitoring (MeSuM) system, for the operational modes of: (a) SBRO filtration, (b) SBRO flushing, and (c) SSRO-PR desalting. Streams S1 and S2 are the raw feed streams before and after filtration pretreatment, respectively; S3 and S4 denote the RO element feed and concentrate streams, respectively; streams S6 and S7 are those of the concentrate recycle and discharge, respectively; and stream S9 is the discharged flow portion of concentrate stream S6 during SSRO-PR operation, (d) pilot scale RO system and MeSuM with i) single spiral-wound element in a pressure vessel, ii) pre-treatment cartridge filters, iii) system controls and data acquisition/processing, iv) dark chamber for plate-and-frame membrane cell, v) imaging system. .... 122

**Fig. 5-2.** Membrane Surface Monitoring system (MeSuM) (a) 3-D design of the membrane cell with 1) permeate port, 2) feed port, 3) concentrate port, 4) a digital camera, 5) 3D slide table, 6) the mechanical valve, V2 (**Fig. 5-1**), (b) photograph of the plate-and-frame acrylic membrane cell blocks with 7) o-ring, 8) and stainless steel plate spacer, and 9) engraved feed channel, (c) photograph of the assembled MeSuM system, and (d) photograph of the system with 10) the stainless-steel dark cover, 11) peristaltic pump for DI water flushing, and 12) electrical box... 126

**Fig. 5-3.** Graphical user interface on the Membrane Monitoring system..... 127

**Fig. 5-4.** Prediction of gypsum saturation index at the membrane surface (at the element exit), at the end of a filtration period, i.e.,  $(SI_{g,m})_{exit}^f$ , for the raw feed solution of  $SI_g=0.4$  (**Table 5-1**) and at a given  $(SI_{g,m})_{exit}^o$  of 0.73 (same as test condition #1a, **Table 5-2**) at the beginning of the filtration period in stable SBRO operation with flushing periods of (a)  $\Theta_{FL}= 1$  and (b)  $\Theta_{FL}= 3$  for an element single-pass recovery of  $Y_{SP}=9.5\%$ . ..... 133

**Fig. 5-5.** Profiles of gypsum saturation index at membrane surface (at the RO element exit) during SBRO and SSRO-PR tests (a) #1a, (b) #1b, and (c) #1c, for which the time-average  $(SI_{g,m})_{exit}$  was 1.2, 1.6 and 1.9, respectively, as indicated with dashed horizontal lines (also designating the conditions for SSRO-PR operation)..... 135

**Fig. 5-6.** Salinity (mg/L, TDS) - time profiles of RO concentrate at the element exit and the corresponding RO element feed pressure during SBRO and SSRO-PR (solid dashed horizontal lines) operations (test runs #1 and #2, **Table 5-2**) at equivalent  $(SI_{g,m})_{exit}$  of (a) 1.2, (b) 1.6, and (c) 1.9, respectively, with the corresponding overall RO recovery range of 40% - 65%..... 136

**Fig. 5-7.** Development of membrane surface scaling by gypsum crystals at  $t = 12$  and 24 h during (a) SBRO and (b) SSRO-PR scaling test (run #1a and #2a, respectively, **Table 5-2**) at overall water recovery of  $Y=50$  and 40%, respectively and at the same average saturation index at membrane wall of  $SI_{g,m} = 1.2$ . The inset views are processed images of smaller segments of the monitored area. The diagonal streaks (indicated with an arrow) are impressions resulting from the membrane spacer..... 137

**Fig. 5-8.** Evolution of gypsum crystal number density,  $\bar{N}$ , (# of crystals/surface area) on the membrane surface in SBRO and SSRO-PR operations at various level of gypsum saturation index at membrane wall ( $SI_{g,m}$ ). Note: The  $SI_{g,m}$  varies with time in SBRO (as illustrated in **Fig. 5-5**), and thus the time average of  $SI_{g,m}$  was indicated on the figure..... 138

**Fig. 5-9.** Variation of the crystallization induction time ( $t_{Ci}$ ) with respect to the gypsum saturation index at the membrane surface,  $(SI_{g,m})_{exit}$ , at RO element exit. The vertical data bars indicate the  $(SI_{g,m})_{exit}$  range and average values during SBRO operation and filled circles denote the SSRO-PR  $(SI_{g,m})_{exit}$  value equal to the indicated time-average value in SBRO operation (**Fig. 5-5**)...... 139

**Fig. 5-10.** Progression of percent membrane surface coverage by gypsum scale during SSRO-PR and multi-cycle SBRO operations at gypsum supersaturation level of  $SI_{g,m} = 1.2 - 1.9$ ..... 141

**Fig. 5-11.** Gypsum crystal growth ( $A_0$  is the initial area of the tracked crystal) at the time-average SBRO  $(SI_{g,m})_{exit}$  of 1.2, 1.6 and 1.9 (**Table 5-2**) and at the equivalent values for SSRO-PR operation. The data represent the average over 3-5 separate gypsum crystals of initial areas in the range of  $A_0 = 40 - 80 \mu\text{m}^2$  with vertical bars indicating the minimum and maximum values. (Note: the observed crystallization induction times at the indicated  $(SI_{g,m})_{exit}$  values are provided in **Fig. 5-9** and **Table 5-3**)...... 143

**Fig. 5-12.** (a) Growth of gypsum crystal (located at RO element exit) during a single filtration period of up to 20 min, as per the diffusional growth model (**Eq. (5-5)**), for SBRO operation in which the level of gypsum saturation at the beginning of the flushing period was set as  $(SI_{g,m})_{exit}^o = 0.73, 0.86, \text{ and } 0.99$ , corresponding to conditions of test run #1a, 1b, and 1c, respectively (**Table 5-2**) with (a) raw feed water saturation of  $SI_g = 0.4$  (**Table 5-1**), and  $(SI_{g,m})_{exit}^o = 0.25$  (with

corresponding raw feed  $SI_g$  of 0.18, indicated with dotted line), and (b) Variation of  $(SI_{g,m})_{exit}$  during the filtration period, obtained as per the approach described in **Section 5.3.4**, and **Section 5.4.1**. The analysis assumed complete membrane solute rejection,  $Y_{SP}$  of 9.5%, gypsum ion diffusivity ( $D$ ) of  $9.23 \times 10^{-6} \text{ cm}^2/\text{s}$  [62], effective crystal density ( $\rho_s$ ) of  $2.7 \text{ g/cm}^3$  [87], and membrane  $15 \text{ cm/s}$  channel cross-flow velocity. .... 146

**Fig. 5-13.** Gypsum crystal (located at RO element exit) diameter (of initial size  $d_0=0.5 - 5 \mu\text{m}$ ) decrease due to dissolution during flushing period for a gypsum supersaturation index at the membrane surface at the element exit,  $(SI_{g,m})_{exit}$ , of (a) 0.5 and (b) 0.1. It is noted that crystals of the size formed by the end of a filtration period, as illustrated in **Fig. 5-12**. would not dissolve to any significant degree over a flushing time greater by even a factor of about three greater than the 100 s flushing time employed in the current study. .... 148

**Fig. A.1** Process flow diagram of FLERO RO system. Steams S1 and S2 are the raw feed streams before and after filtration pretreatment, respectively, and S3 and S4 represent the RO element feed and concentrate streams, respectively. Streams S6 and S7 are those of the concentrate recycle and discharge, respectively, and S9 is the discharged flow portion of the concentrate stream S6. Pressure, flow rate, and conductivity transmitters are indicated with PT, FT and CT, respectively. .... 150

**Fig. A.2.** FLERO system showing: (a) physical design with components layout, (b) system body construction, (c) electrical circuit box, and (d) assembled spiral wound RO system with permeate production capacity of  $\sim 400$  gallons/day at various water recoveries up to 90% where 1) DC motor for the main pump, 2) the port for feed and the concentrate streams 3) aluminum cooling block for electrical box, 4) electrical box with a computer and input/output module 5) pressure vessel for a single 2.4 in x 40 in RO membrane element, 6) port for the raw feed stream 7) cartridge filters in pretreatment module, 8) feed tank, 9) pressure transmitters, 10) power cord (110V AC). .... 151

**Fig. A.3.** Flexible RO process control strategy. Black solid arrows indicate the direction of water flow, and dotted arrows indicate the signal toward the actuators and controllers. .... 153

**Fig. A.4.** Graphical user interface of the pilot FLERO system with 1) system status/warning message box, 2) system status indicators for power, pressure, and temperature, 3) process control box for operating modes (i.e., semi-batch, continuous, etc.), operation time, and overall water recovery, 4) control box for flow automation, 5) features for data monitoring and storage, 6) real-time graphical report of fluid configuration and sensor measurements. .... 154

**Fig. A.5.** Pressure relief valve on the pressure intensifier (Clark Pump, Spectra Watermakers, San Rafael, CA). .... 155

**Fig. B.1.** Water system in a small remote community without (a) and with (b) RO water treatment with concentrate recycle. 158

**Fig. B.2.** Onsite testing of RO well water treatment for the study communities. The RO test system (**Appendix A**) was operated at water recovery of 90% in SSRO-PR. The dashed line denotes the nitrate MCL (10 mg/L as N) and the recommended upper salinity level (500 mg/L TDS) for drinking water. The error bar indicates the salinity and nitrate range of measurement uncertainty. .... 162

**Fig. B.3.** Nitrate concentration in the RO product water for treatment using a high nitrate rejection membrane (M-2) over a range of product water recovery for initial feed nitrate concentration of 13-40 mg/L as N. The solid curves are prediction of  $C_p = C_0 \cdot (1 - R_s)(1 - Y_{sp}) / [1 - R_s Y - Y_{sp}(1 - R_s)]$  (as per **Equations (3-16) and (3-17), Section 3.2.3**). (Note: RO recovery must be maintained below 94%-99% in order to ensure that the product water meets both the MCL and SMCL with respect to nitrate and salinity, respectively, and that the feed pressure remains below the maximum allowed pressure for the RO element)..... 163

## List of Tables

<b>Table 2-1.</b> Induction times at various saturation level for CaSO <sub>4</sub> .....	23
<b>Table 2-2</b> Recommended system configuration with commercial spiral wound RO membranes	35
<b>Table 2-3.</b> Relevant prior work on high recovery RO desalination with concentrate recycling. .	46
<b>Table 3-1.</b> SSRO-PR desalination experimental conditions.....	65
<b>Table 4-1.</b> SBRO experimental conditions.....	104
<b>Table 5-1.</b> RO Feed solution.....	121
<b>Table 5-2.</b> Experimental conditions.....	130
<b>Table 5-3.</b> Observed crystallization induction time.....	137
<b>Table A-1</b> In-line sensor positions and measurement ranges. ....	152
<b>Table B-1.</b> Study sites.....	161
<b>Table B-2.</b> Summary of water quality analysis .....	161



## **Acknowledgements**

I would like to thank my advisor Prof. Yoram Cohen for his unqualified guidance, supports and instruction throughout my study in UCLA. He has demonstrated, by example, the growth and achievement in science can only be made via continuous self-examination and unlimited curiosity. I must also thank Dr. Anditya Rahardianto for providing me the opportunity to work on challenging problems across multiple disciplines. Special thanks to undergraduate laboratory assistants Yeunha Kim, Yian Chen, Alhad Deshpande, and Adria Gojgini for bringing tremendous creativity and motivation to our group and my study. Lastly, I truly appreciate the patience, support, and understanding from my loving family, Yue-Fei Lee, Eunyue Lee, and Eun-Ah Lee. This work was supported by California Department of Water Resources, U.S. Bureau of Reclamation, Electric Power Research Institution, Naval Facilities Engineering Command, United States Office of Naval Research, and UCLA Water Technology Research (WaTeR) Center. Lastly, I would also like to acknowledge the support from Korean Institute of Chemical Engineers (KIChE), Hanwha Total/Chemical company, and North American Membrane Society (NAMS) for generous fellowship awards.

## VITA

July 28, 1982	Born: Seoul, S. Korea
2007	B.S. Chemical Engineering University of California, Berkeley
2008-2011	Samsung Austin Semiconductor, LLC
2011-2012	Lam Research Corporation

## PUBLICATIONS AND PRESENTATIONS

1. **T. Lee**, A. Rahardianto, Y. Cohen\*, (2019) “Flexible reverse osmosis (FLERO) desalination, *Desalination*, 452, 123-131.
2. **T. Lee**, A. Rahardianto, Y. Cohen\*, (2019) “Multi-Cycle Operation of Semi-Batch Reverse Osmosis (SBRO) Desalination”, *Journal of Membrane Science*, (*In Press*).
3. **T. Lee**, J.Y. Choi, Y. Cohen\*, (2019) “Gypsum Scaling Propensity in Semi-Batch RO and Steady-State RO with Partial Recycle (SSRO-PR)”, *Journal of Membrane Science*, (*In Press*).
4. J. Choi, **T. Lee**, Y. Chen, A. Rahardianto, and Y. Cohen\*, (2019) “On the Feasibility of Nitrate Removal from Impaired Small Community Well Water via a Novel Flexible RO (FLERO) System”, *Journal of Environmental Management*, (*In Review*).
5. J. Choi, **T. Lee**, Y. Cohen\*, et al., (2019) “Observed Induction Time in Seeded Gypsum Crystallization”, *Industrial & Engineering Chemistry Research*, (*In Review*).
6. J. Choi, **T. Lee**, Y. Chen, A. Rahardianto, Y. Cohen\*, (2019) “Novel flexible RO system (FLERO) Integrated with Portable Online Monitoring System for Nitrate and Salinity Reduction in Remote Communities”, (*In Preparation* >70%).
7. Y. Cohen, A. Rahardianto, **T. Lee**, (2016) “System and method for flexible low-energy membrane-based liquid purification”, *U.S. Patent Application* No. US20170334747A1.
8. Y. Cohen, A. Rahardianto, **T. Lee**, (2017) “Autonomous Low Energy Consumption Cyclic Desalination Systems”, U.S. Department of the Interior Bureau of Reclamation,

Desalination and Water Purification Research and Development Program Report No. 179.

9. **T. Lee**, A. Rahardianto, Y. (2018) Cohen, Impact of intermittent feed water flushing on surface mineral scaling during semi-batch reverse osmosis operation, AIChE Conference, Pittsburgh, PA and 2018 NAMS Conference Lexington, KY
10. **T. Lee**, A. Rahardianto, Y. (2017) Cohen, Energy consumption for semi-batch RO desalination, International Congress on Membranes and Membrane Processes (ICOM), San Francisco, CA
11. **T. Lee**, A. Rahardianto, Y. Cohen, (2017) Application of Semi-Batch Reverse Osmosis (RO) Operation for Water Purification in Small Communities, AIChE Conference, Minneapolis, MN
12. **T. Lee**, A. Rahardianto, Y. Cohen, (2016) Operational Flexibility of Process Systems for Membrane-based Water Treatment and Desalination, AIChE Conference, San Francisco, CA
13. **T. Lee**, A. Rahardianto, Y. Cohen, (2016) Small flexible reverse osmosis system for off-grid water purification and desalination, North American Membrane Society (NAMS) Conference, Seattle, WA

# Chapter 1 Introduction

## 1.1 Background

Population rise, increased agricultural and livestock production, environmental pollution, and impending impact of global climate change have created imminent threats to water sustainability [1-5]. Presently, nearly 25% of the world population (~1.9 billion people) lives in regions of water scarcity, and it is estimated that 2/3 will be living under water-stressed conditions by 2030 [6]. In this regard, continued advancements in water treatment technologies remain critical to address rising disparities in water availability and demand [7, 8]. In order to diversify the portfolio of safe water resources, desalination methods have been established to separate the dissolved salts from the feed stream producing permeate water of low salt contents.

Early desalination methods, which used thermal processing, include multi-stage flash (MSF), multiple effect distillation (MED), and vapor compression (VC) (**Fig. 1-1**). Thermal processing uses thermal and electrical energy for vaporization and condensation to attain high quality product water.

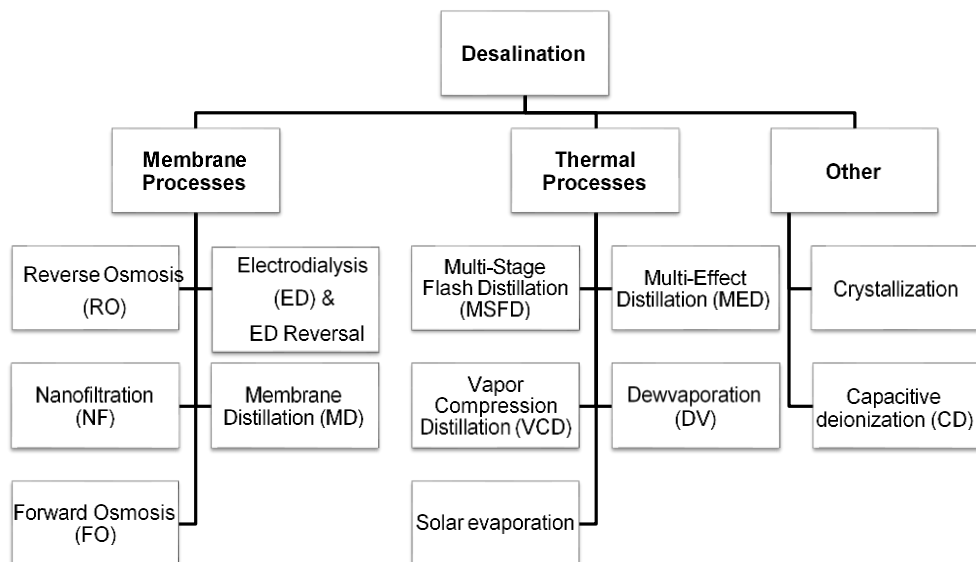


**Fig. 1-1.** Desalination technologies

On the other hand, membrane processes (e.g., forward osmosis, membrane distillation, reverse osmosis, etc.) utilize semi-permeable membrane, which allow selective permeation of water molecules while rejecting most dissolved salts achieving separation of permeate water from concentrate (brine) water. RO is a process where external pressure is exerted on the feed-side of RO membrane, which has higher selectivity for water relative to dissolved salts. As a result, clean permeate water is separated (desalinated) by the RO membrane as product from the concentrate (brine) stream (**Fig. 1-2**).

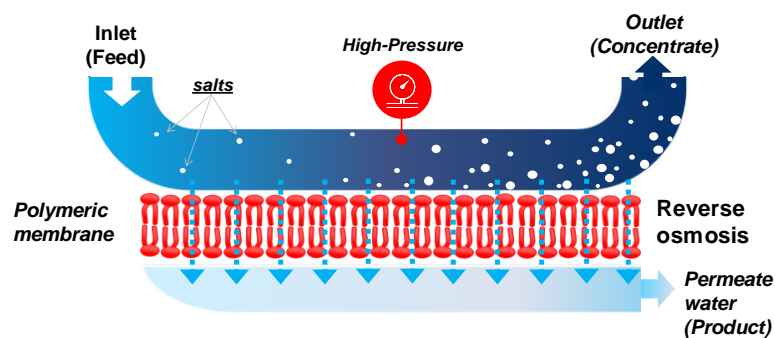


**Fig. 1-2.** Reverse osmosis membrane desalination.

With development of highly permeate membranes in the mid 1990's [9] coupled with advances in hydraulic energy recovery devices (ERD) [10], RO has gained popularity for its operational simplicity and reliability given its diverse and well-established supply chain of off-the-shelf components and consumables (e.g., membrane elements, prefilters, compatible water treatment additives and membrane cleaning chemicals, etc.) [11-13]. The RO process is easily scalable whereby both small- and large-scale RO plants can use similar types of membrane elements and pressure vessels (**Fig. 1-3**). RO accounts for about 65% of the present worldwide desalination capacity [12, 14, 15], followed by multi-stage flash evaporation (21%) with 14% of the remaining capacity being due to MED, VC, and electrodialysis (ED). (**Fig. 1-1**). Other desalination methods that have been explored include forward osmosis and membrane distillation.

Forward osmosis (FO) is an osmotic process utilizing thermolytic draw solution to extract permeate water from the saline feed solution. Membrane distillation (MD), on the other hand, is a thermally driven membrane separation, which takes advantage of high selectivity of water vapor across the membrane pores. Applications of FO and MD processes are limited, relative to pressure-driven reverse osmosis (RO), as they require locally available low-grade heat sources [16, 17].



**Fig. 1-3.** (Left) Photograph of the desalination plant at Orange County, California (Capacity of 378,000 m<sup>3</sup>/day) [18], and (Right) a small mobile RO desalination plant (capacity of 45.4 m<sup>3</sup>/day) [19, 20]. The same size membrane elements (8”) are used in both plants demonstrating the scalability of RO desalination.

Desalination is generally categorized based on the source water salinity. Brackish water is considered to be of salinity above 1,000 mg/L total dissolved solids (TDS), but below that of seawater being in the range of ~33,000 mg/L – 42,000 mg/L TDS. Owing to constructions of mega-sized RO desalination plants, the current worldwide total desalination capacity reached 95.4 million m<sup>3</sup>/day of which seawater desalination constitutes 59%, followed by inland brackish water (22%), and river water desalination (19%) [21-23]. For example, in little over a decade, Israel achieved upto drinking water for 60% of their population from mega-sized RO desalination plants: Ashkelon with water production capacity of 396,000 m<sup>3</sup>/day; Hadera with 525,000 m<sup>3</sup>/ day; and Sorek (the world's largest operating plant) with 624,000 m<sup>3</sup>/day [24, 25]. In the United States, the largest seawater desalination plant in the western hemisphere was constructed in Carlsbad, California (2016), to convert upto 204,000

m<sup>3</sup>/day of Pacific seawater into drinking water. Presently, about 18,000 desalination plants are operated yearly producing 35 billion m<sup>3</sup> desalinated water in 150 countries around the globe. The production capacity is expected to increase by 54 billion m<sup>3</sup> per year by 2030 [23, 26].

RO systems are designed with a single or multiple stages (**Fig. 1-4a** and **Fig. 1-4b**, respectively), which can have multiple pressure vessels with membrane elements. The number of stages and membrane elements are adjusted depending on the quality of the source water and the target overall water recovery, defined as the volume of product water per unit volume of feed water. For multi-stage RO systems, the concentrate (or reject) of each stage becomes the feed stream for the following stage to increase overall water recovery.

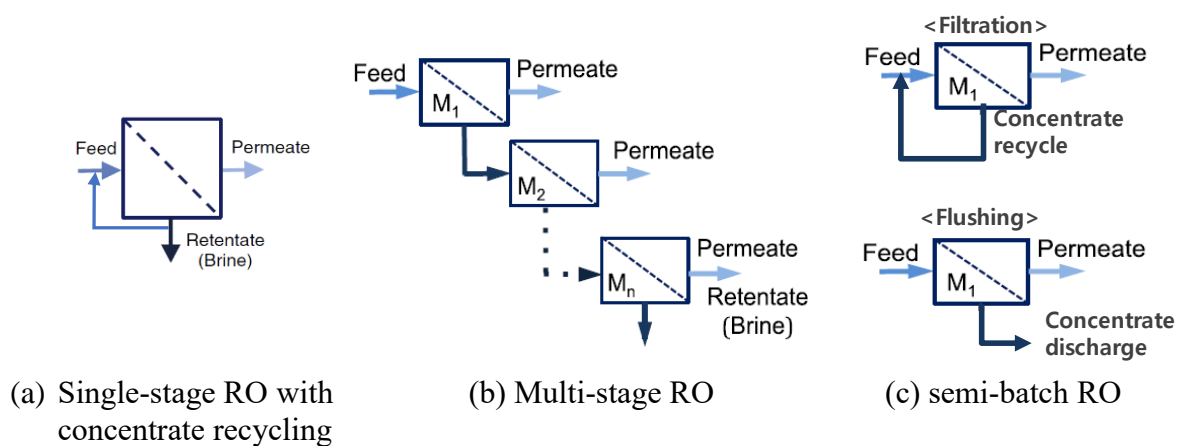


**Fig. 1-4.** Examples of different RO system configurations.

Multi-stage configuration is advantageous in maintaining the permeate flux across the entire feed channel by implementing the inter-stage booster pump (BP), which also reduces energy cost by eliminating the necessity for high capacity feed pump for the first stage [27]. Given the complexity of membrane network, coupled with incorporation of various types of hydraulic components (e.g., high pressure pump, booster pump, energy recovery device, etc.), multi-stage configuration is generally considered adequate for large scale desalination plants

operated under constant treatment targets (e.g., permeate productivity, water recovery) and feed water composition (e.g., seawater).

For RO systems that cannot be properly staged (e.g., due to limited system footprint), a concentrate recycle can be utilized where a portion of the concentrate stream is recycled and mixed with the raw feed water, then fed back to the membrane elements to help increase the system recovery (**Fig. 1-4a**). RO operation with concentrate recycling is an effective method to reduce installation cost given that the number of system components (membranes, BP, etc.) can be reduced [28-35]. Concentrate recycling for high recovery operation also alleviates environmental concern from disposal of the highly concentrated brine water (particularly in inland brackish water desalination [36]). However, the necessity of operating at increased flux to maintain production capacity demands higher applied pressure as well as membranes of low fouling and mineral scaling (e.g., deposition of colloidal particles, organic and inorganic constituents onto the membrane surface) [37-40]. Accordingly, the range of attainable overall water recovery with concentrate recycling is generally limited (a) to avoid (or reduce) the onset of membrane fouling or scaling, and (b) to maintain the applied pressure within allowed operating range. Accordingly, optimal operational strategies are needed to optimize energy consumption and membrane fouling/scaling resistance while maximizing product water recovery.

Depending on the operational characteristics of the RO processes, concentrate recycling for constant permeate productivity (i.e., without frequent operator intervention causing system downtime) can be generally categorized into steady state RO with partial concentrate recycling (SSRO-PR) and semi-batch (SBRO) (**Fig. 1-4a** and **Fig. 1-4c**, respectively). In SSRO-PR, a portion of brine effluent is diverted into the raw-feed stream, while the remainder is discharged.



SSRO-PR enables a control over cross flow velocity in the concentrate channel to for minimal concentration polarization effect [37, 44] maintaining optimal operating range for hydraulic components (e.g., high-pressure pump, circulation pump, etc.) and low saturation level at the membrane wall. Concentrate recycling provides an additional degree of freedom with respect to product water recovery [32, 41]. However, increased target water recovery in SSRO-PR requires higher energy input, and thus there will always be a tradeoff between the desired water productivity and energy utilization. In this regard, it is expected that integration of suitable energy recovery devices for RO operations with concentrate recycling should provide additional flexibility enabling desalting operation over a wide range of salinity. Thus, to investigate the potential of SSRO-PR operation with energy recovery, it is necessary to develop accurate analysis framework to map out its energy footprint and technical feasibility.

Semi-batch RO (SBRO, **Fig. 1-4c**) is inherently unsteady state that is characterized by cyclic operation of RO filtration and concentrate flushing. During the RO filtration period, the concentrate stream is continuously mixed with the raw-feed water, supplied at a rate equivalent to the permeate production to achieve 100% water recovery. As a result, salts accumulate in the concentrate (i.e., feed) channel requiring periodic raw feed water flushing to refresh the concentrate channel. During the RO filtration period, the applied pressure is gradually increased to maintain constant permeate flux, and compensate for the rise in osmotic pressure upon total concentrate recycling in the RO filtration period. Accordingly, the energy cost in SBRO with sufficiently small single pass water recovery theoretically approaches to that of multi-stage RO with infinite stages [42]. Theoretical prediction of energy consumption for SBRO operation has been established by many researchers for idealistic plug flow assuming complete concentrate flushing using the volume of raw feed water equivalent to the volume of

the membrane vessel [27, 42, 43]. However, these conditions are not often encountered in practical application [44, 45] given complex hydrodynamics conditions within the concentrate channel due to the presence of channel spacers [46, 47]. Thus, it is essential to develop accurate characterization of cleaning efficacy during the flushing period to properly analyze the energy footprint of SBRO relative to conventional single pass RO without concentrate recycle (SSRO-SP) or SSRO-PR.

Recent studies [48, 49] have suggested that mineral scaling in RO desalting can be averted to some degree in SBRO operation where the system is periodically flushed with the undersaturated raw feed water. During the concentrate flushing period, the holdup brine (i.e., “concentrate”) in the RO system is flushed (discharged) out of the system with the RO raw feed water, while permeate production may be continued [50] (depending on the set feed pressure) at a recovery that is governed by the system configuration in a continuous single pass RO. It has been argued that, SBRO flushing should return the RO membrane to its clean condition, thus reducing the propensity for mineral salt nucleation and growth [48] or resetting of the mineral salt “crystallization induction clock” [51, 52].

In SBRO, the concentration of total dissolved solids increases over the course of each filtration cycle. Accordingly, depending on the feed water saturation and system operating conditions (i.e., permeate flux and crossflow velocity), the concentration of sparingly soluble mineral salts can exceed saturation. However, periodic flushing aims to discharge the accumulated concentrate volume in the RO system and restore the system to its initial filtration condition (i.e., the first cycle). Therefore, it is reasonable to ponder as to the impact of such cyclic filtration and flushing operation on mineral scaling propensity. Here we note that steady state RO with partial recycle (SSRO-PR) also typically aims to achieve high recovery with a

smaller system footprint relative to conventional SSRO-SP operation. In both SBRO and SSRO-PR the RO concentrate is recycled and thus it is of interest to compare the propensity for mineral scaling in the above two approaches.

## **1.2 Problem statement**

To alleviate environmental concern and reduce costs for concentrate (brine) disposal in RO processes, it is desired to increase permeate water recovery. Concentration recycling is an effective method to increase the overall RO water recovery at a reduced system footprint, thereby enhancing operational flexibility. In RO desalting with concentrate recycling, a portion of the concentrate (reject) stream from the membrane element train is recirculated to attain the desired level of water recovery. While continuous concentrate discharge is allowed in steady state RO operation with concentrate recycling (SSRO-PR), total concentrate recycle is employed in semi-batch RO operation (SBRO); the latter requiring periodic concentrate flushing. Elevated water recovery via concentrate recycling method leads to higher operating range of the RO concentrate salinity, which in turn increases the osmotic pressure and the saturation level of mineral scalants.

It is known that the salinity at the membrane surface dictate the osmotic pressure across the RO membrane as well as the saturation level of mineral scalants. Therefore, the RO concentrate salinity at the membrane surface must be determined in order to quantify energy consumption and mineral scaling propensity. However, given the interplay of hydrodynamics and salts dispersion in the membrane channel, it is difficult to determine the variation of RO concentrate salinity particularly in cyclic SBRO operation. The above is due to the presence of salt dispersion in the feed channel, which may cause incomplete feed water replacement or

membrane surface cleaning within the given flushing period. It is necessary to characterize the flushing efficacy for a given membrane in order to develop a predictive model for membrane surface concentration during SBRO desalting with concentrate recycling. Predictive models, based on adequate engineering fundamentals including mass transfer, and steady- and unsteady state material balances, is vital for the design and optimization of RO desalting with concentrate recycling.

### **1.3 Research objectives**

The goal of the present study was to develop a theoretical framework for evaluating reverse osmosis (RO) membrane desalting with concentrate recycling with respect to water recovery and energy consumption. Based on fundamental process models, which account for solute material balances and permeate flux, a predictive approach was developed for (a) solute concentration within the RO circuit and at the membrane element exit, and (b) RO element feed pressure, both for unsteady-state semi-batch (i.e., cyclic) RO (SBRO) and steady state RO (SSRO) operations. The impact of concentrate recycle ratio in SSRO-PR and efficacy of intermittent concentrate flushing on energy consumption in SBRO desalting operations were quantified via both theoretical and via experimental studies. Also, mineral scaling propensity was evaluated experimentally using a pilot scale RO system aided by a novel real-time direct membrane surface observation system.

The major objectives of the study were to:

1. Develop a modeling framework to predict the optimal operating conditions (e.g., pressure, water recovery, energy recovery efficiency) of RO desalting with concentrate recycling, for given feed water quality, with respect to minimizing energy consumption;

2. Evaluate the energy footprint of desalting operation with concentrate recycling in the SSRO-PR and SBRO for operation up the thermodynamic crossflow restriction;
3. Develop an optimal SBRO and SSRO-PR systems design and operational strategies considering the effects of concentrate flushing efficacy; and
4. Evaluate mineral scaling propensity in SSRO-PR and SBRO operations by quantifying the degree of crystal nucleation and growth kinetics, and assess the impact of the efficacy of concentrate flushing in SBRO operation.

## 1.4 Dissertation structure

The research objectives were accomplished via a combination of theoretical modeling and experimental validation using a pilot scale spiral wound RO system. Theoretical models were formulated based on coupled mass balance and membrane flux equations. The pilot-scale spiral wound RO system was developed to: (a) demonstrate both steady-state RO with partial concentrate recycling (SSRO-PR) and semi-batch RO (SBRO) operations on a single platform, (b) evaluate and optimize process conditions, and (c) compare with predictions from theoretical analyses for required energy consumption. A membrane surface monitoring (MeSuM) system was integrated with the spiral wound RO system for direct membrane surface observation in order to quantify and compare mineral scaling kinetics in terms of crystal number density and single crystal growth rates using image analysis.

A literature review and relevant background information are provided in **Chapter 2**. **Chapter 3** describes an operational approach steady state RO with partial concentrate recycling (SSRO-PR), which allows the implementation of operational flexibility, in terms of handling both a wide range of source water salinity and recovery on a single system platform.

Operational flexibility of SSRO-PR was enabled by RO process-decomposition, which enables fluid flow regulation at low pressure and adjustable product water recovery. In this chapter, the specific energy up to the thermodynamic limit in SSRO-PR operation is evaluated in order to quantify the theoretical minimum energy consumption and investigate the impact of the efficiency of the energy recovery and per-pass product water recovery.

**Chapter 4** introduces an alternative approach for achieving operational flexibility with respect to water recovery through SBRO, which employs total concentrate recycle and periodic concentrate flushing in a cyclic RO operational desalting strategy. In this approach, the overall system water recovery is a function of the RO filtration and flushing durations. This chapter provides a description of the time-dependent RO feed and concentrate profiles to assess the energy consumption as a function of water recovery relative to steady-state RO. Considering the flushing efficacy in SBRO, **Chapter 4** also provides analytical models which allow prediction of (a) cycle-to-cycle concentrate salinity rises due to incomplete (concentrate) flushing, and (b) specific energy consumption (SEC) with respect to overall permeate water recovery. Using a pilot-scale flexible RO system, SBRO operation and its energy demand were demonstrated over a wide range of water recovery.

In **Chapter 5**, mineral scaling propensity in SSRO-PR and SBRO operations were compared using gypsum as model scalant. In order to unambiguously assess mineral scaling under in SBRO operation, a direct real-time membrane surface imaging system was developed to detect the onset of membrane scaling. RO desalination tests in both SBRO and SSRO-PR were carried out at various water recoveries to quantify nucleation rate and crystal growth. Based on the mineral scaling kinetics, effectiveness of periodic raw-feed water flushing in SBRO operation was evaluated.

## Chapter 2 Literature Review

### 2.1 Reverse Osmosis Desalination

#### 2.1.1 Reverse osmosis

In reverse osmosis (RO) processes, high pressure is applied to a feed solution allowing selective permeation of a solute lean product water (permeate) through a semi-permeable membrane, while rejecting solutes including colloidal particles, organic residues, and dissolved ions [53-56]. As a result, a solute-rich brine stream (the concentrate) is generated as byproduct which may require post-treatment before discharging. The production of a permeate product requires applied pressure to be greater than the feed-side osmotic pressure. The permeate water flux through the membrane is dictated by the difference between the applied pressure ( $\Delta P$ ) and the osmotic pressure ( $\Delta\pi$ ) differences across the membrane given by [57-59]:

$$J_v = L_p(\Delta P - \sigma \cdot \Delta\pi) \quad (2-1)$$

in which  $J_v$  and  $L_p$  are the volumetric permeate flux and membrane water permeability, respectively, and  $\sigma$  is the reflection coefficient which indicates the selectivity of water passage relative to salt passage across the membrane [60]. The transmembrane hydraulic and osmotic pressures can be written as  $\Delta P = P_b - P_p$  and  $\Delta\pi = \pi_m - \pi_p$ , respectively, where subscripts  $m$ ,  $b$ , and  $p$  denote the membrane surface, bulk solution (in the membrane channel), and permeate solution, respectively. The intrinsic salt rejection by the membrane is defined as:

$$R_{S,int} = 1 - \frac{C_p}{C_m} \quad (2-2)$$

where  $C_p$  and  $C_m$  are the salt concentrations in the permeate and at the feed-side of the membrane, respectively. It is noted that the reflection coefficient is typically considered unity

( $\sigma \approx 1$ ) for RO membranes with high salt rejection. The osmotic pressure, in a solution, can be generally approximated by the van't Hoff equation [61, 62] for low to moderately saline (up to about 80,000 mg/L TDS [63]) as  $\pi = i \cdot c \cdot R \cdot T$  where  $c$  is the salt concentration,  $R$  is the ideal gas constant,  $T$  is the temperature (K), and  $i$  is the dimensionless van't Hoff factor.

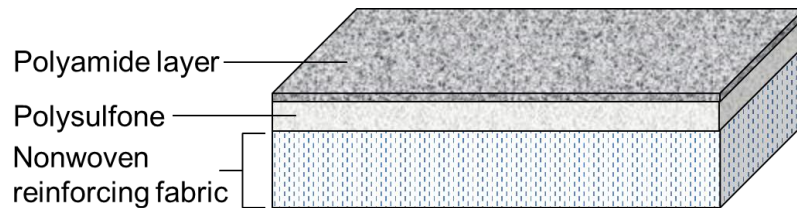


**Fig. 2-1.** Schematic depiction of a cross section of a thin-film composite membrane illustrating dense polyamide layer (PA) skin located on top of the polysulfone (PS) support layer (adapted from [64]).

Since the early development of the asymmetric cellulose acetate (CA) RO membrane by Loeb and Sourirajan [65], membrane materials have continued to evolve to achieve high water permeability with low salt passage [9]. The current state-of-the-art reverse osmosis membranes typically comprised of a thin aromatic polyamide (~200 nm thickness) active layer coated over a porous supporting polysulfone or polyester layer (~40  $\mu\text{m}$ ) [66].

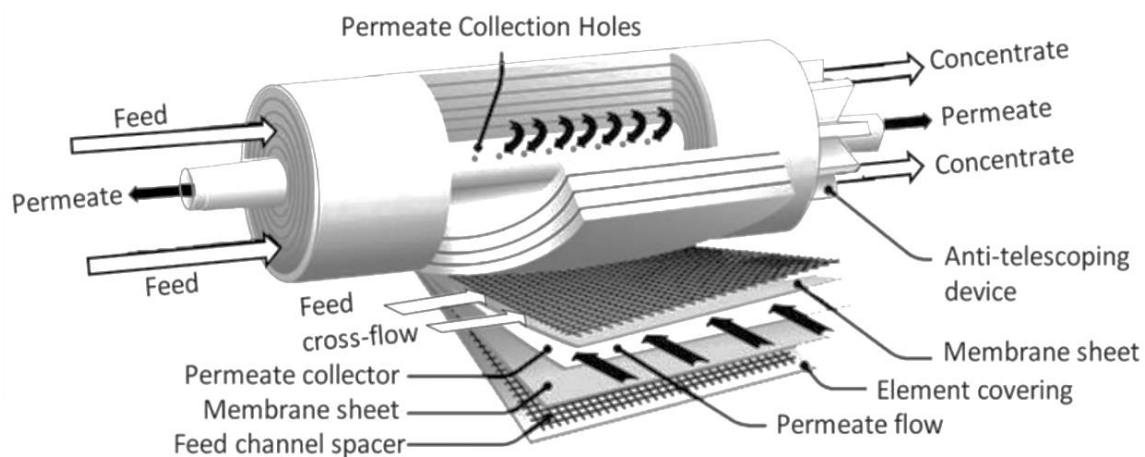


**Fig. 2-2.** Schematic of a spiral-wound RO membrane element [22].



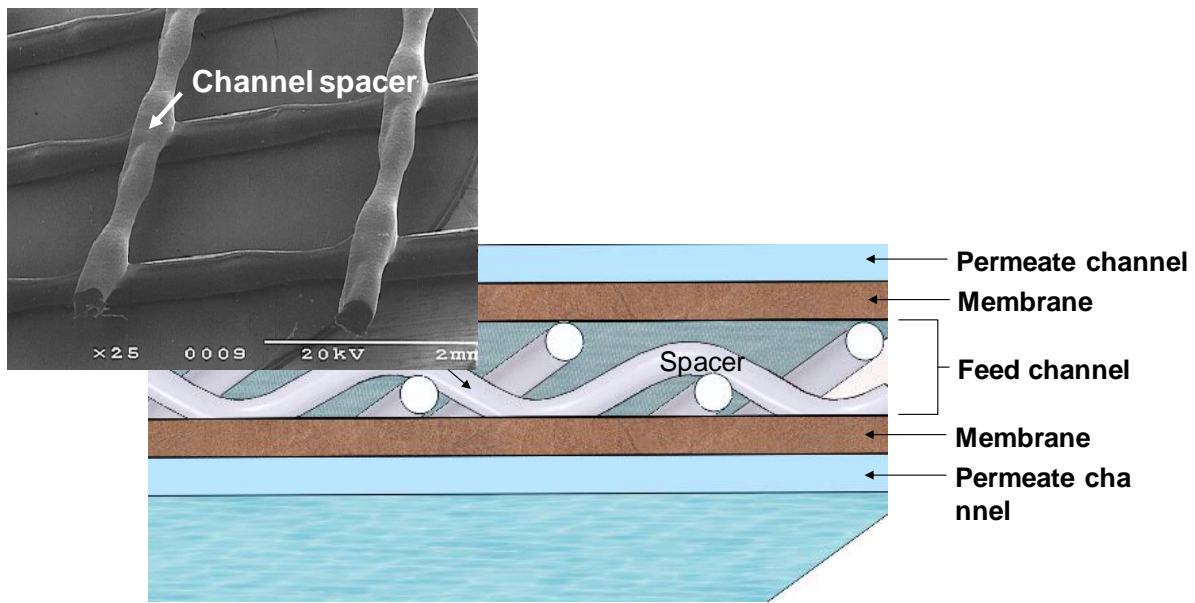


**Fig. 2-3.** Cross-section of symmetrical spiral wound envelope with spacer mesh in feed channel providing structural integrity (SEM view of feed spacer adapted from [67]).

For commercial applications of RO technology, the spiral wound RO configuration (**Fig.2-2**) has been commonly used to provide a large membrane surface area per unit volume of a membrane element [68, 69]. In this configuration, feed channel between two membrane sheets is supported by a channel spacer to provide structural integrity and maintain the opening of the channel. The permeate channel is also configured with channel spacers, also known as a “permeate carrier” or “permeate collector”. Through this permeate channel, the permeate water spirals toward the central product collection tube (**Fig.2-2**). The cross-section of symmetrical feed channel in spiral-wound RO element is described in **Fig. 2-3**.

### 2.1.2 Concentration polarization

In order to prevent deposition of foulants onto the membrane surface, RO desalination is carried out in a crossflow configuration (**Fig. 2-4**). The incoming saline feed water flows tangentially across the membrane surface as the selective permeation of clean water across the

membrane surface occurs in a direction perpendicular to the feed flow causing increased local salt concentration near and at the membrane surface (**Fig. 2-4**). This phenomenon is known as concentration polarization (CP). The degree of concentration increase near the membrane wall, relative to the bulk concentration, is commonly estimated by the one-dimensional single film model [70-72].

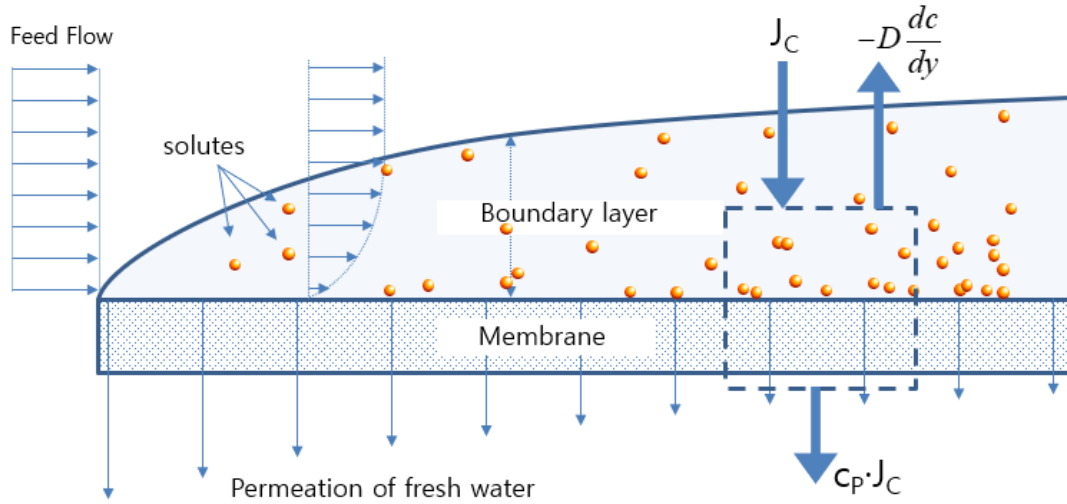


**Fig. 2-4.** Development of concentration polarization in the concentration boundary layer. As the feed flow along the membrane and water permeates across the membrane, the solute accumulates at the membrane surface. The box with a dashed line represents the control volume for the solute material balance in **Eq. (2-3)**.

A salt material balance around the control volume indicated on **Fig. 2-2** leads to

$$J_v \cdot c = J_v \cdot c_p - D \frac{dc}{dy} \quad (2-3)$$

where  $J_v$  is the permeate volumetric flux,  $c$  is the solute concentration in the boundary layer (at a distance of  $y$  from the membrane surface),  $D$  is the solute diffusion coefficient in water, and  $c_p$  is the salt concentration in the permeate stream. Equation (2-3) can be solved subject to the boundary conditions of i)  $c = c_m$  at  $y = 0$  and ii)  $c = c_b$  at  $y = \delta$  where  $c_m$  and  $c_b$  are the solute concentration at the feed-side membrane wall and in the bulk solution, respectively, and  $\delta$  is concentration boundary layer thickness. The solution of **Eq. (2-3)** leads to the following

classical film model of concentration polarization:

$$\frac{c_m - c_p}{c_b - c_p} = \exp(J_v \cdot \delta / D) \quad (2-4)$$

Concentration polarization progressively increases along the length of the RO feed channel and becomes most severe towards the membrane exit as the concentration boundary layer increases.

### 2.1.3 Mineral scaling

Mineral scaling on a membrane surface is the result of precipitation of sparingly soluble inorganic salts (e.g., calcium carbonate ( $\text{CaCO}_3$ ), calcium sulphate ( $\text{CaSO}_4 \cdot 2\text{H}_2\text{O}$ ), barium sulphate ( $\text{BaSO}_4$ ), strontium sulphate ( $\text{SrSO}_4$ ), calcium phosphate ( $\text{Ca}_3\text{PO}_4$ ), etc. [64, 73-75]). RO membrane desalination is particularly vulnerable to mineral scaling as it may (a) reduce the active surface area [76, 77] (**Fig. 2-5**), (b) cause membrane damage [51], and (c) reduce permeability. Consequently, mineral scaling reduces permeate water productivity over time requiring higher differential pressures to compensate for the productivity loss.

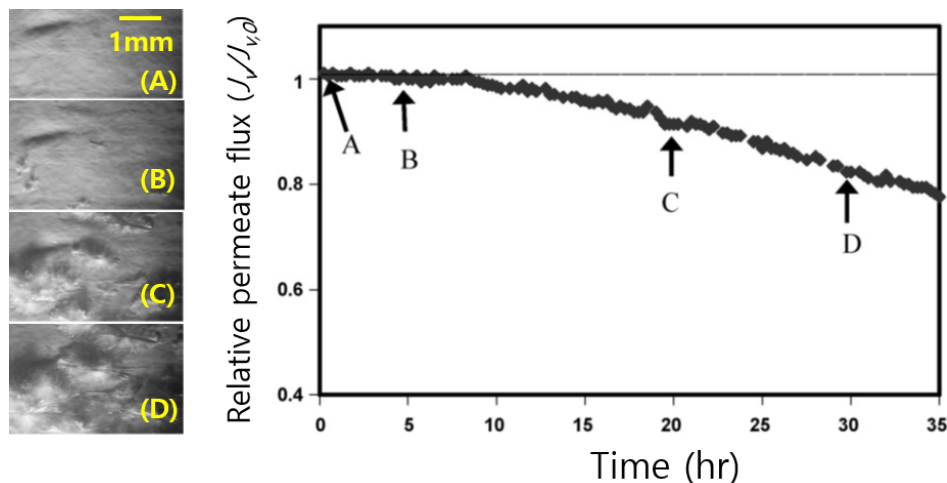


**Fig. 2-5.** (Left) photographs describing the development of gypsum crystals on a membrane surface causing (right) relative permeate flux decline (where  $J_{v,0}$  is initial permeate flux from a scale-free membrane surface) [51] in a plate-and-frame RO channel. (note: The TDS of the raw feed solution was 7,990 ppm having the gypsum saturation index (SI) of 0.77, while the SI at membrane surface was 2.1. The RO system was operated at 1.72 MP with a crossflow velocity of 5.9 cm/s.

Susceptibility of RO membrane processes to impacts from membrane scaling has promoted rigorous investigations to characterize nucleation phenomena in membrane system [48, 56, 64, 73, 78]. The two mechanisms for scale formation in the RO system are (a) homogeneous nucleation forming stable nuclei uniformly throughout the supersaturated solution (known as “bulk crystallization” followed by growth and deposition, and (b) heterogeneous nucleation promoting formation of nuclei directly on the surface of a foreign structure (e.g., membrane surface) followed by growth (Fig. 2-6).

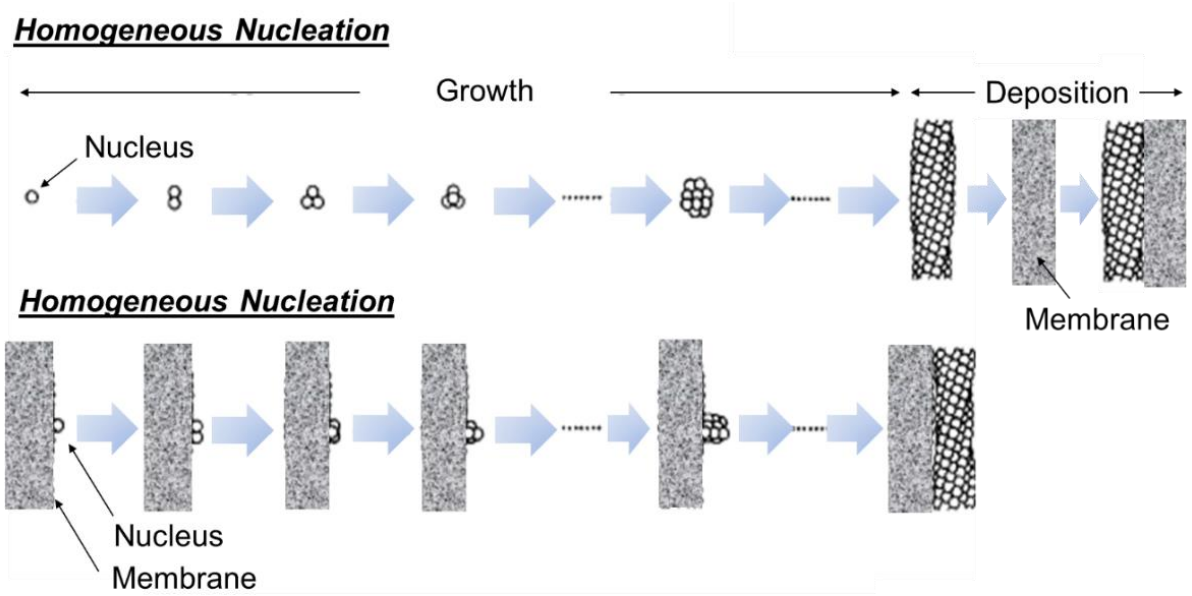


**Fig. 2-6.** Description of two nucleation pathways in a membrane system. Homogeneous nucleation occurs through bulk crystallization followed by crystal deposition onto the membrane surface, whereas in heterogeneous nucleation, a nucleus forms directly at the surface of the membrane (adapted from [79]).

In high recovery RO desalting, the concentration of mineral salts in the feed side of the membrane channel can rise above their solubility limits. As a consequence, mineral scaling can occur [80-82] directly on the membrane surface due to heterogeneous nucleation (Fig. 2-6), and subsequent crystal growth [83, 84]. In principle, mineral scaling may also occur due to deposition of mineral crystals that may form in the bulk solution in the RO membrane channel;

however, studies have shown that mineral scaling due to crystallization directly onto the membrane surface is dominant, relative to crystallization in the bulk solution, in RO operations [85]. Membrane scaling can lead to membrane surface blockage and thus permeate productivity loss (i.e., flux decline), which can ultimately shorten the membrane lifespan [64, 86-88].

Homogeneous nucleation process can be described thermodynamically [89] considering the free energy cost ( $\Delta G^*$  in J) the nucleus above the nucleation barrier (**Fig. 2-7**) given by:

$$\Delta G^* = \frac{4}{3}\pi\gamma r_c^2 \quad (2-5)$$

in which  $\gamma$  is the specific surface energy of the crystal-solution interface ( $J/m^2$ ) and  $r_c$  is the critical radius ( $m^2$ ) of the stable particle, defined as:

$$r_c = \frac{2\gamma \cdot v}{k_B T \ln SI} \quad (2-6)$$

where  $v$  is the molecular volume of the particle ( $m^3$ ),  $T$  is the absolute temperature (K),  $k_B$  is the Boltzmann constant ( $1.38 \times 10^{-23}$  J/K), and  $SI$  is the saturation index given by:

$$SI = \frac{IAP}{K_{SP}} \quad (2-7)$$

where  $IAP$  is the ion activity product, and  $K_{SP}$  is the solubility product at chemical equilibrium. The classical nucleation theory [89] describes the rate of nucleation ( $J_N$ ,  $\#/cm^2h$ ) of  $N$  particles with respect to time,  $t$ , as shown below:

$$J_N = \frac{dN}{dt} = A_N \exp\left(-\frac{a_N}{(\ln(SI))^2}\right) \quad (2-8)$$

in which  $A_N$  is the pre-exponential factor [90], and  $a_N$  is defined as:

$$a_N = \frac{16\pi\gamma^3 v^2 f(\theta)}{3(k_B T)^3} \quad (2-9)$$

where  $f(\theta)$  is the heterogeneous nucleation factor of value between 0 and 1 ( $0 < f(\theta) < 1$ ). The heterogeneous nucleation factor is considered unity in the absence of foreign particles (i.e., the conditions for homogeneous nucleation) in the supersaturated solution. The rate of heterogeneous nucleation is affected mainly by the membrane surface topology, roughness, chemistry, and solution supersaturation.

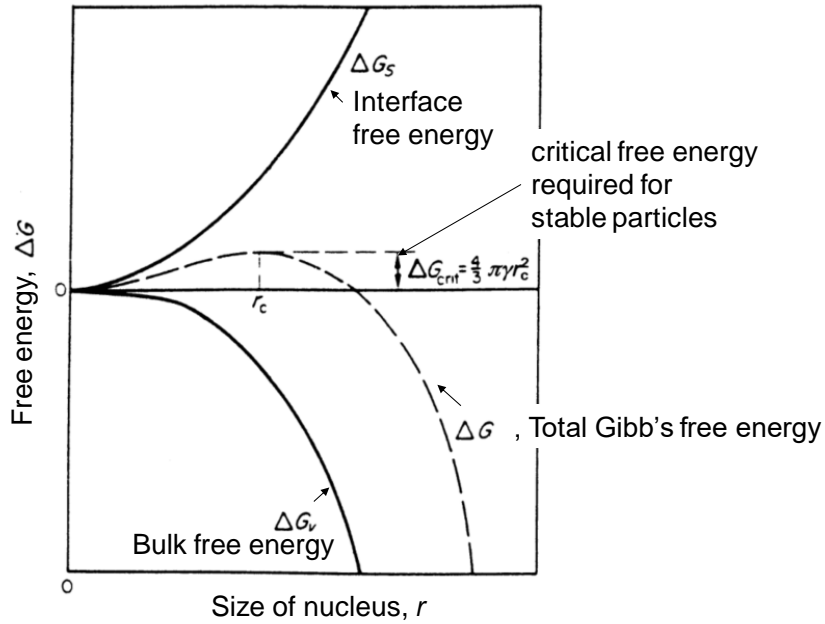


**Fig. 2-7.** Variation of Gibbs' free energy with particle reduces. The critical free energy ( $\Delta G_{crit}$ ) at  $r=r_c$  is required to form a stable nucleus (adapted from [89]).

As shown in **Eq. (2-6)**, the saturation level (represented with  $SI$ ) is the most critical [73, 91] factor determining the size of the stable nucleus (i.e., the critical radius). In RO processes, the  $SI$  is the highest near the liquid (feed solution)-solid (membrane surface) interface as solute concentration increases at the membrane surface due to selective permeation of water across the membrane causing concentration polarization (**Section 2.1.2**). Therefore, heterogeneous nucleation is dominant unless very high  $SI$  (i.e.,  $SI \geq 2$ ) condition exists [92, 93] (**Fig. 2-8**).

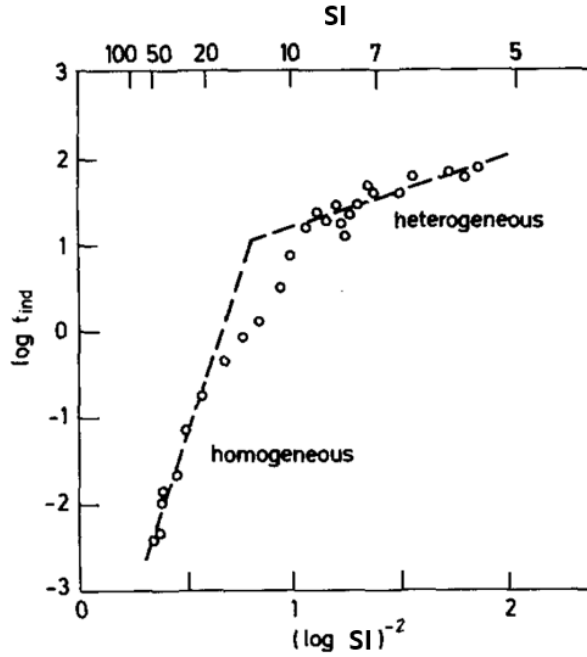


**Fig. 2-8.** Induction period as a function of saturation index for  $\text{CaCO}_3$  precipitation at  $25^\circ\text{C}$  (adapted from [92, 94]) with dominant nucleation pathways indicated on the figure.

The nucleation or crystallization induction time, which is considered to be the time delay before the first detectable crystal appears in a saturated solution, is related to the rate of nucleation [92] as:

$$t_{ind} = J_N^{-1} \quad (2-10)$$

in which  $t_{ind}$  is the induction period. Substituting **Eq. (2-8)** into **Eq. (2-10)**, the crystallization induction time can be related to the specific surface energy according to:

$$\ln(t_{ind}) = \frac{16\pi v^2 f(\theta)}{3(\ln(SI))^2} \left( \frac{\gamma}{k_B T} \right)^3 - \ln(A_N) \quad (2-11)$$

Various detection methods have been suggested to determine the nucleation induction times for different scalant species [81, 83, 95, 96] including detection of (a) turbidity increase, (b)  $\text{Ca}^{2+}$  reduction, (c) permeability decrease, or (d) increase of frictional pressure drop. He et al. [95, 97] evaluated the induction times for  $\text{CaSO}_4$  and  $\text{CaCO}_3$  in bulk solution by monitoring

variation of the solution turbidity and  $\text{Ca}^{2+}$  cation. Using this method, the above study evaluated the effect of temperature and ion activity in order to characterize nucleation process in bulk solution. Using the method of monitoring the turbidity rise and calcium ion concentration decline in a stirred crystallization vessel, Shih et al. [83] demonstrated the approach to ranking antiscalant effectiveness in retarding mineral salt crystallization. Shih et al. in later study [85] used a plate-and-frame membrane test cell to investigate surface nucleation in a saturated solution with calcium sulfate by eliminating the crystals in bulk solution before surface deposition using a media filter. Shih et al. characterized the formation of scaling by both monitoring the permeate flux decline and by membrane surface imaging via high-resolution scanning electron microscopy (SEM) [85]. The above study clearly showed a progressive development of surface gypsum crystal demonstrating the pathway of mineral scaling via heterogeneous nucleation on a membrane surface (**Fig. 2-9**).

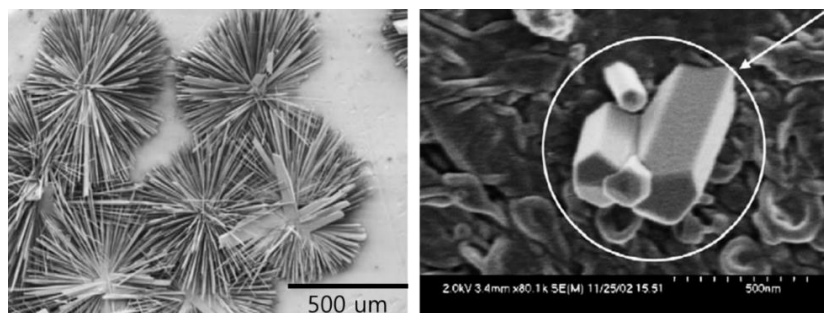


**Fig. 2-9.** Gypsum scaling on the membrane surface on SEM images (note: the experiment conducted using a feed solution at  $SI_{gypsum}$  of 1.01 on a membrane system with a permeate flux of 32–50 L/m<sup>2</sup>/h at 20°C and 689 kPa using TFC-ULP polyamide membrane; adapted from [85])

In order to improve the detection sensitivity for mineral scaling on the membrane surface, Hasson *et al.* [96] relied on permeability monitoring in spiral wound RO system operated with a supersaturated gypsum feed solution in a feed vessel. In the above study, the feed vessel received concentrate and permeate stream from the RO membrane for continuous recirculation



of the solution in total recycle mode. The above study demonstrated rapid permeability decline due to gypsum mineral scaling in a membrane system, as also evidenced by turbidity increase in the RO feed stream. In a later study, Li et al. [98] adopted the permeability monitoring method in spiral wound RO membrane system (similar to that in [96]) to provide inhibitory effectiveness of various antiscalant in a membrane system. Despite the convenience of indirect detection methods for mineral scaling (e.g., turbidity, permeability monitoring), inconsistent measurement of crystallization induction time (**Table 2-1**), primarily due to the difference in detection resolution, remains a major challenge. In order to overcome the above challenge, Karabelas et al. [84] employed a direct membrane surface analysis from a flat-sheet membrane module for incipient gypsum scaling on the membrane surface using an Energy Dispersive X-ray spectrometry unit (EDS) connected to the Scanning Electrode Microscopy (SEM) system. The SEM analysis in the above study demonstrated incipient of gypsum micro particles on the membrane surface immediately (i.e., without crystallization induction time) under supersaturated feed solution.

In an effort to provide early detection of mineral scaling via direct surface monitoring without process interruption of RO desalination, Cohen et al. [99] introduced an ex-situ direct membrane observation method (**Fig. 2-10**). In this method, the membrane surface images were captured at fixed time interval (typically every 5 – 20 min.) using high resolution digital camera through a semi-transparent plate-and-frame membrane cell. As a diagnostic system, the membrane monitoring system was connected to a spiral wound RO system to provide rapid and real-time membrane surface observation tool for particulate deposition on the membrane surface. While it was infeasible to capture nanoscale nuclei formation even with the high-resolution digital imaging system, this technique provided reliable and reproducible estimation

of the crystal induction period as reported in multiple studies [46, 51, 73-75, 100-102]. The observed induction times of gypsum crystallization both in bulk solution and in membrane system are compared in **Table 2-1**.

**Table 2-1.** Induction times at various saturation level for CaSO<sub>4</sub>

Authors	<i>SI</i> CaSO <sub>4</sub>	Reynolds number	Measurement Criteria for determination of the induction time	Nucleation mechanism	Induction time (min)
Li et al. (2018) [98]	1.4 – 4.2	NA*	Increase in solution turbidity	Homogeneous nucleation in a stirred solution	300 – 20
	1.4 – 2.5	430	Reduction in membrane permeability	Heterogeneous nucleation in a membrane system	50 – 25
	2.5 – 4.2	6800			240 – 60
Hasson et al. (2001) [81]	2.75	NA	Permeate flux decline, pressure drop, turbidity, and Ca <sup>2+</sup> measurement	Heterogeneous nucleation in a membrane system	78
	2.79				61
	3.13				42
	3.64				32
	3.90				27
	4.23				16
He et al. (1994) [95]	1.59	NA	Reduction in Ca <sup>2+</sup> concentration and accompanied by increase in solution turbidity	Homogeneous nucleation in a stirred solution	1840
	1.85				400
	2.03				245
	2.33				107
	2.73				68
	3.02				34
	3.23				19
	3.72				13
	4.03				10
4.54	4				
Uchymiak et al. (2008) [73]	1.30	213	Direct membrane surface observation	Heterogeneous nucleation in a membrane system	600
	1.43	159			500
	1.67	159			89
	1.72	144			30
Packter A. (1974) [103]	1.5	NA	Direct membrane surface observation using an optical microscope	Heterogeneous nucleation induced by dust particles in a stirred solution	200
	2.0				140
	2.5				90

\*NA – not applicable

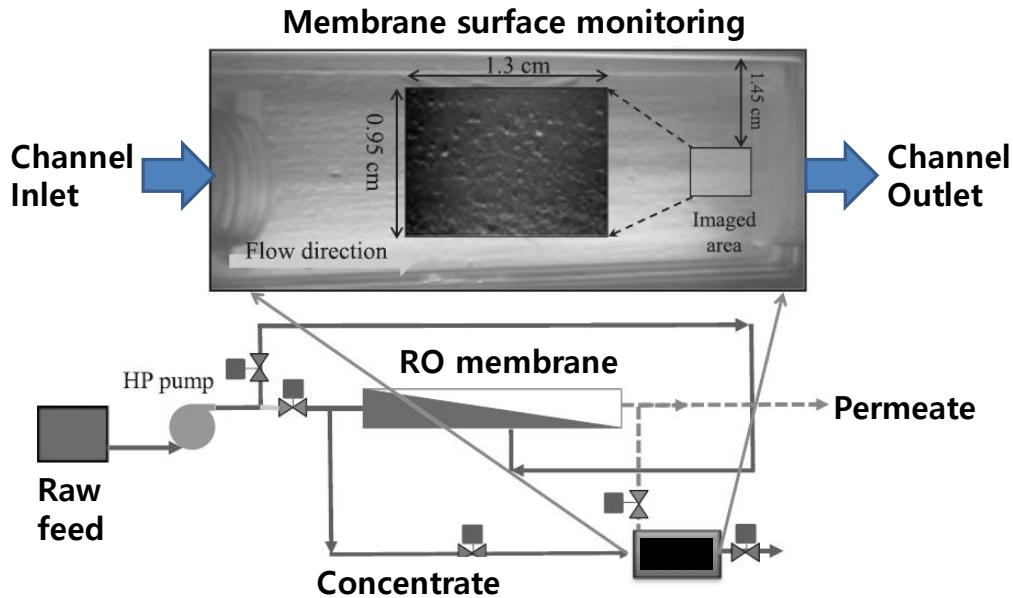


**Fig. 2-10.** Schematic of RO desalting system integrated with ex-situ membrane surface monitoring [99] for early detection of mineral scale (adapted from [100]).

#### 2.1.4 Surface mineral prevention methods

Conventional methods of mineral scale mitigation in RO desalination include: (a) feed water acidification to control the solubility of certain mineral salts (e.g., primarily for calcium carbonate scale control) [104, 105], (b) ion-exchange water softening to remove pre-cursors divalent ions of the potential mineral scalants from the RO feed water [106], and (c) antiscalant addition to the RO feed water to suppress mineral salt nucleation and crystal growth [89, 107, 108]. Acidification is appropriate for decreasing the rate of precipitation of mineral salts whose solubility is affected by the level of pH (e.g., calcium carbonate, silica, calcium phosphate, etc.). **Figure 2-11** illustrates the variation of the saturation level of selected mineral scalants with respect to pH in a water sample collected from a brackish water source with TDS of 11,020 in an agricultural area (San Joaquin Valley, California). It is noted that the application of acidification for scale control is limited to specific type of scalants [104] as listed above, and the high material cost from continuous acid dosing (e.g.,  $H_2SO_4$ ) is burdensome [109].

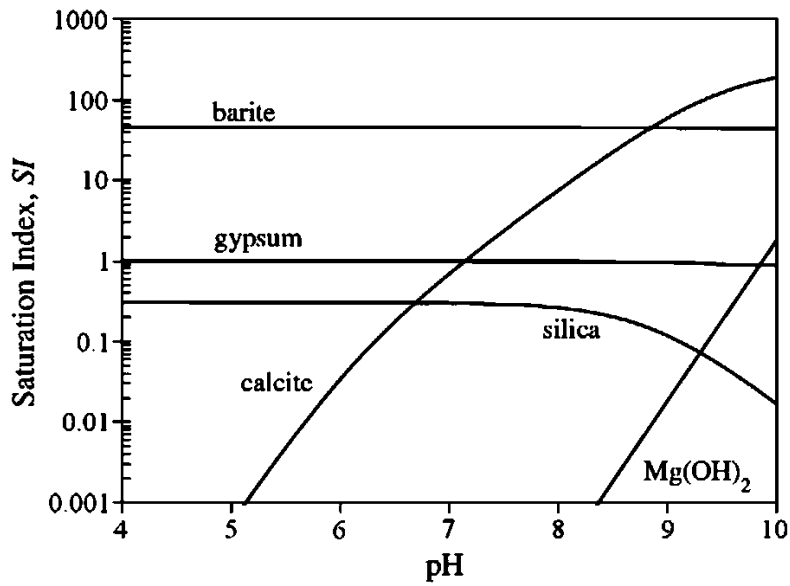
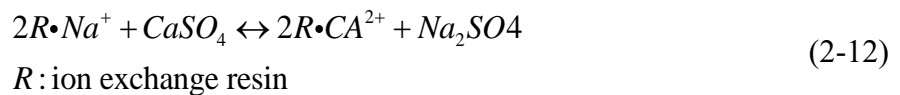


**Fig. 2-11.** Variation of saturation indices with pH for brackish water at TDS of 11,020 ppm (from a site in California San Joaquin Valley [110]).

Ion exchange technique utilizes cation or anion resins (typically in the shape of a small porous plastic bead [111]) which allows exchange of one type of ion for another dissolved ion of the same charge. For example, base anion resins exchange hydroxyl ( $\text{OH}^-$ ) or bicarbonate ( $\text{HCO}_3^-$ ) ions for other anions. Cation resins exchange hydrogen ions ( $\text{H}^+$ ) or monovalent sodium ions,  $\text{Na}^+$ , with divalent cations as calcium,  $\text{Ca}^{2+}$ , and magnesium,  $\text{Mg}^{2+}$  (**Eq. 2-12**) [112]. An example of an ion exchange reaction for  $\text{Ca}^{2+}$  using cation resin is provided in **Eq. (2-12)**.



Ion exchange is an effective method for reducing water hardness without necessitating continuous acid or antiscalant dosing [113]. However, major challenges remain such as the slow ion exchange process and high operating/maintenance cost associated with periodic replacement or regeneration of ion-exchange resins.

Addition of antiscalant agents is most commonly used in RO desalination to control the precipitation of sparingly soluble salts in supersaturated feed solutions. Antiscalant molecules in the feed solution target the positive charges of the nuclei distorting the crystal shapes (Fig. 2-12) to decrease the rate of crystal nucleation and growth by increasing the surface energy of crystal nuclei [102, 114]. Common antiscalant additives to the RO feed water are polyacrylic acid, carboxylic acid, or phosphonates [83]. The predetermined antiscalant dosing must be maintained according to the solution composition and saturation level with respect to the target scalant. Consequently, methods for detection of pertinent process parameters that are relevant to mineral scaling (e.g., SI, permeate flux, etc.) are critical to determine proper antiscalant dosing. Other approaches include periodic RO elements permeate flush [115, 116] and feed-flow reversal in which is suitable when the raw feed water is sufficiently undersaturated [52, 100, 117]. In both of the above approaches the intent is to remove (via dissolution) the mineral scalants at a reasonable early stage of their formation.

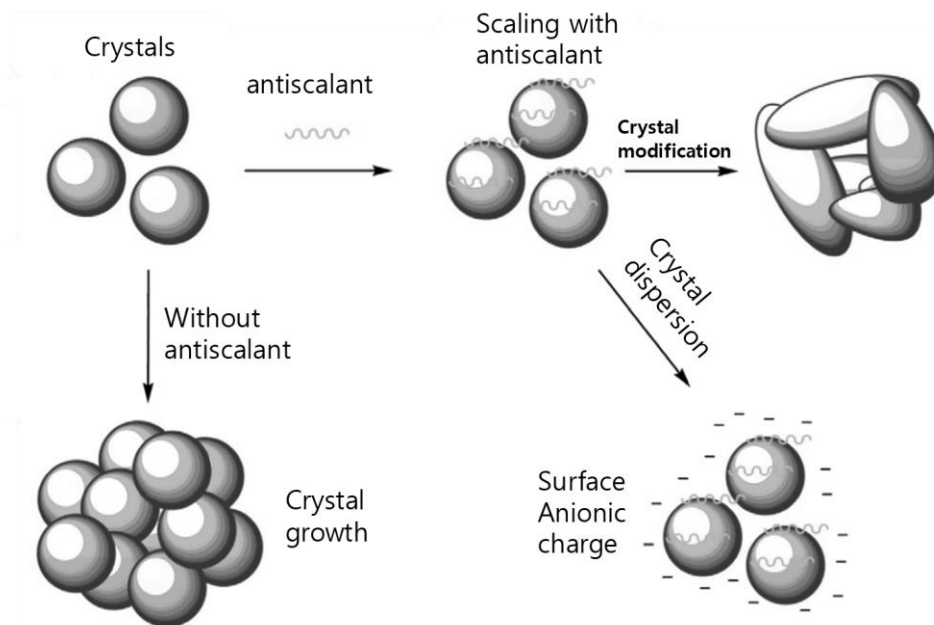


**Fig. 2-12.** Description of scaling inhibition via addition of antiscalant (adapted from [118]).

### 2.1.5 Energy consumption in RO desalination

In RO desalination, high pressure is applied to the saline feed water to ensure permeate productivity over the entire surface area of the membrane (i.e., no inward flux of water from the permeate side). Water desalting by RO process requires higher pressure, compared to other types of membrane processes (e.g., nanofiltration) [119-122], as the difference in osmotic pressure between solute-lean permeate and solute-rich concentrate water is much greater in RO processes. An illustrative schematic of RO system with a high-pressure pump is shown in **Fig. 2-13**.

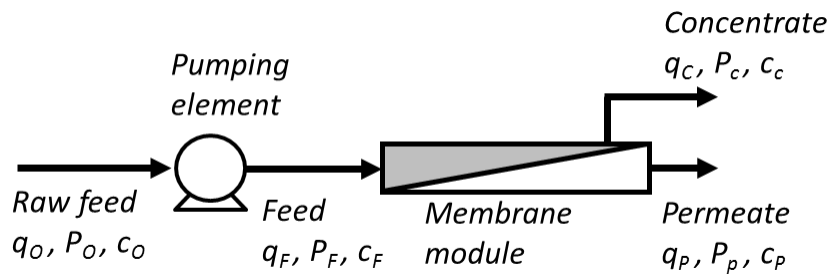


**Fig. 2-13.** Schematic of simplified RO system with a high-pressure pump, where  $q_f, q_c,$  and  $q_p$  are the flow rates of the feed, retentate, and permeate, respectively,  $c_f, c_c, c_p,$  and  $c_m$  are the concentrations at the feed, retentate, permeate, and at the membrane surface, respectively, and  $P_f, P_c,$  and  $P_p$  are the pressures of the feed, retentate, and permeate, respectively.

The applied pressure in RO desalination is typically in the range of 2–20 bar (30–290 psi) for brackish water (BWRO), which generally produces potable water with total dissolved solids (TDS) less than 500 mg/L [123] from brackish water resources of TDS in the range of 1,000–10,000 mg/L [124]. The applied pressure required for seawater RO (SWRO) desalination is in the range of 40–80 bar (600–1200 psi) due to the high TDS of seawater of ~35,000–42,000 ppm [15, 125-127]. Energy consumption due to the required high pressure is one of the primary factors affecting the cost of water desalination, generally responsible for 20-30% and 30-44% of the total water production cost for brackish water and seawater desalination, respectively

[22, 34, 128-130]. Accordingly, a significant effort has been devoted to decrease the operating cost of RO desalination by reducing the energy cost per volume of permeate product (i.e., specific energy consumption or *SEC*) [34, 35, 131-134] given by:

$$SEC = \frac{\dot{W}_{pump}}{\eta_P \cdot q_P} \quad (2-13)$$

where  $\eta_P$  is the pump efficiency,  $q_P$  is the volumetric flow rate of the permeate stream, and  $\dot{W}_{pump}$  is the rate of work done by the pump, which can be written as given below assuming negligible pressure drop within the RO module,

$$\dot{W}_{pump} = \Delta P_F \cdot q_F \quad (2-14)$$

in which  $q_F$  is the volumetric flow rate of the feed stream,  $\Delta P_F$  is the transmembrane pressure defined as

$$\Delta P_F = P_F - P_O \quad (2-15)$$

where  $P_F$  is the feed pressure and  $P_O$  is the pressure of the raw feed, which can be reasonably assumed to be the same as that of the permeate water. Combining **Eqs. (2-13) – (2-15)**, a simple expression of the SEC can be obtained as a function the transmembrane pressure:

$$SEC = \frac{\Delta P_F}{\eta_P \cdot Y_{SP}} \quad (2-16)$$

where  $Y_{SP}$  is the per-pass (or “once-through”) water recovery defined as:

$$Y_{SP} = \frac{q_P}{q_F} \quad (2-17)$$

As implied by **Eq. (2-16)**, for a given pump efficiency and water recovery (i.e.,  $\eta_P$  and  $Y$ ), the specific energy consumption is dictated by the transmembrane pressure exerted by the pumping

element in the system. In RO desalting, the transmembrane pressure must be greater than the brine osmotic pressure in order to ensure permeation production over the entire surface area of the membrane (Eq. (2-1), Fig. 2-4). Accordingly, a lower limit (known as the thermodynamic restriction of the cross-flow RO desalting [134, 135]) is imposed on the transmembrane pressure as:

$$\Delta P_F \geq \Delta \pi_{exit} = \frac{\pi_o}{1 - Y_{SP}} \quad (2-18)$$

in which  $\pi_o$  is the feed osmotic pressure. Accordingly, Zhu et al. [136] provided the expression for the minimum energy cost for the process of single-stage (and single pass) RO desalting, at the limit of thermodynamic restriction, by combining Eq. (2-9) and (2-11):

$$SEC_{tr} = \frac{\pi_o}{\eta_P \cdot Y_{SP} (1 - Y_{SP})} \quad (2-19)$$

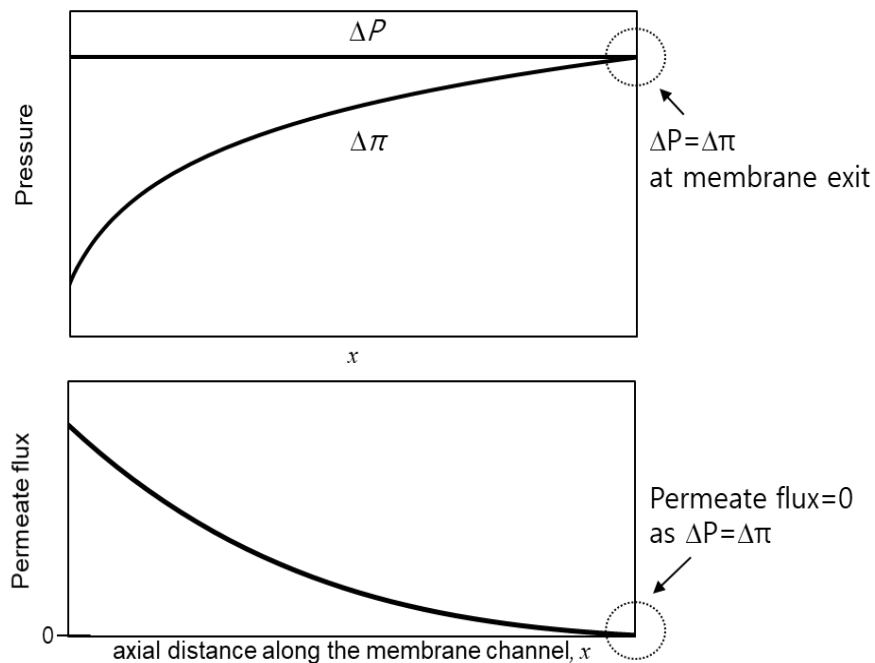


**Fig. 2-14.** Schematic illustration of the thermodynamic restriction for crossflow RO desalting. As the brine osmotic pressure increases toward the membrane exit, the permeate flux diminishes. At the limit of the thermodynamic restriction, the applied pressure is at a level equivalent to the osmotic pressure in the brine stream exiting the membrane element.



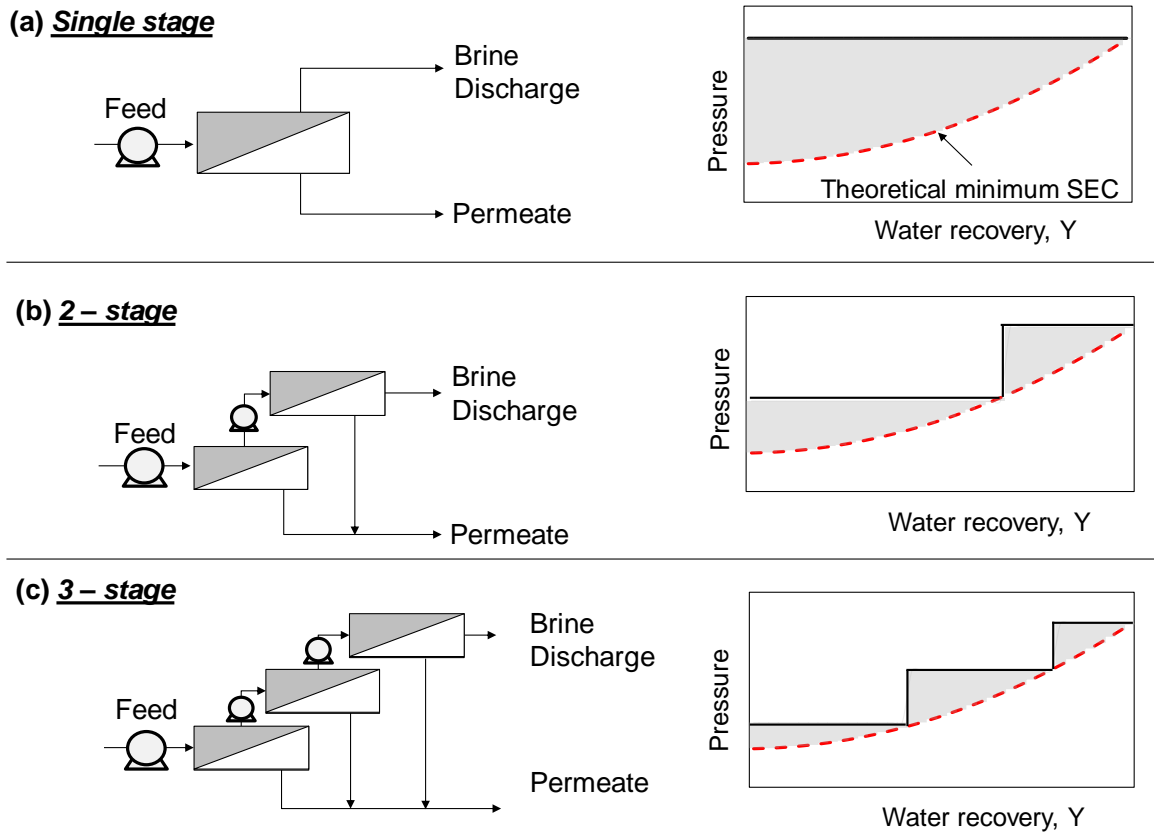


**Fig. 2-15.** Comparison of RO process configurations in (a) single stage, (b) 2-stage, and (c) 3-stage RO with interstage booster pumps. The minimum applied pressure (for permeate production) is indicated with dotted curve.

Single-stage RO requires high feed pressure at the membrane inlet (greater than or equal to the brine osmotic pressure at the exit from the membrane element/train) to ensure the permeate productivity along the entire RO membrane surface. Multi-stage configuration (**Fig. 2-15**) has the advantage of reducing the energy foot-print (with respect to water recovery) [32] by allowing incremental increase of the feed pressure to each stage thereby reducing the irreversible energy loss. **Equation (2-20)** provides the expression for the SEC in multi-stage RO assuming 100% efficient pumps at the limit of the thermodynamic restriction [29, 136],

$$SEC_{ir} = \frac{\pi_o}{Y} \left[ \frac{2}{\sqrt[N]{1-Y}} - (N-1) \right] \quad (2-20)$$

in which  $N$  is the number of stages. **Fig. 2-15** illustrates reduced amount of excess pressure in

multi-stage RO configurations. It has been reported that, in multi-stage RO configuration with interstage booster pumps, energy consumption can be reduced by 15 – 40% depending on pump efficiencies [58, 137, 138]. However it is emphasized that increased number of membrane stages may cause significant expense in system installation and maintenance [136].

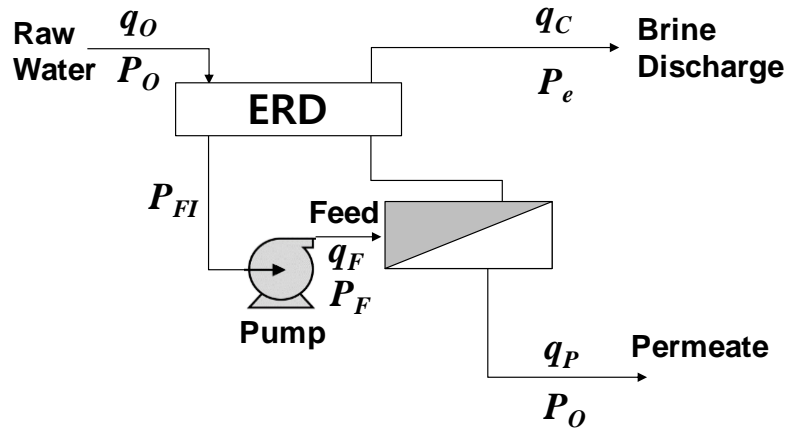


**Fig. 2-16.** Schematic illustration of single-stage RO system with an energy recovery device (ERD: energy recovery device).

One of the most important breakthroughs in RO desalination technology that significantly reduced the RO energy footprint was the development of energy recovery devices (ERD) [10, 139-143]. The main function of an ERD is to transfer hydraulic energy from the exiting high pressure concentrate stream back to the feed stream (schematically illustrated in **Fig. 2-16**) in order to lower the required energy input. The required pump work is reduced as described by the following expression:

$$\dot{W}_{pump} = \Delta P_F (q_F - \eta_{ER} \cdot q_C) \quad (2-21)$$

where  $\eta_{ER}$  is the efficiency of energy recovery device, and  $q_C$  is the concentrate stream the flow rate whose hydraulic energy is recovered to pressurize the raw-feed water. Accordingly, the specific energy consumption for a single-stage RO desalting with the use of an ERD is given by:

$$SEC_{tr} = \frac{(1 - \eta_{ER}(1 - Y))}{\eta_P \cdot Y} \frac{\pi_0}{(1 - Y)} \quad (2-22)$$

Incorporation of an ERD effectively reduces the required pump work leading a drastic SEC reduction, particularly for RO operation at low recovery (**Fig. 2-17**). The incorporation of an ERD in seawater RO (SWRO) desalination, the *SEC* was reported to reduce from 20 kWh/m<sup>3</sup> in 1970's [144] to only 1.8 kWh/m<sup>3</sup> [13, 130, 145, 146] recovery in present days at 50% product water recovery. Given that the theoretical minimum specific energy consumption in SWRO, for 50% recovery, in the absence of pressure drop in the membrane module is 1.6 kWh/m<sup>3</sup> [22] (**Fig. 2-18**), the process of RO desalting is now considered the most energy efficient desalination technology which is rapidly replacing the traditional thermal desalting technologies (e.g., multi-stage flash, multi-effect evaporation, and etc.) [10].

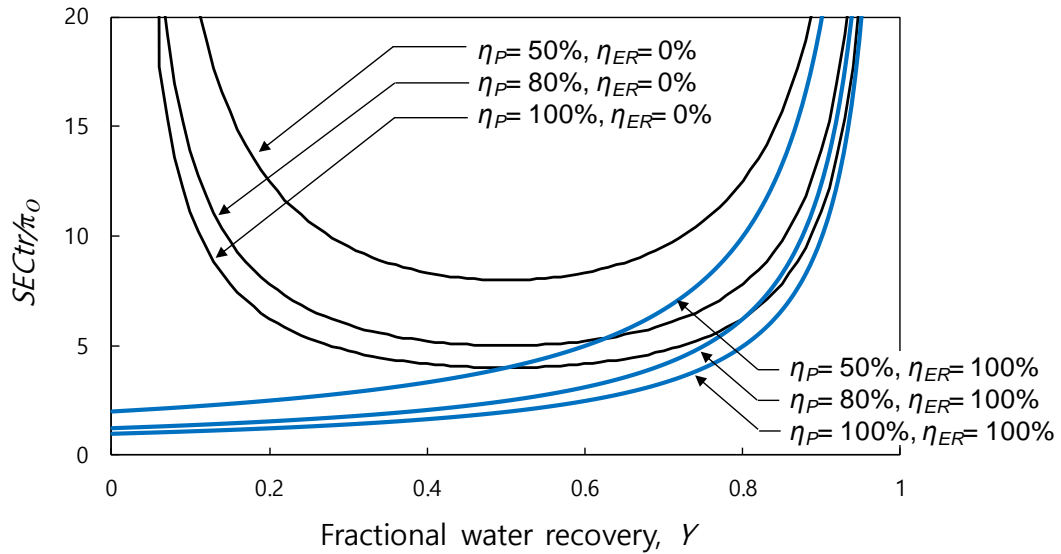


**Fig. 2-17.** Variation of the specific energy consumption normalized by the feed osmotic pressure, at the limit of the thermodynamic restriction, with respect to the fractional water recovery in a single-stage RO evaluated with and without an energy recovery device (as per Eq. (2-19) and (2-20), respectively) for pump efficiencies of  $\eta_P=50, 80, 100\%$ .

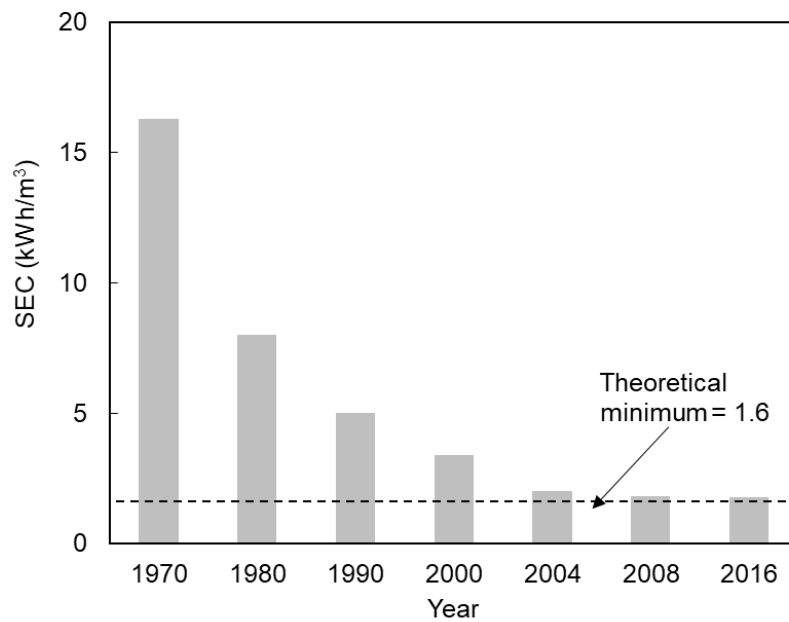


**Fig. 2-18.** The SEC in RO desalination of seawater (35,000 mg/L TDS) at 50% water recovery relative to the theoretical minimum energy requirement (indicated by the dashed line) [22, 144, 145, 147].

## 2.2 Operational approaches for RO processes

### 2.2.1 Steady-state RO process

In a typical steady state RO (SSRO) process, the feed water is continuously fed to the membrane module, while the concentrate discharge and the permeate stream exit the membrane module at a constant flow rate (**Fig. 2-13**). In SSRO operation, process parameters (e.g., pressure, flow rates, etc.) do not vary with respect to time, and thus the process conditions for system components (e.g., pumps) can be maintained within the optimal operating range, provided that water quality remains time invariant. Due to the physical pressure limitation of RO membranes, water recovery from a single element,  $Y_{SP}$  (**Eq. (2-17)**), is typically limited in the range of 5 – 15%. In order to overcome the above limitation, multi-stage configuration is commonly adapted (**Fig.2-19**) in order to achieve higher product water recovery in SSRO operation.

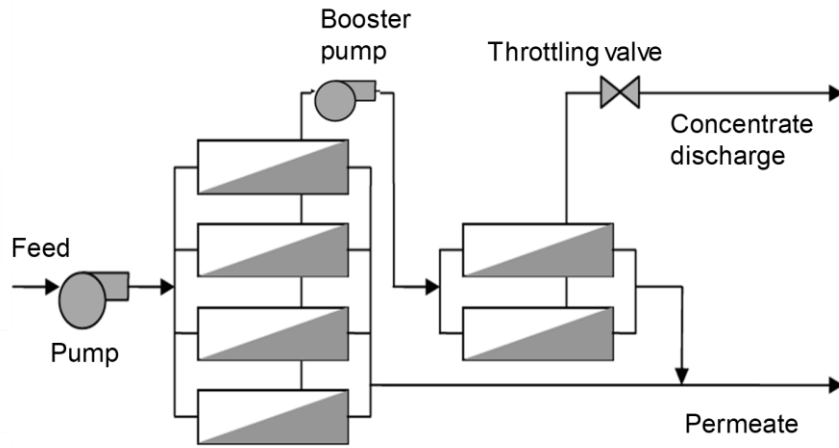


**Fig. 2-19.** Two-stage RO configuration with one high-pressure pump before the first stage, and a booster pump before the 2<sup>nd</sup> stage (adapted from [148]).

Multi-stage RO process configuration involves multiple membrane elements connected in series. The number of stages and membrane elements in each stage are determined based on the overall target water recovery [149]. The number of membrane elements ( $N_M$ ) can be calculated based on the total (targeted) volumetric flow rate of the permeate ( $q_P$ ) divided by the average volumetric flow rate of the permeate allowed for each element ( $\overline{q_{PE}}$ ):

$$N_M = \frac{q_P}{\overline{q_{PE}}} \quad (2-23)$$

The  $\overline{q_{PE}}$  can be calculated from the product of the membrane surface area ( $A_M$ ) and the average permeate flux ( $\overline{J_v}$ ) given by:

$$q_{PE} = \overline{J_v} \cdot A_M \quad (2-24)$$

Most membrane manufacturers specify the effective membrane surface area, recovery per element, recommended permeate flux for their commercial membranes, and suitability for desalting specified water types [150]. Specific RO network configurations are also recommended for overall water recovery target [148] as shown in the example of **Table 2-2**.

Standard multi-stage RO process configurations typically consist of one or more hydraulic components (e.g., pumps), coupled with a throttling valve to relieve the pressure of the concentrate stream to be discharged out of the system safely (**Fig. 2-19**). Thus, multi-stage RO is most suitable for deployment in locations with a source of stable water quality (e.g., ocean, river, etc.). The efficiency of RO feed pump and ERD is largely dependent on hydrodynamic conditions (e.g., volumetric flow rates, and hydraulic pressure [151]; **Fig. 2-20**); thus, it is critical to provide and maintain optimal RO operating conditions. Therefore, on RO systems with highly integrated system components (e.g., multi-stage RO), variations in the operating condition can cause a severe irreversible energy loss from sub-optimal operation of numerous system components. **Figure 2-20** shows an example of the variation of pump efficiency with respect to the flow rate.

**Table 2-2** Recommended system configuration with commercial spiral wound RO membranes

Number of Stages, N	Overall recovery
1	< 60%
2	60 – 70%
3	>75%

Note: The above recommendation assumes 6 membrane elements in each stage for the permeate flux of 8~30 GFD [148].

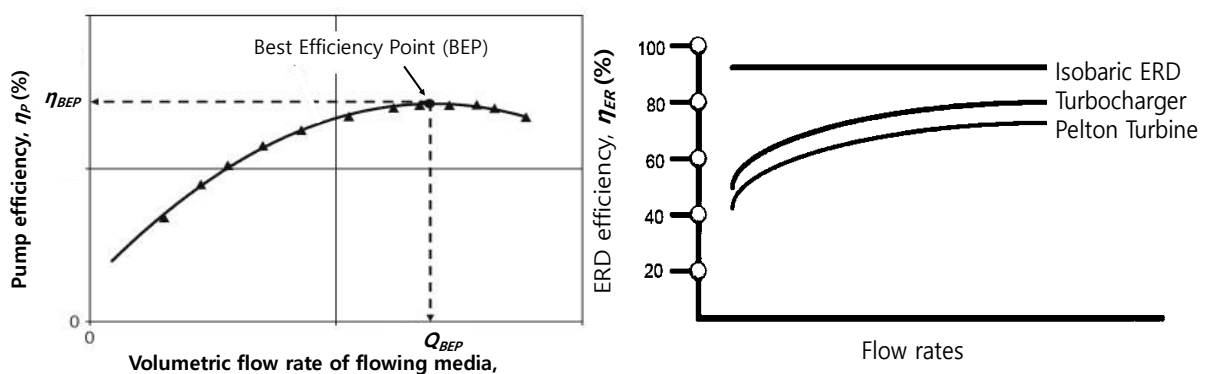


**Fig. 2-20.** Example of (Left) pump, and (Right) ERD efficiency trends with respect to volumetric flow rate (adapted from [152] and [140], respectively).

For small-scale RO systems with a small system footprint, partial concentrate recycling is beneficial to enhance the water recovery. In steady-state RO with partial concentrate recycle (SSRO-PR, Fig. 2-21), a part of the concentrate is continuously mixed with the raw-feed water, and the mixture is introduced to the membrane module entry while maintaining a constant permeate productivity.

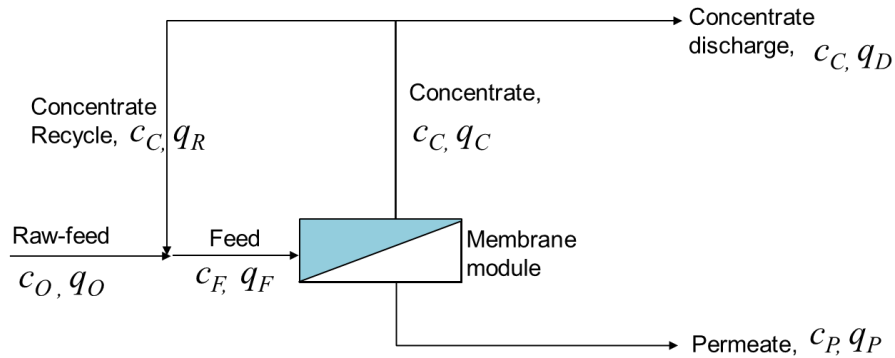


**Fig. 2-21.** Schematics of RO desalination with partial concentrate recycle (i.e., the remainder concentrate water is discharged from the system) where  $c$  indicates salt concentration, and  $q$  indicates the volumetric flow rates ( $O$ : raw-feed,  $R$ : concentrate recycle,  $C$ : concentrate,  $D$ : concentrate discharge,  $P$ : permeate water).

Given the operation of steady state RO (SSRO) at constant flow rates in the entering (i.e., the raw-feed water) and exiting (i.e., concentrate discharge and permeate water) streams, the following salt material balance can be established:

$$c_O \cdot q_O = c_C \cdot q_D + c_P \cdot q_P \quad (2-25)$$

where  $c$  is the salinity (in mg/L), and  $q$  is the volumetric flow rate (in L/s), subscripts  $O$ ,  $C$ ,  $D$ , and  $P$  indicate raw feed, concentrate exiting the membrane module, concentrate discharge, and permeate streams, respectively (Fig. 2-21). In this configuration, the overall water recovery ( $Y$ ) can be defined in terms of the volumetric flow rates of the raw feed and the permeate water streams as given by:

$$Y = \frac{q_P}{q_O} \quad (2-26)$$

It is important to recognize that partial concentrate recycle allows one to vary the overall water recovery ( $Y$ ) by adjusting the flow rates of the raw feed water, while maintaining constant flow rates the RO element feed, concentrate, and permeate (i.e.,  $q_F$ ,  $q_C$ , and  $q_P$ , respectively). **Figure 2-22** describes the simultaneous variation of the flow rate of each stream in SSRO operation with partial concentrate recycle allowing a wide range setting of the overall water recovery. Therefore, SSRO with partial concentrate recycle is an effective method to increase water recovery for a small-scale RO system. Due to mixing between the raw feed ( $q_O$ ) and the recycled concentrate stream ( $q_R$ ), the feed water salinity increases with the target overall water recovery. Consequently, when concentrate recycle is adapted the membrane feed needs to be evaluated to determine the optimal operating condition for the system (e.g., antiscalant dosing, pretreatment methods).

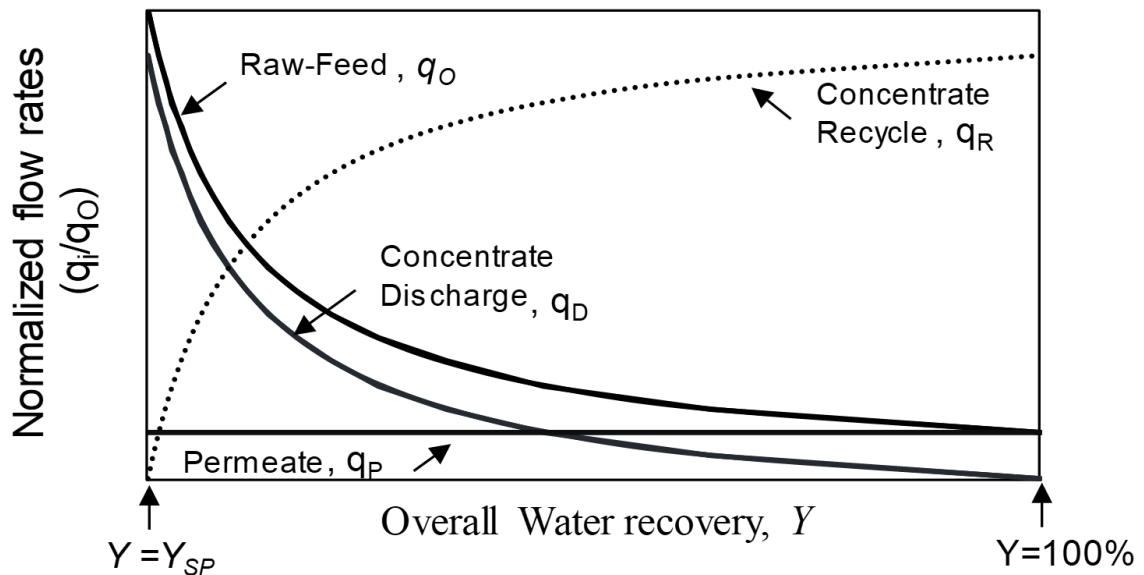


**Fig. 2-22.** Variation of the volumetric flows with respect to the overall system recovery for a constant permeate flow ( $q_P$ ) where  $Y$  is the per-pass water recovery.



### 2.2.2 Unsteady-state RO operation

Increased concern about environmental issues associated with concentrated brine management [4, 153, 154] and costly post-treatment [155] have led increased interest in high recovery RO processing utilizing concentrate recycle to decrease brine discharge. One such process is that of unsteady state semi batch RO (SBRO) operation [156], which allowed by two holding tanks, which alternatively store accumulated concentrate holdup **Fig. 2-23**. While one tank is connected to the RO membrane module, the other tank is disconnected to discharge the concentrate holdup, and refill with the fresh raw feed.

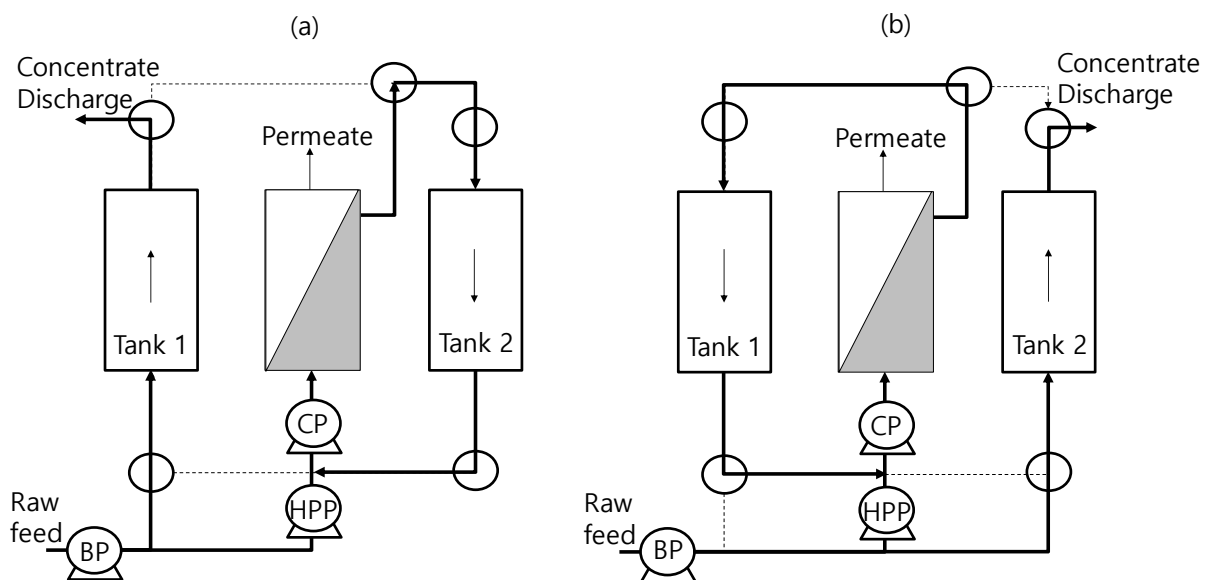


**Fig. 2-23.** Schematic of SBRO process with two external holding tanks (T1 and T2) with a booster pump (BP), high pressure pump (HPP) and a circulation pump (CP) (adapted from [156]).

An alternative approach is that of SBRO operation without external holding tanks [157] consisting of a filtration period followed by concentrate flushing. During the filtration period, RO desalting is accomplished in the mode of total concentrate recycle (**Fig. 2-24a**). Permeate water is continuously produced at a flow rate equal to the flow rate of the saline raw-feed water

entering the system (i.e.,  $q_P = q_O$ ), thereby achieving 100% water recovery during the filtration period. The filtration process is then followed by the flushing in order to discharge the concentrate holdup once the physical element pressure threshold (e.g., maximum operating pressure) is reached or when the flushing period is set to attain optimal energy utilization. During the flushing period, the concentrate stream exiting the membrane module is no longer recycled, and only the fresh raw feed (source) water is fed to the system (**Fig. 2-24b**). The filtration and flushing processes are repeated alternately one after the other enabling continuous permeate productivity. The approach described above is often referred to as Semi-Batch RO (SBRO) or Closed-Circuit Desalination (CCD) [22, 27, 29, 42, 43, 63, 147, 158-167].

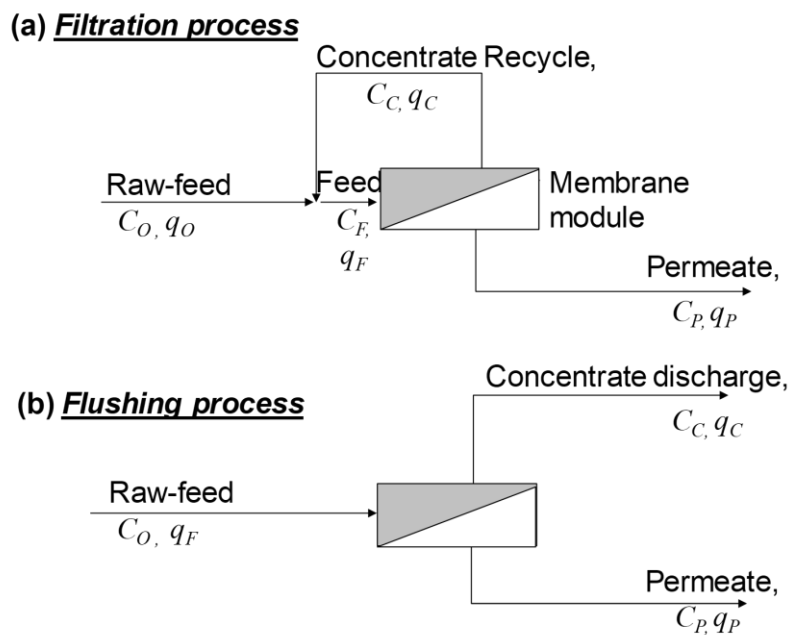


**Fig. 2-24.** Schematic of the two modes of operation in semi-batch RO process without external holding tank: (a) the filtration process, (b) the flushing process with continuous permeate production.

The overall water recovery in semi-batch RO is defined in terms of the cumulative volume of the raw-feed water input ( $Q_O$ ) and the cumulative volume of the permeate production ( $Q_P$ ) given by:

$$Y = \frac{Q_P}{Q_O} \quad (2-27)$$

where  $Q_O$  and  $Q_P$  can be written in terms of the process time in each operating mode as shown in **Fig. 2-25** and expressed in terms of the filtration and flushing durations ( $t_{FT}$  and  $t_{FL}$ , respectively) below:

$$\begin{cases} Q_P = q_{P,FT} \cdot t_{FT} + q_{P,FL} \cdot t_{FL} \\ Q_O = q_{O,FT} \cdot t_{FT} + q_{O,FL} \cdot t_{FL} \end{cases} \quad (2-28)$$

in which  $q_P$  and  $q_O$  indicate the volumetric flow rate of the permeate and the raw-feed water streams, respectively, and subscripts  $FT$  and  $FL$  indicate the filtration and the flushing periods, respectively.

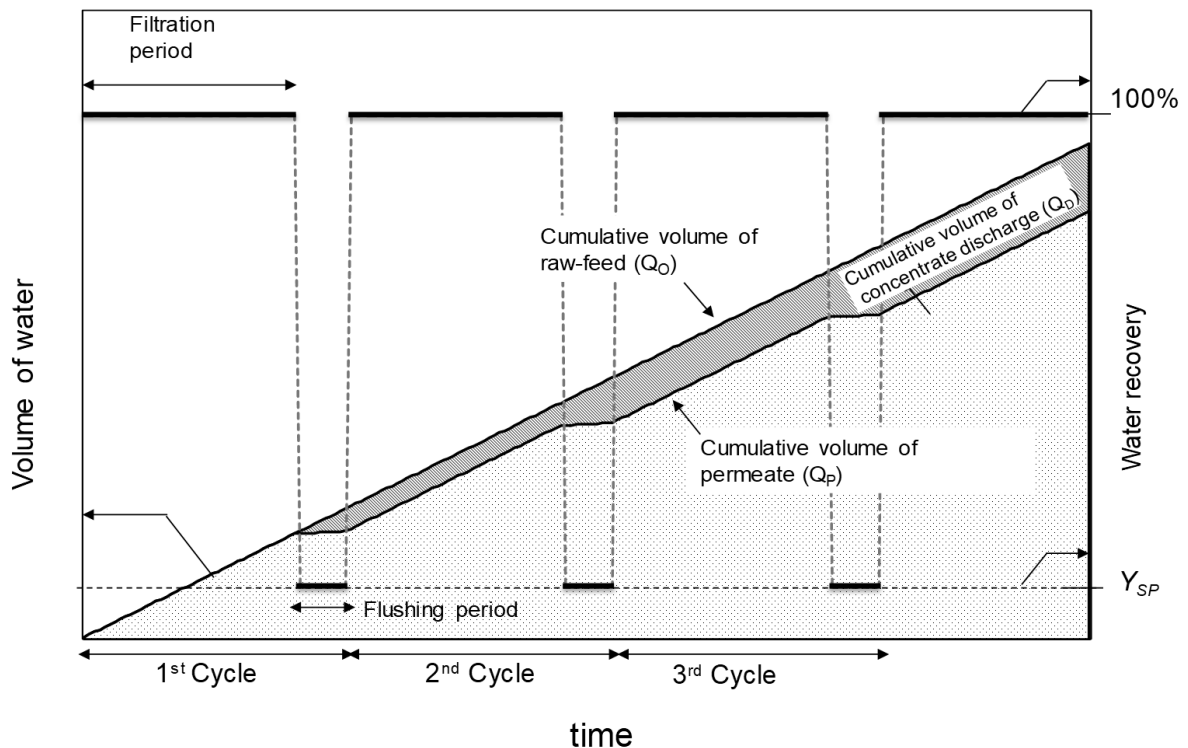


**Fig. 2-25.** Variation of the cumulative volume of raw-feed water ( $Q_O$ ), the permeate production ( $Q_P$ ), and the concentrate discharge ( $Q_D$ , indicated with the shaded area between the  $Q_O$  and  $Q_P$  curves) during SBRO filtration and the flushing periods. The water recovery in each operating period is indicated on the secondary vertical axis.

Assuming that there is no permeate production during the flushing period (i.e.,  $q_{P,FL}=0$ ), Qui et al. [29] reported the following simple analytical model for the theoretical minimum specific energy consumption in SBRO in terms of the overall water recovery ( $Y$ ),

$$SEC_{ir} = \pi_o \left[ 1 + \frac{Y}{2 \cdot (1-Y)} \right] \quad (2-29)$$

The above model for SBRO predicts competitive  $SEC$  with multi-stage systems with interstage booster pumps (**Fig. 2-26**). However, it is noted that the above model was developed based on assumptions of negligible concentration polarization, complete salt rejection without considering the energy consumption in the flushing period.

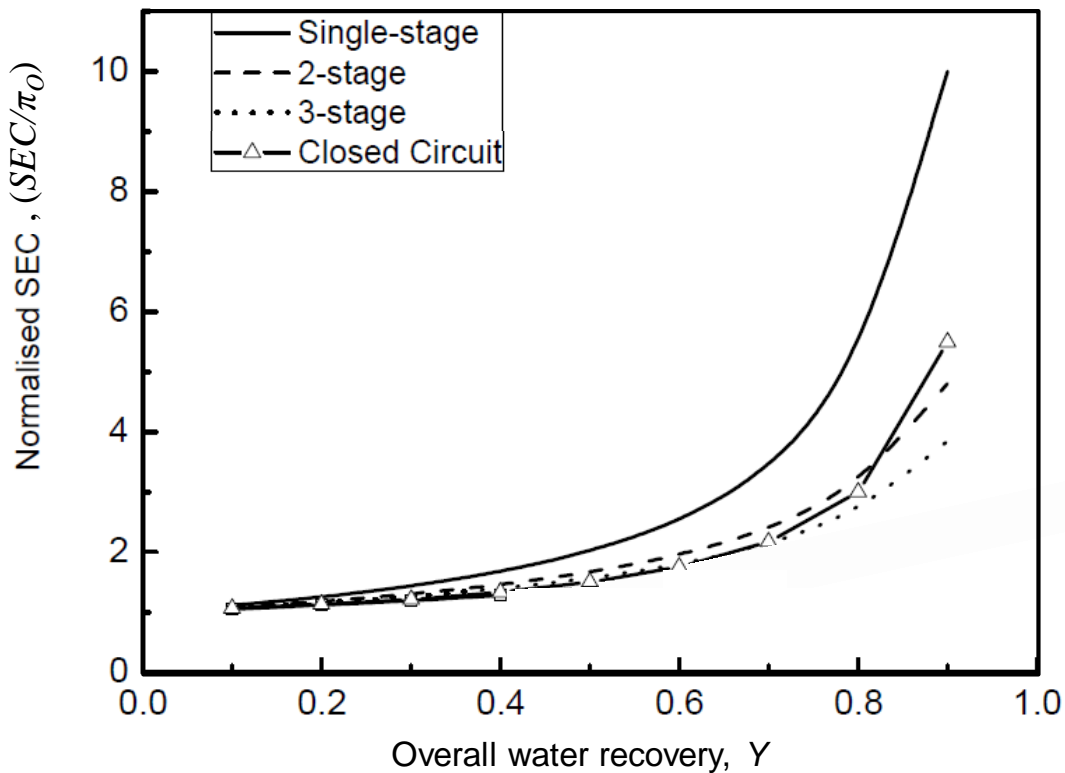


**Fig. 2-26.** Comparison theoretical minimum specific energy cost (normalized by the raw-feed osmotic pressure) in semi-batch RO and steady-state RO with ERD on 1, 2, and 3 stages system platforms [29].

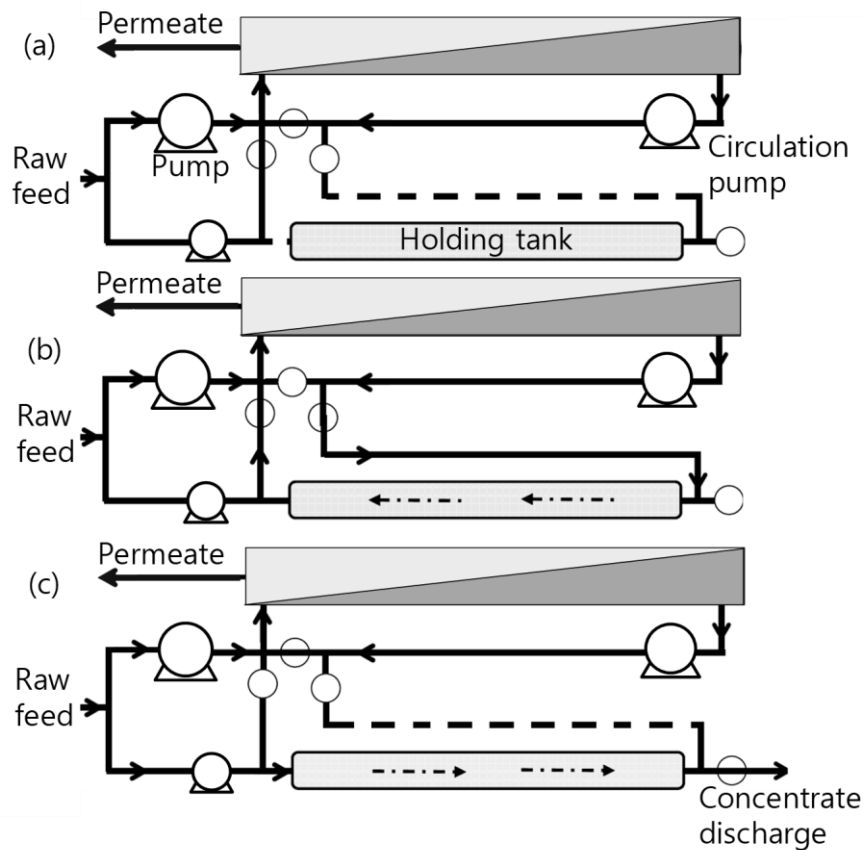


**Fig. 2-27.** Schematic of the two modes SBRO operation with holding tank: (a) the filtration process with total concentrate recycle, (b) the flushing process with raw feed water from the holding tank, and (c) the concentrate discharge process from the holding tank (adapted from [168]).

Schuetze et al., [165, 166] experimentally demonstrated the concept of SBRO operation using a pilot-scale spiral wound SBRO system with an external holding tank to store concentrate discharge during the flushing period (**Fig. 2-27**). The above study used NaCl feed solution at various salinity levels (1000 – 5000 ppm) for high-recovery (68-91%) and demonstrated that the energy efficiency of SBRO, comparable to conventional RO systems [11, 22, 130]. Schuetze et al. reported SEC of 0.59 kWh/m<sup>3</sup> for 88% overall water recovery for desalting 2500 ppm NaCl solution. The above SEC is lower than the reported SEC of 0.80 kWh/m<sup>3</sup> for desalination of 2680 mg/L TDS brackish water at 88.2% recovery [158] for a commercial SBRO system that consisted of a single stage with four membrane elements. The

above study noted the practical limitation of SBRO associated with head loss at valves and fittings (for mix, split, bending, contractions, and expansions) due to extensive concentrate recycling. Efraty et al. [168] also used a pilot scale SBRO system with four parallel membrane modules (of 4 element in each) and an holding tank (referred to as side conduit in [168], **Fig. 2-27**). The above study demonstrated desalination of 41,000 mg/L TDS Mediterranean feed water, and reported *SEC* of 1.9 – 2.3 kWh/m<sup>3</sup> for desalting at 48% recovery. The above reported *SEC* is about 30% higher than the theoretical minimum *SEC* of 1.6 kWh/m<sup>3</sup> for seawater desalination at recovery of 50% with 100% pumping efficiency [145], and is comparable to the lowest reported *SEC* of 1.8 kWh/m<sup>3</sup> for conventional SSRO with an ERD (**Fig. 2-16**) [145].

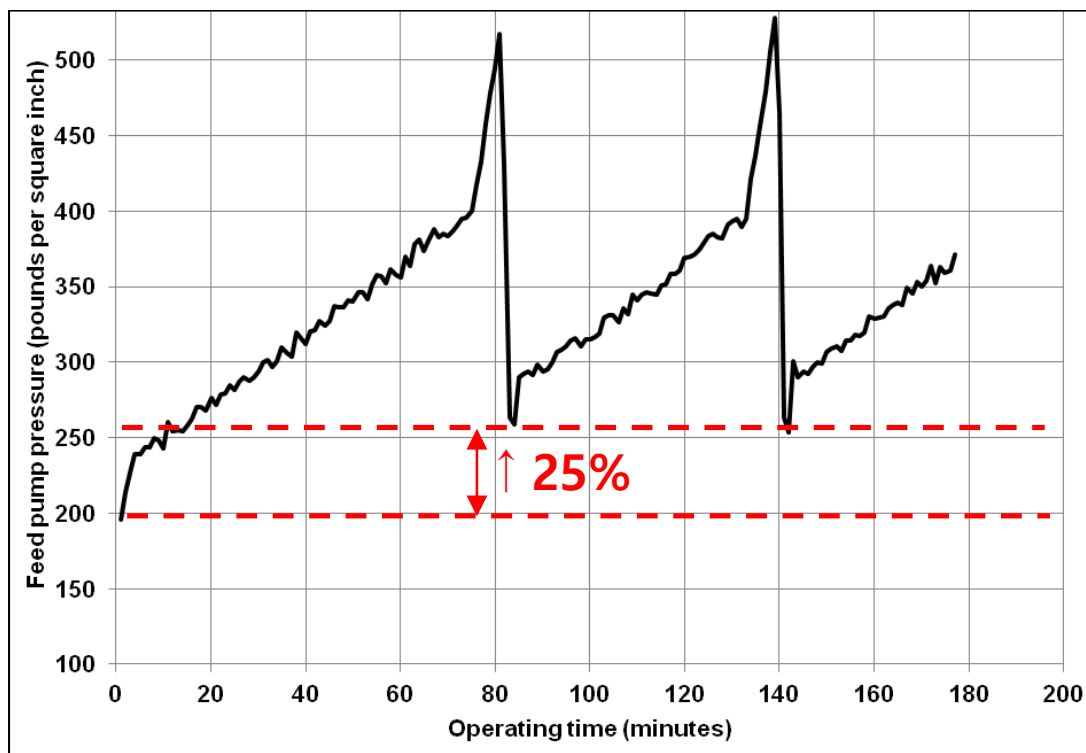


**Fig. 2-28.** Variation of the feed pressure during semi-batch RO operation from a pilot-scale RO system for desalting brackish well water (at the Brackish Groundwater National Desalination Research Facility in Alamogordo, New Mexico) of 5,900 ppm TDS, feed flow rate ( $q_F$ ) of 0.6 gpm, and the permeate flux of 16 gfd (adapted from [165]) using brackish water spiral wound membrane (Filmtec BW30-2540, Dow Corporation, Midland, Michigan).

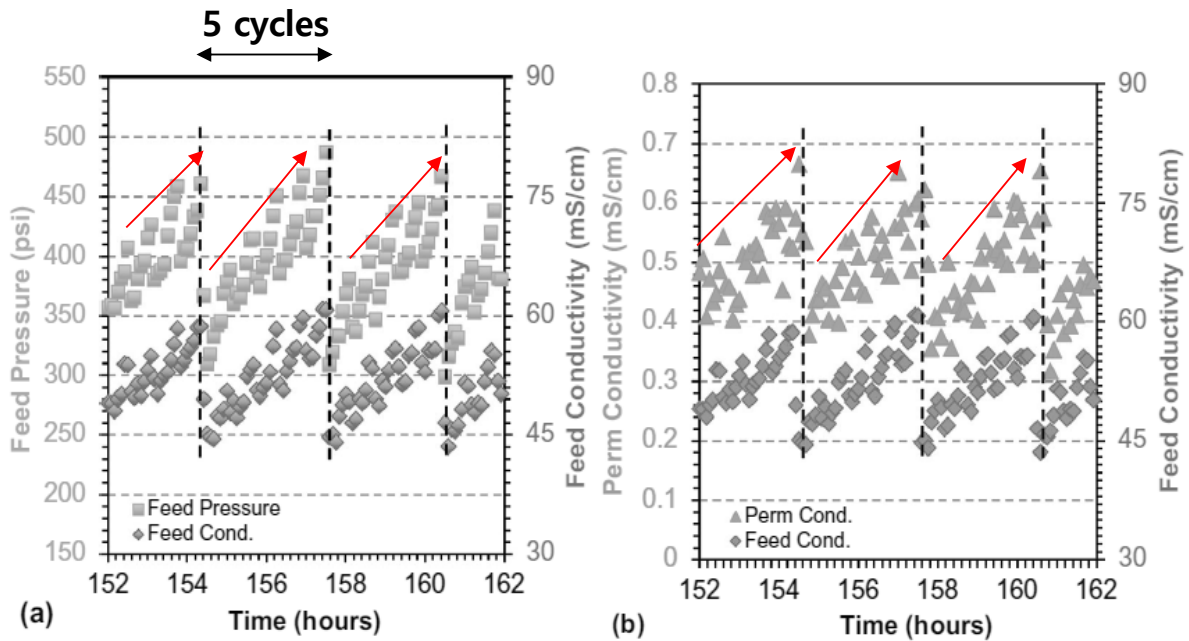


**Fig. 2-29.** Variation of (a) feed pressure and feed conductivity, and (b) permeate conductivity with respect to time during SBRO operation for desalting brackish water pf 16,049 ppm TDS with BW30 brackish water RO membrane in a plate-and-frame membrane cell for overall water recovery at  $Y=35 - 40\%$  (adapted from [49]).

However, it should be recognized that RO feed pressure increased with number of filtration-flushing cycle count, which may lead to higher SEC. For example, Schuetze et al. [165, 166] reported that the required RO feed pressure in the 2<sup>nd</sup> filtration-flushing cycle increased about 25% relative to the that in the first cycle (**Fig. 2-28**). Another SBRO study [49] using bench scale plate-and-frame membrane cells also reported about 5-10% increase of the required applied feed pressure with consecutive filtration-to-flushing cycle, as well as rise in feed conductivity, and permeate conductivity (**Fig. 2-29**). Therefore, the above study required implementation of two consecutive concentrate flushing (i.e., flushing periods were extended by a factor of 2) every five cycles in order to ensure adequate excess concentrate flushing. As a consequence of the extended flushing period, larger volume of raw feed water (i.e., the flushing media) was consumed, which adversely affects the overall water recovery of SBRO

operation (**Fig. 2-25**). The above behavior is not surprising given the presence of salt dispersion in the spiral wound RO membrane concentrate channel (i.e., feed channel), as evident in multiple publications [44, 169, 170].

Previous investigations [29, 42, 43, 171] on the theoretical energy consumption assumed SBRO operation under plug flow condition that neglects the impact of salt dispersion during concentrate flushing. Given the complex structure of RO membrane channels [69] and various hydraulic components in RO systems, it is critical to characterize residence time distribution (RTD) [169, 170], and its impact on the SEC in multi-cycle SBRO operation. Accordingly, the impact of salt dispersion on the specific energy consumption in SBRO processes is discussed in-depth in **Chapter 4**.

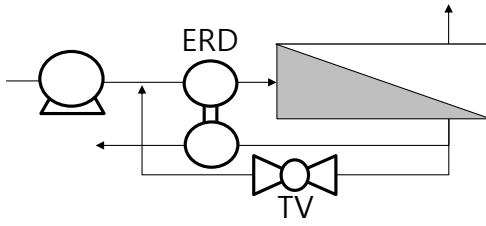
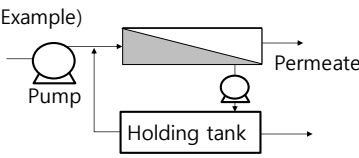
The unique operating characteristic of unsteady-state SBRO process, whereby the system refreshes the RO system with the fresh raw-feed water by implementing periodic flushing process (**Fig. 2-24b**), has been claimed to retard or prevent mineral scaling. For example, it was argued in [48] that surface mineral scaling can be prevented ensuring that the filtration period is shorter than the crystallization induction time. It was further claimed that periodic raw-feed water flushing can remove/dissolve any formed scale (provided that the feed water is undersaturated with respect to the sparingly soluble mineral salts that are of concern). As a result, the membrane surface would be reset to its clean condition, thereby decreasing the propensity for mineral salt nucleation and growth. In such an approach, one may assume that the flushing process can be initiated to rapidly recover the initial saturation level in the RO system holding once the pre-determined scaling level is reached during the filtration period. However, given that surface crystallization depends not only on the solution characteristics but also on the type of substrate or surface [172], a complete reset of the membrane surface (free

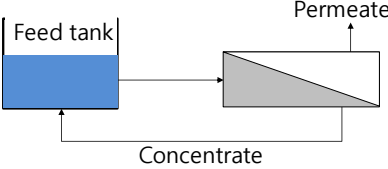


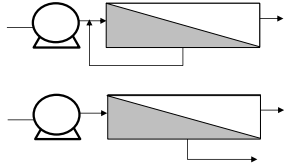
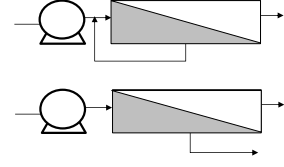
from mineral scaling) may be difficult to achieve with concentrate flushing in SBRO operation. Accordingly, in **Chapter 5**, the impact of concentrate flushing in SBRO operation on mineral scaling propensity, with gypsum as model scalant, was experimentally evaluated relative to steady state RO operation with partial concentrate recycle (SSRO-PR). A summary of the relevant prior work is provided in **Table 2-3**.

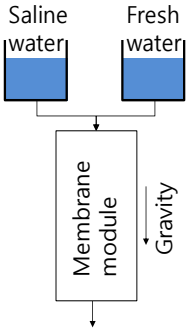
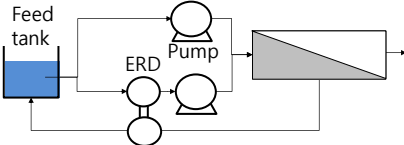
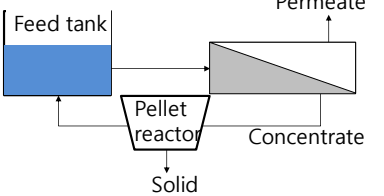
**Table 2-3.** Relevant prior work on high recovery RO desalination with concentrate recycling.

Authors	Assertions, claims, contributions and shortcomings
Bratt 1989 US Patent 4814086A [156]	<p><b>Assertions/Claims:</b></p> <ul style="list-style-type: none"> <li>▪ RO desalination with concentrate recycle with external holding tank enables continuous permeate productivity at high recovery.</li> </ul> <p><b>Contributions:</b></p> <ul style="list-style-type: none"> <li>▪ First introduction of SBRO system design with external holding tanks (<b>Fig. 2-23</b>).</li> </ul> <p><b>Shortcomings:</b></p> <ul style="list-style-type: none"> <li>▪ Implementation of external holding tanks may require large system footprint, and increase capital cost for installation.</li> </ul>
Szucz & Szucs 1991 US Patent 6797173B1 [173]	<p><b>Assertions/Claims:</b></p> <ul style="list-style-type: none"> <li>▪ The energy consumption in SBRO process is significantly less than conventional steady state RO desalination.</li> </ul> <p><b>Contributions:</b></p> <ul style="list-style-type: none"> <li>▪ First introduction of periodic and sequential concentrate recycling consisting of a water purification phase with total concentrate recycle (<b>Fig. 2-24a</b>), and concentrate discharging phase without concentrate recycle (<b>Fig. 2-24b</b>)</li> </ul> <p><b>Shortcomings</b></p> <ul style="list-style-type: none"> <li>▪ Proof of the concept was not provided.</li> <li>▪ Depending on the operating mode, the membrane feed flow rate may significantly vary, and thus affect the growth and thickness of the concentration</li> <li>▪</li> </ul>

<p>Oklegas 2004 US Patent 6797173B1 [174]</p>	<p><b>Assertions/Claims:</b></p> <ul style="list-style-type: none"> <li>Energy recovery device can be implemented into the RO process with high-pressure concentrate recycling to minimize irreversible energy loss associated with concentrate pressure throttling</li> </ul>  <p><b>Contributions:</b></p> <ul style="list-style-type: none"> <li>A process with concentrate recycling as means to recover hydraulic energy from the brine flow.</li> </ul> <p><b>Shortcomings:</b></p> <ul style="list-style-type: none"> <li>Suboptimal handling of irreversible energy loss at the concentrate throttling valve (TV).</li> <li>Lacks prediction or experimental verification of the performance of the proposed design concept</li> </ul>
<p>Efraty <i>et al.</i> (2009- 2015) [157, 175- 182]</p>	<p><b>Assertions/Claims:</b></p> <ul style="list-style-type: none"> <li>SBRO with or without external holding tanks provides lower energy consumption and reduced fouling/scaling relative to conventional steady state processes.</li> </ul>  <p><b>Contributions:</b></p> <ul style="list-style-type: none"> <li>Detailed semi-batch processes under variable pressure with and without external concentrate holding tanks [176, 182] (<b>Fig. 2-23</b> and <b>Fig. 2-24</b>, respectively).</li> <li>Demonstrated the CCD desalination approach using a commercial RO systems with various types of source water [177, 179-181].</li> </ul> <p><b>Shortcomings:</b></p> <ul style="list-style-type: none"> <li>The process without energy recovery device may lead to energy loss during concentrate flushing phase.</li> <li>SBRO SEC comparison was made against conventional SSRO systems with ERD efficiency of 70-80%. The SEC in SSRO can be significantly reduced with highly efficient ERDs.</li> <li>Arguments regarding energy saving or fouling reduction remain questionable without definitive supporting data.</li> </ul>
<p>Schuetze, Rainwater, and Song (2014) [165, 166]</p>	<p><b>Assertions/Claims:</b></p> <ul style="list-style-type: none"> <li>Experimental data demonstrated the potential of small scale SBRO system to operate at SEC comparable to those published for conventional large-scale steady state RO systems at recoveries greater than 75%.</li> </ul> <p><b>Contributions:</b></p> <ul style="list-style-type: none"> <li>The concept of SBRO with an external holding tank (similar to <b>Fig. 2-27</b>) was demonstrated using a pilot scale system</li> <li>Systematic investigation to address practical challenges such as head loss caused by extensive concentrate recycling at increased circulation flow.</li> </ul>

	<p><b>Shortcomings:</b></p> <ul style="list-style-type: none"> <li>▪ Lacks quantitative analyses for predictions of energy consumption, and validation based on experimental data.</li> <li>▪ The experimental data suggests cycle-to-cycle increase in feed water conductivity and pressure; however, the study lacked long term (i.e., multi-cycle) demonstration of the efficacy of SBRO operation.</li> </ul>
<p>Barello <i>et al.</i> (2015) [183]</p>	<p><b>Assertions/Claims:</b></p> <ul style="list-style-type: none"> <li>▪ The large variation of feed pressure and feed salinity during SBRO operation significantly affects the water and salt permeability across the membrane.</li> </ul>  <p><b>Contributions:</b></p> <ul style="list-style-type: none"> <li>▪ Provided laboratory experiments and process modeling to evaluate impacts of feed pressure and feed salinity on water and salt passage across the membrane that may affect RO batch performance.</li> </ul> <p><b>Shortcomings:</b></p> <ul style="list-style-type: none"> <li>▪ No consideration of other RO characteristics such as SEC or membrane fouling for optimization of RO desalting with total concentrate recycle.</li> </ul>
<p>Qiu <i>et al.</i> (2012) [29]</p>	<p><b>Assertions/Claims:</b></p> <ul style="list-style-type: none"> <li>▪ SBRO operation provides comparative SEC to that of the 3-stage system with a recovery of 80%.</li> <li>▪ Costly ERDs and booster pumps can be avoided with SBRO, thereby lowering installation, operation, and maintenance costs.</li> </ul> <p><b>Contributions:</b></p> <ul style="list-style-type: none"> <li>▪ Provided analytical models for the SEC of SBRO operation without an external holding tank (<b>Fig. 2-24</b>).</li> <li>▪ Comparative analysis between batch, semi-batch, and continuous RO desalination to explore potential energy savings enabled by concentrate-recycling</li> </ul> <p><b>Shortcomings:</b></p> <ul style="list-style-type: none"> <li>▪ Modeling was limited to SBRO process without permeate production during the flushing period.</li> <li>▪ Oversimplified the SBRO process ignoring the effects of concentration polarization, salt rejection, energy recovery, solute dispersion, and corresponding loss of flushing efficacy.</li> </ul>
<p>Zhu <i>et al.</i> (2012) [63]</p>	<p><b>Assertions/Claims:</b></p> <ul style="list-style-type: none"> <li>▪ SBRO requires higher SEC than a steady state single-stage RO process with an ERD.</li> </ul> <p><b>Contributions:</b></p> <ul style="list-style-type: none"> <li>▪ (Chapter 9) Provided detailed SEC analysis and overall process cost for RO with total concentrate recycling (<b>Fig. 2-24a</b>) considering system down time for intermittent flushing</li> </ul> <p><b>Shortcomings:</b></p>

	<ul style="list-style-type: none"> <li>▪ Operational benefits such as reduced concentration polarization effects from increased cross flow velocity were ignored</li> <li>▪ SEC analysis was limited to SBRO operation without permeate production during the concentrate flushing phase.</li> <li>▪ Impact of salt accumulation during cyclic SEBO operation was not reflected in SEC modeling</li> </ul>
<p>Lin <i>et al.</i> (2015) [42]</p>	<p><b>Assertions/Claims:</b></p> <ul style="list-style-type: none"> <li>▪ SBRO without external holding tank provides potential energy saving relative to single-stage RO</li> <li>▪ Membrane fouling and scaling can be reduced in SBRO by increasing the crossflow to generate greater hydrodynamic shear</li> </ul>  <p><b>Contributions:</b></p> <ul style="list-style-type: none"> <li>▪ Provided modeling study of SEC in SBRO (<b>Fig. 2-24</b>) in terms of overall water recovery, and compared to conventional steady state RO processes in single- and multi-stage configurations.</li> </ul> <p><b>Shortcomings:</b></p> <ul style="list-style-type: none"> <li>▪ SBRO analysis was limited to the filtration period with permeate production at total concentrate recycling ignoring the impact of flushing efficacy on the SEC and water recovery.</li> <li>▪ Concentration polarization effect was not accounted.</li> <li>▪ Did not provide experimental data to validate various claims.</li> </ul>
<p>Werber <i>et al.</i> (2017) [43]</p>	<p><b>Assertions/Claims:</b></p> <ul style="list-style-type: none"> <li>▪ SBRO provides significant energy savings comparable to multi-stage RO processes with inter-stage booster pump and ERDs.</li> </ul>  <p><b>Contributions:</b></p> <ul style="list-style-type: none"> <li>▪ Provided energy analysis for SBRO process without external holding tank (<b>Fig. 2-24</b>) considering process inefficiencies (i.g., frictional losses, concentration polarization).</li> <li>▪ Provided numerical modeling of SEC for SBRO operation based on a fourth order Runge-Kutta method.</li> </ul> <p><b>Shortcomings:</b></p> <ul style="list-style-type: none"> <li>▪ Did not account for the SEC during the flushing period.</li> <li>▪ Analysis was limited to plug flow condition that allows complete concentrate flushing within the system space time (termed “the characteristic time of the system” in [43]).</li> <li>▪ Did not provide experimental data</li> </ul>

<p>Qiu <i>et al.</i> (2011) [44]</p>	<p><b>Assertions/Claims:</b></p> <ul style="list-style-type: none"> <li>▪ Salt dispersion in RO feed channel causes higher SEC, relative to the ideal plug flow condition</li> </ul> <p><b>Contributions:</b></p> <ul style="list-style-type: none"> <li>▪ Quantified the impact of solute dispersion on RO concentrate salinity profile during the concentrate flushing period based on Taylor's analysis.</li> <li>▪ Provided experimental data to validate the theoretical model for salinity variation during the concentrate flushing period in the presence of salt dispersion.</li> </ul> <p><b>Shortcomings:</b></p> <ul style="list-style-type: none"> <li>▪ Discussed the impact of solute dispersion in RO concentrate channel using a single membrane element system without a pump. Concentrate flushing was conducted using gravity flow fed to the membrane module.</li> <li>▪ Did not demonstrate the impact of salt dispersion on SEC or membrane fouling/scaling in practical SBRO applications.</li> </ul> 
<p>Warsinger <i>et al.</i> (2018) [48]</p>	<p><b>Assertions/Claims:</b></p> <ul style="list-style-type: none"> <li>▪ SBRO provides enhanced inorganic fouling resistance relative to conventional steady-state RO processes.</li> </ul> <p><b>Contributions:</b></p> <ul style="list-style-type: none"> <li>▪ Developed an analytical framework for assessing the onset of mineral scaling during SBRO operation based on the comparison of the fluid residence time and nucleation induction time for crystallization in solution supersaturated with sparingly soluble salts.</li> </ul> <p><b>Shortcomings:</b></p> <ul style="list-style-type: none"> <li>▪ Did not provide experimental data to validate the comparative analysis.</li> <li>▪ Claims regarding the crystallization induction time were based on published data for nucleation in bulk solution, rather than for crystallization on membrane surfaces.</li> </ul> 
<p>Drak <i>et al.</i> (2017) [163]</p>	<p><b>Assertions/Claims:</b></p> <ul style="list-style-type: none"> <li>▪ SBRO reduces membrane mineral scaling.</li> </ul> <p><b>Contributions:</b></p> <ul style="list-style-type: none"> <li>▪ Integrated SBRO operation with a pellet/fluidized bed reactor to further improve resistance to mineral scaling.</li> <li>▪ Used brine solution from an existing RO plant supersaturated with calcium carbonate and silica to achieve &gt;90% recovery.</li> </ul> <p><b>Shortcomings:</b></p> <ul style="list-style-type: none"> <li>▪ Integration of salt precipitation unit may increase capital cost and system footprint.</li> <li>▪ Did not show experimental data for conventional steady state RO operation or SBRO operation without fluidized bed, to clearly examine effects of SBRO operation for scaling mitigation</li> </ul> 

Riley *et al.*  
[49]

**Assertions/Claims:**

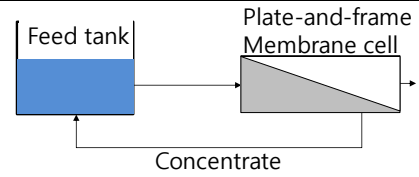
- SBRO reduces minimal scaling and organic fouling relative to conventional steady state RO.

**Contributions:**

- Provided experimental data from long-term (over 900 filtration-flushing cycles) SBRO evaluation using a bench scale plate-and-frame membrane cell.
- Experimental data demonstrated decreased water permeability during the filtration period due to reversible fouling, and recovery of the water permeability loss following the concentrate flushing period.

**Shortcomings:**

- Model solution lacked major mineral scalants (e.g., calcium sulfate dihydrate, calcium carbonate, or silica). Thus, the results were limited to organic fouling from dissolved organic carbon, DOC (at 113 mg/L from BTEX, n-alkanes, proteins, biopolymers, humic substances).
- Claimed absence of fouling based on indirect fouling detection methods (e.g., permeability monitoring), which may not provide adequate sensitivity.



# **Chapter 3 Steady State RO Desalination with Partial Concentrate Recycling for Operational Flexibility**

## **3.1 Overview**

Efforts are increasing to diversify the water portfolio in various regions around the world through upgrading of otherwise underutilized and impaired inland water sources. Given the wide range of inland water quality and the geographical distribution of water resources, it is critical for RO systems to have sufficient flexibility for desalination over a wide range of feed water recovery and salinity. However, ensuring both operational flexibility and energy efficiency is challenging in conventional configuration of RO systems that operate in the mode of single pass feed flow through a membrane train. In such systems the allowable ranges of feed and permeate flow rates are typically narrow in order to: (a) maximize the utilization of membrane surface area, and (b) reduce the propensity of membrane element fouling and/or mineral scaling. The above operational constraints impose limits on the attainable product water recovery and thus the permeate productivity for a given membrane element array design. Correspondingly, energy optimal operation of ERDs and pumps is also constrained to a narrow flow rate range.

Partial concentrate recycling provides an additional degree of freedom with respect to product water recovery in steady state RO operation (SSRO-PR), and can be integrated with suitable energy recovery devices [32, 41]. In principle, optimal integration of ERD with RO operation under the condition of partial recycle can provide the dual benefit of a single RO desalination platform capable of operating over wide ranges of product recovery and salinity, while also providing a degree of energy recovery. With implementation of an energy recovery

device, SSRO-PR operation can be enabled using a relatively low-pressure pump, even for seawater desalination. However, increasing recovery increases energy consumption; thus, there is a tradeoff between the desired productivity and reduction in energy utilization. Accordingly, this chapter presents an analysis framework and experimental data to assess SSRO-PR and to demonstrate operational flexibility with respect to product water recovery.

### 3.2 Steady state RO with partial recycling (SSRO-PR) system operation with energy recovery and concentrate recycle

#### 3.2.1 SSRO-PR design and operation

The present study builds on the important realization that method of concentrate recycling can only be effectively integrated in RO processes when the fluid regulation could be decoupled from the main membrane process (**Fig. 3-1**).

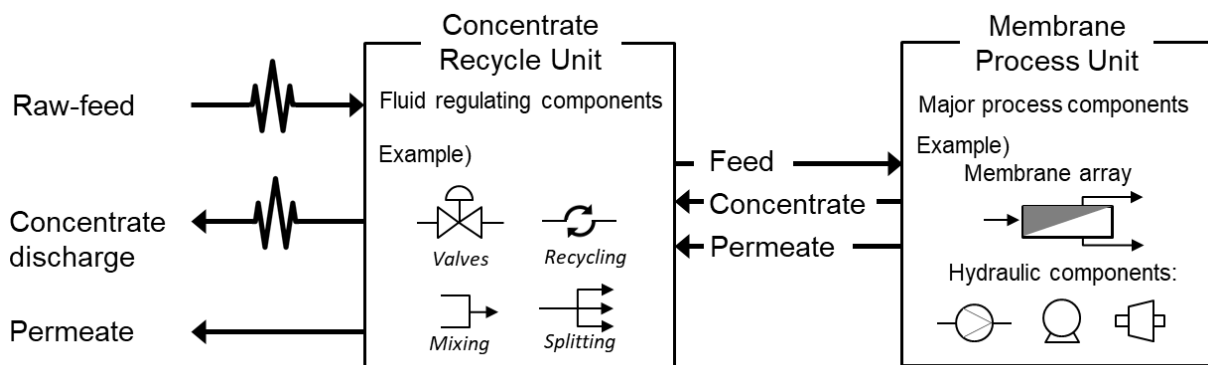


**Fig 3-1.** Schematic illustration of the concept of process system decomposition in flexible RO. The membrane process unit (MPU) maintains constant (optimal) flow rate of feed, concentrate and permeate streams, and per-pass water recovery ( $Y_{SP}$ ), while the concentrate-recycle unit (CRU) provides control over the overall system water recovery ( $Y$ ) by fluid regulation (in source, concentrate discharge, and concentrate recycle streams). The MPU must integrate hydraulic components for pressure-generation and energy recovery in addition to the membrane array for water treatment.



In the present approach of process decomposition, two key functional groups fluidly connected on a single RO system platform:

- (a) Membrane Process Unit (MPU) provides for liquid separation at constant flow rate for optimal performance of system components
- (b) Concentrate Recycle Unit (CRU) provides customized flow regulation to extend operational flexibility

The steady state RO with partial concentrate recycling (SSRO-PR) configuration analyzed in the present study is one that integrates an energy recovery device (ERD) with concentrate recycle. SSRO-PR operation can be conceptually and operationally decomposed into two separate but connected process units (**Fig. 3-2**) consisting of a membrane process unit (MPU) and a concentrate recycle unit (CRU). The MPU components (membrane array, driving force generation, and energy recovery) are integrated so that the RO element feed flow rate ( $q_F$ ), concentrate flow rate ( $q_C$ ) exiting the membrane module, and thus product recovery in a single-pass through the membrane array ( $Y_{SP}=q_P/q_F$ ) can remain fixed at the optimal level, within equipment design limits and optimal energy efficiency. The ERD in the MPU serves to recover energy from the concentrate stream and whereby the recycled concentrate stream ( $q_R$ ) is directed to the feed-side of the RO pump. The feed is pre-pressurized by the RO feed pump (from a pressure  $P_O$  to  $P_{FL}$ ) while the ERD recovers energy from the concentrate stream and depressurizes the concentrate effluent from the membrane module from  $P_{CH}$  to  $P_{CL}$  in order to intensify the pressure (i.e., from  $P_{FL}$  to  $P_{FH}$ ) of the MA feed to the level needed for achieving the product flow rate set-point in the MA. In principle, suitable ERDs include (but are not limited to) pressure exchangers or intensifiers (e.g., Clark Pump) [142]. The pressure exchanger reduces energy utilization by splitting the feed flow whereby the majority of this

flow is provided via the feed pump and the remainder is through the pressure exchanger; however, the pressure generated by the feed pump must be the same as in the pressure exchanger. In contrast, a pressure intensifier reduces energy utilization by reducing the required feed pump outlet pressure. This is a major operational benefit as it allows the use of relatively low-pressure pumps, even for desalting high salinity source water. It is noted, however, that in practice, pressure intensifiers are mostly available for small systems, yet are simple with respect to operational control, while pressure exchanger are usually more suitable for larger systems.

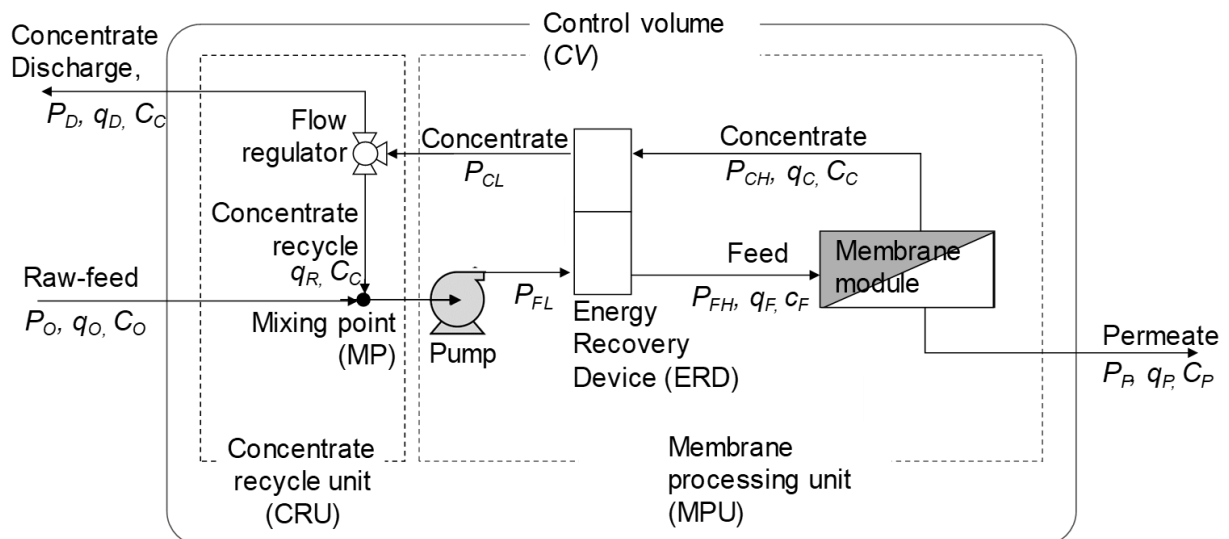


**Fig. 3-2.** SSRO-PR configuration with an energy recovery device (ERD). The raw feed water pressure is raised from  $P_o$  to  $P_{FL}$  by the feed pump and the ERD intensifies the pump outflow stream pressure from  $P_{FL}$  to  $P_{FH}$  by utilizing the hydraulic pressure of the concentrate stream from the membrane module. Note:  $q_i$  and  $c_i$  and  $P_i$  are the flow rate, salt concentration and pressure of the indicated stream  $i$ .

The concentrate-recycle unit (CRU), which provides feed ( $q_F$ ) to and receives concentrate ( $q_C$ ) from the MPU (**Fig. 3-2**) via the ERD, controls the overall system product recovery ( $Y = q_P/q_o$ ) by regulating the system inlet flow of raw feed ( $q_o$ ) and system outlet flow of the concentrate discharge ( $q_D$ ). This arrangement avoids the need for a recirculation pump (i.e., for

the concentrate) while enabling the use of relatively low-pressure RO module feed pump. In the CRU, the system outlet waste flow ( $q_D$ ) is taken from a portion of the MPU concentrate ( $q_C$ ). The remaining portion is the concentrate recycle stream ( $q_R$ ) is mixed in the CRU with the system inlet raw feed stream ( $q_O$ ) to generate the membrane array feed stream ( $q_F$ ). By regulating the recycled concentrate flow rate ( $q_R$ ) and keeping the MPU feed flow rate fixed (i.e.,  $q_F=q_O +q_R$ ), the incoming raw feed flow rate ( $q_O$ ); thus, the overall system product recovery ( $Y=q_P/q_O$ ) can be varied in a flexible manner without the need to change the flow rates of the streams in the MPU (**Fig. 3-2**).

Based on a material balance about the mixing point (MP on **Fig. 3-2**), the variation of the concentrate recycle flow rate ( $q_R$ ), with respect to the overall and the single pass water recoveries ( $Y$  and  $Y_{SP}$ , respectively), can be written as:

$$q_R^* = \frac{1}{Y_{SP}} - \frac{1}{Y} \quad (3-1)$$

where  $q_R^*$  indicate the concentrate recycle flow rate normalized by the permeate water flow rate ( $q_R^* = q_R / q_P$ ). It is noted that the normalized RO element feed ( $q_F^* = q_F / q_P = 1 / Y_{SP}$ ) and the normalized raw-feed ( $q_O^* = q_O / q_P = 1 / Y$ ) water flows are simply reciprocals of the single-pass and the overall water recoveries, respectively. The overall water recovery ( $Y$ ) can be written, making use of **Eq. (3-2)**, in terms of the recycle ratio,  $R$  (defined as  $R = q_R / q_O$ , where  $q_R$  and  $q_O$ , and the raw feed stream flow rates, respectively) as follows:

$$Y = Y_{SP} \cdot (1 + R) \quad (3-2)$$

Given the above, the direct RO membrane processing unit inlet feed, concentrate and recycle streams flow rates, with respect to the overall water recovery ( $Y$ ), depend on the membrane train single single-pass recovery ( $Y_{SP}$ ) and concentrate recycle ratio. The overall system

recovery ( $Y$ ), which is governed by the single-pass recovery and the concentrate recycle ratio (**Eq. (3-2)**), is constrained by  $Y_{SP} < Y < 1$  and  $0 \leq R \leq (1 - Y_{SP}) / Y_{SP}$ . As an illustration, the FLERO operation is maintained at constant permeate and RO module feed flow rates by adjustments of the concentrate recycle ratio and raw-feed flow rate as described in **Section 0** for the present experimental system (**Section 3.3.2**).

### 3.2.2 SSRO-PR energy utilization

The specific energy consumption (SEC) for desalination is determined from [132, 136],

$$SEC = \frac{\dot{W}_p}{\eta_p q_p} \quad (3-3)$$

in which  $q_p$  is the permeate flow rate, and  $\dot{W}_p$  is the required pressure work to achieve the prescribed desalination working pressure [136],

$$\dot{W}_p = \Delta P_f (q_F - \eta_{ER} q_C) \quad (3-4)$$

$\Delta P_f = P_f - P_o$  where  $P_f$  and  $P_o$  are the pressures of the feed entering the membrane array and of the raw feed water, respectively, and  $q_F$  and  $q_C$  are the volumetric flow rates of the RO membrane feed and the concentrate exiting the membrane module, respectively. Thus, combining **Eqs. (3-3)** and **(3-4)** leads to the following expression for  $SEC$  for RO desalting:

$$SEC = \frac{(1 - \eta_{ER} \cdot (1 - Y_{SP}))}{\eta_p Y_{SP}} \Delta P_f \quad (3-5)$$

where  $Y_{SP}$  is the single-pass water recovery ( $Y_{SP} = q_p/q_F$ ). Assuming that the pressure of the depressurized permeate and the raw feed are essentially identical (i.e.,  $P_p \sim P_o$ ), the thermodynamic crossflow restriction applies for a single pass RO train, i.e.,

$$\Delta P_f \geq (\pi_{exit} - \pi_p) \cong \frac{1 - Y_{SP}(1 - R_s)}{1 - R_s \cdot Y - Y_{SP}(1 - R_s)} \pi_o \quad (\text{Section 3.2.3})$$

where  $\pi_o$  is the raw feed stream osmotic pressure, and  $R_s$  is the observed membrane salt rejection (.e.,  $R_s = 1 - C_p/C_f$  in which  $C_p$  and  $C_f$  are the permeate and feed streams salt concentrations, respectively). The above thermodynamic restriction refers to minimum SEC, at a given recovery, whereby permeate productivity occurs along the entire RO element train up to the exit point of the tail element where the permeation driving force [184].

Given that the salt concentration is highest at the membrane exit, the transmembrane pressure ( $\Delta P$ ) must be greater than the transmembrane osmotic pressure at the membrane exit ( $\Delta P \geq \Delta \pi$ ) in order to maintain positive permeate flux over the length of the membrane train with the flux diminishing to zero only at the exit point from the membrane array (i.e., hence the condition of  $J_v \geq 0$ ). Therefore, given the classical expression for the permeate flux [61, 132] (**Eq. (2-1)**), the transmembrane pressure at the exit of the RO tail element ( $\Delta P_{exit}$ ) can be expressed as

$$\Delta P_{exit} = (J_v / L_p + \Delta \pi)_{exit} \quad (3-6)$$

The transmembrane pressure at the membrane exit can be expressed as  $\Delta P_{exit} = \Delta P_f - (\delta p)_{loss}$  where  $\Delta P_f$  is the transmembrane pressure at the RO element inlet and  $(\delta p)_{loss}$  is the hydraulic pressure loss (i.e.,  $P_f = P_{exit} + (\delta p)_{loss}$ ). Using **Eq. (3-6)**,  $\Delta P_f$  can then be expressed as  $\Delta P_f = J_{v,exit} / L_p + (\pi_{m,exit} - \pi_{p,exit}) + (\delta p)_{loss}$  where  $J_{v,exit}$  is the permeate flux and  $\pi_{m,exit}$  and  $\pi_{p,exit}$  are the osmotic pressures at the membrane surface and in the permeate, respectively, all at the exit location from the last membrane element.

The osmotic pressure at the membrane surface ( $\pi_{m,exit}$ ) can be estimated based on the salt

concentration at the membrane surface given the level of concentration polarization modulus (i.e.,  $CP=C_m/C_b$  where  $C_m$  and  $C_b$  are the solute concentrations at the membrane surface and the bulk solution, respectively) for the specific type of membrane element (**Section 3.3.3**).

Therefore, one can estimate  $\pi_{m,exit} = CP \cdot \pi_{exit}$ , where  $\pi_{exit}$  is the osmotic pressure based on the mixed-cup average concentration of the concentrate stream exiting the RO membrane train. The osmotic pressure can be reasonably taken to be a linear function of salt concentration [61] which is a reasonable approximation for dilute NaCl solution up to  $\sim 320,000$  g/L TDS [185]. Also, for the case of a saline water source composed of single salt (as in the present study) or one dominated by a given salt, it is reasonable to consider  $CP$  for the major salt to be a representative average across species. Given the above, the applied feed pressure,  $\Delta P_f$ , can be express as

$$\Delta P_f = J_{v,exit} / L_p + CP \cdot \pi_{exit} - \pi_p + (\delta p)_{loss} \quad (3-7)$$

Since that  $CP \geq 1$  and the approximation that  $\pi_{exit} \gg \pi_p$ , which is reasonable for high rejection RO desalination, upon substitution for  $\pi_{exit}$  (based on a mass balance on the RO system, **Section 3.2.3**), **Eq. (3-7)** can be written as:

$$\Delta P_f = \frac{J_{v,exit}}{L_p} + CP \cdot \frac{1 - Y_{SP}(1 - R_S)}{1 - R_S \cdot Y - Y_{SP}(1 - R_S)} \pi_o + (\delta p)_{loss} \quad (3-8)$$

and the specific energy consumption (**Eq. (3-5)**) for FLERO operation ( $SEC_{FLERO}$ ) can be expressed in a dimensionless form as follows,

$$\left( SEC^* \right)_{FLERO} = \frac{SEC_{FLERO}}{\pi_o} = \frac{(1 - \eta_{ER}(1 - Y_{SP}))}{\eta_p Y_{SP}} \left( \frac{J_{v,exit}}{L_p \cdot \pi_o} + \frac{CP \cdot (1 - Y_{SP}(1 - R_S))}{1 - R_S \cdot Y - Y_{SP}(1 - R_S)} + \frac{(\delta p)_{loss}}{\pi_o} \right) \quad (3-9)$$

For operation up to the thermodynamic restriction, as one approaches the exit from the membrane element (or membrane train), the net driving force for permeation diminishes and

so does the permeate flux [186] and thus  $CP \rightarrow 1$ . Therefore, at the membrane channel exit region the bulk and membrane surface salt concentrations are identical; thus, the  $SEC$  (Eq. (3-9)) approaches the theoretical minimum (i.e., for the condition of  $\Delta P_f = \Delta \pi_{exit}$ ) given by:

$$\left( SEC_{TR}^* \right)_{FLERO} = \frac{(1 - \eta_{ER}(1 - Y_{SP}))}{\eta_P Y_{SP}} \left( \frac{1 - Y_{SP}(1 - R_S)}{1 - R_S \cdot Y - Y_{SP}(1 - R_S)} + \frac{(\delta p)_{loss}}{\pi_O} \right) \quad (3-10)$$

It is noted that for a conventional single-pass RO operation the dimensionless SEC (i.e.,  $SEC_{SPRO}^*$ ) is readily obtained from Eq. (3-9) by setting  $Y=Y_{SP}$  leading to

$$\left( SEC^* \right)_{SPRO} = \frac{SEC_{SPRO}}{\pi_O} = \frac{(1 - \eta_{ER}(1 - Y))}{\eta_P Y} \left( \frac{J_{v,exit}}{L_p \cdot \pi_O} + CP \cdot \frac{1 - Y \cdot (1 - R_S)}{1 - Y} + \frac{(\delta p)_{loss}}{\pi_O} \right) \quad (3-11)$$

which for operation up to the thermodynamic restriction (i.e.,  $CP=1$ ) reduces to

$$\left( SEC_{TR}^* \right)_{SPRO} = \frac{(1 - \eta_{ER}(1 - Y))}{\eta_P Y} \left( \frac{1 - Y(1 - R_S)}{1 - Y} + \frac{(\delta p)_{loss}}{\pi_O} \right) \quad (3-12)$$

### 3.2.3 Salt material balance in FLERO operation

A steady-state salt balances around the overall FLERO system (Fig. 3-2) and RO membrane module are given by the following expressions:

$$q_O C_O - q_D C_C - q_P C_P = 0 \quad (3-13)$$

$$q_F C_F - q_C C_C - q_P C_P = 0 \quad (3-14)$$

in which  $q$  and  $C$  are the volumetric flow rate and salt concentration of the various streams designated by subscripts  $O$ ,  $C$ ,  $P$ , and  $F$  that indicate the raw-feed, RO concentrate, permeate, and RO membrane module feed streams, respectively. Given the definitions for a single-pass water recovery for a single element or membrane train ( $Y_{SP} = q_P/q_F$ ) and observed salt rejection ( $R_S = 1 - C_P/C_F$ ), Eq. (3-14) can be re-written as:

$$1/(1-R_S) - (1-Y_{SP})C_C/C_P - Y_{SP} = 0 \quad (3-15)$$

Similarly, **Eq. (3-13)** can be expressed in terms of the overall system water recovery ( $Y$ ) and  $Y_{SP}$  as:

$$C_o/C_P - (1-Y)C_C/C_P - Y = 0 \quad (3-16)$$

Given that the osmotic pressure ( $\pi$ ) of the different streams can be reasonably approximated to vary linearly with salt concentration [61]; Equations **(3-15)** and **(3-16)** can be combined to obtain the osmotic pressure ( $\pi$ ) of the concentrate (brine) stream exiting the RO membrane module in terms of the overall ( $Y$ ) and single-pass recovery ( $Y_{SP}$ ):

$$\frac{\pi_{exit}}{\pi_o} \cong \frac{C_C}{C_o} = \frac{1 - Y_{SP}(1 - R_S)}{1 - R_S \cdot Y - Y_{SP}(1 - R_S)} \quad (3-17)$$

### 3.3 Experimental

#### 3.3.1 Materials and solutions

Laboratory desalting experiments were carried out using aqueous saline solutions prepared by dissolving reagent-grade sodium chloride (Fisher Scientific Pittsburgh, PA) in deionized (DI) water. For the present study, a single spiral wound brackish water RO membrane element (2.5" × 40" FilmTec XLE-2540, Dow, Midland, MI Dow) was utilized that provided active membrane surface area of 2.6 m<sup>2</sup>, average water permeability of 4.6 L/m<sup>2</sup>·h·bar (measured at operating pressure of 10 bar) and 99% salt rejection based on 500 ppm NaCl solution at 25 °C and 6.9 bar [187]. The feed solution in a 200 L polyethylene tank was continuously stirred by a mechanical mixer and maintained at 20±1°C using a recirculating chiller (VWR Scientific 1171-P, Radnor, PA). Prior to RO being fed to the RO unit, the saline feed solution was filtered through a sequence of three cartridge microfilters of sizes 20 µm, 5 µm (pleated 2-1/2"x10",



Ocean Link Inc., Portsmouth, RI), and 0.2  $\mu\text{m}$  (Polysulfone Plastic, Harmsco, North Palm Beach, Florida).

### 3.3.2 Pilot spiral-wound RO system for SSRO-PR operation

Steady-state RO operation with partial concentrate recycling (SSRO-PR) was investigated using a small pilot-scale system (described in **Appendix A**) with the experimental layout described in **Fig. 3-3**. Briefly, the system is equipped with a single spiral wound RO element of size 2.5-inch (diameter) x 40-inch (length) in a pressure vessel rated up to 70 bars. The manufacturer recommended conditions for element operation was specified as inlet flow rate range of 0 – 1.4  $\text{m}^3/\text{h}$  (equivalent to crossflow velocity range of 0 – 0.57  $\text{m/s}$ ) and permeate flux range of 0 – 1.2  $\times 10^3 \text{ L/m}^2/\text{d}$  (30  $\text{gfd}$ ).

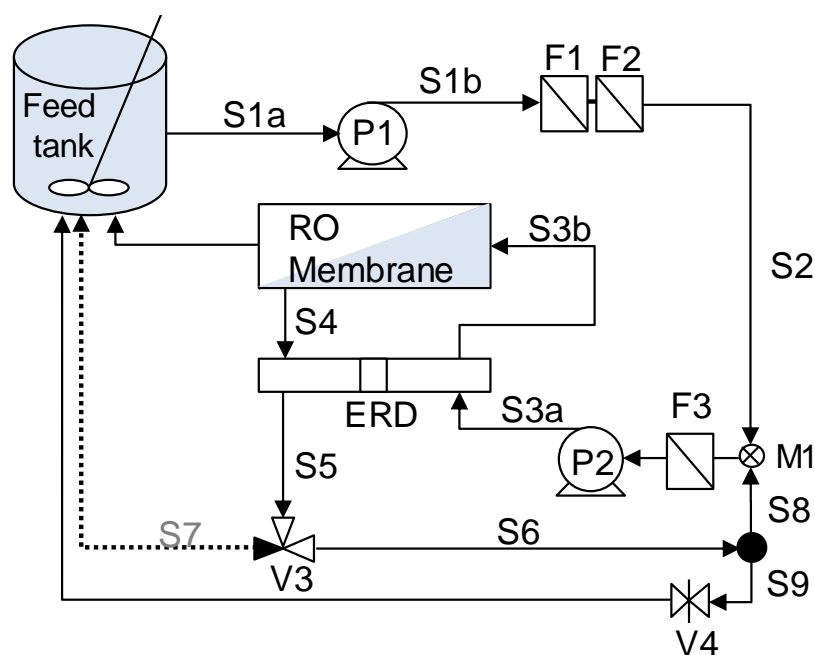


**Fig. 3-3.** Schematic diagram of the SSRO-PR system showing the location and arrangement of actuated valves, membrane module, energy recovery device (ERD), and pumps. Streams S1 and S2 are the raw feed streams before and after filtration pretreatment, respectively, and S3 and S4 represent the RO element feed and concentrate streams, respectively. Streams S6 and S7 are those of the concentrate recycle and discharge, respectively, and S8 and S9 are the recycled and discharged portions of the total concentrate stream, S6, respectively, during SSRO-PR operation

The RO system permeate production capacity was up to 1.5 m<sup>3</sup>/d (400 gal/day) for brackish water of 5000 mg/L TDS salinity operating at up to 90% recovery or 1.4 m<sup>3</sup>/d (360 gal/day) for seawater (35,000 mg/L TDS) desalination. For the current membrane (XLE-2540) the single-pass water recovery was kept in the range of 9.3±0.3 %. The electrical conductivities in the raw feed, membrane element feed, RO concentrate, and permeate streams were monitored in order to determine TDS in each stream from EC-TDS correlation obtained from a multi-electrolyte thermodynamic stream simulator [188] (**Appendix A.2**).

### 3.3.3 Concentration polarization

In order to determine the osmotic pressure at the RO element exit location, the concentration at the membrane was estimated using a suitable expression for the concentration polarization modulus ( $CP$ ). The recommended expression for  $CP$  for spiral-wound elements (**Table 3.9** in [187]) which is valid for the membrane element used in the present work [148] was  $CP_i = (C_m / C_b)_i = \exp(0.7Y_i)$ , in which subscript  $i$  denotes element  $i$ ,  $C_m$  and  $C_b$  denote the bulk and membrane surface salinities, respectively, and  $Y_i$  is the element  $i$  recovery. It noted that when elements are connected in series there is significant mixing at the interspace between elements and thus the individual element  $CP$  is governed by its single-pass recovery. Moreover, the single-pass recovery for an element is constrained (typically in the range of ~10-20% [187]). Given the above  $CP$  expression, the element average  $CP$  is given by  $\overline{CP} = [1/Y_{SP}] \cdot \int_0^{Y_{SP}} CP dY = 1.43(\exp(0.7Y_{SP}) - 1)/Y_{SP}$ .

### 3.3.4 SSRO-PR desalination experiments

Desalination tests were carried out to demonstrate wide range of overall water recovery from the process between  $Y \sim 9.3$  and 88% by adjusting the recycle ratio,  $R$  (Eq. (3-2)), in the range of 0 –9. In all cases, the system permeate flux and the feed flow rate to the RO element were maintained constant at  $560 \pm 25 \text{ L/m}^2 \cdot \text{d}$  ( $13.9 \pm 1 \text{ gfd}$ ) and  $0.66 \pm 0.3 \text{ m}^3/\text{h}$  ( $2.9 \pm 0.1 \text{ gpm}$ ) respectively, which were within the range of operating conditions recommended for the RO element used in the current study. The observed salt rejection,  $R_s$ , over the range of feed water salinity and system recovery for XLE2540 element was  $97 \pm 1\%$ . Prior to the start of each test, the spiral wound system was conditioned for 30 min by operating the system without concentrate recycling by (i.e.,  $R=0$  and  $Y=Y_{SP}$ ), using the feed solution at a permeate flow rate of 1.0 L/min at applied pressure of 10 bars. Subsequently, the concentrate recycle flow rate ( $q_R$ ) was increased to achieve the target overall water recovery ( $Y$ ). All tests were carried out in a total recycle mode (i.e., permeate and retentate streams were continuously recycled to the stirred feed reservoir, Fig. 3-3) in order to maintain constant raw-feed water composition throughout the experiments.

The RO desalting experiments were carried out for the conditions listed Table 3-1 for a saline NaCl feed solutions in the concentration range of  $\sim 860 - 37,000 \text{ mg/L TDS}$ . The permeate flux for the various tests was in the range of  $514-585 \text{ L/m}^2 \cdot \text{d}$  and the crossflow velocity in the membrane element was maintained at  $0.23 \text{ m/s}$ . This crossflow velocity was within the typical range ( $0 - 0.57 \text{ m/s}$ , [187]) for desalting with spiral-wound RO elements. It is also noted that the RO module feed and exit pressures were monitored and the pressure loss was in the range of  $(\delta p)_{loss} / P_f = 0.01 - 0.08$ .

**Table 3-1. SSRO-PR desalination experimental conditions**

Test	$C_o$ (ppm)	Water recovery, $Y$ (%)	$J_v$ (L/m <sup>2</sup> ·d)	Recycle Ratio, $R$	Transmembrane Pressure,			$C_C$ (ppm)	$C_P$ (ppm)
					$P_{FL}$ (bar)	$P_{FH} - P_P$ (bar)	$P_{CH} - P_P$ (bar)		
1.1		9.3	569	0.0	3.2	5.7	5.3	998	36
1.2		39.5	572	3.3	3.4	6.2	5.7	1477	44
1.3		44.8	583	3.7	3.4	6.4	6.1	1509	40
1.4		55.9%	580	5.0	3.5	6.6	6.2	1904	53
1.5	860	57.3	585	5.0	3.4	6.7	6.4	1918	49
1.6		63.2	576	5.8	3.5	7.2	6.8	2516	68
1.7		69.9	582	6.3	3.5	7.3	6.9	2650	64
1.8		78.1	580	7.3	3.6	8.2	7.9	3622	87
1.9		81.3	583	7.5	3.6	8.3	8.0	4076	93
1.1		86.2	577	8.1	3.8	9.4	9.1	5612	133
2.1		9.6%	565	0.0	3.5	9.9	9.6	5576	128
2.3		45.9	584	3.8	3.9	11.9	11.5	7779	169
2.4	4900	62.9	579	5.6	4.3	15.2	14.9	12080	261
2.5		77.8	576	7.2	4.8	21.2	20.9	18886	413
2.6		87.6	562	8.9	5.9	29.2	29.1	29208	717
3.1			9.5	514	0.0	4.2	14.9	14.2	11585
3.2		44.5	579	3.7	4.8	19.2	18.4	16938	353
3.3	11,000	57.0	571	5.3	5.5	23.3	22.5	22122	474
3.4		61.1	563	5.7	5.6	24.5	23.7	23604	496
3.5		66.1	533	6.1	5.8	27.2	26.5	27071	609
3.6		71.0	534	6.9	6.2	30.0	29.2	30498	683
4.1	22,000	9.0	544	0.0	5.3	24.3	23.5	23379	492
4.2		42.4	524	3.8	6.5	31.9	31.2	33016	759
5.1	37,000	9.0	526	0.0	7.2	37.0	36.3	39419	947

Note: all experimental runs were carried out at the crossflow velocity of 23 cm/s and the RO element feed flow rate,  $q_F = 0.66$  m<sup>3</sup>/h

### 3.4 Results and Discussion

#### 3.4.1 Flexibility of SSRO-PR operation

In the spiral wound RO system (Fig. 3-2), the overall system product recovery ( $Y=q_P/q_O$ ) is controlled by the recycle ratio ( $R=q_R/q_O=Y/Y_{SP}-1$ , where  $Y \geq Y_{SP}$ ) through independently adjusting the raw feed and recycle flow rates to within the system physical limitations. A higher system recovery can be attained by operating at an increased recycle ratio. It is noted, however, that the single pass recovery can be maintained constant by adjusting the required feed pressure up to the limit imposed by the system feed pump. In principle, one could utilize a high recycle flow rate ( $q_R$ ) to reduce concentration polarization and hence reduce the feed pressure requirement for the desired flux (Section 2-2). An illustration of the above behavior is provided in Fig. 3-4, generated using the pilot SSRO-PR system, over a wide range of raw feed water salinity 860 – 37,000 mg/L NaCl) for which the single pass recovery was set at ~9.3%.

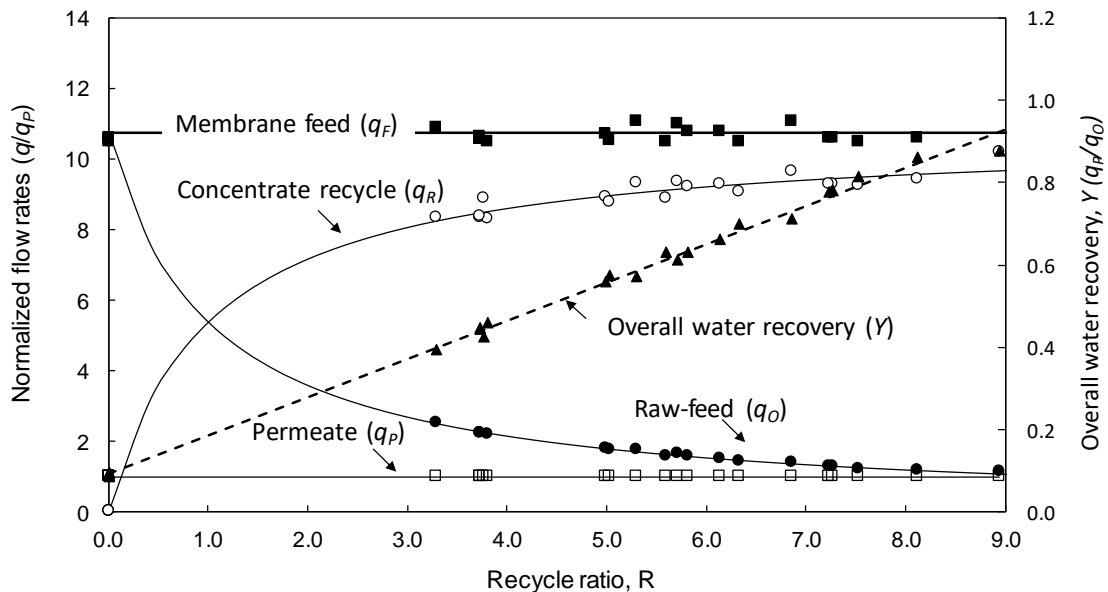


**Fig. 3-4.** Variation of the volumetric flow rates normalized with respect to the permeate flow rate ( $q_P$ ) for a RO unit with a single spiral-wound element for operation with a constant  $Y_{SP}$  of 9.3%. The data for the RO unit were generated, for feed solutions of salinity in the range of 860 – 37,000 ppm, by varying the raw-feed and concentrate recycle flow rates to maintain a constant membrane element feed and permeate flow rates.

The operational scenario for the SSRO-PR unit is such that a constant permeate production can be achieved over a wider range of overall system recovery. In this operation the membrane element inlet feed flow rate (and thus RO retentate crossflow velocity) is maintained constant. Here we note that with the present membrane element quality permeate was produced, from source water of wide-salinity range, that is suitable for potable and non-potable applications. Permeate salinity in some cases was in exceedance of the recommended standard (i.e., 500 - 600 mg/L TDS). However, it is emphasized that for high permeate quality (for drinking water production) can be achieved by utilizing a membrane of higher salt rejection.

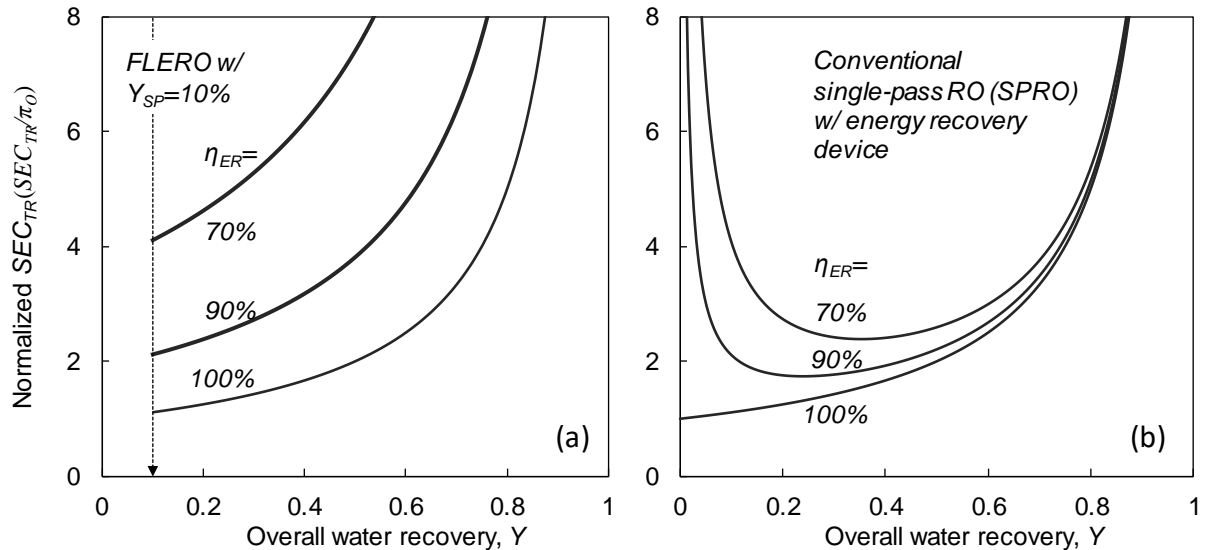


**Fig. 3-5.** Variation of specific energy consumption ( $SEC$ ), normalized with respect to the osmotic pressure of the raw feed solution ( $\pi_0$ ), for operation up to the thermodynamic restriction and ideal membrane (i.e., 100% salt rejection), with respect to overall water recovery ( $Y$ ) and ERD efficiency ( $\eta_{ER}$ ) for: (a) SSRO-PR with single-pass water recovery of  $Y_{SP}=10\%$  (recycle ratio varied with overall recovery as per **Eq. (3-2)**), and (b) conventional single-pass RO (SPRO) with an ERD (**Eq. 3-12**).

A comparison of the specific energy consumption for a SSRO-PR (**Fig. 3-5a**) and conventional single-pass RO (SPRO, **Fig. 3-5b**) systems, for operation up to the crossflow thermodynamic restriction and assuming negligible element pressure losses

( $(\delta p)_{loss} / \pi_o \ll 1$ ), is shown in **Fig. 3-5** in terms of the normalized SEC (i.e.,  $SEC_{TR}^* = SEC_{TR} / \pi_o$ ;  $(\delta p)_{loss} / \pi_o \ll 1$ ). This illustration is for the case of an ideal pump (i.e.,  $\eta_p=1$ ), membrane of 100% salt rejection and where the example SSRO-PR system has a maximum single pass recovery (i.e., without concentrate recycle) of 10% as in the present single-element test system. For the scenario of an ideal ERD (i.e.,  $\eta_{ER}=1$ ), the energy footprint for SSRO-PR and SPRO are identical and at the lowest achievable level. However, for an ERD of less than 100% efficiency ( $\eta_{ER} < 1$ ), SSRO-PR requires a higher SEC, for a given water recovery, relative to SPRO. The lowest SEC of SSRO-PR operation (**Fig. 3-5a**) is always at the point at which the system operates such that the overall recovery is at its single pass recovery ( $Y=Y_{SP}$ ).

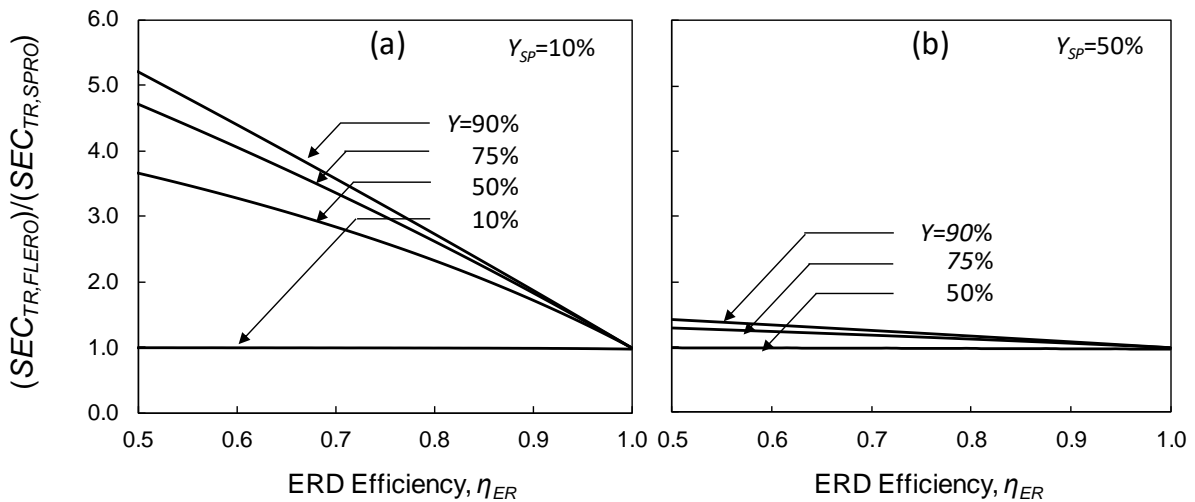


**Fig. 3-6.** Comparison of the SEC of SSRO-PR with single pass RO (SPRO, i.e., without concentrate recycle) for operation up to at the crossflow thermodynamic restriction (Section 2.2 for ideal membranes (i.e., 100% salt rejection) and for the case of as in Fig. 3, with respect to ERD efficiency for different levels of overall product water recovery ( $Y$ ). The single pass recovery was set as (a) 10% and (b) 50%.

The effect of single-pass recovery on the SEC in SSRO-PR, relative to SPRO, for operation up to the thermodynamic crossflow restriction is shown in **Fig. 3-6**. It is apparent from comparison of SPRO with SSRO-PR systems capable of 10% (**Fig. 3-6a**) relative to 50% (**Fig 3-6b**) single-pass recovery, that the SPRO advantage in terms of energy efficiency is reduced with increased ERD efficiency and as the SSRO-PR single pass recovery approaches (i.e., with increased number of membrane elements in the system) the overall recovery achieved with the SPRO system. The above suggests that it is preferable to utilize high efficiency ERD in a SSRO-PR system if reduction of energy utilization is critical relative to operational flexibility (i.e., with respect to overall recovery). Although SSRO-PR operation requires higher SEC relative to SPRO, the former has the advantage of a single system that is able to operate over a wide range of overall product water recovery without the need for adding elements as would be the case for SPRO system.

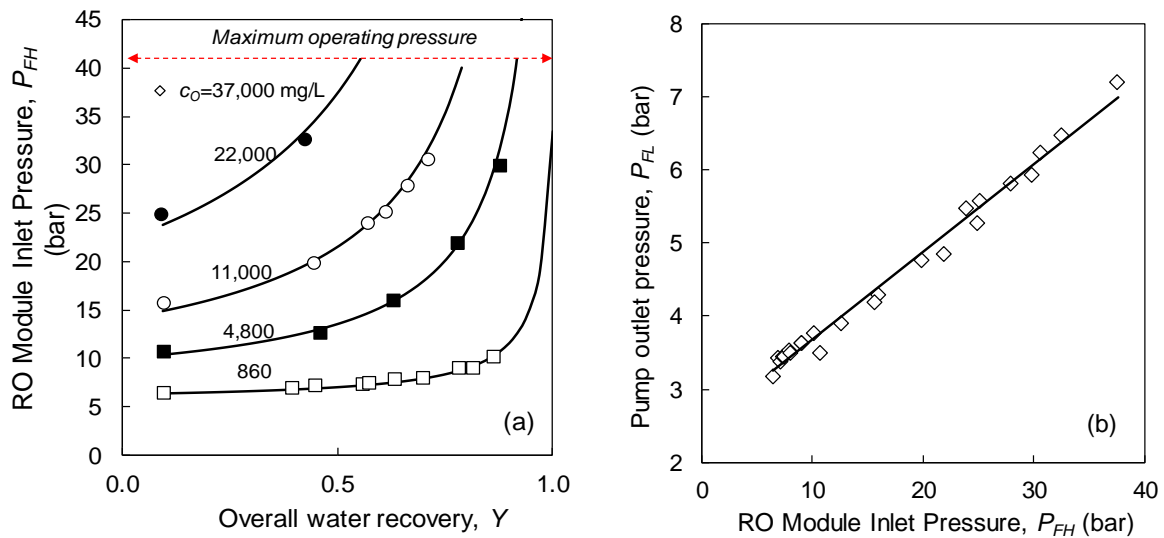


**Fig. 3-7.** (a) Variation of the RO module feed pressure ( $P_{FH}$ ) with respect to overall water recovery ( $Y$ ) for desalination of raw-feed water at various salinities ( $C_0$ ) at a constant membrane feed ( $q_F$ ) and permeate ( $q_P$ ) flow rates of 10.9 L/min and 1.0 L/min, respectively, for a SSRO-PR system utilizing a single 2.5-inch RO element (single-pass recovery of  $9.3 \pm 0.3\%$ ) and observed salt rejection of  $97 \pm 1\%$ . (b) RO feed pump outlet pressure required to achieve the RO module feed pressure for attaining the overall recoveries at the pressures indicated in **Fig. 3-7(a)**.



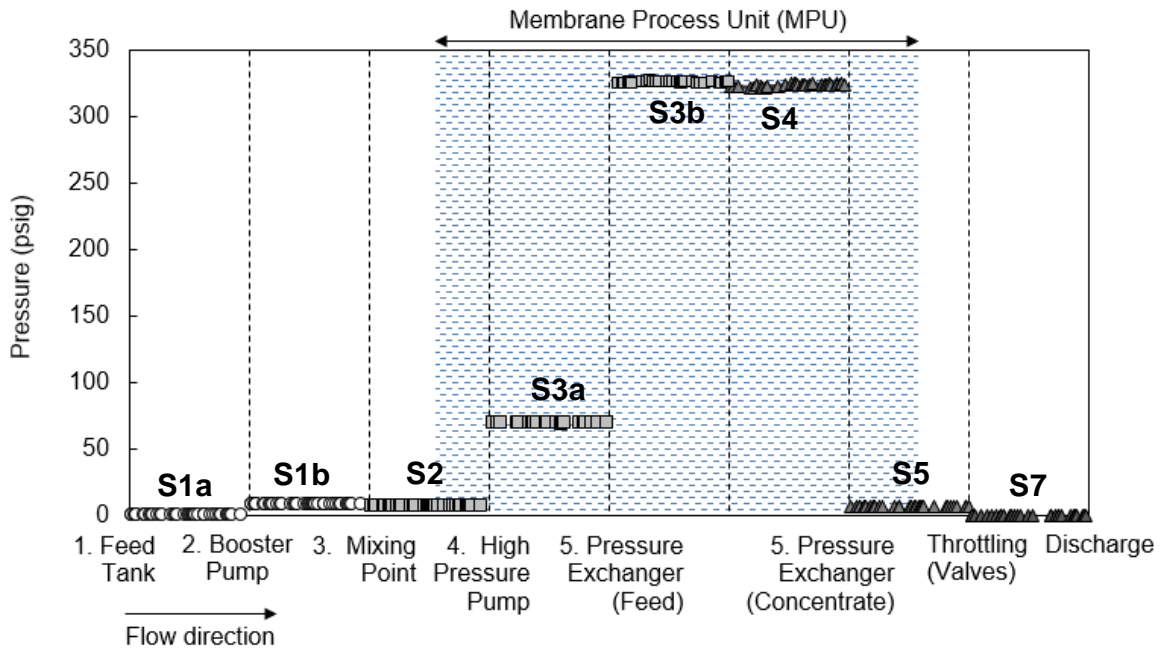


**Fig. 3-8.** Variation of the hydraulic pressure in each fluid stream involved in SSRO-PR system described in described in **Fig. 3-3** with the membrane process unit (MPU) indicated with the shaded area (for treatment of 11,000 ppm *NaCl* source water at the target water recovery (*Y*) of 45% in test run#3.2, **Table 3-1**).

The present approach allows minimization irreversible energy dissipation by isolating the fluid regulations in CRU at low pressure to mitigate the impact of concentrate throttling and mixing. **Fig. 3-8** illustrates the variation of the hydraulic pressure as fluid particles travel along the pipeline of the RO system. From the viewpoint of system operation, it is important to consider the required RO module inlet pressure (i.e.,  $P_{FH}$ ) which is plotted in **Fig. 3-7a** for the various desalting tests conducted with the present experimental SSRO-PR test system. The manufacturer specified upper operational limit for the RO element was 41 bar (600 psi) [187], and thus desalting of seawater was feasible (required  $\sim 37$  bar) at the single pass recovery level of 9.0%. Desalting of solutions up to the level of seawater salinity was feasible. Given the use of an ERD, as a pressure intensifier in the RO system, the required feed pump outlet pressure was significantly lower than the RO module operating pressure (**Fig. 3-7b**). However, one

should recognize that the upper limit of achievable recovery will be dictated by the upper pressure constraint on the membrane element, maximum attainable feed pump outlet pressure and any physical pressure constraints on other system components (e.g., pipe fittings, high-pressure pump, etc.).

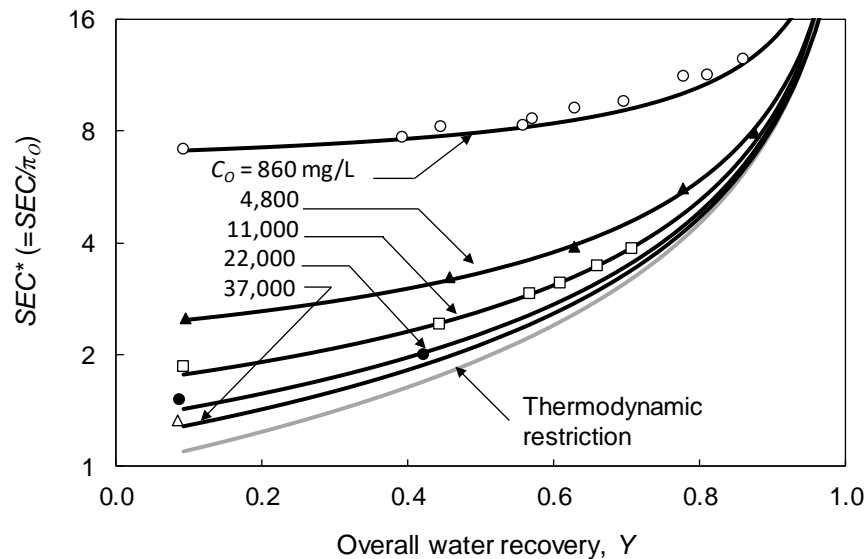


**Fig. 3-9.** RO element specific energy consumption as experimentally determined (based on element feed pressure and normalized with respect to the raw-feed water osmotic pressure) compared with theoretical predictions (Eq. 3-9) as a function of overall water recovery ( $Y$ ) for a range of raw-feed water salinities (Table 3-1). (Note: the SEC in units of kWh/m<sup>3</sup> can be obtained from  $SEC = A \cdot SEC^* \pi_o$ , where the osmotic pressure  $\pi_o$  is given in bar and  $A=0.0278$  is a proportionality constant).

RO systems are typically not designed with the objective of being operated at the minimum SEC, primarily due to various practical constraints associated with system capital cost, footprint and operational considerations, and capital cost considerations. At the same productivity, a SSRO-PR operation would require a smaller number of membranes relative to single-pass RO. Although the element SEC approached the thermodynamic limit with increased source water salinity (Fig. 6), operation up to the thermodynamic restriction was not feasible with the present test RO system given the use of a single element (Fig. 3-9). The

SSRO-PR element SEC was thus higher than the theoretical minimum (Eq. 3-10) but the experimental data closely matched the SEC predictions (Eq. 3-9) over the range of recoveries and feed water salinities. As in any practical system, the overall system energy consumption would clearly depend on the pump and ERD efficiencies.

### 3.4.2 Alternate SSRO-PR Configurations

Although the analysis presented in the present study focused on a specific SSRO-PR configuration (Fig. 3-2), it is important to recognize that some energy recovery devices such as pressure exchangers [142] can only operate in parallel with the main feed pump (P1) as depicted in Fig. 3-10. In this case, a booster pump (P2) downstream of the feed-side ERS is needed. Both ERD-P2 and P1 must provide the same level of feed pressurization (i.e.,  $P_{FH3} - P_{FL1} = P_{FH2} - P_{FL3} = P_{FH1} - P_{FL2}$ ) for achieving the product flow set-point in the membrane array (MA).

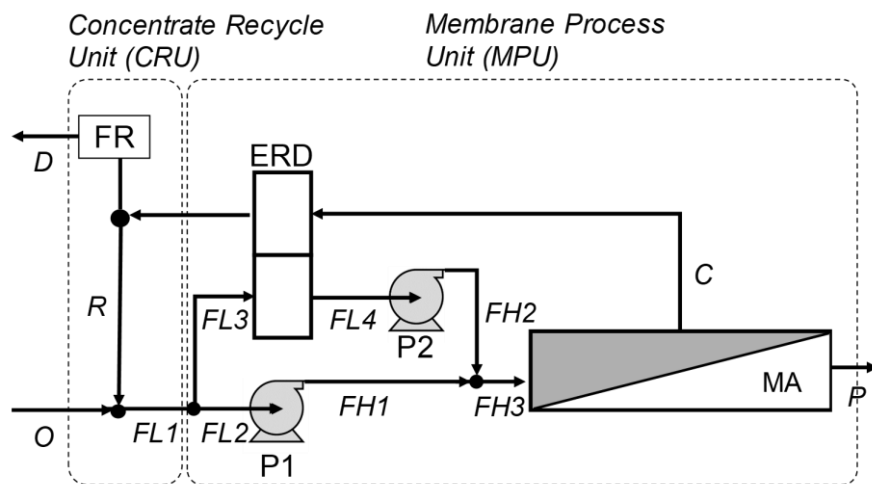


**Fig. 3-10.** A SSRO-PR configuration with a membrane array (MA) and an energy recovery device (ERD) installed in parallel with the feed pump (P1) and requiring a booster pump (P2). The recycled concentrate flow is adjusted with a flow regulator (FR). (Notation: *O*-raw feed, *C*-concentrate, *P*-permeate, *D*-discharge, *R*-recycled concentrate, *FL1*-combined raw feed (*O*) and recycle (*R*) streams, *FL2*-inlet flow to pump P1, *FL3*-split flow from *FL1* to ERD, *FL4*-feed from ERD to pump P2, *FH1* and *FH2* - pumps P1 and P2 outflows, respectively, and *FH3*-

membrane feed into MA.

It is also possible to configure a SSRO-PR system operation with multiple membrane arrays arranged with multiple pressurization stages, which can reduce the specific energy consumption. For example, as shown in **Fig. 3-11**, a two-stage SSRO-PR system can utilize a feed pump to generate the required pressure for the 1<sup>st</sup>-stage MA. An ERD device is then utilized as an intermediate stage pressure booster to generate the pressure required for the 2<sup>nd</sup>-stage MA by recovering energy from its concentrate. In the SSRO-PR configurations shown in **Figs. 3-10** and **3-11**, the concentrate recycle units (CRUs) are identical whereby a single flow regulator (FR) is utilized to control the flow rate of the brine (concentrate) discharge stream, thus providing an indirect control of the concentrate recycle stream. In the above examples, an optional backflow preventer may be beneficial in the concentrate recycle stream. Alternatively, one can utilize an adjustable three-way directional valve at the MPU concentrate splitting point (i.e., between “R” and “D”; **Fig. 3-10**) or use any other suitable flow regulation method.

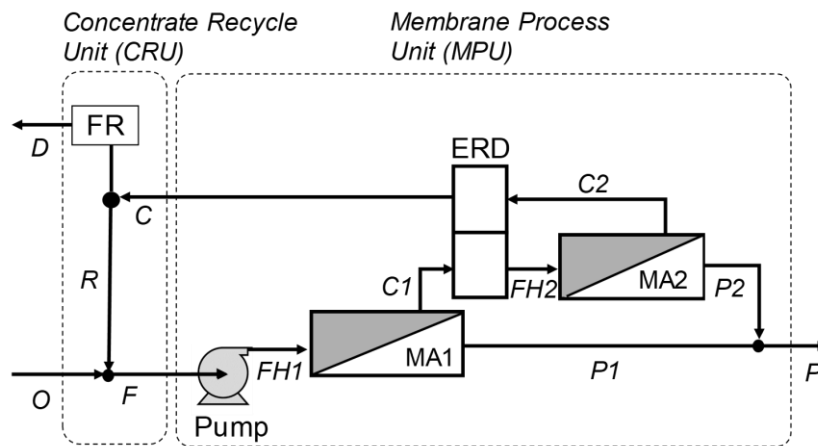


**Fig. 3-11.** An example of a RO configuration with an energy recovery device (ERD) installed as an interstage pressure booster between membrane stages 1 (MA1) and 2 (MA2). A flow regulator (FR) regulates the fraction of the concentrate that is recycled to the feed (*R*). Streams: *O*-raw feed, *R*-recycled concentrate, *F*- combined raw feed (*O*) and concentrate recycle (*R*), *D*-brine discharge, *FH1* – pump 1 outlet flow as feed into MA1, *FH2* – ERD outlet of MA1

Concentrate (*CI*) as feed to MA2, *C2* - concentrate from MA2, *C*- MA2 concentrate after ERD, *PI* - permeate from MA1, *P2* - permeate from MA2, and *P* – combined MA1 and MA2 permeate

Finally, it is noted that operation flexibility can also be attained in semi-batch and batch RO configurations. Batch RO can be used to desalt a given reservoir volume (placed in the recycle stream) by operating with total concentrate recycle without continuous raw water input nor concentrate discharge [29]. Semi-batch RO (SBRO) operation would be with continuous raw water input but with unsteady-state dissolved salt accumulation in the system due to either total or high recycle ratio ( $R \gg 0$ ). Both batch and semi-batch operation, however, require system flushing with low salinity feed in order to reset the system to its starting operating condition (i.e., initial salinity level equivalent to the raw feed water). The period of reset and loss of productivity would impact the average flux, the overall recovery attained and thus the specific energy consumption. Although unsteady state semi-batch approach of RO desalting has been reported [29, 147, 183, 189], there is potential for improvement through optimal a pressure intensifier ERD integration in such systems.

### **3.5 Summary**

Desalination operation in which a RO system is configured with a pressure intensifier and operated in a partial recycle mode was investigated. Theoretical analysis and experiments with a small-scale spiral wound RO system demonstrated steady state RO with partial concentrate recycling (SSRO-PR) operation over wide ranges of permeate recovery and salinity and with fluid flow regulation. The system operation is essentially decomposed into a membrane process unit (MPU) and a concentrate recycling unit (CRU) outside of the MPU at low pressure, which avoids undesirable energy loss from hydraulic stream mixing or throttling. The specific energy

consumption for the SSRO-PR configuration is admittedly higher than that of conventional single pass RO with energy recovery. However, SSRO-PR provides greater flexibility, with respect to product water recovery, with a single platform, while enabling desalting using a relatively low-pressure RO feed pump. A SSRO-PR configuration would be ideal for small-scale applications. Its large-scale application would depend on the ability to adapt the use of pressure intensifiers or other types of energy recovery devices of sufficient efficiency for large desalination capacity. While the current results suggest the benefit of operational flexibility, SSRO-PR field evaluations are warranted that will also consider potential fouling and scaling relative to single-pass RO in order to establish the full-range of long-term benefits of the approach.

## **Chapter 4 Multi-Cycle Operation of Semi-Batch Reverse Osmosis (SBRO) Desalination**

### **4.1 Overview**

Semi-batch reverse osmosis (SBRO) is an unsteady-state cyclic process consisting of a filtration period followed by a short flushing period. In the filtration period the RO concentrate stream is fully recycled to the RO feed, mixed with the raw-feed water and fed to the membrane module. In this operational mode, the raw feed and permeate flow rates are equal and thus the system operates at 100% recovery. During filtration, salt concentration increases in the RO unit holdup volume (i.e., in both the RO elements and hydraulic components). As a consequence, the applied feed pressure must be gradually raised to maintain the prescribed constant permeate production. Once the target production capacity is reached, or when the applied pressure reaches the imposed constraint (e.g., system maximum pressure rating), the excess concentrate salinity buildup in the system is flushed (without recycle) with the raw feed water and a new filtration cycle is subsequently initiated. In SBRO, the raw feed water volume required for flushing/concentrate discharge from the RO system is a critical parameter that affects water recovery, osmotic pressure buildup (during the filtration period), and thus specific energy consumption.

In this chapter, SBRO operation was investigated, via process modeling and using a small-scale SBRO pilot, to evaluate the impact of concentrate flushing efficacy. Process model analysis and experimental data, considering progressive SBRO cycles of filtration and concentrate flushing, illustrated progressive cycle-to-cycle concentrate salinity rise due to incomplete (concentrate) flushing and a corresponding SEC increase. In all cases, however, a stable cycle-to-cycle operation was ultimately achieved. Flushing duration that was longer than

the RO system convective residence time improved flushing of the excess concentrate salinity. However, for a given recovery, longer flushing required longer filtration. Analysis is also presented comparing the SEC for an ideal SBRO (i.e., complete flushing of excess concentrate salinity) relative to a single-pass RO (SPRO), and to actual SBRO system operation. It is then shown that quantitative assessment of concentrate flushing efficacy via concentrate salinity monitoring is critical for assessment of SBRO effectiveness.

## 4.2 Analysis

### 4.2.1 Water recovery in semi-batch RO (SBRO)

The semi-batch RO (SBRO) configuration considered in the present study is shown in **Fig. 4-1**. In this SBRO system, permeate water is produced (at a flow rate  $q_P$ ) during a desalination period (hereinafter termed “filtration” period) with total concentrate recycle. The concentrate flow rate is  $q_c = ((1 - Y_{SP}) / Y_{SP}) \cdot q_P$  and the single-stage RO recovery level is  $Y_{SP} = q_P / q_F$ , where  $q_F$  is the feed flow rate into the lead RO element. During the filtration period, permeate water is produced at a flow rate that is equal to the raw feed flow rate  $q_o$ ; hence, the system operates at total concentrate recycle and 100% overall product water recovery ( $Y$ ). Operation at total recycle during the filtration period leads to progressive increase of concentrate salinity in the RO holdup volume. Therefore, the feed pressure must correspondingly be raised in order to maintain the set constant permeate productivity. Once the applied feed pressure reaches a critical set point (e.g., either the desired permeate production volume for a given period or the maximum allowable feed pressure), the RO system concentrate holdup volume is flushed with the raw feed water (**Fig. 4-1b**) during which the permeate productivity continues at the level of the single-pass recovery ( $Y_{SP}$ ).



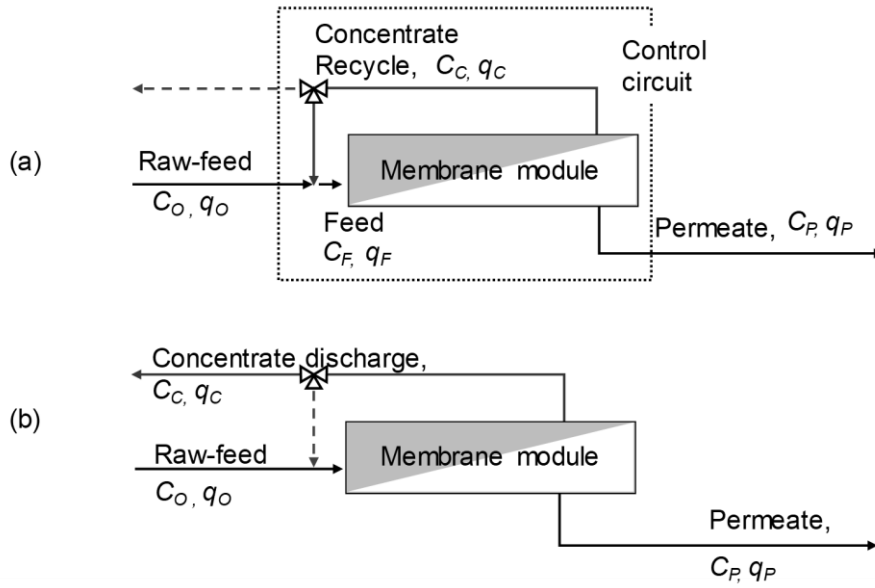


**Fig. 4-1.** Semi-batch RO (SBRO) process showing the operational configurations of (a) filtration period (the control volume for salt balance in **Eq. (4-6)** is indicated by the dotted line), and (b) flushing period with continued permeate production. (MA - membrane array;  $C_i$  and  $q_i$  are the salt concentration and flow rate, respectively, where the subscript  $i$  denotes one of the following:  $O$ - raw feed,  $F$ - RO element feed,  $P$ - permeate, and  $C$ - concentrate.

Although during flushing one can operate at low pressure without permeate productivity, such an operation as reported in a number of previous studies [42, 43, 159] would reduce the recovery attained over a complete filtration/flushing cycle. The overall SBRO product water recovery ( $Y$ ) for a full cycle (i.e., filtration followed by flushing) is given by  $Y = Q_P / Q_O$  (**Eq. 2-27**), where  $Q_O$  and  $Q_P$  are the raw-feed water inflow and permeate volumes over a full cycle, respectively, expressed as:

$$Q_P = \int_0^{t_{FT}} q_P dt + \int_{t_{FT}}^{t_{FT}+t_{FL}} q_P dt \quad (4-1)$$

$$Q_O = \int_0^{t_{FT}} q_O dt + \int_{t_{FT}}^{t_{FT}+t_{FL}} q_O dt \quad (4-2)$$

in which  $t$  is the process time,  $t_{FT}$  and  $t_{FL}$  denote the filtration and flushing durations, respectively, and  $q_O$  is the raw feed water flow rate, whereby  $q_O = q_P$  during the filtration period (**Fig. 4-1a**). For operation at a permeate flow rate of  $q_p$  and raw feed water flow rate of  $q_o$ , the

overall SBRO recovery is determined as:

$$Y = \frac{\int_0^{t_{FT}} q_P dt + \int_{t_{FT}}^{t_{FT}+t_{FL}} q_P dt}{\int_0^{t_{FT}} q_O dt + \int_{t_{FT}}^{t_{FT}+t_{FL}} q_O dt} \quad (4-3)$$

in which  $t_{FT}$  and  $t_{FL}$  are the filtration and flushing durations, respectively. During the filtration period,  $q_O=q_P$  (i.e., total recycle operation). Also, permeate productivity during flushing is kept at the same level as during the filtration period. However, during flushing, the raw feed water flow rate is increased to match the SBRO element filtration period flow rate (i.e.,  $q_O=q_F=q_P/Y_{SP}$ ). Accordingly, the overall recovery can be expressed as,

$$Y = \frac{q_P t_{FT} + q_P t_{FL}}{q_P t_{FT} + q_F t_{FL}} \quad (4-4)$$

For optimal SBRO operation, the inlet element flow rate during both filtration and flushing is kept the same (i.e.,  $q_F$ ), and given that the element (or element train) per-pass recovery, i.e.,  $Y_{SP}=q_P/q_F$ , would be typically maintained (i.e., due to element characteristics and imposed operational constraints), the overall system water recovery ( $Y$ ) can be expressed as:

$$Y = \frac{Y_{SP} \cdot (t_{FT}/t_{FL}) + Y_{SP}}{Y_{SP} \cdot (t_{FT}/t_{FL}) + 1} \quad (4-5)$$

For specific case of SBRO operation without or with negligible permeate production during the flushing period (i.e.,  $q_P=0$ ), **Eq. (4-5)** reduces to  $Y = [Y_{SP} (t_{FT}/t_{FL})] / [Y_{SP} (t_{FT}/t_{FL}) + 1]$ .

**Equation (4-5)** indicates that the overall SBRO system water recovery increases as the flushing period is shortened relative to the filtration period. In the limit of  $t_{FT}/t_{FL} \rightarrow \infty$  the overall recovery  $Y \rightarrow 100\%$  and  $Y \rightarrow Y_{SP}$  as  $t_{FT}/t_{FL} \rightarrow 0$  (**Fig. 4-2**). Clearly, as the design single-pass recovery for a given SBRO increases, the prescribed overall recovery can be attained at a reduced filtration period relative to the flushing period. It is also important to note from **Eq.**

(4-5) that, for a given target water recovery, the required filtration duration is governed by the flushing duration. This suggests that a longer flushing duration would necessitate a longer filtration duration.

It stressed that previous studies have generally implied that complete SBRO flushing can be achieved with a raw feed water volume that is equivalent to the SBRO system holdup volume. Complete flushing in the context of SBRO operation is resetting (or returning) the RO system such that the RO unit feed salinity (i.e.,  $q_F$ , **Fig. 4-1**) to the state as in the first filtration cycle. However, as illustrated in the present work (**Sections 4.4.1 and 4.4.2**), effective SBRO system flushing within a single system space time may not be practically realizable. Incomplete flushing would lead to a higher applied feed pressure requirement and correspondingly higher energy consumption (**Sections 4.2.3 and 4.2.5**). Effective flushing can be attained by increasing the flushing duration or Ro elements feed flow rate; but, this in turn could either reduce the overall recovery or necessitate longer filtration duration (**Eq. (4-5)**).

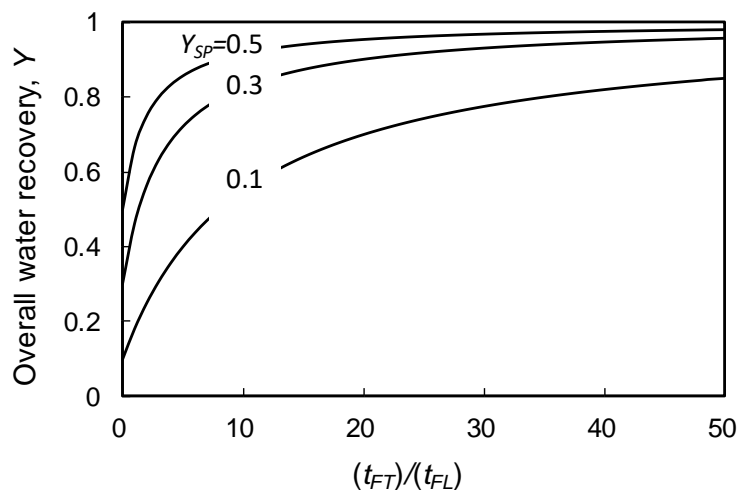


**Fig. 4-2.** Overall SBRO system water recovery ( $Y$ ) dependence on RO filtration time-flushing time ratio (i.e.,  $t_{FT}/t_{FL}$ ) and single-pass water recovery of  $Y_{SP} = 0.1, 0.3, 0.5$ , as per **Eq. (4-5)**.

### 4.2.2 Filtration period

During the filtration period raw feed water having salt concentration of  $C_O$  is fed to the SBRO system (**Fig. 4-1a**). Salt concentration increases along the RO train to the level of  $C_C$  and the concentrate recycle stream is mixed with the raw feed water resulting in a feed stream to the RO module of concentration  $C_F$  (**Fig. 4-1a**). The average salt concentration in the SBRO circuit,  $\bar{C}$ , can be determined from an unsteady state salt balance for the filtration period (**Fig. 4-1a**) expressed as:

$$V \frac{d\bar{C}}{dt} = q_O C_O - q_P C_P \quad (4-6)$$

in which  $V$  the SBRO circuit volume (**Fig. 4-1a**), and where  $C_O$  and  $C_P$  are the salt concentrations of the raw-feed and the permeate streams, respectively, and  $t$  is the time during the filtration period.

Similarly, to the overall mass balance shown in **Eq. (4-6)**, the salt balance about the RO membrane element (or array) for the filtration period in SBRO operation is given by,

$$\frac{dm}{dt} = q_F C_F - q_C C_C - q_P C_P \quad (4-7)$$

in which  $dm/dt$  denotes the salt mass ( $m$ ) accumulation rate in the RO element feed channel,  $q$  and  $C$  are the volumetric flow rate (L/min) and salt concentration (mg/L) of various streams designated by subscripts  $F$ ,  $C$ , and  $P$  indicating the RO element feed, concentrate, and the permeate streams, respectively. Given that the magnitude of the RO filtration period is typically much greater than the single pass system space time, Pseudo-Steady-State (e.g.,  $dm/dt \cong 0$ ) can be reasonably assumed in order to establish the relationship between the instantaneous feed and the concentrate water salinities at the RO element inlet and outlet, respectively. Thus, considering constant single pass RO recovery ( $Y_{SP} = q_P/q_F$ ), the salt material balance in **Eq.**

(4-7) can be written for the feed water salinity ( $C_F$ ) at RO element inlet as:

$$C_F = (1 - Y_{SP})C_C + Y_{SP}C_P \quad (4-8)$$

Accordingly, using **Eq. (4-7)**, the average permeate concentration ( $C_P$ ) can be related to the brine concentration at the RO element exit ( $C_C$ ), as given by

$$C_P = \frac{(1 - Y_{SP})(1 - R_S)}{1 - Y_{SP}(1 - R_S)} C_C \quad (4-9)$$

in which  $R_S$  is the observed membrane salt rejection (defined as,  $R_S = 1 - C_P/C_F$ ).

Combining Equations (4-8) and (4-9), and given the approximation of  $\bar{C} = (C_F + C_C)/2$  (note,  $C_F < \bar{C} < C_C$ ), it can be shown that  $\bar{C} = \left[ (2 - 2Y_{SP} + Y_{SP} \cdot R_S) / (2(1 - Y_{SP}(1 - R_S))) \right] C_C$ .

Therefore, the rate of increase in salinity of the concentrate recycle stream can be approximated as  $d\bar{C}/dt \approx (2 - 2Y_{SP} + Y_{SP} \cdot R_S) / (2(1 - Y_{SP}(1 - R_S))) dC_C/dt$ . Given the above relationships, the brine concentration ( $C_C$ ) during the filtration period can be described by the following expression:

$$\frac{dC_C^*}{d\Theta} = \frac{2Y_{SP}}{2 - Y_{SP} - Y_{SP} \cdot (1 - R_S)} \left( (1 - Y_{SP} \cdot (1 - R_S)) - (1 - Y_{SP})(1 - R_S) C_C^* \right) \quad (4-10)$$

where  $C_C^*$  is the brine concentration at the membrane exit, normalized with respect to the raw feed water concentration (i.e.,  $C_C^* = C_C/C_O$ ), and  $\Theta$  is dimensionless time ( $\Theta = t/\tau$ , in which  $\tau$  is the space time defined as  $\tau = V/q_F$  where  $q_F$  is the RO feed flow rate). Given the reasonable approximation of linear dependence of the osmotic pressure ( $\pi$ ) on salt concentration [61, 185], **Eq. (4-10)** can be solved, with the approximation of an invariant salt rejection as was the case in the present work (i.e.,  $R_S = 99.3 \pm 0.3\%$ ) over the range of encountered operational salinity (**Fig. 4-4**), to obtain the dimensionless brine osmotic pressure at the RO element exit location ( $\pi_C$ )

for the  $n^{\text{th}}$  cycle as a function of process time, yielding:

$$\frac{(\pi_C^*(\Theta))_{FT}^{(n)} - (\pi_C^*)_{i,FT}^{n=1} / (1-R_S)}{(\pi_C^*)_{i,FT}^{(n)} - (\pi_C^*)_{i,FT}^{n=1} / (1-R_S)} = \exp\left(-\frac{2(1-Y_{SP})(1-R_S)}{2-Y_{SP}-Y_{SP}\cdot(1-R_S)} \cdot Y_{SP} \cdot \Theta\right) \quad (4-11)$$

in which the superscript  $n$  designates the filtration cycle number. Normalized with respect to the raw feed osmotic pressure ( $\pi_0$ ), the dimensionless osmotic pressures at the element exit during and at the beginning of filtration period  $n$  are denoted in **Eq. (4-11)** by  $(\pi_C^*(\Theta))_{FT}^{(n)}$  and  $(\pi_C^*)_{i,FT}^{(n)}$ , respectively. In **Eq. (4-11)**,  $(\pi_C^*)_{i,FT}^{n=1}$  is the dimensionless osmotic pressure (at the element exit) at the beginning of the first filtration cycle ( $n=1$ ), which can be obtained from **Eqs. (4-8)** and **(4-9)** given linear approximation between osmotic pressure and salinity [61], as:

$$(\pi_C^*)_{i,FT}^{n=1} = \frac{(\pi_C)_{i,FT}^{n=1}}{(\pi_O)_{i,FT}^{n=1}} = \frac{(1-(1-R_S)Y_{SP})}{(1-Y_{SP})} \quad (4-12)$$

in which subscripts  $FT$  and  $i$  designates the filtration period and its beginning (i.e.,  $\Theta=0$ ), respectively. It is noted that, based on a pseudo-steady state salt balance about the RO module, the osmotic pressure at the entrance to the membrane element ( $\pi_F$ ) is equivalent to the raw feed osmotic pressure ( $\pi_C$ ), and thus  $\pi_F/\pi_C = (1-Y_{SP})/(1-(1-R_S)Y_{SP})$  for the first cycle at initial condition. Similarly, the mixed-cup element entrance salt concentration ( $C_F$ ) is related to the exit concentration ( $C_C$ ) as  $C_F/C_C \approx \pi_F/\pi_C$ . It is stressed that the above analysis is restricted to RO membranes of high salt rejection for which  $R_S \rightarrow 1$ . In fact, for such membranes, **Eq. (4-10)** reduces to  $dC_C^*/d\Theta = 2Y_{SP}/(2-Y_{SP})$ , and thus the variation of the concentrate osmotic pressure (at the element exit) during each filtration period, for any given cycle, can be approximated by,

$$\left(\pi_C^*(\Theta)\right)_{FT}^{(n)} = 2Y_{SP}/(2-Y_{SP})\Theta + \left(\pi_C^*\right)_{i,FT}^{(n)} \quad (4-13)$$

**Eq. (4-13)** indicates that the concentrate osmotic pressure (at the element exit) varies linearly with time during each filtration period. It is stressed that  $\left(\pi_C^*\right)_{i,FT}^{(n)}$  (at the beginning of the filtration period in  $n^{th}$  cycle) is dictated by the concentrate osmotic pressure, at the element exit, at the end of the previous cycle flushing period (**Section 4.2.3**). The filtration duration (i.e.,  $\Theta_{FT} = t_{FT} / \tau$ ) determines the exit element osmotic pressure at the end of this period (i.e.,  $\left(\pi_C^*\right)_{f,FT}^{(n)}$ ).

It is noted that the salt rejection in **Eq. (4-12)**,  $R_S = 1 - C_P/C_F$ , can be taken to be invariant with concentration for reasonably high salt rejecting membranes as confirmed for the operating conditions and membrane (RE-2540BE) of the present work (**Section 0, Table 4-1 and Fig. 4-4**).

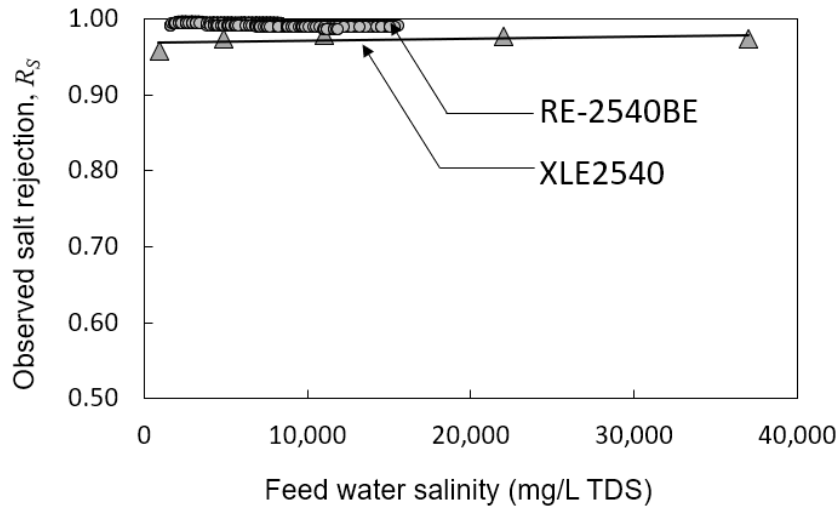


**Fig. 4-3.** Observed salt rejection ( $R_S$ ) for the present CSM RE2540-BE membrane ( $R_S=0.993\pm0.003$ ) and data for DOW XLE2540 membrane based on the data from [190]) ( $R_S=0.97\pm0.01$ ) demonstrating reasonable invariance of  $R_S$  with feed water salinity.

### 4.2.3 Concentrate flushing period

At the end of each filtration period (Section 4.2.2) the concentrate holdup from the SBRO system is flushed with the fresh raw-feed water in a single-pass flow mode (i.e., without concentrate recycle; Fig. 4-1b). Once the concentrate salinity at the RO element exit (or the applied pressure) increases to a predetermined level that triggers flushing, raw feed water is directed to the RO system during a flushing period of operation without concentrate recycle. As a consequence, there is an abrupt (i.e., essentially a step) reduction in the RO feed stream salinity ( $C_F$ ) from the high level at filtration period end to the raw water feed salinity at the beginning of the flushing period. As flushing proceeds, the concentrate salinity (at the element exit) decreases from its level at the SBRO filtration period end,  $(C_C)_{f,FT}$ , to the value attained at the flushing period termination (i.e.,  $(C_C)_{f,FL}$ ). The concentrate salinity at the RO element exit at the end of the flushing period (i.e., also the beginning of subsequent filtration period) will depend on the efficacy of excess salinity flushing from the RO system. The progressive flushing efficacy can be quantified as:

$$F(\Theta_{FL}) = \frac{(C_C)_{i,FL}^{(n)} - (C_C)_{f,FL}^{(n)}}{(C_C)_{i,FL}^{(n)} - (C_C)_{i,FT}^{n=1}} = \frac{(C_C)_{f,FT}^{(n)} - (C_C)_{i,FT}^{(n+1)}}{(C_C)_{f,FT}^{(n)} - (C_C)_{i,FT}^{n=1}} \quad (4-14)$$

where  $(C_C)_{i,FL}^{(n)}$  and  $(C_C)_{f,FL}^{(n)}$  are the concentrate salinity (at the element exit) for cycle  $n$  beginning and end of flushing period  $n$ , respectively (also equivalent to the end and beginning element exit salinity values of  $(C_C)_{f,FT}^{(n)}$  and  $(C_C)_{i,FT}^{(n+1)}$  of filtration periods  $n$  and  $n+1$ , respectively),  $(C_C)_{i,FT}^{n=1}$  is the concentrate salinity at the beginning of the first cycle filtration period (i.e.,  $n=1$ ), and  $\Theta_{FL} = t_{FL} / \tau$ .  $F(\Theta)$  can be determined experimentally for the system



under consideration at its operating conditions (**Section 4.4.1**). It is noted that the function represented by **Eq. (4-14)** is akin to the cumulative residence time distribution (RTD) function [191], i.e.,  $\int_0^{\Theta_{FL}} E(\Theta) d\Theta = F(\Theta_{FL})$ , where  $E(\Theta)$  is the RTD function.

The concentrate salinity at the RO element exit at the end of each successive SBRO flushing period becomes the filtration concentrate salinity at the beginning of the subsequent cycle (i.e.,  $(C_C)_{f,FL}^{(n)} = (C_C)_{i,FT}^{(n+1)}$ ). Accordingly, by combining equations **(4-11)** and **(4-14)**, and iteratively solving for progressive filtration-to-flushing cycles, as detailed in **Section 4.2.3.1**.

#### 4.2.3.1 Osmotic pressure during variation during the SBRO filtration period

Given the first cycle concentrate osmotic pressure at the filtration period beginning,  $(\pi_C)_{i,FT}^{n=1}$  (**Eq. (4-12)**), one can obtain the brine osmotic pressure at the end of the RO filtration period in the first cycle,  $(\pi_C^*)_{f,FT}^{n=1}$ , by solving **Eq. (4-11)** to yield:

$$\frac{(\pi_C^*)_{f,FT}^{n=1} - (\pi_C^*)_{i,FT}^{n=1} / (1 - R_S)}{(\pi_C^*)_{i,FT}^{n=1} - (\pi_C^*)_{i,FT}^{n=1} / (1 - R_S)} = \exp\left(-\frac{2(1 - Y_{SP})(1 - R_S)}{2 - Y_{SP} - Y_{SP}(1 - R_S)} Y_{SP} \Theta_{FT}\right) \quad (4-15)$$

Given the concentrate osmotic pressure at the end of the filtration period for cycle 1, one can obtain the concentrate osmotic pressure (at the element exit) at the filtration period beginning for the subsequent cycle,  $(\pi_C^*)_{i,FT}^{(n=2)}$ , for a given flushing efficacy ( $F(\Theta_{FL})$ ; **Eq. (4-14)**),

$$(\pi_C)_{i,FT}^{n=2} = (\pi_C)_{f,FT}^{n=1} - \left( (\pi_C)_{f,FT}^{n=1} - (\pi_C)_{i,FT}^{n=1} \right) \cdot F(\Theta_{FL}) \quad (4-16)$$

Following the above recursive process one can arrive at the following series expression for the concentrate osmotic pressure (at the element exit) at the beginning of filtration period  $n$  (i.e.,

$(\pi_C^*)_{i,FT}^{(n)}$ ):

$$\frac{(\pi_C^*)_{i,FT}^{(n)} - \frac{(\pi_C^*)_{i,FT}^{n=1}}{1-R_S}}{(\pi_C^*)_{i,FT}^{n=1} - \frac{(\pi_C^*)_{i,FT}^{n=1}}{1-R_S}} = \left[ \begin{array}{l} F(\Theta_{FL}) \\ +F(\Theta_{FL}) \cdot (1-F(\Theta_{FL})) \exp\left(-\frac{2(1-Y_{SP})(1-R_S)}{(1-Y_{SP})+1-Y_{SP}(1-R_S)} Y_{SP} \cdot \Theta_{FT}\right) \\ +F(\Theta_{FL}) \cdot (1-F(\Theta_{FL}))^2 \exp\left(-2\frac{2(1-Y_{SP})(1-R_S)}{(1-Y_{SP})+1-Y_{SP}(1-R_S)} Y_{SP} \cdot \Theta_{FT}\right) \\ \dots\dots\dots \\ +F(\Theta_{FL}) \cdot (1-F(\Theta_{FL}))^{n-2} \exp\left(-(n-2)\frac{2(1-Y_{SP})(1-R_S)}{(1-Y_{SP})+1-Y_{SP}(1-R_S)} Y_{SP} \cdot \Theta_{FT}\right) \\ +(1-F(\Theta_{FL}))^{n-1} \exp\left(-(n-1)\frac{2(1-Y_{SP})(1-R_S)}{(1-Y_{SP})+1-Y_{SP}(1-R_S)} Y_{SP} \cdot \Theta_{FT}\right) \end{array} \right] \quad (4-17)$$

one can obtain the following expression for the concentrate osmotic pressure, at the element exit for the beginning of each cycle filtration period,  $(\pi_C^*)_{i,FT}^{(n)}$  (also equivalent to the value at the end of the preceding flushing period, i.e.,  $(\pi_C^*)_{f,FL}^{(n-1)}$ , from a geometric series within the square bracket in the above equation can be converges such that  $(\pi_C^*)_{i,FT}^{(n)}$  is given by:

$$\frac{(\pi_C^*)_{i,FT}^{(n)} - \frac{(\pi_C^*)_{i,FT}^{n=1}}{1-R_S}}{(\pi_C^*)_{i,FT}^{n=1} - \frac{(\pi_C^*)_{i,FT}^{n=1}}{1-R_S}} = \left[ \frac{F(\Theta_{FL}) - F(\Theta_{FL}) \cdot (1-F(\Theta_{FL}))^n \exp\left(-n\frac{2(1-Y_{SP})(1-R_S)}{(1-Y_{SP})+1-Y_{SP}(1-R_S)} Y_{SP} \Theta_{FT}\right)}{1 - (1-F(\Theta_{FL})) \exp\left(-\frac{2(1-Y_{SP})(1-R_S)}{(1-Y_{SP})+1-Y_{SP}(1-R_S)} Y_{SP} \cdot \Theta_{FT}\right)} + (1-F(\Theta_{FL}))^n \exp\left(-(n-1)\frac{2(1-Y_{SP})(1-R_S)}{(1-Y_{SP})+1-Y_{SP}(1-R_S)} Y_{SP} \cdot \Theta_{FT}\right) \right] \quad (4-18)$$

For the stable cycle-to-cycle SBRO operation the concentrate osmotic pressure (at the element exit) at the beginning of the filtration period can be determined by taking the limit of  $n \rightarrow \infty$ ,  $(\pi_C^*)_{i,FT}^{n \rightarrow \infty}$ ,

$$\frac{\left(\pi_C^*\right)_{i,FT}^{n \rightarrow \infty} - \left(\pi_C^*\right)_{i,FT}^{n=1}}{\left(\pi_C^*\right)_{i,FT}^{n=1} - \left(\pi_C^*\right)_{i,FT}^{n=1}} = \left[ \frac{F(\Theta_{FL})}{1 - (1 - F(\Theta_{FL})) \exp\left(-\frac{2(1 - Y_{SP})(1 - R_S)}{(1 - Y_{SP}) + 1 - Y_{SP}(1 - R_S)} Y_{SP} \cdot \Theta_{FT}\right)} \right] \quad (4-19)$$

Given the expression for  $\left(\pi_C^*\right)_{i,FT}^{n \rightarrow \infty}$ , concentrate osmotic pressure during the filtration period,  $\left(\pi_C^*\right)_{FT}^{n \rightarrow \infty}$ , can be determined from using **Eq. (4-11)** leading to the following expression:

$$\frac{\left(\pi_C^*\right)_{FT}^{n \rightarrow \infty} - \left(\pi_C^*\right)_{i,FT}^{n=1} / (1 - R_S)}{\left(\pi_C^*\right)_{i,FT}^{n \rightarrow \infty} - \left(\pi_C^*\right)_{i,FT}^{n=1} / (1 - R_S)} = \exp\left(-\frac{2(1 - Y_{SP})(1 - R_S)}{(1 - Y_{SP}) + 1 - Y_{SP}(1 - R_S)} \cdot Y_{SP} \cdot \Theta\right) \quad (4-20)$$

It is noted that, for a membrane with complete salt rejection ( $R_S=100\%$ ),  $\left(\pi_C^*\right)_{FT}^{n \rightarrow \infty}$  can be obtained from **Eq. (4-13) (Section 4.2.2)** leading to:

$$\left(\pi_C^*(\Theta)\right)_{FT}^{n \rightarrow \infty} = \frac{2Y_{SP}}{(2 - Y_{SP})} \cdot \Theta + \left(\pi_C^*\right)_{i,FT}^{n \rightarrow \infty} \quad (4-21)$$

#### 4.2.4 RO concentrate osmotic pressure variation over progressive SBRO cycles

Given the expressions for the osmotic pressure variation during the filtration (**Eq. (4-11)**) and its beginning filtration condition as defined in (**Eq. (4-18)**) for the  $n^{\text{th}}$  cycle, one can show that the RO element exit concentrate concentration and thus the osmotic pressure at the filtration period (**Eq. (4-18)**) will rise with successive filtration/flushing cycles until a stable condition is attained. Such a behavior is illustrated in **Figs. 4-4** and **4-5** for the specific case of a single-pass recovery of 10% (e.g., when a single RO element is utilized), for a membrane having 100% rejection, and fixed filtration and flushing periods and for different levels of

flushing effectiveness as quantified by  $F(\Theta_{FL})$ , which is considered in this example to be invariant from cycle-to-cycle.

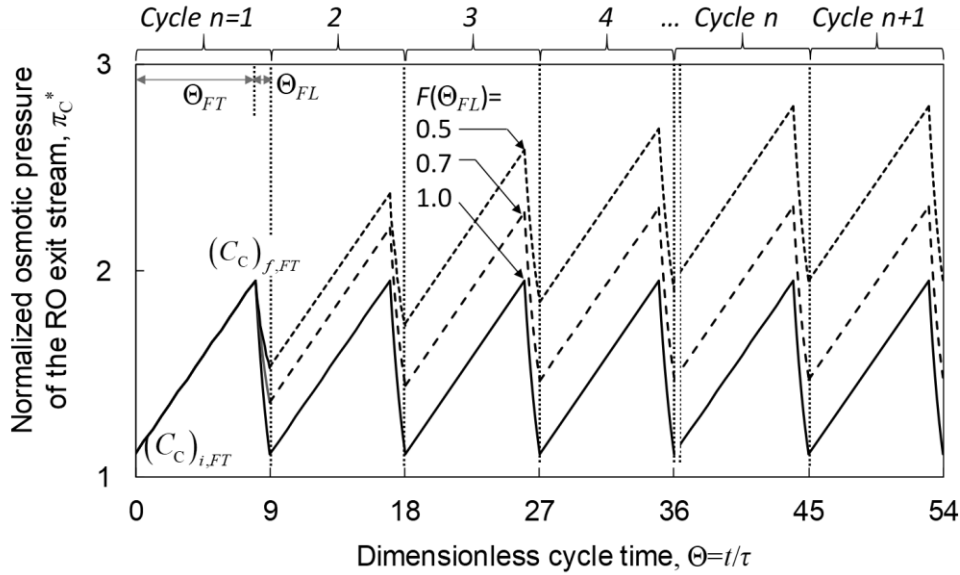


**Fig. 4-4.** Filtration and flushing periods time profiles of the normalized concentrate osmotic pressure at the RO element exit,  $\pi_c^* = \pi_c / \pi_o$ . SBRO operation is illustrated schematically over multiple cycles as per **Eqs. (4-11)** and **(4-18)** at fixed flushing efficacy of  $F(\Theta_{FL})=0.5, 0.7$  and  $1.0$ , flushing period of  $\Theta_{FL}=1$  and overall water recovery of 50% at a fixed single pass recovery of 10% and complete salt rejection (i.e.,  $R_S=1$ ). Note: the RO feed osmotic pressure for each cycle is related to the exit element osmotic pressure as described in **Section 4.2.2**.

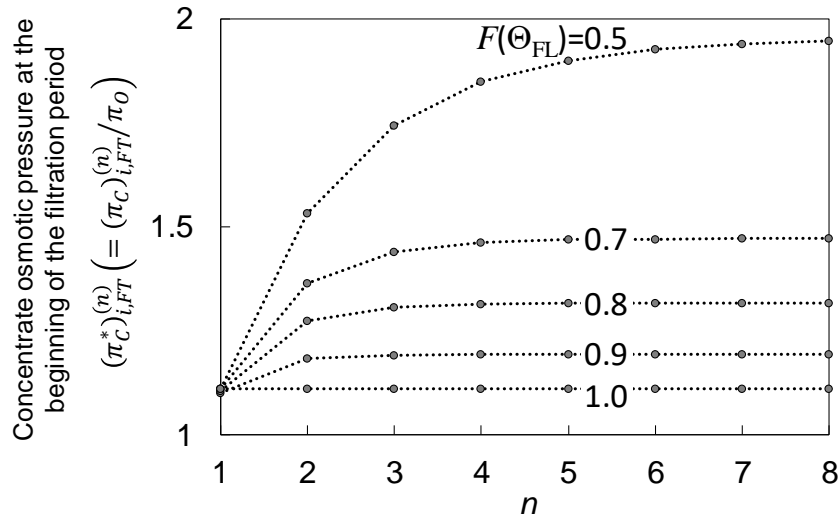


**Fig. 4-5.** Variation of the concentrate osmotic pressure at the beginning of each successive filtration period  $n$ ,  $(\pi_c^*)_{i,FT}^{(n)}$ , normalized by the raw-feed water osmotic pressure  $((\pi_c^*)_{i,FT}^{(n)} = (\pi_c)_{i,FT}^{(n)} / \pi_o)$  as per **Eq. (4-18)** at various level of flushing efficacy ( $F(\Theta_{FL})$ , **Eq.**

(4-14) of 0.5, 0.7, 0.8, 0.9, and 1.0 for a given flushing period of  $\Theta_{FL}=1$  for overall system recovery target of 50% (i.e.,  $Y=0.5$ ) with complete salt rejection ( $R_S=1$ ) and fixed single pass water recovery of 10% (i.e.,  $Y_{SP}=0.1$ ). (Note: element inlet osmotic pressure is determined as per the relation in **Section 4.2.2**).

It is apparent from the above example (**Fig. 4-4**) that, with greater flushing efficacy (i.e.,  $F(\Theta_{FL}) \rightarrow 1$ ), the cycle-to-cycle element exit osmotic pressure at the beginning of each filtration period will readily reach a stable value. As  $F(\Theta_{FL})$  decreases, a higher salinity level will progressively build in the RO circuit which will increase the osmotic pressure, and thus the required applied pressure to achieve the prescribed permeate flow rate. As shown in **Fig. 4-5**, for the same conditions as in **Fig. 4-4**, the osmotic pressure of the SBRO concentrate (and thus the inlet feed stream to the RO element) would increase with successive cycles until a steady value is reached. For example, for  $F(\Theta_{FL})=0.5$  a rise in the element exit osmotic pressure at the filtration period beginning,  $(\pi_C^*)_{i,FT}$ , of up to a factor of 1.76 (or up to a factor of 1.95 for the element inlet osmotic pressure) would be reached within 8 cycles. In contrast, for the case of complete flushing (i.e.,  $F(\Theta_{FL}) = 1$ ) the element feed and (exit) concentrate salinity at the beginning and end of the filtration and flushing periods would be cycle-to-cycle invariant. The above illustration emphasizes that effective flushing is critical to attaining efficient if the goal is to reduce energy consumption, as well as avoid increased salt passage.

Incomplete concentrate flushing (i.e.,  $F < 1$ ) would lead to a successive cycle-to-cycle rise in the element exit osmotic pressure (and correspondingly the element inlet osmotic pressure) at the beginning of successive filtration periods as can be ascertained from **Eq. (4-18)**. As can be conjectured from the examples of **Figs. 4-4** and **4-5**, one should expect that the element exit concentrate osmotic pressure at the beginning of the filtration period will ultimately reach a stable value (identical from cycle-to-cycle), i.e.,  $(\pi_C^*)_{i,FT}^{n \rightarrow \infty}$ . This condition can be determined

from **Eq. (4-18)** in the limit of  $n \rightarrow \infty$  (where  $(\pi_C^*)_{i,FT}^{n=1}$  is given by **Eq. (4-12)**) and is given as:

$$\frac{(\pi_C^*)_{i,FT}^{n \rightarrow \infty} - (\pi_C^*)_{i,FT}^{n=1} / (1 - R_S)}{(\pi_C^*)_{i,FT}^{n=1} - (\pi_C^*)_{i,FT}^{n=1} / (1 - R_S)} = \left[ \frac{F(\Theta_{FL})}{1 - (1 - F(\Theta_{FL})) \exp\left(-\frac{2(1 - Y_{SP})(1 - R_S)}{2 - Y_{SP} - Y_{SP}(1 - R_S)} \cdot Y_{SP} \cdot \Theta_{FT}\right)} \right] \quad (4-22)$$

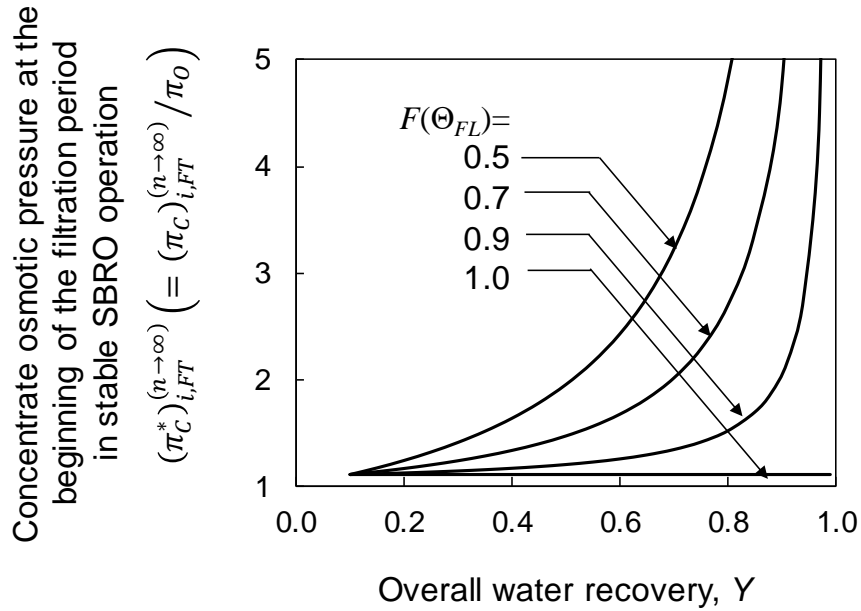


**Fig. 4-6.** The concentrate osmotic pressure at the RO element exit (i.e.,  $(\pi_C^*)_{i,FT}$ ) for the case in which the SBRO operation has reached its stable condition (i.e.,  $n \rightarrow \infty$ ) with respect to the overall water recovery,  $Y$  (as per **Eq. (4-22)**) at the flushing efficacy in the range of  $F(\Theta_{FL}) = 0.5 - 1$  for a flushing period equal to the system convective residence time (i.e.,  $\Theta_{FL} = 1$ ) for a membrane of 100% salt rejection, and fixed single pass water recovery of 10% (i.e.  $Y_{SP} = 0.1$ ).

An illustration of the variation of the concentrate osmotic pressure at the element exit with overall system recovery is provided in **Fig. 4-6** for SBRO at its stable cycle-to-cycle operation (i.e.,  $n \rightarrow \infty$ ), for the same SBRO specifications as in **Fig. 4-4**. As the flushing efficacy decreases both  $(\pi_C^*)_{i,FT}^{n \rightarrow \infty}$  and the RO element inlet osmotic pressure of filtration step will increase and dramatically once the overall target recovery increases above about 70%. In the special case of ideal flushing (i.e., when  $F(\Theta_{FL}) = 1$ ), the cycle-to-cycle osmotic pressure, at the beginning of

each filtration period, would remain unaltered and equivalent to that which existed at the initial filtration cycle (i.e.,  $n = 1$ ). If complete flushing is not realized, the needed applied pressure during each filtration period, to maintain the target permeate flow rate, would rise with progressive cycles but would ultimately reach a stable value. Consequently, the energy expenditure would also rise up to the condition of stable successive cycles.

In principle, cycle-to-cycle stabilization may be rapidly achieved if the flushing duration is sufficiently long (i.e., equivalent to an increasing raw feed water flushing volume) relative to the filtration duration ( $t_{FL} \gg t_{FT}$ ). Under this operational scenario, the average salinity in the SBRO system will be reinstated to the condition at the beginning of the first cycle. However, in such case, for a given filtration duration, the overall product water recovery will decrease and with increasing flushing time it will ultimately approach the single-pass RO system recovery (**Eq. (4-5); Section 4.2.1**). Such overall water recovery decrease can be avoided by shortening the flushing time, but with a tradeoff of prolonging the filtration duration leading to higher average salinity in the SBRO system, and, consequently, increased energy consumption. Clearly, flushing efficacy is a critical SBRO operational parameter. It is emphasized that the flushing efficacy will depend on the specific SBRO system configuration and the convective residence time within the system. Based on the present data discussed in **Section 4.4.1**,  $F(\Theta_{FL})$  should be expected to increase with the flushing duration ( $\Theta_{FL}$ ), but this dependence is non-linear.

#### **4.2.5 Specific energy consumption**

The specific energy consumption (SEC) for desalination for a given SBRO operational cycle (i.e., filtration followed by flushing) is the total energy consumption per unit volume of

produced permeate [132, 136] as given by,

$$SEC_{SBRO} = \frac{\int_0^{t_{cycle}} \frac{\dot{W}_p(t)}{\eta_p} dt}{\int_0^{t_{cycle}} q_p dt} \quad (4-23)$$

in which  $t_{cycle}$  is the process time for a single cycle (i.e.,  $t_{cycle} = t_{FT} + t_{FL}$ ) and  $\eta_p$  is the pump efficiency. The required desalination pressure work,  $\dot{W}_p(t)$ , will depend on the efficiencies of the feed pump and energy recovery device (if used in the system) and is given as [136, 190],

$$\dot{W}_p(t) = \Delta P_f(t)(q_f - \eta_{ER}q_c) \quad (4-24)$$

where  $\Delta P_f(t) = P_f(t) - P_o$  in which  $P_f(t)$  and  $P_o$  are pressures of the feed entering the RO membrane element(s) and of the raw feed water, respectively, and  $\eta_{ER}$  is the overall efficiency of energy recovery in the system. It is emphasized that the energy required for desalination separation by the RO element (or element train) is for the condition of an ideal pump ( $\eta_p = 1$ ) and without considering energy recovery (i.e.,  $\eta_{ER} = 0$ ). In **Eq. (4-24)**, the transmembrane pressure at the RO element inlet can be expressed as  $\Delta P_f = (P_{exit} - P_o) + \delta P_{loss}$ , where  $\delta P_{loss}$  is the pressure loss in the membrane element and  $P_{exit}$  is the feed-side pressure at the element exit location. Under the condition of an unpressurized permeate stream at essentially atmospheric pressure, it is reasonable to set  $P_o = P_p$ . Therefore,  $\Delta P_f = \Delta P_{TMP,exit} + \delta P_{loss}$ , where the transmembrane pressure is given as  $\Delta P_{TMP,exit} = (P_{exit} - P_o)$  and can be estimated from the classical permeate flux expression (i.e.,  $J_v = L_p (\Delta P_{TMP} - \sigma \cdot \Delta \pi)$ , [61]) to yield the following:

$$\Delta P_{TMP,exit} = J_{v,exit} / L_p + \sigma \cdot \Delta \pi_{exit} \quad (4-25)$$

in which  $J_{v,exit}$  and  $L_p$  are the permeate flux at the RO element exit and membrane water permeability, respectively, and  $\sigma$  is the reflection coefficient (considered to be about unity for



high salt rejection RO membranes). The transmembrane osmotic pressure is  $\Delta\pi_{exit} = (\pi_m)_{exit} - \pi_p$ , where  $\pi_p$  and  $(\pi_m)_{exit}$  are osmotic pressures of the permeate stream and the membrane surface at element exit, respectively. As a reasonable estimate  $(\pi_m)_{exit} = CP_{exit} \cdot \pi_C$  in which  $CP_{exit}$  is the concentration polarization modulus (i.e.,  $CP = C_m/C_b$  where  $C_m$  and  $C_b$  are the solute concentrations at the membrane surface and the bulk solution, respectively [192, 193]) that can be estimated for spiral-wound RO elements either empirically (Section 3.3.3) or based on whole element CFD analysis [194]. Therefore, given  $CP$  at the element exit, the applied feed pressure (relative to the raw feed pressure) is approximated as  $\Delta P_f = J_{v,exit} / L_p + (\delta p)_{loss} + CP_{exit} \cdot \Delta\pi_C$ . Considering the reasonable approximation of  $\Delta\pi_C \cong \pi_C$  (at the element exit) in typical RO processes where  $\pi_C \gg \pi_p$ , the SBRO SEC can be expressed as:

$$SEC_{SBRO} = \left( \int_0^{t_{FT}} \dot{W}_p(t) dt + \int_{t_{FT}}^{t_{FT}+t_{FL}} \dot{W}_p(t) dt \right) / \left( \int_0^{t_{FT}} q_P dt + \int_{t_{FT}}^{t_{FT}+t_{FL}} q_P dt \right) \quad (4-26)$$

in which  $\dot{W}_p(t)$  is given as,

$$\dot{W}_p(t) = \frac{(q_F - \eta_{ER} q_C)}{\eta_P} \left( \frac{J_{v,exit}}{L_p} + CP_{exit} \cdot \pi_C + (\delta p)_{loss} \right) \quad (4-27)$$

The first and the second integrals in both the nominator and denominator in Eq. (4-26) represent the contributions of the filtration and flushing periods, respectively, to the SEC. The permeate flux at the element exit ( $J_{v,exit}$ ) from the single pass train (single or multiple elements) can be estimated relative to the average permeate flux,  $\bar{J}_v$  (Section 4.2.5.1), and along with the term  $CP_{exit} \cdot \pi_{exit}$  can be expressed, following the approximation provided in [132, 136], as:

$$\frac{J_{v,exit}}{L_p} + CP_{exit} \cdot \pi_{exit} = \frac{\overline{J}_v}{L_p} + \overline{CP} \frac{(1 - Y_{SP})}{1 - Y_{SP}(1 - R_S)} \frac{\ln(1/(1 - Y_{SP}))}{Y_{SP}} \pi_C \quad (4-28)$$

in which  $\overline{CP}$  is the average concentration polarization for a given RO element. **Equation (4-28)** is derived by considering that concentrate mixing takes place between pressure vessels and that  $CP$  at the exit location of each RO train element is governed by the same single-pass recovery (**Section 3.3.3**) over the practical range of operational feed pressure [142, 195]. Single-element recovery in RO systems is generally constrained to a low value ( $\leq 15\%$ ) in order to avoid over-fluxing the permeate across the membrane element [190, 196] beyond the membrane manufacturer specifications. Under such conditions  $CP_{exit}$  will be proximal to the element average  $CP$  (**Section 3.3.3**).

Temporal variation of the concentrate osmotic pressure at the element exit during the SBRO filtration cycle ( $(\pi_C)_{FT}$ ) can be determined from the salt mass balance equations described in **Section 4.2.2**. Obtaining the temporal profile of the RO system concentrate salinity at the system exit (and thus  $(\pi_C)_{FT}$ ) is challenging since dispersion is invariably system specific. However, given that for practical the SBRO operation the flushing period has to be significantly shorter than the filtration period (i.e., in order to attain reasonable RO recovery), it is reasonable to utilize a linear RO concentrate salinity-time profile as shown in the present work (**Section 4.4.1**) and reported in previous SBRO work [49, 162, 166].

The case of SBRO operation with non-pressurized concentrate flushing, in which there is negligible permeate productivity, would lead to reduced overall cycle recovery. Also, it is worth noting that for continuous permeate production throughout each SBRO cycle, hydraulic energy expenditure will occur during the flushing period, albeit lower than during the filtration period. Both of the above cases can be considered via the above analysis, without a loss of generality.

In the present work, the more reasonable approach of constant permeate productivity is considered over the entire SBRO cycle [197]. For the above operational scenario, considering the special case of invariant pump and ERD efficiencies, negligible frictional losses and constant element-to-element single pass recovery, one can show that the SEC as deduced from Eqs. (4-26) – (4-28) is given by:

$$SEC_{SBRO}^* = \frac{SEC_{SBRO}}{\pi_O} = \frac{(1-\eta_{ER})(1-Y_{SP})}{\eta_P Y_{SP}} \left( \frac{\bar{J}_v}{L_p \pi_O} + \overline{CP} \frac{(1-Y_{SP})}{1-Y_{SP}(1-R_S)} \frac{\ln(1/(1-Y_{SP}))}{Y_{SP}} \cdot \frac{\int_0^{t_{cycle}} \pi_C^* dt}{t_{cycle}} \right) \quad (4-29)$$

in which  $\pi_C^*$  during the filtration period is determined from Eq. (4-11) and based on the approximation of a short flushing period (i.e.  $t_{FT} \gg t_{FL}$ ) during which the temporal concentrate salinity profile can be taken to be linear, and thus  $\left(\pi_C^*\right)_{cycle} \approx \left(\pi_C^*\right)_{FT}$ . Once consecutive SBRO cycles stabilize (i.e., the cycle-to-cycle element inlet and exit concentrations are reproduced at the beginning and end of each filtration period), the last term in Eq. (4-29) can be obtained from integration of Eq. (4-22) which can be shown to lead to  $\left(\int_0^{t_{FT}} \pi_C^* dt\right) / t_{FT} = \left(\pi_C^*\right)_{FT}^{n \rightarrow \infty}$ . Given the expression for the brine osmotic pressure  $\left(\pi_C^*\right)_{FT}^{n \rightarrow \infty}$  during the filtration period in a stable cycle-to-cycle SBRO operation (Eq. (4-20)), the normalized cycle average osmotic pressure at the element exit for the condition of a stable cycle-to-cycle operation,  $\left(\pi_C^*\right)_{FT}^{n \rightarrow \infty}$ , can be obtained from integration of Eq. (4-11) to yield,

$$\left(\pi_C^*\right)_{FT}^{n \rightarrow \infty} = \frac{1}{\Theta_{FT}} \int_0^{\Theta_{FT}} \left(\pi_C^*\right)^{n \rightarrow \infty} d\Theta = \left(\pi_C^*\right)_{i,FT}^{n=1} / (1-R_S) + \left( \left(\pi_C^*\right)_{i,FT}^{n \rightarrow \infty} - \left(\pi_C^*\right)_{i,FT}^{n=1} / (1-R_S) \right) \times \frac{2-Y_{SP}-Y_{SP}(1-R_S)}{2(1-Y_{SP})(1-R_S) \cdot Y_{SP} \Theta_{FT}} \left[ 1 - \exp\left( -\frac{2(1-Y_{SP})(1-R_S)}{2-Y_{SP}-Y_{SP}(1-R_S)} \cdot Y_{SP} \Theta_{FT} \right) \right] \quad (4-30)$$

It is noted that for operation up to the thermodynamic restriction, as one approaches the RO element exit, the net driving force  $NDP = (\Delta P - \sigma \Delta \pi) \rightarrow 0$  and thus  $J_{v,exit} \rightarrow 0$  at the element exit. For the above condition at the crossflow thermodynamic restriction limit, the bulk and membrane surface salt concentrations are identical (i.e.,  $CP_{exit} \rightarrow 1$ ), and hence the normalized SEC (i.e.,  $SEC_{SBRO,TR}^* = SEC_{SBRO,TR} / \pi_0$ ) is reduced from **Eq. (4-29)** to:

$$SEC_{SBRO,TR}^* = \frac{(1 - \eta_{ER} (1 - Y_{SP}))}{\eta_P Y_{SP}} \left( \overline{\pi_C^*} \right)_{cycle}^{n \rightarrow \infty} \quad (4-31)$$

In the special case of ideal SBRO operation (i.e., complete flushing for which  $F(\Theta_{FL})=1$ ), the cycle-to-cycle osmotic pressure at the membrane exit at the commencement of each filtration cycle remains unaltered (i.e.,  $(\pi_C^*)_{i,FT}^{n \rightarrow \infty} = (\pi_C^*)_{i,FT}^{n=1}$ ). For the above case and an ideal membrane (i.e., complete salt rejection) the average cycle osmotic pressure for complete flushing is given as  $\left( \overline{\pi_C^*} \right)_{cycle} = (Y - Y_{SP}) / ((2 - Y_{SP})(1 - Y) + 1 / (1 - Y_{SP}))$  (**Section 4.2.3.1**). Thus, given **Eq.(4-31)**, the corresponding minimum SEC at the limit of thermodynamic restriction (with complete concentrate flushing) can be expressed as:

$$\left( SEC_{SBRO,TR}^* \right)_{plug-flow} = \frac{(1 - \eta_{ER} \cdot (1 - Y_{SP}))}{\eta_P Y_{SP}} \left( \frac{(Y - Y_{SP})}{(2 - Y_{SP})(1 - Y)} + \frac{1}{(1 - Y_{SP})} \right) \quad (4-32)$$

The SEC for SBRO operation at the thermodynamic limit for different levels of flushing efficacy (**Eq.(4-31)**), relative to that of the ideal SBRO case (**Eq. (4-32)**) and for steady state single-pass RO (SPRO), is illustrated in **Fig. 4-7**. This example is for the case of 10% single pass recovery, complete salt rejection and ideal feed pump (i.e.,  $\eta_p = 1$ ) and energy recovery ( $\eta_{ER} = 1$ ) for both SPRO and SBRO, and where the SBRO flushing is set equal to the convective RO system residence time (i.e.  $\Theta_{FL} = 1$ ). As shown in **Fig. 4-7**, under the ideal

scenario of complete concentrate flushing ( $F(\Theta_{FL}) = 1$ ), SBRO operation would be at a lower energy consumption ( $SEC_{SBRO,TR}^*$ ) relative to SPRO (i.e.,  $SEC_{SPRO,TR}$ ) at the same recovery and assuming similar pump and energy recovery efficiencies. However, when the flushing efficiency is reduced the SEC for SBRO will increase relative to the ideal SBRO case (i.e.,  $F(\Theta_{FL}) = 1$ ).

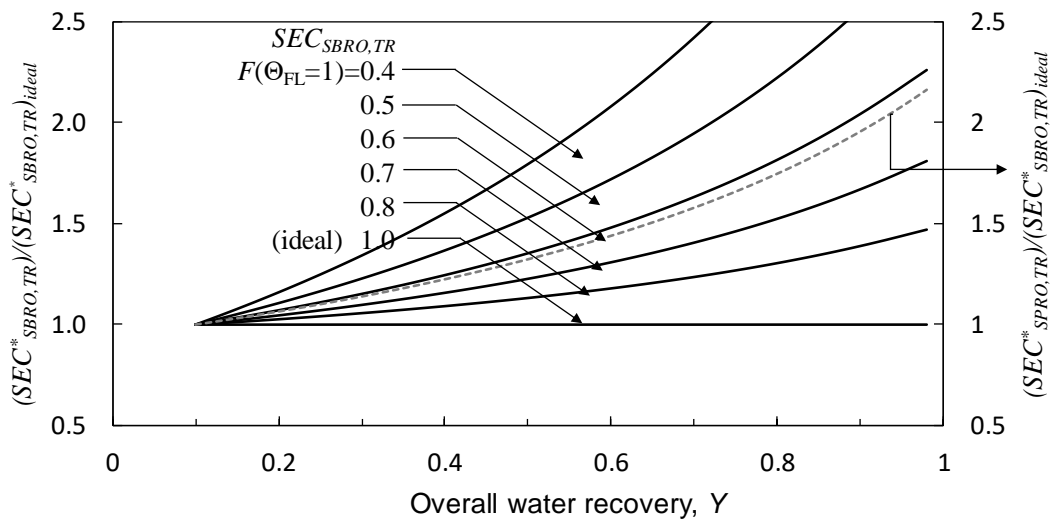


**Fig. 4-7.** Specific energy consumption (SEC) in SBRO dependence on overall system recovery ( $Y$ ) and flushing effectiveness ( $F$ ) of duration  $\Theta_{FL}=1$ , at the thermodynamic restriction relative to ideal SBRO (i.e., complete concentrate flushing),  $(SEC_{SBRO,TR})_{ideal}$ , as per Eqs. (4-31), (4-32) and (4-33) for salt rejection ( $R_S$ ) of 100% and single-pass water recovery ( $Y_{SP}$ ) of 10%. The dashed curve represents the SEC at the thermodynamic limit for SPRO relative to ideal SBRO.

It is noted that the SEC for SPRO operation at the thermodynamic restriction limit (**Fig. 4-7**) as reported previously [190] is given as

$$SEC_{SPRO,TR} / \pi_o = SEC_{SPRO,TR}^* = \left[ \frac{(1 - \eta_{ER}(1 - Y))}{\eta_P Y} \right] \left[ \frac{(1 - Y \cdot (1 - R_S))}{(1 - Y)} \right] \quad (4-33)$$

The above  $SEC_{SPRO,TR}^*$  is equivalent to SBRO operation with flushing efficacy characterized by  $F(\Theta_{FL}) = 0.62$ . SBRO operation for which  $F(\Theta_{FL}) = 0.62$  would lead to higher SBRO

SEC relative to SPRO (i.e.,  $SEC_{SPRO,TR}^* < SEC_{SBRO,TR}^*$ ). Here it is noted that for RO system operation away from the thermodynamic restriction, the SEC for SPRO ( $SEC_{SPRO}$ ), when considering negligible pressure losses, can be obtained from the relation provided in [190],

$$\left(SEC^*\right)_{SPRO} = \frac{(1 - \eta_{ER}(1 - Y))}{\eta_P Y} \left( \frac{J_{v,exit}}{L_p \cdot \pi_O} + CP_{exit} \cdot \frac{1 - Y \cdot (1 - R_S)}{1 - Y} \right) \quad (4-34)$$

Clearly, the efficacy of concentrate flushing will depend on system configuration (and its physical components) and the flushing conditions (i.e., e.g., crossflow velocity). Therefore, comparison of the SEC among actual different SBRO systems and various SPRO systems should be made with full consideration of the flushing efficacy as per the analysis presented in **Section 4.2.3**. While flushing duration longer than the convective residence time is feasible (i.e.,  $\Theta_{FL} > 1$ ), for a fixed filtration period, this would lower the attainable recovery (**Section 4.2.1**). Increasing the filtration time to maintain the recovery would then necessitate longer filtration time (**Section 4.2.1**) and consequently higher applied pressure at the end of the filtration period (**Section 4.2.5**). Therefore, it is critical to compare the SEC for different RO systems at the same overall recovery and permeate productivity. Also, it is stressed that while **Fig. 4-7** gives the impression of a highly optimistic SBRO performance (relative to SPRO), one must recognize that complete concentrate flushing, within a the system convective residence time, would not be easily realizable in practical SBRO systems of spiral-wound elements and where various system hydraulic components are present that may increase solute dispersion during the flushing period. Accordingly, in order to evaluate SBRO performance, with respect to concentrate flushing efficacy and its impact on the desalination SEC, a systematic experimental methodology is presented in **Sections 0** and **0**.

#### 4.2.5.1 Element average permeate flux

The permeate flux varies along the element and as illustrated in **Fig. 4-8** the flux at the element exit (for single-pass element recovery of below about 10%), is essentially equal to the average flux,  $\bar{J}_v$ , when  $\bar{J}_v / (L_p \cdot \pi_o) \geq 10$ . In the present study, and as expected for RO operation in which the element recovery is in the vicinity of ~10%, deviation of the flux at the exit location from that of the average was negligible (i.e.,  $J_{v,exit} / \bar{J}_v \sim 1$ ), which allows for the simplification of the analysis as presented in **Section 4.2.5**.

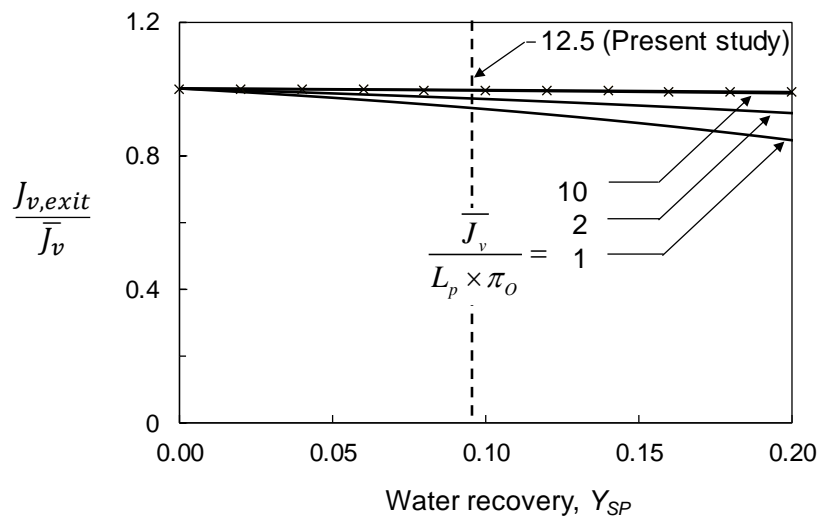


**Fig. 4-8.** Variation of the permeate flux at the membrane exit ( $J_{v,exit}$ ) relative to the average permeate flux ( $\bar{J}_v$ ), as per **Eq. (4-28)** at various level of normalized average permeate flux,  $\bar{J}_v^* = \bar{J}_v / (L_p \cdot \pi_o) = 1, 2,$  and  $10$  with respect single pass water recovery ( $Y_{SP}$ ) for ideal membrane (i.e., 100% salt rejection). The  $\bar{J}_v^*$  for the RO system utilized for the present study was  $12.5$  as indicated on the figure.

## 4.3 Experimental

### 4.3.1 Materials and model solution

The aqueous model solution was prepared by dissolving reagent-grade sodium chloride (Fisher Scientific Pittsburgh, PA) in deionized (DI) water. The feed solution in a 757 L (200 gal) polyethylene tank was continuously stirred by a mechanical mixer and maintained at  $20 \pm 1^\circ\text{C}$  using a recirculating chiller (VWR Scientific 1171-P, Radnor, PA). Prior to being fed to the RO system, the feed solution was then filtered through a sequence of three cartridge microfilters of sizes  $20\ \mu\text{m}$ ,  $5\ \mu\text{m}$  (pleated 2-1/2"x10", Ocean Link Inc., Portsmouth, RI), and  $0.2\ \mu\text{m}$  (Polysulfone Plastic, Harmsco, North Palm Beach, Florida). The present SBRO system was fitted with a single spiral-wound RO element (CSM RE2540-BE, Toray Chemical Korea Co., Seoul, Korea) having a  $2.5\ \text{m}^2$  active membrane surface area, average water permeability of  $2.4\ \text{L}/\text{m}^2\cdot\text{h}\cdot\text{bar}$  (measured at operating pressure of 10 bar), salt rejection of 99.5% determined using a 2,000 mg/L NaCl solution at  $25\ ^\circ\text{C}$  and 15 bar [148]. The pilot flexible RO system (detailed in **Appendix A**) was adapted SBRO operations. The SBRO system had an overall holdup volume of 4.1 L, and with RE2540-BE membrane, it provided a fixed per-pass recovery of about 9.2%. The electrical conductivities (*EC*) were monitored in each flowing streams in order to quantify variability of salinities in each stream based on the *EC*-TDS correlation in **Appendix A.2**.

### 4.3.2 Semi-batch RO desalination

The SBRO desalination experiments were carried out with NaCl feed solutions of concentration of 1000 mg/L. All experiments were carried out such with the SBRO arrangement as shown in **Fig. 4-9**. In all of the SBRO runs, the produced permeate and



concentrate streams were returned to the feed reservoir (**Fig. 4-9**) throughout the multi-cycle (of filtration-flushing) SBRO operation.

Prior to each experiment, the SBRO system was conditioned for 30 min in a single-pass mode by pumping the model solution through the system at a membrane feed flow rate ( $q_F$ ) of 11 L/min at feed pressure of ( $P_f$ ) of 10 bars. During the RO filtration period the SBRO is operated with the brine-discharge valve (V-2) completely closed to allow the concentrate stream to continuously mix with the raw feed water which was maintained at the same constant flow rate ( $q_0$ ) for all experiments. At the end of the filtration period of each cycle, flushing of the excess concentrate salinity from the system was accomplished by closing the concentrate recycle valve and opening the brine discharge valve. In this flushing operational mode, only the fresh raw feed stream was introduced to the RO membrane module.

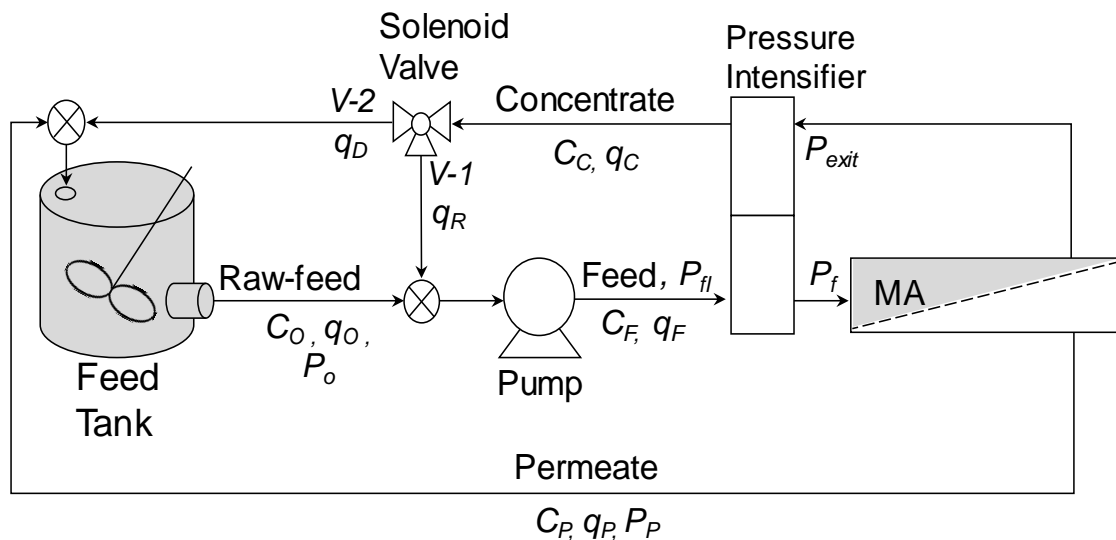


**Fig. 4-9.** Experimental setup for SBRO operation with a RO stage consisting of a single element (MA) where  $C_i$ , and  $q_i$  indicate salt concentration and flow rate of stream  $i$  (note: subscript  $i$  denotes one of the following:  $O$ -raw feed,  $F$ -RO element feed,  $C$ -RO concentrate,  $P$ -permeate, and  $D$ -brine discharge stream).

The RO system was operated in a sequential manner alternating between filtration and the flushing modes, while maintaining constant permeate flow rate equal to the RO feed flow. The operating conditions for the different experimental runs are provided in **Table 4-1**. It is noted that the range of operating conditions is consistent with the manufacturer recommended element permeate flux range of  $4.9 \times 10^2 - 1.2 \times 10^3$  L/m<sup>2</sup>·d (12 – 30 gfd) to maintain >99% NaCl rejection over the operating pressure range of 6.4 – 15.5 bar [148].

SBRO experiments (**Table 4-1**) were carried out over a cycle (filtration followed by flushing) time in the range 3.6 – 60 min for which the overall product water recovery was in the range of 9.2 – 79 % with set normalized flushing times ( $\Theta_{FL}=t_{FL}/\tau$ ) of 1.0, 2.2, and 4.4. SBRO experiments were carried out at each set of operating conditions for a period up to the stable cycle-to-cycle operation, in which the salinity of the concentrate at the element exit at the beginning and end of progressive cycles filtration periods showed less than 1% variation. At the termination of each experimental run the SBRO was cleaned by circulating DI water through the system channel for 30 min at a flow rate 11 L/min and 3 bar feed pressure.

The efficacy of excess salt flushing, as described in **Section 4.2.3**, was determined by monitoring the concentrate salinity at the element exit as a function of time. The raw water feed volume used for flushing was about 4.4 time the SBRO holdup concentrate volume delivered at the same element feed flow rate, ( $q_F$ ), used during the filtration period (i.e., equivalent to a flushing time that is 4.4 times the system space time). The flushing efficiency at any time during the flushing period was calculated as,

$$F(\Theta_{FL}) = \left( (C_C)_{f,FT} - C_C(\Theta)_{FL} \right) / \left( (C_C)_{f,FT} - (C_C)_{i,FT}^{n=1} \right) \quad (4-35)$$

where  $C_C(\Theta)_{FL}$  is the concentrate salinity (at the element exit) at time,  $\Theta$ .

**Table 4-1. SBRO experimental conditions**

Run #	Overall Water Recovery, $Y$ (%)	$t_{FT}$ ( $\Theta_{FT}$ )	$t_{FL}$ ( $\Theta_{FL}$ )	Initial cycle $n=1$		Stable cycle $n=N^{(a)}$		$N^*$	$F(\Theta_{FL})$
				$(C_C)_{i,FT}^{n=1}$ (mg/L)	$(C_C)_{f,FT}^{n=1}$ (mg/L)	$(C_C)_{i,FT}^{n \rightarrow \infty}$ (mg/L)	$(C_C)_{f,FT}^{n \rightarrow \infty}$ (mg/L)		
1	9.2%								
2.a	46%	7.7		1116	1998	2023	2790	7	0.46
2.b	62%	15.2	23 sec	1115	2646	2712	4215	7	0.48
2.c	74%	27.2	(1.0)	1145	4279	3803	6510	6	0.50
2.d	79%	35.7		1133	4661	4813	8079	7	0.47
3.a	46%	16.8		1150	2280	1782	3882	4	0.77
3.b	62%	32.0	50 sec	1110	4305	2153	5986	4	0.79
3.c	74%	58.7	(2.2)	1150	7080	3386	9997	4	0.75
3.d	79%	77.3		1100	8910	3351	11676	4	0.79
4.a	46%	34.7		1180	4515	1522	5578	3	0.92
4.b	62%	66.7	100 sec	1100	7415	1717	8800	3	0.92
4.c	74%	117.3	(4.4)	1060	11900	2097	14100	3	0.92
4.d	79%	154.7		1040	15610	2296	16770	3	0.92

<sup>(a)</sup> $N$  is defined as the cycle count required for establishing the stable (reproducible) concentrate concentration profile in which the concentrate salinity at the beginning of filtration period  $n$  differs from that of cycle  $n-1$  by less than 1%. Note: all experimental runs were carried out at raw feed salinity of 1,000 mg/L TDS, permeate flux of  $24.2 \pm 0.2$  L/(m<sup>2</sup>·hr) (equivalent to permeate flow rate of  $q_P = 1.0 \pm 0.05$  L/min), crossflow velocity of 19 cm/sec; the RO element feed flow rate,  $q_F = 11 \pm 0.05$  L/min at which the system space time ( $\tau$ ) was 23 s.

## 4.4 Results and Discussion

### 4.4.1 Multi cycle semi-batch RO (SBRO) operation

In SBRO operation, as discussed in Sections 4.2.3, non-ideal flushing leads to progressive increase of successive filtration periods RO element feed water salinity until a stable cycle-to-cycle operation is reached (Table 4-1 and Fig. 4-10).

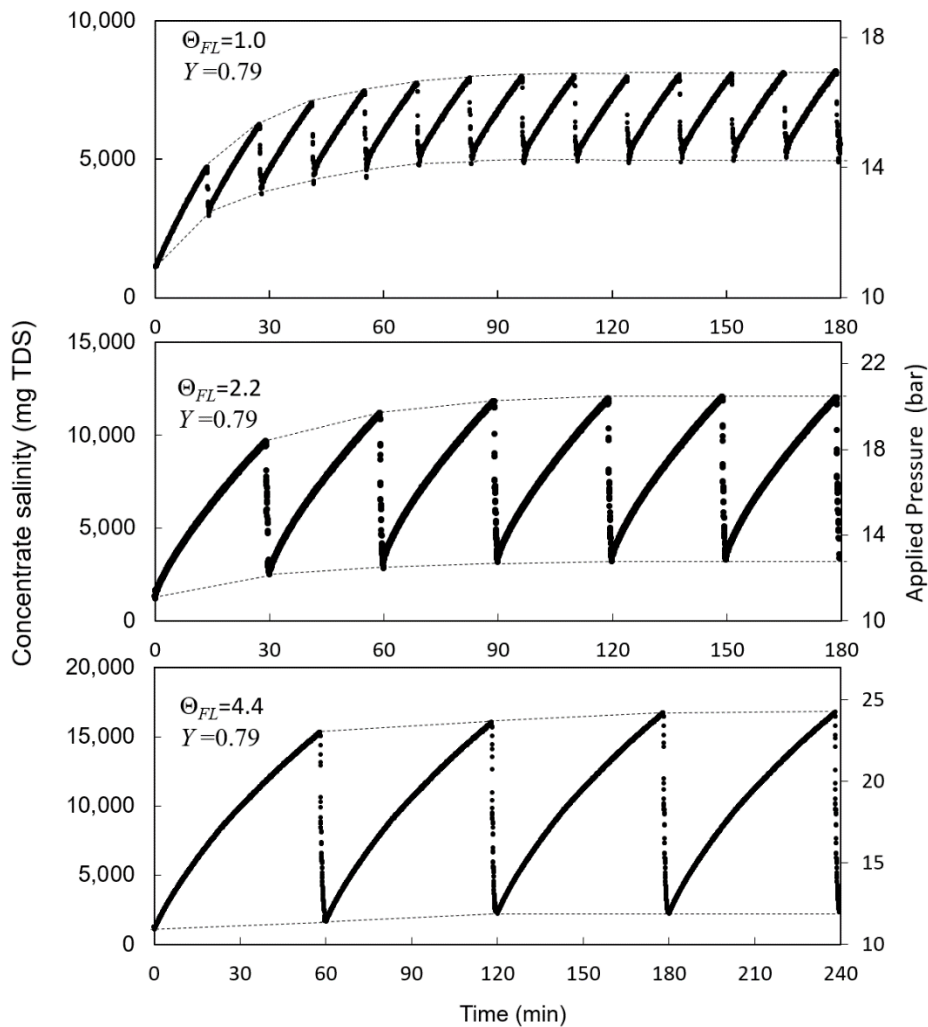


**Fig. 4-10.** Temporal profiles of SBRO concentrate stream salinity (mg/L TDS) at the RO element exit for cyclic SBRO at overall water recovery ( $Y$ ) of 79% (Runs #2d, 3d, and 4d; Table 4-1) for a fixed permeate ( $q_P$ ) and RO element feed ( $q_F$ ) flow rates (Table 4-1) and for flushing duration of  $\Theta_{FL} = 1, 2.2$  and 4.4. The dashed lines represent the element exit concentrate salinity at the beginning and end of each filtration cycle. Note: the RO element feed salinity is related to the exit element salinity as per  $C_F/C_C = (1 - Y_{SP}) / (1 - (1 - R_S)Y_{SP})$  (Section 4.2.2).

As summarized in **Table 4-1**, for the recovery range of 46%-79% and flushing duration in the range of  $\Theta_{FL}=1 - 4.4$ , the stable filtration period cycle-to-cycle salinity of the element feed and exit streams were all higher than their values at the initial (i.e., first) SBRO cycle. Complete flushing of the excess accumulated salt from the RO system was not attainable for a flushing period equal to the convective residence time ( $\Theta_{FL}=1$ ). For a given recovery (for the same raw feed water salinity and element crossflow velocity), lengthening of the flushing period required a longer filtration period.

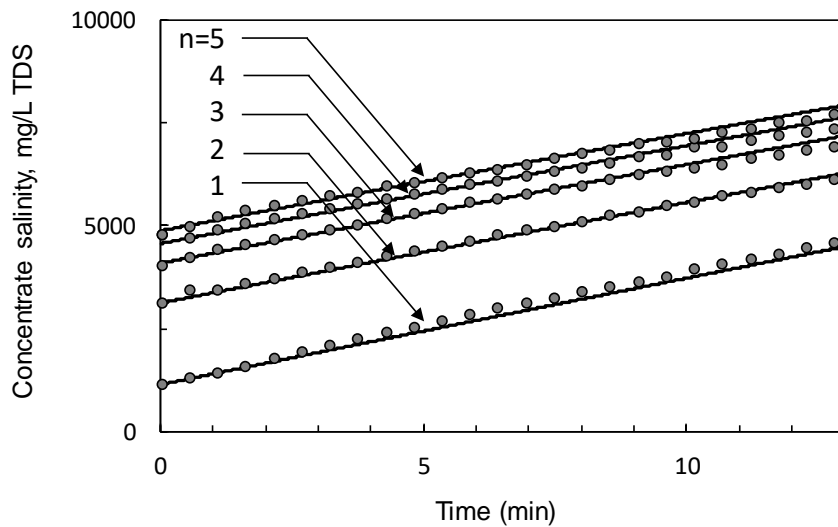


**Fig. 4-11.** Predictions (solid lines) and experimental data (filled circles) of salinity profile (as per Eq. (4-11)) during a filtration period for multiple cycles for Test Run #2d (**Table 1**) for SBRO operation at overall recovery of 79% and raw feed salinity of 1,000 mg/L TDS.

The progressive salinity rise of the RO unit feed and concentrate during the filtration period is illustrated in **Fig. 4-10**, for the conditions of Runs #2d, 3d, and 4d, (**Table 4-1**). Model predictions of the element exit salinity rise during the filtration periods (**Section 4.2.2**) closely match the experimental data as shown in **Fig. 4-11**. Correspondingly the applied pressure increases over the filtration duration and a lower applied pressure is required during the flushing period (**Section 4.4.2**). As shown in **Fig. 4-10**, the stable cycle-to-cycle concentrate salinity at the beginning and end of filtration period can rise significantly above those for the

initial (i.e., first) SBRO cycle. This is a consequence of incomplete flushing of the excess concentrate salinity from the system. With increased flushing duration, for a given target recovery, a longer filtration period is required and as a consequence a higher salinity at the filtration period end.

For the test conditions over the recovery range of  $Y = 0.46 - 0.79$ , the filtration period element feed and concentrate exit salinity of the stable cycle-to-cycle operation rose by factor of 1.8 – 4.2, 1.5 – 3.0, and 1.3 – 2.2 for  $\Theta_{FL}$  of 1, 2.2 and 4.4, respectively, relative to the initial SBRO cycle (i.e.,  $n=1$ ) (**Fig. 4-12**). As expected, for a given recovery, a longer flushing duration required a longer filtration period and, as a consequence, a greater rise in the filtration period salinity. Opting for a shorter flushing period, higher rise in the stable cycle-to-cycle filtration period RO unit salinity and thus higher SEC as discussed in **Section 4.2.5**. Clearly, a shorter flushing period is desirable, but even at the minimum flushing condition of  $\Theta_{FL}=1$  the concentrate salinity at the beginning and end of the filtration period increased significantly (e.g., by a factor of 6.9 and 2.4, respectively, for  $Y=0.79$  in run #2d) above those at the initial (i.e.,  $n=1$ ) cycle. As shown in the example of **Fig. 4-12 – 4-16**, for a fixed flushing duration of  $\Theta_{FL}=1$ , increased recovery necessitated a longer filtration period; this resulted in a higher stable cycle-to-cycle element exit concentrate salinity at the beginning and end of the filtration period by factors of 1.8 – 4.2 and 1.4 – 1.7, respectively, relative to the first cycle ( $n=1$ ) filtration period over the recovery range of  $Y = 0.46 - 0.79$ .

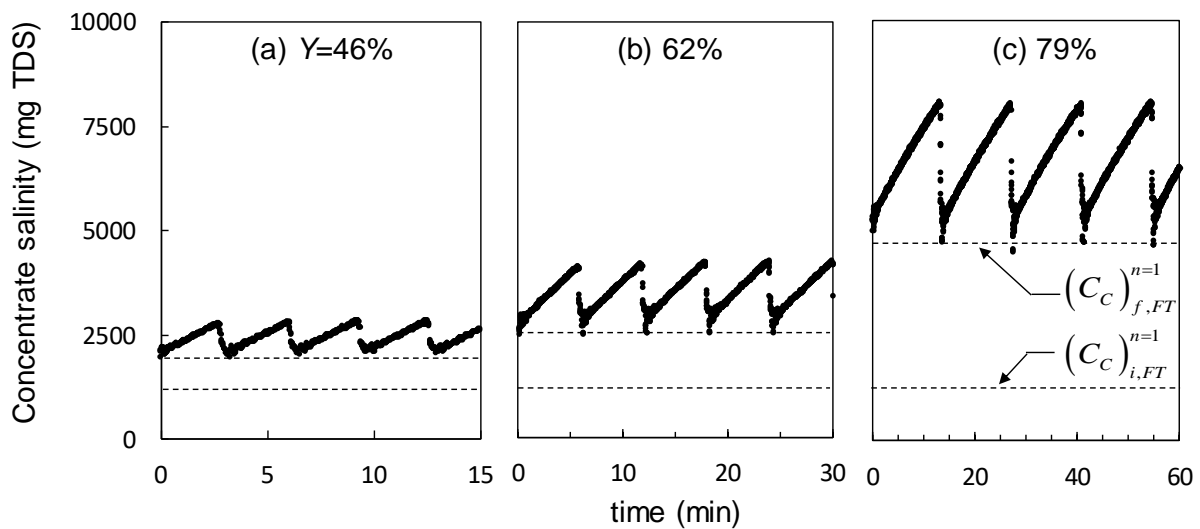


**Fig. 4-12.** SBRO concentrate salinity (mg/L, TDS) at the RO element exit for stable cycle-to-cycle SBRO operation for overall water recovery of 46%-79% and flushing period of  $\Theta_{FL} = 1$  (Runs 2a, 2b, and 2d, **Table 4-1**). The dashed lines indicate as a reference the salinity at the SBRO element exit at the filtration period beginning ( $(C_C)_{i,FT}^{n=1}$ ) and end ( $(C_C)_{f,FT}^{n=1}$ ).

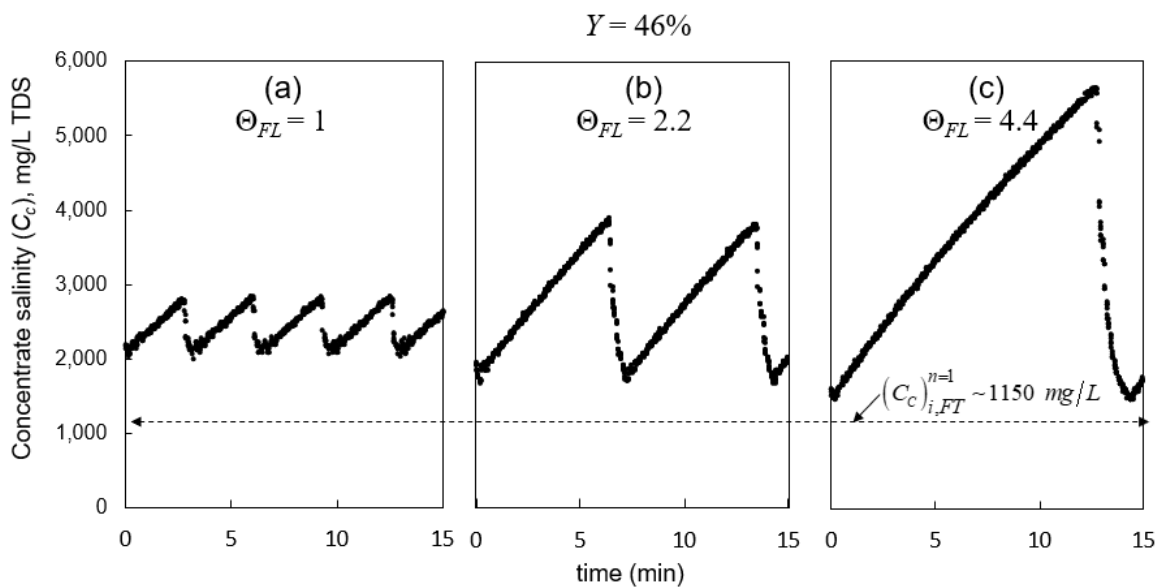


**Fig. 4-13.** Salinity of the concentrate exiting the RO unit ( $C_C$ ) in stable cycle-to-cycle SBRO operation for water recovery of 46 % and flushing durations of (a)  $\Theta_{FL} = 1.0$ , (b)  $\Theta_{FL} = 2.2$ , and (c)  $\Theta_{FL} = 4.4$ .

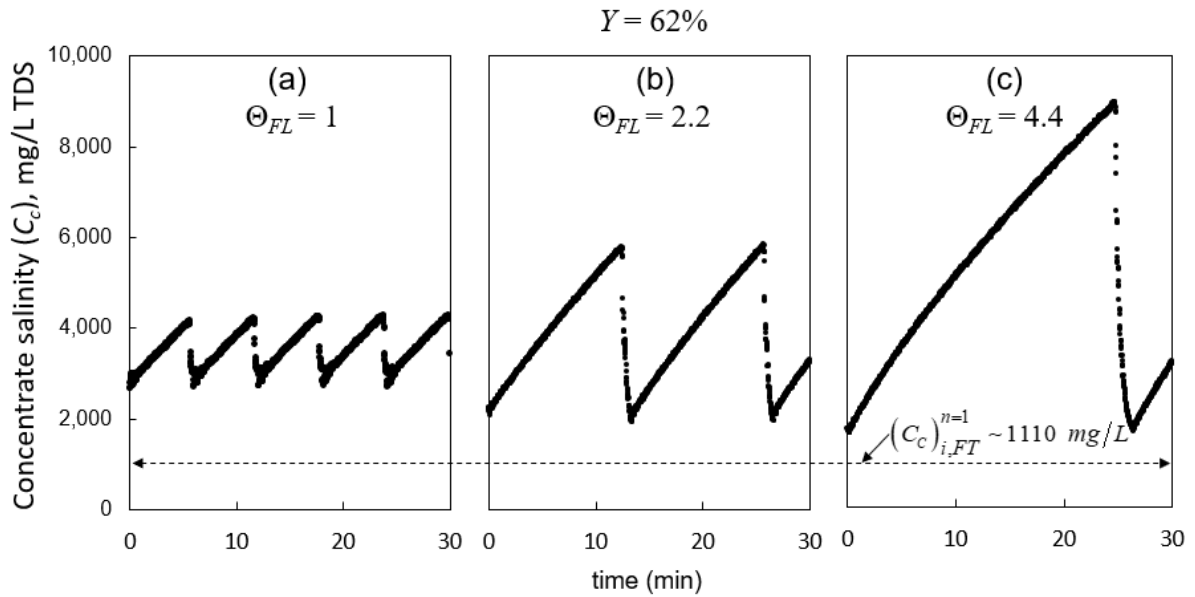


**Fig. 4-14.** Salinity of the concentrate exiting the RO unit ( $C_c$ ) in stable cycle-to-cycle SBRO operation for water recovery ( $Y$ ) of 62 % for flushing durations of (a)  $\Theta_{FL}=1.0$ , (b)  $\Theta_{FL}=2.2$ , and (c)  $\Theta_{FL}=4.4$ .

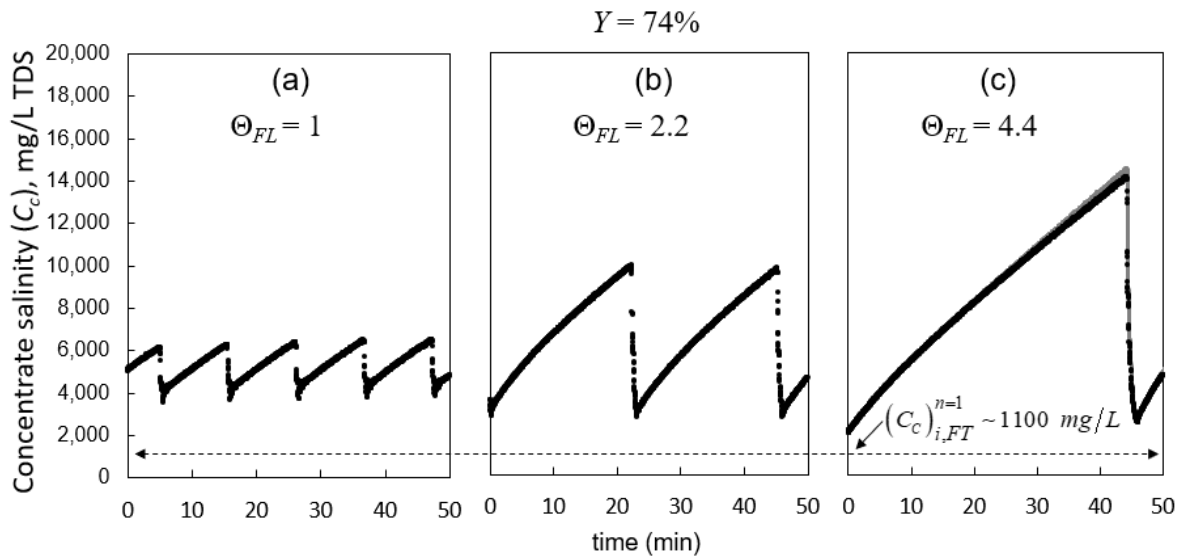


**Fig. 4-15.** Salinity of the concentrate exiting the RO unit ( $C_c$ ) in stable cycle-to-cycle SBRO operation for water recovery ( $Y$ ) range of 74% for flushing durations of (a)  $\Theta_{FL}=1.0$ , (b)  $\Theta_{FL}=2.2$ , and (c)  $\Theta_{FL}=4.4$ .



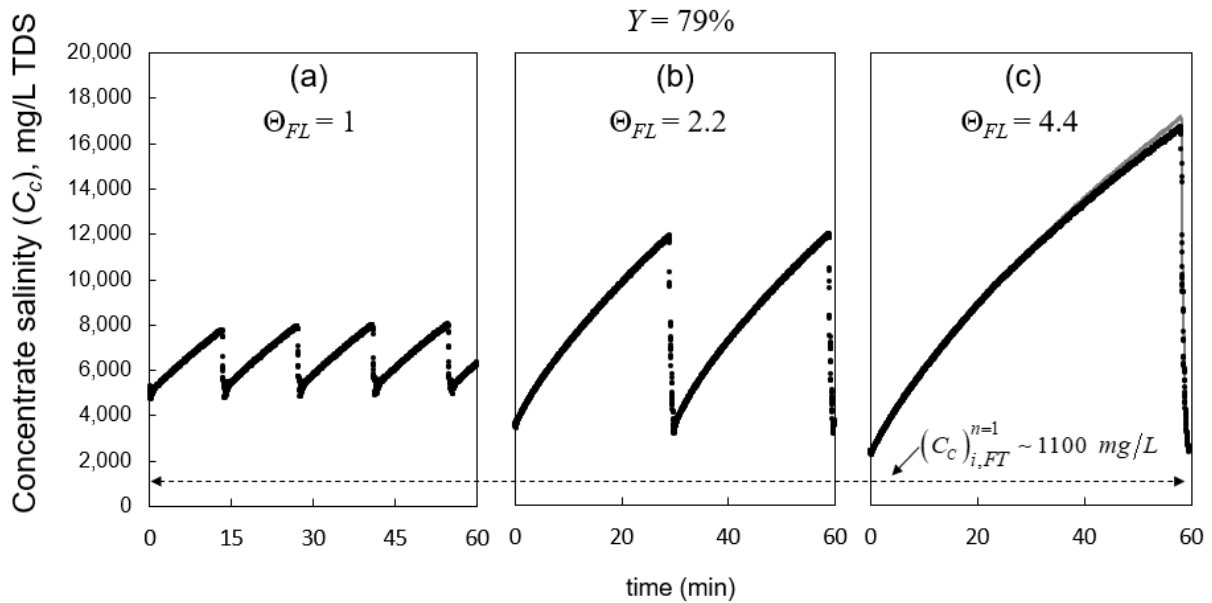


**Fig. 4-16.** Salinity of the concentrate exiting the RO unit ( $C_c$ ) in stable cycle-to-cycle SBRO operation for water recovery ( $Y$ ) of 79 % for flushing durations of (a)  $\Theta_{FL}=1.0$ , (b)  $\Theta_{FL}=2.2$ , and (c)  $\Theta_{FL}=4.4$ .

The cycle-to-cycle increase of the element inlet and exit salinity at the beginning of the filtration period in each cycle in the SBRO operation is due to incomplete flushing of the accumulated excess salt in the RO system. As shown in **Fig. 4-17**, it is clear that, in order to achieve complete flushing of the excess salt from the system (i.e.,  $F(\Theta_{FL})=1$ ), one would have to employ an impractically long flushing duration which would in turn lead to either a significant reduction in the overall recovery (see **Eq. (4-5)**) or an increase in the filtration duration (e.g., see **Fig. 4-2**). For the given flushing duration ( $\Theta_{FL} = 4.4$ ), the flushing efficacy, as shown in **Fig 4-17**, was nearly identical with variability of less than  $\pm 5\%$  over the test condition of the element exit concentrate salinity at the end of the filtration periods,  $(C_c)_{f,FT}$ , in the range of 5,578 – 16,770 mg/L TDS.

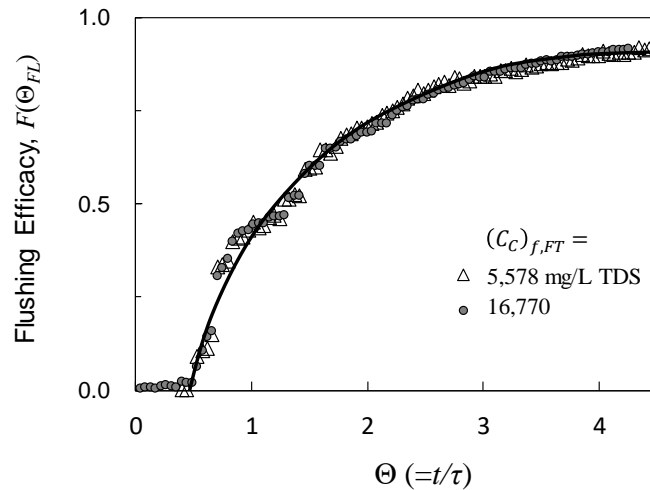


**Fig. 4-17.** Variation of the flushing efficacy  $F(\Theta_{FL})$  (Eq. (4-35), Section 4.2.3) with flushing time ( $\Theta=t/\tau$ , where  $t$  and  $\tau$  are the time and the convective residence time) in response to a change in SBRO operation from total concentrate recycle to a single-pass RO operation (i.e., SPRO) for raw feed salinity of 1,000 mg/L TDS. Note:  $F(\Theta_{FL})$  is shown for the cases of concentrate salinity at the SBRO element exit at the end of the filtration periods (i.e., prior to flushing) of 5,578 and 16,770 mg/L TDS.

The similarity of  $F(\Theta)$  over the range of test conditions, as shown in Fig 4-17, is not surprising given the expected similar impact of dispersion at the same flow rate employed for the tests listed in Table 4-1. The above suggests that given  $F(\Theta)$  function, for a specific SBRO system feed and permeate flow rates (i.e.,  $q_F$  and  $q_p$ , respectively), one can estimate the inlet and exit element salinities for the filtration and flushing periods over a wide recovery range (Eqs. (4-11) and (4-18)).

One may be tempted to argue that perhaps near ideal flushing under plug flow may be reached if an SBRO system can be designed such that dispersion is only of consequence in the RO element. However, dispersion studies (Fig. 4-18) with spiral-wound RO elements [44, 45] suggests that, complete concentrate flushing would have to be of duration significantly greater than the convective residence time (approximately by a factor of 2 – 4) for these RO elements. Moreover, achieving complete flushing of commercially deployable SBRO systems, within one convective residence time (or single holdup volume), would require having ideal plug-flow, without dispersion,

throughout the entire SBRO system (i.e., RO element and all relevant system hydraulic components). Accordingly, it is argued that for proper evaluation and comparison of the operation of SBRO systems, it is essential to compare the dispersion behavior via quantification of the effectiveness of excess concentrate flushing and its impact on the SEC as discussed in **Section 4.2.4**.

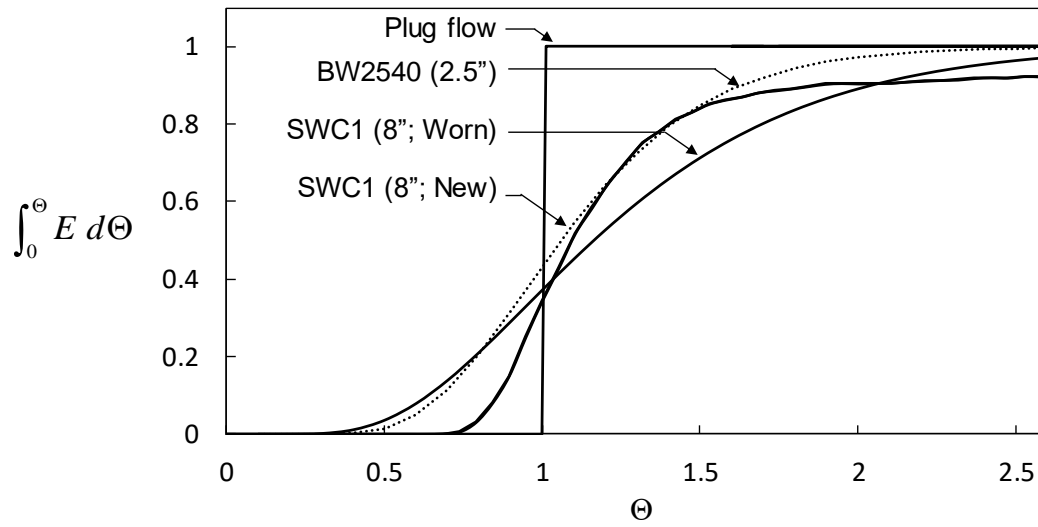


**Fig. 4-18.** Cumulative RTD function (**Section 2.3**) for spiral wound RO elements based on data reported in [44, 45] for 2.5” bench-scale (BW2530, FILMTEC) spiral wound RO elements in [44] and for 8” industrial module (SWC1, Hydronautics) in new and worn condition in [45] at cross flow velocity of about 4, 7, and 10 cm/s, respectively.

#### 4.4.2 Energy consumption

The SBRO performance data and model predictions demonstrated that SBRO operation is highly dependent on the post-filtration flushing efficacy. Incomplete excess salinity flushing (post-filtration) leads to progressive rise in the RO unit salinity (**Fig. 4-10**) until a stable cycle-to-cycle operation is reached and correspondingly a higher required applied pressure (**Figs. 4-19a-c**).

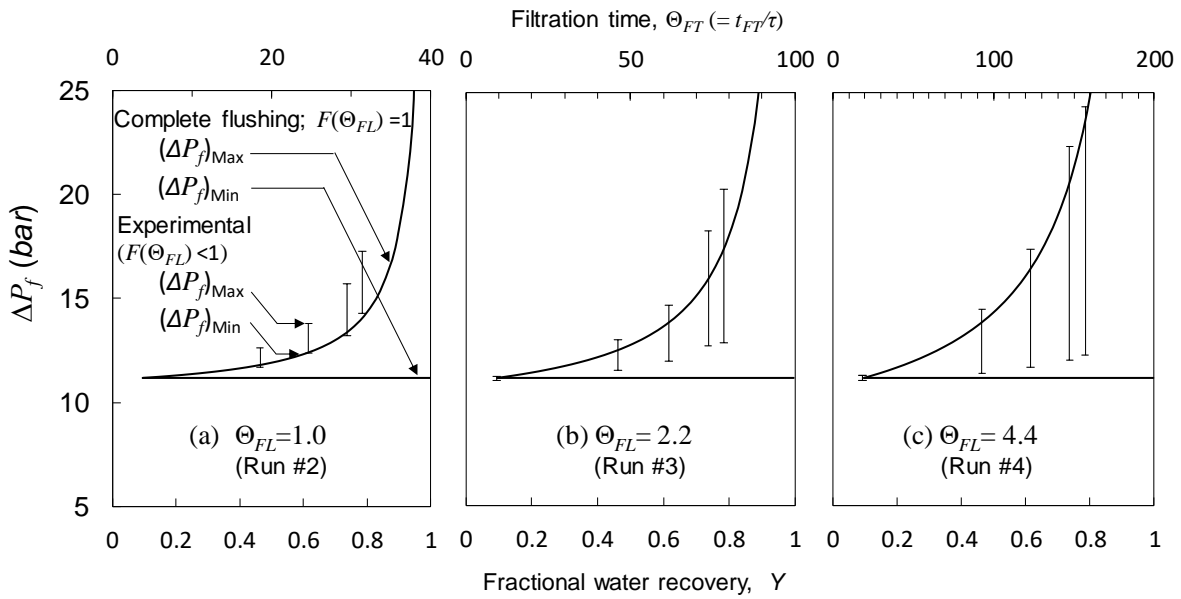


**Fig. 4-19.** The range of SBRO membrane element inlet applied feed pressure ( $\Delta P_f$ ) at different levels of overall water recovery ( $Y$ ) for flushing durations ( $\Theta_{FL}$ ) of (a) 1.0 (Run #1), (b) 2.2 (Run#2), and (c) 4.4 (Run #4) where the range of  $F(\Theta_{FL})$  values are provided in **Table 4-1**. The upper solid curve and horizontal solid line represent the applied pressure for ideal SBRO operation at the beginning,  $(\Delta P_f)_{min}$ , and end,  $(\Delta P_f)_{max}$ , of the filtration period, respectively; Note, ideal SBRO operation refers to complete flushing (i.e.,  $F(\Theta_{FL}) = 1.0$  as; **Eqs. (4-11), (4-25), and (4-28)**). Note: the upper horizontal axis provides the filtration time ( $\Theta_{FT}$ ) scale based on **Eq. (4-5)** for the indicated flushing duration.

Inter-cycle salt accumulation in the SBRO system is reduced with longer flushing and as a consequence the applied pressures, both at the beginning and end of the filtration cycle, for a given recovery, can approach the applied pressures for ideal SBRO operation (i.e.  $F(\Theta_{FL}) = 1.0$ ). However, the longer required filtration duration (to attain the target recovery) leads to increased energy consumption as is also evident from **Eqs. (4-23) and (4-26)**. The tradeoff, however, is that a longer filtration period is needed to achieve the set recovery; thus, a higher concentrate buildup necessitates the application of a greater applied pressure (i.e., above that of the ideal case; **Fig. 4-19a**). For example, at recovery of 79%, upon increasing the flushing duration from  $\Theta_{FL} = 1$  to 4.4 (i.e., by a factor of 4.4), the required filtration duration increased by a factor of 4.3 (i.e., from 13.4 min to 58 min).

The SBRO SEC required for the separation (i.e., desalination) accomplished in the RO element itself for the stable cycle-to-cycle operation is shown in **Fig. 4-20** for the operating conditions listed in **Table 4-1**. The above example provides the experimentally determined and model predicted element SEC based on **Eq. (4-29)**, in addition to the SEC for ideal SBRO operation (i.e., ideal flushing for which  $F(\Theta_{FL})=1.0$ ; **Eq. (4-14)**) and for SPRO RO (**Eq. (4-33)**). For a given recovery the SEC increases with increased flushing duration since the filtration period must also increase to attain the prescribed recovery. For the present SBRO system, the SEC is above that of SPRO operation. For example, as the overall recovery increases from 50% to 80%, the SEC for SBRO at  $\Theta_{FL}=1$  is about 6% and 16% greater, respectively, than for SPRO and correspondingly 9% and 29% above the SEC for SBRO with ideal flushing.

It is stressed that the above SEC analysis addresses only the fundamental aspect of the SBRO and SPRO separation process as afforded by the operational mode involving the RO elements. Admittedly, the efficiency of energy recovery can have a significant impact, particularly for operations at low single-pass recovery (**Eq. 4-29**). For example, the overall SBRO system SEC for the level of energy recovery of 90% achieved with the present small SBRO system, operating at 10% single-pass recovery, would be about twice that level that would be achieved with an ideal ERD (i.e.,  $\eta_{ER}=1$ ). Operating the same SBRO system but with sufficient elements for 50% single-pass recovery, at the same 90% level of energy recovery, would lead to a system SEC that is 10% higher than for SBRO with an ideal ERD. It is stressed that projections of the actual system SEC for desalination (as opposed to the element separations SEC) for practical/field deployable SBRO systems, as well as for various RO configurations, is challenging since pumps and ERDs efficiencies are likely to vary with the feed pressure, flow rate and recovery [10, 140].

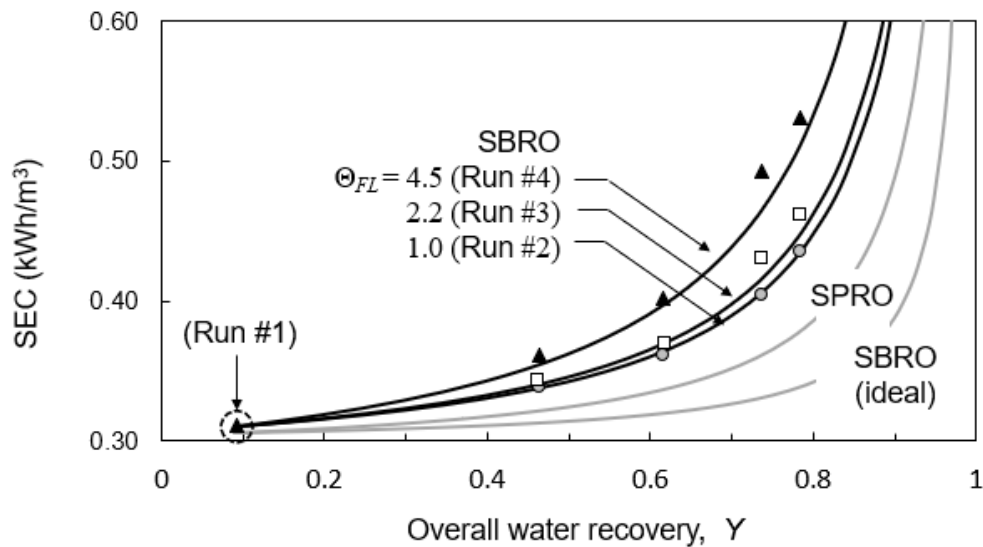


**Fig. 4-20.** RO element specific energy consumption (SEC) experimentally determined as per **Eq. (4-23)** (based on element feed pressure and normalized with respect to the raw-feed water osmotic pressure) as a function of overall water recovery ( $Y$ ) compared with theoretical predictions as per **Eq. (4-29)** at  $\Theta_{FL}=1.0, 2.2,$  and  $4.4$  with fixed salt rejection  $R_S=99.7\%$  and single pass water recovery  $Y_{SP}=9.2\%$ . The results were compared with theoretical predictions in **Eq. (4-33)** for single-pass RO (SPRO; [190]) as well as SBRO operation with ideal flushing of duration equal to the convective residence time (i.e.,  $F(\Theta_{FL})=1$  and where  $\Theta_{FL}=1.0$ ).

In theory, SBRO with ideal flushing would lead to measurably lower SEC than for SPRO. For example, the SBRO SEC for a system with a single pass water recovery of 9.2% would be about 3% and 13% below SPRO for 50% and 80% recovery. In reality, it is infeasible to achieve complete removal of the excess concentrate salinity from the SBRO system within a flushing time equivalent to the convective residence time (for an element flow rate identical for both the filtration and flushing periods). Clearly, the SEC for the SBRO operation will depend on the efficacy of concentrate flushing. Therefore, characterization of practical SBRO systems and their operation must be based on real-time monitoring of the applied pressure during both filtration and flushing periods applied starting with the initial cycle up to and including the condition of stable cycle-to-cycle operation. At the same time, in order to provide a complete characterization of the SBRO system, it is critical to provide the RO element concentrate and/or

feed salinity versus time profiles for over the filtration and flushing periods. Such information, when expressed in terms of the flushing efficacy (or residence time distribution or RTD), can form the basis for direct comparison of the operational characteristics of different SBRO and single-pass RO systems with or without partial concentrate recycling [190].

## **4.5 Summary**

The operation of semi-batch RO (SBRO) desalination was investigated via an operational model and laboratory studies with a focus on evaluating the efficacy of SBRO concentrate flushing and its impact on the specific energy consumption for desalination. SBRO operation was modeled considering progressive SBRO cycles consisting each of an operational period in total recycle mode (i.e., termed as “filtration” period), followed by a short flushing period to remove the excess concentrate salinity that has accumulated in the RO system. Model analysis and experimental data clearly showed that incomplete flushing would lead to increased SEC. Experimental tests over a wide range of product water recovery demonstrated, as expected, improved level of excess salinity removal with increased flushing duration. Longer flushing requires longer filtration duration, which in turn results in higher salinity buildup in the SBRO system and hence a higher SEC. The present small-scale SBRO system did not reveal the potential energy benefits of SBRO (as suggested in literature) relative to single-pass RO (SPRO) operation. However, it was shown that for SBRO operation with complete flushing, and for a duration equivalent to the system convective residence time, SBRO would indeed allow operation at a lower SEC relative to SPRO. The present work suggests, however, that in practical SBRO systems it may not be possible to achieve complete concentrate flushing within a period of one convective residence time. Therefore, in order to properly evaluate and compare

the effectiveness of SBRO systems it is imperative to quantify the efficacy of concentrate flushing by providing detailed data on the concentrate salinity profiles during both the flushing and filtration periods. Such information could then be used to extract the cumulative residence time distribution for unambiguous comparison of SBRO performance as well as determination of the desalination SEC energy based on the present modeling of SBRO cycles and direct measurements of the applied pressure. SBRO operation, while may provide advantages in some cases, depending on the ability of achieve high efficiency concentrate flushing, presents an operational flexibility, as does SPRO with partial recycle [190], in terms of attaining a wide range of recovery using a single system.



# **Chapter 5 Scaling Propensity in RO desalination with concentrate recycling**

## **5.1 Overview**

This chapter presents experimental data comparing mineral scaling propensity in SBRO and SSRO-PR operations using gypsum as a model scalant. Gypsum mineral scaling was quantified based on evolution crystal formation and growth on the membrane surface imaged by ex-situ direct observation membrane surface monitor (MeSuM) interfaced with a spiral-wound pilot scale RO system. Membrane surface image analysis enabled quantification of gypsum scaling kinetics in terms of both the number density of gypsum crystals and the extent of membrane surface scale coverage. Mineral scaling in SSRO-PR operation, at a given level of solution supersaturation, was compared to that in SBRO for operational scenarios at the equivalent time-averaged solution supersaturation, and also for operation at equivalent water recovery. The dissolution rate during the SBRO flushing period was determined in order to estimate the time scale necessary for complete removal of crystals at various size. Also, the growth rates of single crystals in both SBRO and SSRO-PR were evaluated based on the diffusion-growth model.

## **5.2 Introduction**

A comparative analysis of mineral scaling in SBRO versus conventional steady-state single-pass RO (SSRO-SP) was recently reported [48] in which the “membrane exposure time” to supersaturated scalant (calcite and gypsums) solution was compared to the “observed crystallization induction time”; the latter was extracted from data for nucleation/crystallization in solution without added seeds [95]. For SSRO-SP, the membrane exposure time (to the supersaturated solution) was taken to be the period between membrane cleanings (order of

months or longer, [198-200], while, for SBRO, the permeate production (filtration) period (~minutes to hours, [162, 166]) was considered as the relevant exposure time. It was then asserted that, under supersaturated feed water conditions in the membrane module (i.e., w.r.t the target scalant), the period of membrane exposure to the solution in SSRO-SP is likely to be longer than that in SBRO [48]. Given the above, it was argued that the propensity for surface scaling in SBRO can be reduced by maintaining the membrane exposure time to the supersaturated feed below the “crystallization induction time”; the latter was considered to be the nucleation induction time for crystallization in solution reported in [95]. Based on the above argument, it was proposed that for the same RO raw feed water and target water recovery, a lower degree of mineral scaling should be expected in SBRO relative to SSRO-SP.

It is important to note that, to date, experimental data have not been published on membrane mineral scaling to confirm the suggestion that mineral scaling propensity will be lower in SBRO relative to SSRO-SP. Moreover, the use of induction time obtained from crystallization in solution for gaging the propensity for membrane mineral scaling as reported in [48] is questionable given that the heterogeneous crystallization (on membrane surfaces and in the presence of seeds) induction time is significantly shorter, relative to the induction time for crystallization in solution, as documented in previous studies [73, 85, 95]. For example, for gypsum solution that is about 40-70% above saturation, the observed crystallization induction times in membrane scaling tests were in the range of 10 – 0.5 h [73] relative to 30 – 7 h reported for nucleation in a stirred vessel at ~60-85% above supersaturation [95]. High resolution SEM imaging of scaled RO membranes [85] revealed that mineral scaling can be traced to nanoscale crystals that appear to nucleate directly on the membrane surface. A later study reported that there was no clear evidence of a true crystallization induction time on RO membranes (in

single-pass operation) for solutions up to 70% above saturation for gypsum [84].

It should be acknowledged that nucleation is a stochastic process with a distribution of induction times which depends on the level of solution supersaturation [89]. It is often reported that crystallization in solution is governed by homogeneous nucleation above a threshold supersaturation level (with respect to the target mineral salt) while it is regarded as heterogeneous at higher levels of supersaturation [92, 95, 201]. Admittedly, the reported observed crystallization times, for a given operating condition, are likely to depend on the resolution of the employed detection method. Irrespective, of the actual value (or distribution) of induction times, it is irrefutable that the published data suggests that the “observed crystallization induction time” for heterogeneous nucleation (on either RO membranes or the presence of added seeds), as opposed to crystallization in solution (without added seeds), is the relevant induction time for assessing the onset of membrane mineral scaling in RO membrane desalination.

In order to optimize SBRO operation with the aim of achieving high recovery while avoiding the crippling impact of membrane mineral scaling, it is important to quantify membrane surface crystallization kinetics during repeated filtration-flushing cycles. Accordingly, an experimental study was undertaken of mineral scaling under SBRO operation, relative to SSRO-PR (**Section 0**) in which a direct real-time membrane surface imaging was employed (**Section 5.3.3**) to detect the onset of membrane scaling.

## 5.3 Experimental

### 5.3.1 Materials and solution

Scaling experiments were carried out in which calcium sulfate dihydrate ( $\text{CaSO}_4 \cdot 2\text{H}_2\text{O}$ ; i.e., gypsum) was used as the model scalant (**Table 5-1**). The test solutions were prepared by dissolving equimolar amounts (8 mM) of reagent grade  $\text{CaCl}_2 \cdot 2\text{H}_2\text{O}$  and  $\text{Na}_2\text{SO}_4$  (Fisher Scientific, ACS grade, Pittsburgh, PA) in deionized (DI) water in a 757 L (200 gal) polyethylene feed tank, stirred by a mechanical mixer. The solution pH was adjusted to 7.0 by addition of HCl or NaOH. The level of gypsum supersaturation was quantified in terms of the saturation index,  $SI_g = (Ca^{2+})(SO_4^{2-}) / K_{SP}$ , where  $K_{SP}$  is the solubility constant for gypsum at chemical equilibrium,  $(Ca^{2+})$  and  $(SO_4^{2-})$  are the calcium and sulfate ions activities in solution, respectively.

**Table 5-1.** RO Feed solution

Analytes	Concentration (mg/L)
$\text{Na}^+$	367
$\text{Ca}^{2+}$	320
$\text{Cl}^-$	566
$\text{SO}_4^{2-}$	767
TDS <sup>(a)</sup>	2020
$SI_g^{(b)}$ (at 25°C)	0.4
pH	7.0

(a) TDS: Total dissolved solids; (b)  $SI_g$ : gypsum saturation index

The feed to the RO system was maintained at  $25 \pm 1^\circ\text{C}$  using a copper-brazed heat exchanger and a recirculating chiller (VWR Scientific 1171-P, Radnor, PA). The RO system housed a single spiral-wound element measuring 2.5 inch in diameter and 40-inch in length

(CSM RE-2540-BE; Toray Chemical Korea Co., Seoul, Korea) having a 2.5 m<sup>2</sup> active membrane surface area, average water permeability of 2.4 L/m<sup>2</sup>·h·bar (measured at operating pressure of 10 bar), and salt rejection of 99.5% determined using a ~2,000 mg/L NaCl solution at 25 °C and 15 bar [148].

### 5.3.2 Spiral wound RO system for SBRO and SSRO-PR operations

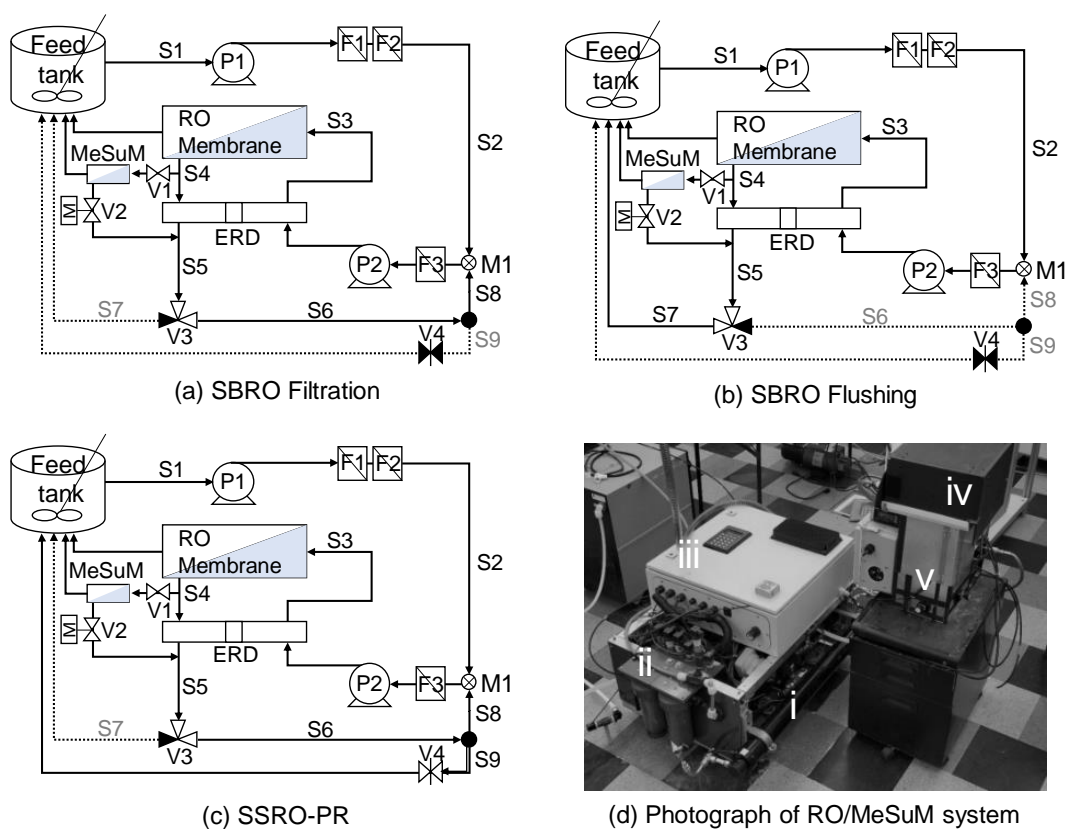


**Fig. 5-1.** Schematic of the experimental setup, for the RO system and the membrane scaling tests that utilized a membrane surface monitoring (MeSuM) system, for the operational modes of: (a) SBRO filtration, (b) SBRO flushing, and (c) SSRO-PR desalting. Streams S1 and S2 are the raw feed streams before and after filtration pretreatment, respectively; S3 and S4 denote the RO element feed and concentrate streams, respectively; streams S6 and S7 are those of the concentrate recycle and discharge, respectively; and stream S9 is the discharged flow portion of concentrate stream S6 during SSRO-PR operation, (d) pilot scale RO system and MeSuM with i) single spiral-wound element in a pressure vessel, ii) pre-treatment cartridge filters, iii) system controls and data acquisition/processing, iv) dark chamber for plate-and-frame membrane cell, v) imaging system.

Scaling tests were conducted using a pilot-scale flexible spiral wound RO system (FLERO; detailed in [190]) that could be operated in the modes of either steady-state RO with partial concentrate recycle (SSRO-PR) or SBRO (i.e., total concentrate recycle during the filtration period with periodic automated flushing). Briefly, the RO system, configured with a brackish water single spiral wound RO element (**Section** Materials and solution), had a permeate production capacity of up to 1.5 m<sup>3</sup>/d (400 gpd) for brackish water of salinity up to 5000 mg/L. Prior to entering the RO system, the raw-feed water was pretreated with cartridges filters of sizes 20, 5 μm (cellulose pleated 2-1/2”x10”, Ocean Link Inc., Portsmouth, RI; F1 and F2, respectively on **Fig. 5-1**).

The pretreated raw feed stream (S1, **Fig. 5-1**) was mixed with a portion of the RO concentrate stream (S8) at the mixing point (M1) to form the RO element feed water. The RO element feed was further pretreated by 0.2 μm plastic filter (Polysulfone Plastic, Harmsco, North Palm Beach, Florida, F3 in **Fig. 5-1**) in order to remove undissolved residue or impurities from entering the membrane module. The feed water was pressurized and conveyed to the RO element using a combination of positive displacement vane pump (Mag Drive, PROCON Products, Smyrna, TN, P2 in **Fig. 5-1**) and a hydraulic pressure intensifier pump (Clark Pump, Spectra Watermakers, San Rafael, CA, ERD in **Fig. 5-1**) which provides an energy recovery function.

The RO element feed and exiting concentrate pressures were monitored using in-line pressure transducers (Type S-20 4-20 mA, Wika, Klingenberg, Germany). The volumetric flow rates of the RO element feed ( $q_F$ ) as well as that of the permeate ( $q_P$ ) were measured by in-line flow transmitters (Signet 8550, George Fischer Signet, Inc. El Monte, CA), and controlled by the pump's DC speed controller (Model NEMA 4X, DART Controls, Zionsville, IN). Electrical

conductivities (*EC*) of the raw feed, membrane element feed, RO concentrate, and permeate streams were monitored with in-line *EC* sensors (Signet 2850, George Fischer Signet, Inc. El Monte, CA) to determine salinity in each stream. Programmable Automation Controller (PAC) served for data acquisition of all sensor measurements and automated control of all actuated valves and system pump. It is noted that the 3-way valve, V3 (**Fig. 5-1**) served to set the system operation for filtration or concentrate flushing, valve V2 enabled control of the membrane monitoring system, and in-line needle valve V4 (ARO 1/2" 104104-N03, Bryan, Ohio) established the level of partial concentrate recycle in SSRO-PR operation.

### **5.3.3 Membrane Surface Monitor**

The ex-situ Membrane Surface Monitoring (MeSuM) system consisted of a plate-and-frame RO membrane cell (**Fig. 5-2**) with a transparent acrylic block in which the feed channel was engraved with a channel height of 2.5 mm, width 2.25 cm and length 5.0 cm and specialized lighting arrangement and optics with a high-resolution imaging (**Fig. 5-2**). The system construction followed the general principles of the UCLA ex-situ scale observation detector (EXSOD) described in-depth elsewhere [51, 75, 100, 202]. The feed pressure was monitored by a pressure transducer (Model Type S-10, Wika, Klingenberg, Germany), permeate flux was measured using a digital flow meter (SLI-2000, Sensirion, Staefa ZH, Switzerland), permeate conductivity was monitored with an on-line conductivity meter (PCS-54, HM Digital, Redondo Beach, CA), pH was measured with a pH meter (Model pH 110, Oakton Research, Vernon Hills, IL), and volumetric flow rate of the brine stream controlled by hydraulic valve actuator (MCJ-050AB, HANBAY, Virginia Beach, VA) was measured with a flow transmitter (McMillan flow 101-7, McMillan Company, Georgetown, TX).

For real-time optical monitoring of the surface of the membrane coupon (on the retentate side), a charge-coupled device (CCD) camera (Dino-Lite Pro AD4113TL-FVW, Torrance, CA) was installed on top of a XY table (drylin SHT-XY-12 Linear module, Igus, East Providence, RI) for precise and reproducible positioning of the camera along the leadscrew system. The membrane cell and the camera module were enclosed in a black nylon polyphenylene oxide (PPO) and aluminum casing, respectively, to prevent interference from external lighting (**Fig. 5-2c**). A PC based data acquisition system was utilized to allow real-time process monitoring and data recording from the MeSuM system (**Fig. 5-3**).



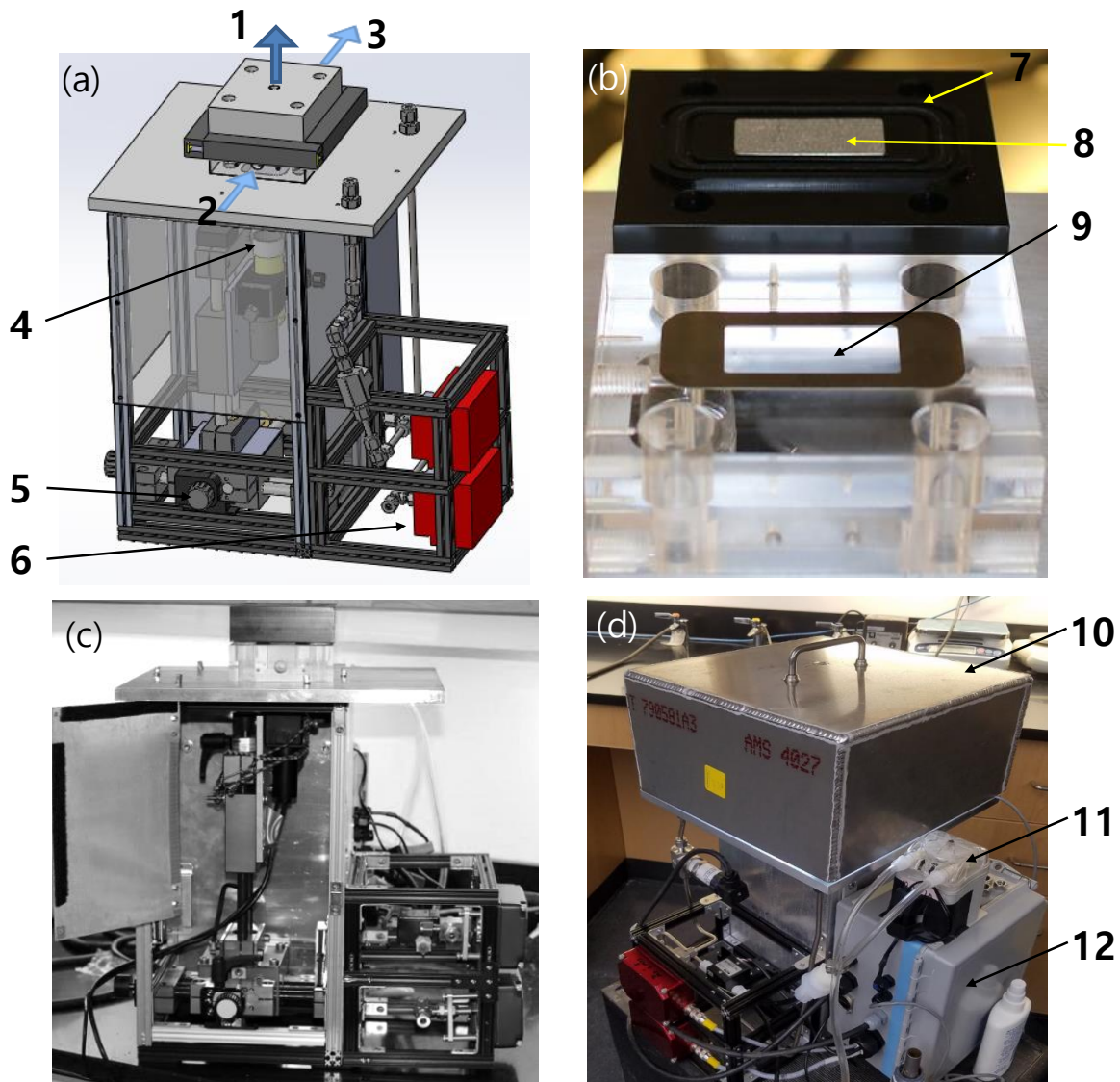


**Fig. 5-2.** Membrane Surface Monitoring system (MeSuM) (a) 3-D design of the membrane cell with 1) permeate port, 2) feed port, 3) concentrate port, 4) a digital camera, 5) 3D slide table, 6) the mechanical valve, V2 (**Fig. 5-1**), (b) photograph of the plate-and-frame acrylic membrane cell blocks with 7) o-ring, 8) and stainless steel plate spacer, and 9) engraved feed channel, (c) photograph of the assembled MeSuM system, and (d) photograph of the system with 10) the stainless-steel dark cover, 11) peristaltic pump for DI water flushing, and 12) electrical box.

MeSuM receives a high-pressure retentate (i.e., concentrate) side-stream from the RO spiral-wound element exit spiral (**Fig. 5-1**). The crossflow velocity in the membrane monitoring cell was adjusted via valve **V2** (**Fig. 5-1**), and given the negligible pressure drop in the MeSuM its

feed pressure was essentially equivalent to the feed pressure at the RO element exit. The MeSuM membrane surface ( $SI_{g,m}$ ) was determined, for the given operating conditions, based on the computational fluid dynamic model for the plate-and-frame flow channel previously described [47] along with detailed quantification of concentration polarization. The MeSuM operation was set to match the  $SI_{g,m}$  values at the element exit and in the MeSuM surface imaging location by adjustment of the crossflow velocity.

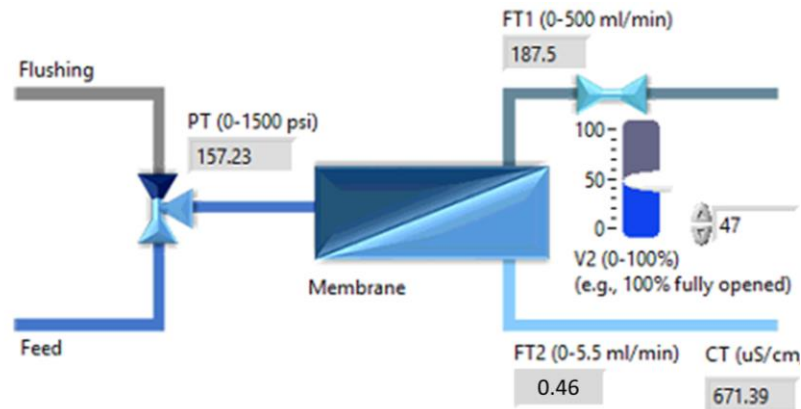


**Fig. 5-3.** Graphical user interface on the Membrane Monitoring system.

The size and number density of surface scale crystals, in the observation region (0.79 cm×0.63 cm), located 1 cm from the channel exit, were determined by specialized image analysis software (ImageJ, v1.52a, 2019) for membrane surface images captured at predetermined time intervals (typically 5-15 minutes). With the current resolution of surface imaging, surface crystals of initial areas in the range of 40 – 80  $\mu\text{m}^2$  were identified and outlined. Subsequently, the crystal number density and area of each crystal ( $A_s$ ) were calculated. Tracking the growth of individual gypsum crystals was carried out for crystals that did not overlap with neighboring crystals over the period of growth being tracked (up to ~10% surface scale coverage). The employed surface imaging system was at a resolution that precluded imaging of nanoscale nuclei and thus the determined rate of crystallization does not reflect real-

time rate of nucleation. However, the approach provides the observed rate of crystal appearance on the membrane surface and surface coverage by gypsum scale which was determined via the image subtraction method described in [75].

### 5.3.4 Gypsum scaling experiments

The overall system water recovery for semi-batch RO (SBRO) operation is defined as  $Y = V_p / V_o$  where  $V_p$  and  $V_o$  are the total volume of produced permeate and supplied raw feed water, respectively. Considering constant permeate productivity both in the RO filtration and the flushing periods (**Fig. 4-1**), the overall SBRO recovery can be written in terms of the filtration and the flushing durations ( $t_{FT}$  and  $t_{FL}$ , respectively) as  $Y = \left( \int_0^{t_{FT}} q_p dt + \int_{t_{FT}}^{t_{FT}+t_{FL}} q_p dt \right) / \left( \int_0^{t_{FT}} q_o dt + \int_{t_{FT}}^{t_{FT}+t_{FL}} q_o dt \right)$ , in which  $q_p$  and  $q_o$  are the permeate and the raw feed flow rates, respectively. Accordingly, the overall recovery ( $Y$ ) in SBRO is governed by the ratio of the durations of  $t_{FT}$  to  $t_{FL}$  and the single-pass system recovery ( $Y_{SP}$ ) as given by the following expression:

$$Y = \left( Y_{SP} \cdot (t_{FT} / t_{FL}) + Y_{SP} \right) / \left( Y_{SP} \cdot (t_{FT} / t_{FL}) + 1 \right) \quad (5-1)$$

In the present study, the concentrate flushing period (100 s) was a factor of ~3 longer than the system convective residence time (i.e.,  $\tau = V/q_F$  in which  $V$  and  $q_F$  are the vessel volume and membrane module feed flow rate, respectively). The above flushing period was selected based on a reasonable tradeoff between reaching the desired range of recovery and flushing efficiency which in the present work allowed the stable cycle-to-cycle operation to be reached within 2-3 filtration/flushing cycles. SBRO operation was facilitated by controlling the three-way solenoid valve V3 (**Fig. 5-1**) in order to shift the operating modes between filtration to flushing (**Fig. 4-1**). During the SBRO filtration period (**Fig. 5-1a**), V3 was set to allow the concentrate

stream (S8) to continuously mix with the pre-treated raw feed water stream (S1). At the filtration period termination, concentrate flushing was initiated by setting V3 to discharge the concentrate stream to the feed tank (**Fig. 5-1b**). In SSRO-PR operation, valve V3 was set to recycle the concentrate stream (S5) from the membrane module to mix (at mixing point M1) with the pretreated raw feed stream (S2), and concentrate recycle level controlled by valve V4 (**Fig. 5-1c**). The overall water recovery ( $Y$ ) for SSRO-PR is given by  $Y = Y_{SP} \cdot (1 + R)$  (**Eq. (3-2)**), in which the recycle ratio is defined as  $R = q_R / q_o$  where  $q_R$  and  $q_o$  are the flow rates of the concentrate recycle and the raw-feed streams, respectively. Scaling tests for both SBRO (filtration and flushing periods) and SSRO-PR operations were carried out at a crossflow velocity of 15 cm/s and RO element feed flow (i.e., equivalent to  $q_F = 8.9$  L/min). The above crossflow velocity was within the range of recommended operating condition for the present membrane element (22 – 29 L/m<sup>2</sup>·h [148]).

Following the approach in [100], the calcium ion concentration in the concentrate stream was determined by correlating the electrical conductivity with the calcium ion concentration, for the present solution of equimolar calcium and sulfate ions. The correlation was derived based on simulation results from a multi-electrolyte thermodynamic simulator [188] for different levels of the feed solution (**Table 5-2**) concentration factors. The resulting relationship for the calcium ion concentration,  $[Ca^{2+}]$  (M), was expressed as  $[Ca^{2+}] = (EC / 160)^{1.25}$ , in which  $EC$  is the solution conductivity (mS/cm). The gypsum saturation index (**Section 5.3.1**), was correlated with the calcium ion concentration as  $SI_g = 62.1 [Ca^{2+}] - 0.125$ . The above correlations, which are consistent with previous work [100], are applicable to  $SI_g$  range of 0.35 – 3.5 and calcium ion concentration range of 7 – 57 mM which are the relevant ranges in the present study.

Consistent with earlier work [190],  $(SI_{g,m})_{exit}$  was obtained given the bulk calcium concentration of the RO concentrate and its calculated value at the membrane surface based on the concentration polarization correlation for the spiral-wound membrane element [148]. Accordingly, the concentration polarization modulus ( $CP$ ) was determined from  $CP = (C_m / C) = \exp(0.7Y_{SP})$ , in which  $C$  and  $C_m$  denote the solute concentration in the bulk and at the membrane surface, respectively.

**Table 5-2.** Experimental conditions

Run	Operating mode	Overall Water Recovery $Y$ (%)	Filtration time, $t_{FT}$ (min)	Recycle Ratio, $R$	Concentrate stream (at RO element exit)	
					$(SI_{g,m})_{exit}$ Average (range)	TDS (mg/L)
1a	SBRO <sup>(a)</sup>	40	9	NA	1.2 (0.73 – 1.7)	2700 – 5500
1b		50	14.3		1.6 (0.86 – 2.4)	3100 – 7700
1c		55	17.7		1.9 (0.99 – 2.8)	3600 – 8900
2a	SSRO-PR	50	NA	4.3	1.2	4100
2b		60		5.3	1.6	5300
2c		65		5.8	1.9	6000

Note: all experimental runs were carried out at a crossflow velocity of 15 cm/s and RO element feed flow rate. The system convective residence time was ~33 s, and the permeate flux was maintained at 19.7 L/(m<sup>2</sup>·hr) (equivalent to permeate flow rate of  $q_P = 0.82 \pm 0.1$  L/min) achieving a single pass water recovery of ( $Y_{SP}$ ) of 9.5%.

Scaling tests were carried out for different levels of time-average  $SI_g$  at the membrane surface at the element exit (i.e.,  $(SI_{g,m})_{exit}$ ). The  $(SI_{g,m})_{exit}$  range of 1.2-1.9 (in **Table 5-2**) were set by the overall recovery given that all tests were maintained at the same RO element feed flow rate. For SBRO these  $(SI_{gm})_{exit}$  are the time-averaged values over the filtration period during which  $(SI_{g,m})_{exit}$  ranged from 0.73 – 2.8 over the range of recovery of 40-55% achieved with filtration time of 9-17.7 min and flushing period of 100 s. Prior to each scaling experiment, the spiral wound RO system (either in SSRO-PR or SBRO modes) along with the interfaced

MeSuM unit were conditioned for 30 min by pumping the model feed solution (**Table 5-1**) through the system without concentrate recycling at a feed flow rate ( $q_F$ ) of 8.9 L/min and feed pressure of ( $P_f$ ) of 10 bars. For both the SBRO and SSRO-PR tests, at the termination of each scaling test, the system was completely cleaned by circulating DI water through the system channel for 30 min at a flow rate 8.9 L/min and 3 bar feed pressure.

## 5.4 Result and discussion

### 5.4.1 Operation of SBRO and SSRO with partial concentrate recycle

The variation of the average concentration of a given solute (as well as salinity in terms of TDS) in the membrane module,  $C_b$ , during filtration in SBRO operation (**Fig. 4-1**) can be assessed from the following solute material balance:

$$V \frac{dC_b}{dt} = q_o C_o - q_p C_p \quad (5-2)$$

where  $C_o$  and  $C_p$  are the solute concentrations in the raw-feed and the permeate streams, respectively, and  $t$  is the filtration duration. Given the approximation of  $C_b = (C_F + C_C)/2$ , where  $C_F$  and  $C_C$  are the concentrations at the element entrance and exit, respectively, and considering an ideal membrane (i.e., 100% salt rejection, it can be shown that and  $C_b = [(2 - Y_{SP})/2] C_C$ . **Equation (5-2)** can be written in terms of the solute concentration at the element exit as  $dC_C^*/d\Theta = 2Y_{SP}/(2 - Y_{SP})$ , in which  $C_C^*$  is the dimensionless solute concentration ratio of the concentrate to that of the raw feed (i.e.,  $C_C^* = C_C/C_o$ ), and  $\Theta$  is the dimensionless time (i.e., **Section 5.3.4**). Therefore, given  $C_C^*$  at the beginning of a given filtration period, i.e.,  $(C_C^*)^o$ , **Eq. (5-2)** can be solved to provide the following expression for

$C_C^*$  as a function of  $\Theta$ , given by:

$$(C_C^*) = 2Y_{SP}/(2 - Y_{SP}) \cdot \Theta + (C_C^*)^o \quad (5-3)$$

The solute concentration, at the end of the SBRO filtration period ( $\Theta = \Theta_{FT}$ ),  $(C_C^*)^f$ , can be obtained from **Eq. (5-3)** as  $(C_C^*)^f = 2Y_{SP}/(2 - Y_{SP}) \cdot \Theta_{FT} + (C_C^*)^o$ . It is noted that the overall water recovery,  $Y$ , in SBRO is governed by the attainable single-pass RO train recovery ( $Y_{SP}$ ) and the ratio of filtration/flushing durations ( $\Theta_{FT}/\Theta_{FL}$ , **Eq. (5-1)** in **Section 5.3.4**). At the end of the filtration period, the solute concentration at the membrane surface (at the element exit),  $(C_{C,m}^*)^f$ , can be determined by incorporating the concentration polarization modulus ( $CP$ , **Section 3.3.3**) in **Eq. (5-3)**, as expressed below:

$$(C_{C,m}^*)^f = CP \left[ 2Y_{SP}/(2 - Y_{SP}) \cdot \Theta_{FT} + (C_C^*)^o \right] \quad (5-4)$$

Given **Eq. (5-4)** and the correlation for the  $SI$ -scalant ion concentration (**Section 5.3.4**), the scalant  $SI$  at the membrane surface at the element exit,  $(SI_{g,m})_{exit}$ , at the beginning and end of the filtration period,  $(SI_{g,m})_{exit}^o$  and  $(SI_{g,m})_{exit}^f$ , respectively, can be obtained. For example, the surface saturation level (at the element exit at the membrane surface) during the filtration period can be obtained as  $(SI_{g,m})_{exit} = 62.1 \left( CP \cdot C_O \cdot \left[ 2Y_{SP}/(2 - Y_{SP}) \Theta + (C_C^*)^o \right] \right) - 0.125$  based on  $SI$ -calcium ion concentration correlation (**Section 5.3.4**). The above analysis predicts increased solute supersaturation at the membrane surface with increased overall recovery as illustrated in **Fig. 5-5**), and with a prolonged flushing period at a given recovery (**Fig. 5-4**). The above behavior is expected given the requirement of a longer filtration period to achieve the target recovery with increased flushing duration.

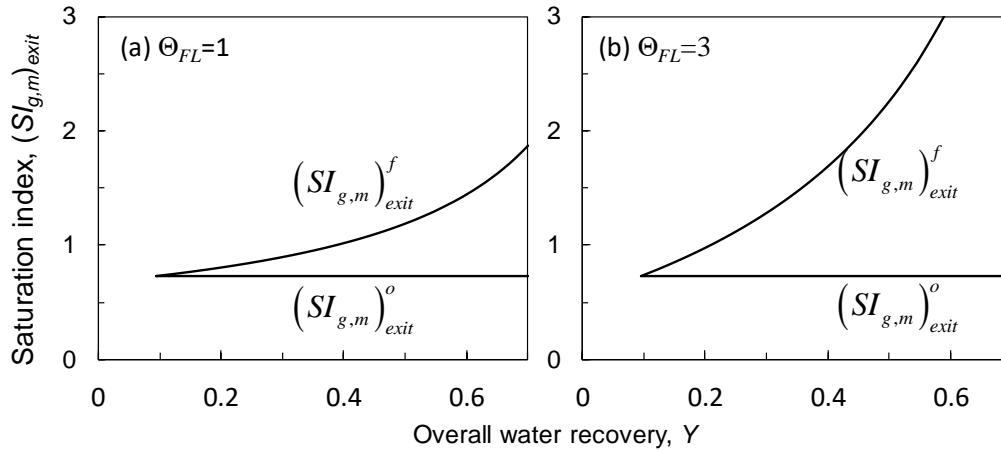


**Fig. 5-4.** Prediction of gypsum saturation index at the membrane surface (at the element exit), at the end of a filtration period, i.e.,  $(SI_{g,m})_{exit}^f$ , for the raw feed solution of  $SI_g=0.4$  (**Table 5-1**) and at a given  $(SI_{g,m})_{exit}^o$  of 0.73 (same as test condition #1a, **Table 5-2**) at the beginning of the filtration period in stable SBRO operation with flushing periods of (a)  $\Theta_{FL}=1$  and (b)  $\Theta_{FL}=3$  for an element single-pass recovery of  $Y_{SP}=9.5\%$ .

In SBRO operation, the concentrate salinity, RO element feed pressure and saturation level for gypsum at the membrane surface, as quantified by the saturation index  $SI_{g,m}$ , all increased over the filtration period as the concentrate stream was continuously recycled (**Table 5-2**, **Fig. 5-5** and **Fig. 5-6**) For SBRO operation with the raw feed solution salinity of 2,020 mg/L TDS the membrane surface gypsum saturation index,  $SI_{g,m}$ , at the RO element exit increased over the filtration period to values up to 1.7, 2.4 and 2.8, for the target overall water recovery of  $Y=40\%$ ,  $50\%$  and  $55\%$ , respectively (**Fig. 5-5**, **Table 5-2**). The time-average  $SI_{g,m}$  values for the above conditions were in the range of 1.2-1.9. During the flushing period the SBRO operated in single-pass mode (i.e., without concentrate recycle) and thus both the concentrate salinity (**Fig. 5-6**) and  $SI_{g,m}$  (**Fig. 5-5**) decreased over the flushing period to below saturation. At the stable cycle-to-cycle SBRO operation both the element concentrate salinity and  $SI_{g,m}$  were consistently reset by the end of the flushing period to the same values at the beginning of the filtration period.



It is important to recognize that the volume of raw feed water supplied to the RO system during the flushing period was upto 3-fold higher than the system holdup volume itself (i.e., equivalent to residence time being 3 times the convective residence time). Yet, the  $SI_{g,m}$  level (at the RO element exit; **Table 5-2**) remained a factor of 1.8-2.5 above the raw feed water  $SI_g$  of 0.4 (**Table 5-1**) at the beginning of the filtration period (i.e.,  $SI_{g,m}=0.73-0.99$ , **Table 5-2**) in multi-cycle SBRO operation. The above behavior is attributed to solute accumulation in the RO system (over the period leading to the stable cycle-to-cycle operation) indicating that complete concentrate flushing could not be attained even with the above reasonably long flushing period. It is noted that, the flushing duration can be further increased to reset the element feed salinity (and thus saturation level with respect to the mineral scale precursors) to the initial condition at the initial SBRO cycle (i.e.,  $t=0$ ). However, a longer flushing period would necessitate a longer filtration period in order to maintain the target overall water recovery (**Section 5.3.4**); this in turn would lead to both higher concentrate salinity and  $SI_{g,m}$  by the end of the filtration period.

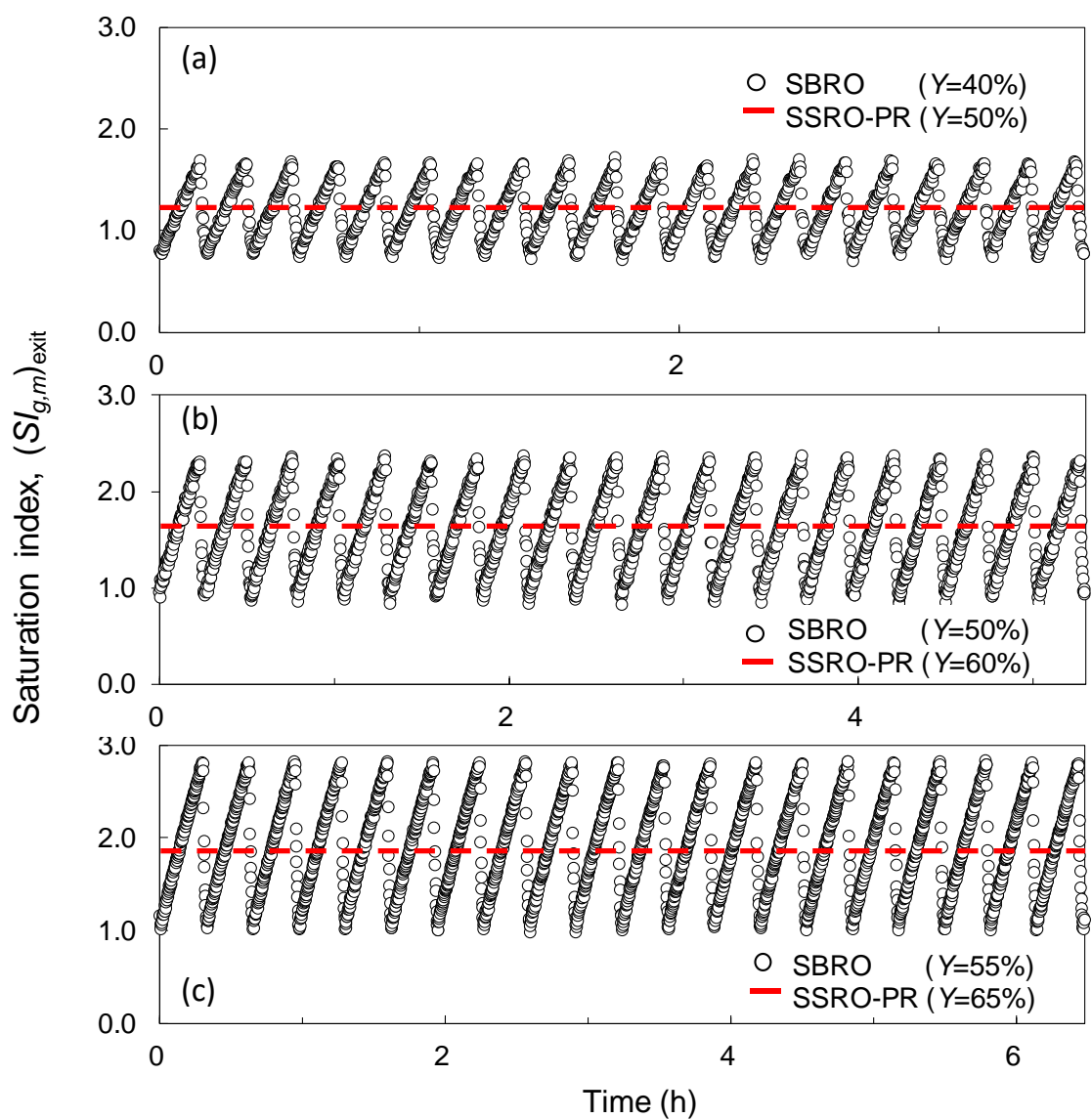


**Fig. 5-5.** Profiles of gypsum saturation index at membrane surface (at the RO element exit) during SBRO and SSRO-PR tests (a) #1a, (b) #1b, and (c) #1c, for which the time-average  $(SI_{g,m})_{exit}$  was 1.2, 1.6 and 1.9, respectively, as indicated with dashed horizontal lines (also designating the conditions for SSRO-PR operation).

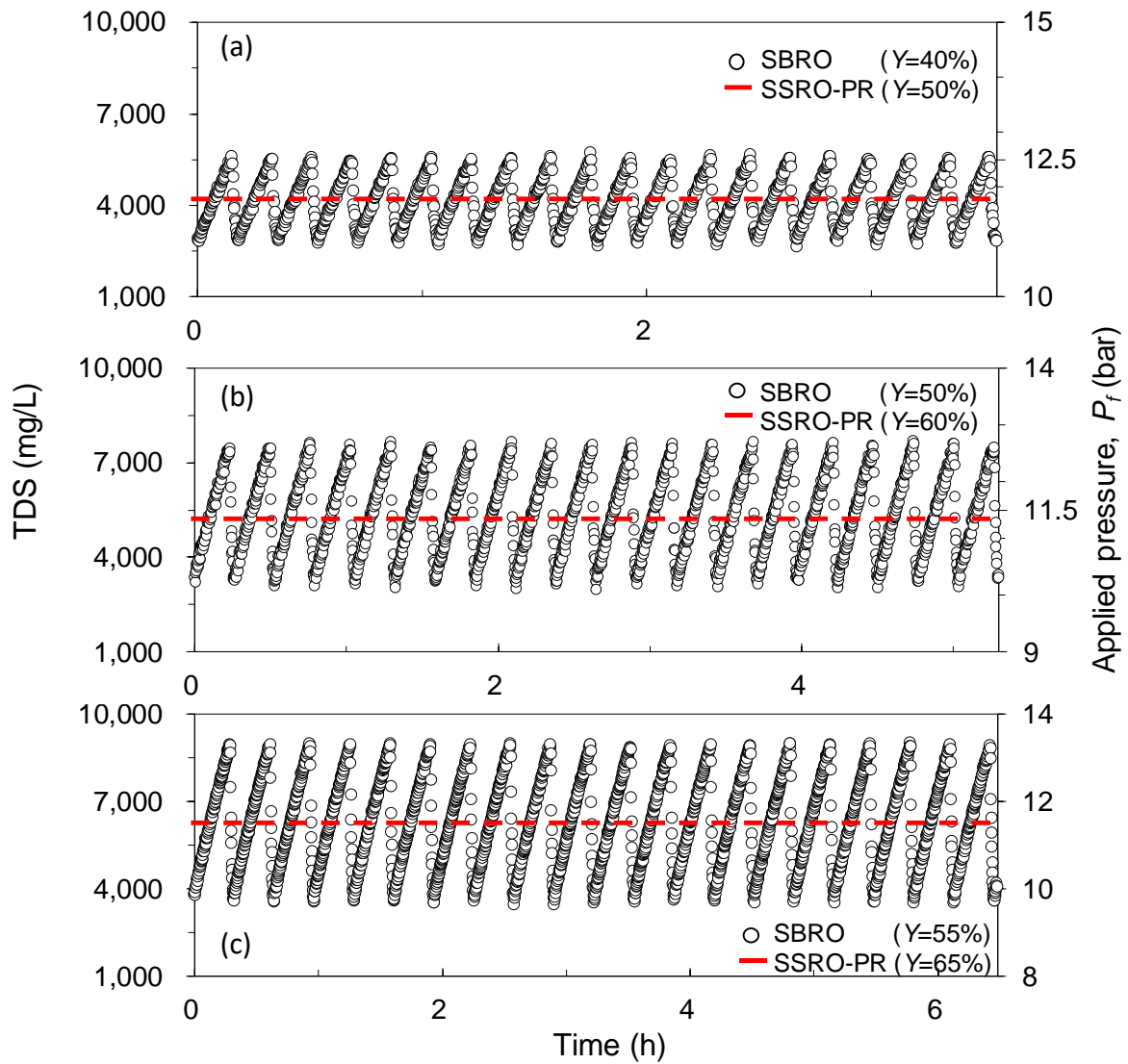


**Fig. 5-6.** Salinity (mg/L, TDS) - time profiles of RO concentrate at the element exit and the corresponding RO element feed pressure during SBRO and SSRO-PR (solid dashed horizontal lines) operations (test runs #1 and #2, **Table 5-2**) at equivalent  $(SI_{g,m})_{exit}$  of (a) 1.2, (b) 1.6, and (c) 1.9, respectively, with the corresponding overall RO recovery range of 40% - 65%.

#### 5.4.2 The onset and evolution of gypsum Scaling

In order to compare the scaling propensity in the SBRO and SSRO-operational modes, SSRO-PR scaling runs were carried out at  $(SI_{g,m})_{exit}$  values that were equal to the time-average values in SBRO operation (**Fig. 5-5**). The onset of gypsum scaling, as well as real-time monitoring of the evolution of the number density and area coverage by gypsum scale were

assessed via a membrane scale monitoring system (Section 5.3.3). Membrane surface monitoring, as illustrated by the typical images shown in Fig. 5-7, clearly demonstrated an increase in gypsum scale coverage with time and a greater degree of scaling in SBRO relative to SSRO-PR.

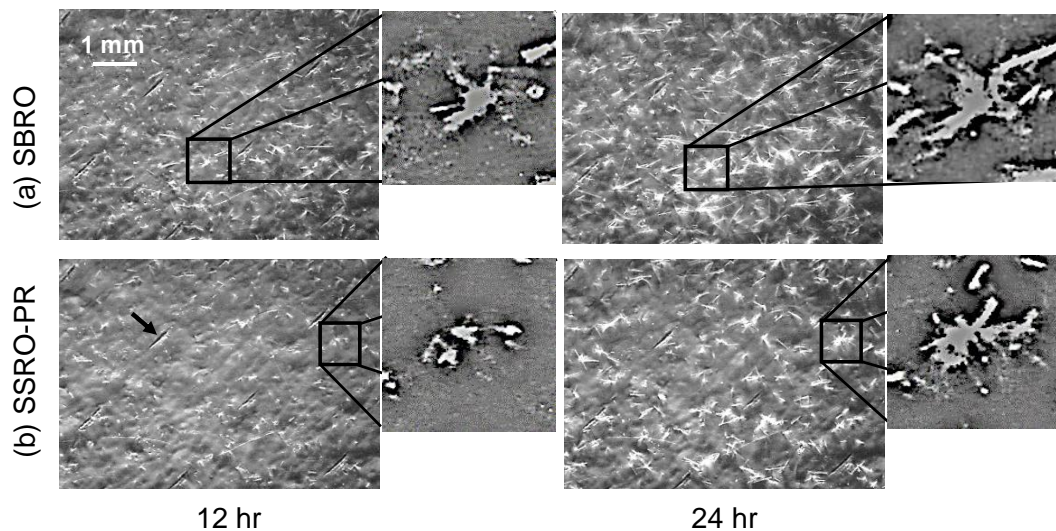


**Fig. 5-7.** Development of membrane surface scaling by gypsum crystals at  $t = 12$  and  $24$  h during (a) SBRO and (b) SSRO-PR scaling test (run #1a and #2a, respectively, Table 5-2) at overall water recovery of  $Y=50$  and  $40\%$ , respectively and at the same average saturation index at membrane wall of  $SI_{g,m} = 1.2$ . The inset views are processed images of smaller segments of the monitored area. The diagonal streaks (indicated with an arrow) are impressions resulting from the membrane spacer.

**Table 5-3.** Observed crystallization induction time

	Test # (Table 2)	$(SI_{g,m})_{exit}$ Ave. (min - max)	$t_{C,i}$ (h)
SBRO	1a	1.2 (0.73 – 1.7)	8.1
	1b	1.6 (0.86 – 2.4)	3.2
	1c	1.9 (0.99 – 2.8)	2.6
SSRO-PR	2a	1.2	12
	2b	1.6	4.4
	2c	1.9	3.0

Note:  $(SI_{g,m})_{exit}$  denotes the gypsum saturation index at the membrane surface at the RO element exit, which increases over the SBRO operation as shown in Fig. 5-5, and  $t_{C,i}$  is the crystallization induction time. The experimental conditions for above tests are provided in Table 2, Section 2.4.

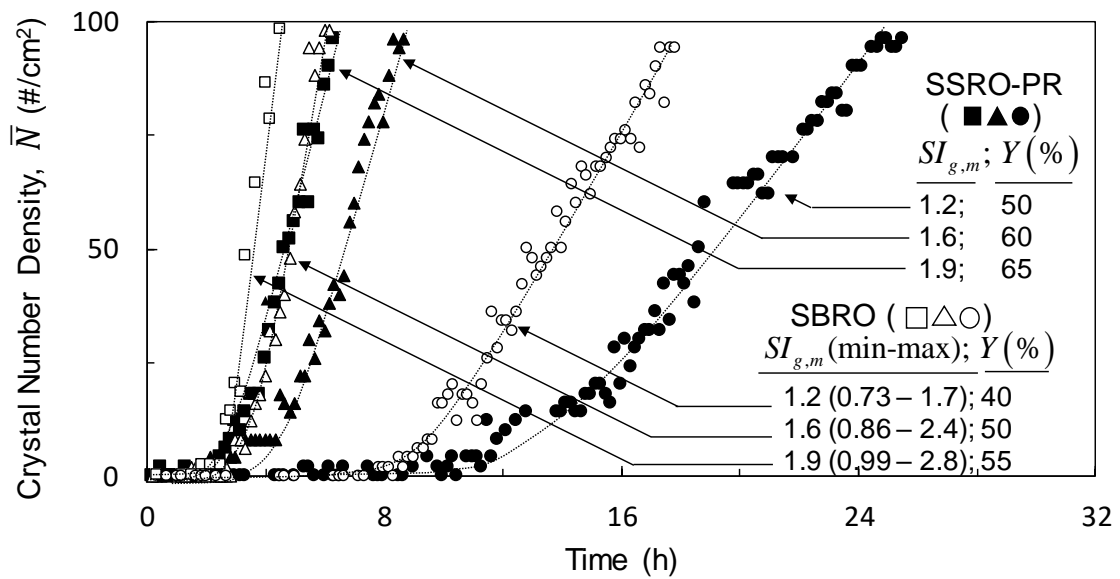


**Fig. 5-8.** Evolution of gypsum crystal number density,  $\bar{N}$ , (# of crystals/surface area) on the membrane surface in SBRO and SSRO-PR operations at various level of gypsum saturation index at membrane wall ( $SI_{g,m}$ ). Note: The  $SI_{g,m}$  varies with time in SBRO (as illustrated in **Fig. 5-5**), and thus the time average of  $SI_{g,m}$  was indicated on the figure.

Although at the same ( $SI_{g,m})_{exit}$  SBRO operation is at a lower recovery than SSRO-PR, when compared at the equivalent level of gypsum supersaturation at the membrane surface, gypsum scaling (in terms of crystal number density) appeared earlier in SBRO (**Fig. 5-8**). Accordingly, as shown in **Fig. 5-7**, the crystallization induction time for SBRO operation, at a given time-average ( $SI_{g,m})_{exit}$ , was shorter relative to SSRO-PR (**Fig. 5-9**, **Table 5-3**). The above behavior should not be surprising given that the rate of nucleation and crystal growth increases with supersaturation which in the SBRO filtration period can significantly surpass the initial value and in fact be significantly above the time-averaged value (as shown by the SI range for each of the SBRO tests; **Fig. 5-7**).

It may be tempting to argue that if the operational filtration period of SBRO is much shorter than the nucleation induction time in the bulk or at the membrane surface (based on continuous single-pass RO operation) then one would not expect scaling to occur in SBRO [48]. However,

it should be recognized that crystal nucleation of sparingly soluble mineral salts is a stochastic process [52, 73]; thus, there will be a distribution of induction times for any given level of supersaturation [203]. Given the above, it is not unreasonable to expect that over the course of multiple operational cycles, once a stable nucleus (or nuclei) is (are) formed (at any point in time during a given filtration period), either directly onto the membrane surface [85] or in the bulk followed by deposition onto the membrane surface, it will grow until the termination of filtration.

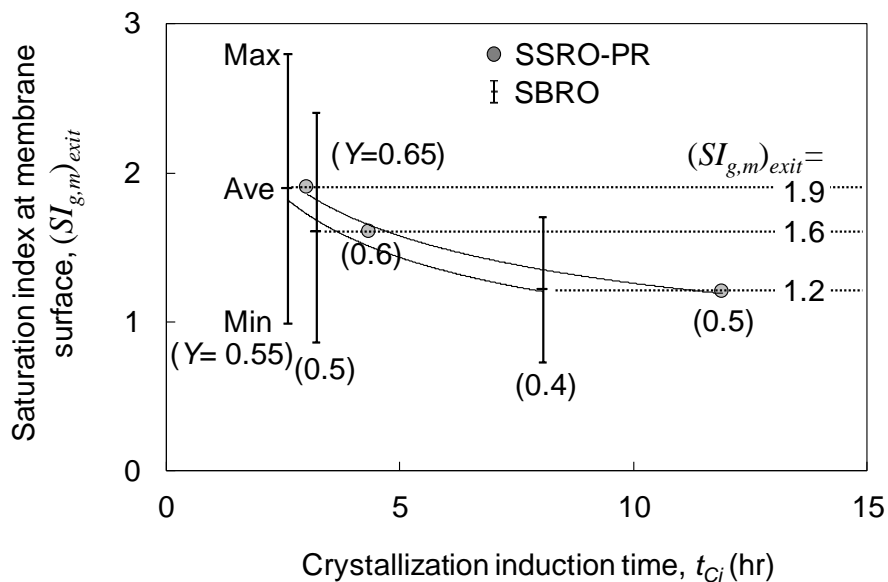


**Fig. 5-9.** Variation of the crystallization induction time ( $t_{Ci}$ ) with respect to the gypsum saturation index at the membrane surface,  $(SI_{g,m})_{exit}$ , at RO element exit. The vertical data bars indicate the  $(SI_{g,m})_{exit}$  range and average values during SBRO operation and filled circles denote the SSRO-PR  $(SI_{g,m})_{exit}$  value equal to the indicated time-average value in SBRO operation (Fig. 5-5).

If complete removal (by dissolution) of the formed crystal is achieved during the flushing period, with the undersaturated raw feed water, then SBRO would indeed provide a significant advantage over conventional RO systems (both without and with partial concentrate recycle). However, in the present work, the buildup of mineral scale with progressive SBRO cycles suggests that complete removal of surface scale (which can be in the nano-scale range, [84])

via flushing was not achieved, even with a flushing period being 3 times the convective residence time. Given that scaling was observed with progressive SBRO cycles, it is likely to conjecture that any remaining fragments of crystals on the membrane surface (post-flushing), smaller in size than those which were detected by the present monitoring system, served as sites for further crystal growth in the subsequent cycle. Consequently, with continued operation, the extent of scale formation increased as quantified by the temporal evolution of the crystal number density (**Fig. 5-8**).

### **5.4.3 Evolution of gypsum scale coverage**

The development of surface scale was quantified in terms of the percent of the monitored area covered by scale as illustrated in **Fig. 5-10**. Scale coverage progression was consistent with the time evolution of the crystal number density (**Fig. 5-8**). Once surface crystals are present at the beginning or formed during a filtration period they will continue to grow (if supersaturated solution condition exists in the membrane channel) until the filtration period ends. Subsequently, such crystals will be reduced in size during flushing due to dissolution to an extent that will depend on the starting crystal size, level of under-saturation of the raw feed water and membrane channel hydrodynamics (**Section 5.4.4.2**). Accordingly, once formed, surface crystals (unless completely removed can grow larger with each successive SBRO cycle.

Overall, scaling is governed by both the rate of nucleation and crystal growth both of which increase with rising level solution supersaturation w.r.t the scale precursors. It is tempting to suggest that scaling will be less pronounced when the induction time for crystallization is shorter than the overall RO system operational time. However, scaling is a stochastic process and thus mineral crystals can nucleate and grow even under the scenario of periodic exposures

of the RO membrane to a supersaturated solution as is the case in SBRO. Of course, the argument that in SBRO operation, the so-called “crystallization induction clock” can be reset periodically with flushing (and thus avoid progressive scaling) is compelling; however, one would have to achieve the ideal condition of complete dissolution (removal) of all nuclei that may have formed during in SBRO filtration. The above condition was not attained in the present work, but it is conceivable that more effective flushing approaches could be developed. However, one must recognize that for high recovery RO and water sources of high scaling propensity, maintaining operational advantage of SBRO in terms of system recovery may be a challenge.

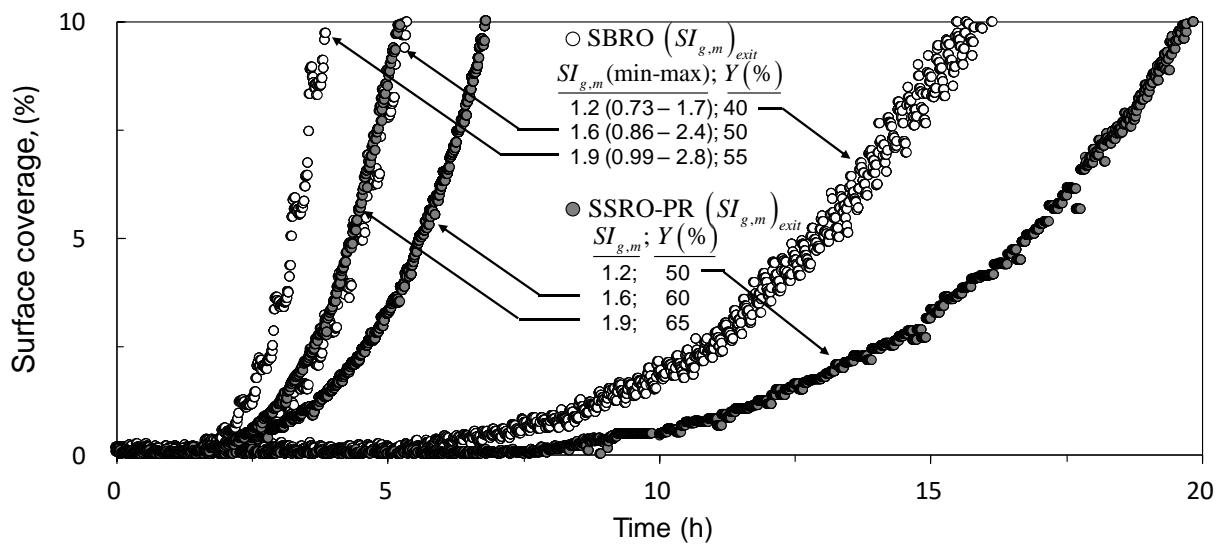


**Fig. 5-10.** Progression of percent membrane surface coverage by gypsum scale during SSRO-PR and multi-cycle SBRO operations at gypsum supersaturation level of  $SI_{g,m} = 1.2 - 1.9$ .



#### 5.4.4 Rate of crystal growth and dissolution

At a given level of gypsum supersaturation at the membrane surface ( $SI_{g,m}$ ), for the same local hydrodynamic conditions, crystal growth rates should be similar [73, 89, 204] in both SBRO and SSRO-PR operations. Gypsum crystal growth rate on the membrane surface can be described by the following simple diffusional growth process [73, 87]:

$$\frac{dM}{dt} = k_C A_S \cdot MW_g (C_b(t) - C_s) \quad (5-5)$$

in which where  $M$  is the gypsum crystal mass,  $A_S$  is the single crystal surface area,  $C_b$  and  $C_s$  are the molar concentrations of calcium ion (note that calcium and sulfate ions concentrations in the present feed solutions were equimolar, **Section 5.3.1**) in the bulk solution at the membrane surface and at saturation (i.e., at the crystal surface), respectively,  $k_C$  is the crystal-fluid mass transfer coefficient [73], and  $MW_g$  is the molecular mass of gypsum. If lateral crystal growth is dominant, relative to vertical crystal development, then **Eq. (5-5)** can be simplified by substituting for  $dM / dt = \rho_s \bar{h} dA_s / dt$ , in which  $\rho_s$  is the crystal solid density and  $\bar{h}$  is the average crystal height over the specified growth period. It is noted that during the SBRO filtration period, the solute concentration, varies essentially linearly with time (**Fig. 5-6**). Accordingly, **Eq. (5-5)** can be solved to yield the time dependence of the surface area, i.e.,  $\ln(A_s / A_o) = \beta t$ , where  $A_o$  is the initial surface area (i.e., at time  $t_o$  when the crystal is first observed), and  $\beta = (\bar{k}_C MW_g / \bar{h} \cdot \rho_s) (\bar{C}_b - C_s)$  in which  $\bar{C}_b$  and  $\bar{k}_C$  are the time-average bulk calcium ion concentration and mass transport coefficient, respectively. The above solution also holds for SSRO-PR operation in which the solute concentration at a given axial position at the membrane surface can be considered to be time-invariant.

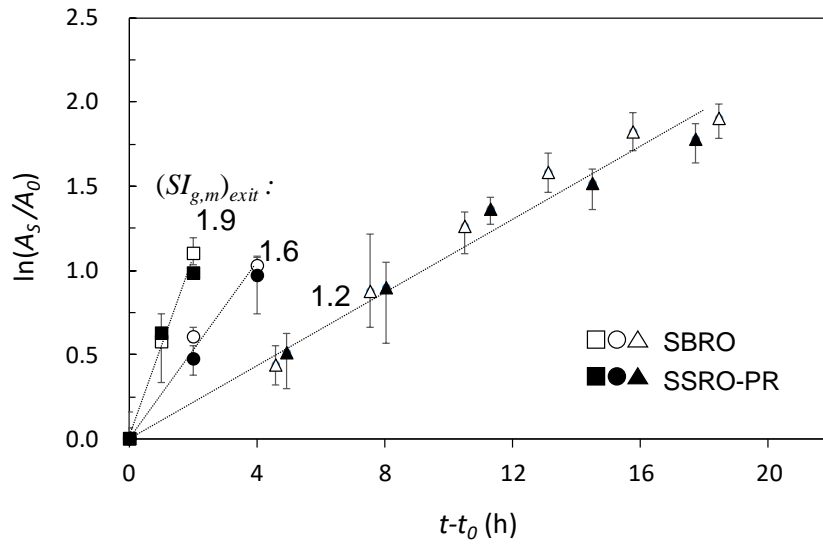


**Fig. 5-11.** Gypsum crystal growth ( $A_0$  is the initial area of the tracked crystal) at the time-average SBRO  $(SI_{g,m})_{exit}$  of 1.2, 1.6 and 1.9 (**Table 5-2**) and at the equivalent values for SSRO-PR operation. The data represent the average over 3-5 separate gypsum crystals of initial areas in the range of  $A_0 = 40 - 80 \mu\text{m}^2$  with vertical bars indicating the minimum and maximum values. (Note: the observed crystallization induction times at the indicated  $(SI_{g,m})_{exit}$  values are provided in **Fig. 5-9** and **Table 5-3**).

The growth data for individual gypsum surface crystals followed the above linear relation of  $\ln(A_s / A_o)$  dependence on time, as shown in **Fig. 5-11**, thus supporting the assertion of diffusion-controlled crystal growth. Moreover, the data reveal that single crystal growth rates, at a given  $(SI_{g,m})_{exit}$  in SSRO-PR and the equivalent time-average value in SBRO are similar. However, the severity of scaling is greater in SBRO compared to SSRO-PR (**Fig. 5-10**). The above behavior is likely to be due to the higher nucleation rate in SBRO in which a higher SI is reached at the end of each filtration period. The question to be asked, however, is if flushing of the SBRO system could be effective in complete dissolution of mineral crystals.

In order to assess the feasible extent of crystal dissolution during the SBRO flushing period, an approximate analysis was carried out to assess the time scale for crystal dissolution due to flushing [73, 205]. Following a simplified analysis in which a surface crystal is taken to be

hemispherical, one can determine the rate of dissolution based on the mass transfer coefficient correlation provided in [73] for gypsum crystals growth/dissolution on RO membranes. For example, for the present set of SBRO scaling tests (**Table 5-2**), crystal nuclei that may have formed during SBRO filtration (once the condition of supersaturation is reached; **Section 5.4.4.1**) can grow, over a filtration period of 9, 14.3 and 17.7 min, up to a size of  $d_{eq}=1.3, 7.1$  and  $14.5 \mu\text{m}$ , respectively (where  $d_{eq}$  is defined as equivalent gypsum crystal diameter for a single crystal,  $d_{eq} = \sqrt{2A_g / \pi}$  [73]). As argued in **Section 5.4.4.2**, crystals of this size would be unlikely to dissolve over the flushing period that was only about a factor of 3 longer than the convective residence time in the SBRO system. For the present feed solution ( $SI_g \sim 0.4$  or  $(SI_{g,m})_{exit}$  of  $\sim 0.5$ , **Table 5-1**) only crystals of size  $< 0.58 \mu\text{m}$  could possibly dissolve over the course of the above flushing period (**Fig. 5-13**). However, incomplete dissolution of the above and larger crystals that would be expected to form over the course of multiple filtration cycles, would then lead to be reflected in progressive growth of these remnants of crystals (post-flushing) over the course of the cyclic SBRO process. Longer SBRO flushing period can increase the effectiveness of scale mitigation, but at the cost of requiring a longer filtration period to attain the target recovery and at a correspondingly elevated  $SI_g$  which would lead to higher rate of mineral salt crystallization. Here it is important to note that scale removal via periodic permeate flush can also be achieved in SSRO-SP as well as SSRO-PR operations. A longer flushing duration and/or frequency in SSRO-PR and SSRO-SP operational modes would also reduce the overall recovery and could lead to increased specific energy consumption.

It is important to note that in RO operation with or without partial recycle, for a given train of RO elements, the solution supersaturation level at membrane surface in the exit of the tail element will be dictated by this element concentration polarization ( $CP$ ) profile and the overall

system recovery. Therefore, for equivalent operating condition with respect to crossflow velocity and overall system recovery, one would expect mineral scaling to be similar in both SSRO-PR and SSRO-SP. Although not assessed in the present study, it is conceivable that crystal remnants that may dislodge from growing surface crystals would recirculate through the element train in SSRO-PR and thereby if deposited onto the membrane surface could lead to a higher mineral scaling propensity relative to single-pass RO operation. Given the above, it is reasonable to conclude that mineral scaling propensity in SBRO which is greater relative to SSRO-PR would also likely to be greater than in SSRO-SP when compared at the same recovery or at the equivalent level of solution supersaturation at the tail element where scaling would be most severe. It should be recognized, however, that mineral scaling often occurs in the presence of organics and bio-foulants that may also affect the onset and evolution of membrane scaling [80]. Thus, it should be of interest to further explore the propensity for organic and biofouling with and without simultaneous occurrence of mineral scaling in SBR and SSRO-PR operations as well as single-pass RO with periodic permeate flushing.

#### 5.4.4.1 Gypsum Crystal growth

Over the duration of SBRO filtration, once nucleated, crystal size evolution over the course of the filtration period can be approximated following a simple model for gypsum crystals taken to be of a semi-hemispherical rosette structure [73, 85]. Accordingly, crystal growth is expressed as in **Eq. (5-5)**, but were the crystal mass is given as  $M = \rho_s (\pi d_{eq}^3 / 12)$ , where  $d_{eq}$  is the equivalent gypsum crystal diameter for a single crystal. A Sherwood number correlation for the crystal growth/dissolution mass transfer coefficient (**Eq. (5-5)**) was reported in [73] as  $(k_c d_{eq} / D) = 0.0052 (v / D)^{1/3} (v_o d_{eq} \rho_s / \mu)^{1.1}$ , in which  $v_o$  is the average cross-flow velocity in

the membrane channel,  $\nu$  is the solution kinematic viscosity, and  $D$  is the diffusivity of the calcium sulfate ion pair, estimated to be  $9.23 \times 10^{-6} \text{ cm}^2/\text{s}$  [62]. Given the above, and the linearity of the concentrate salinity with time (Eq. (5-3)), Eq. (5-5) reduces to  $d(d_{eq})/dt = 2[k_c/\rho_s] \cdot MW_g \cdot (C(t) - C_s)$ , where  $C_m(t)$  is calcium sulfate ion pair concentration at the membrane surface, which can be obtained from Section 5.4.1. The above equation can be solved, given the expression for  $k_c$ , to yield the time profile of  $d_{eq}$ . Crystal growth, over a single filtration period of up to 20 min, is illustrated in Fig. 5-12 for a membrane channel cross-flow velocity of 15 cm/s (i.e., the setting in the present scaling tests), ideal membrane (i.e., 100% salt rejection) and a single-pass recovery of  $Y_{SP} = 0.095$ .

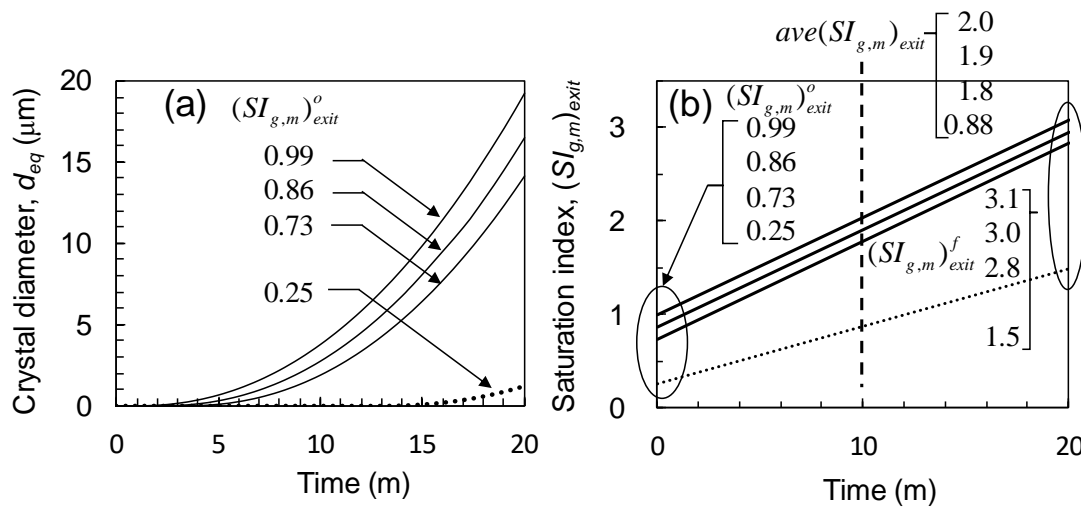


**Fig. 5-12.** (a) Growth of gypsum crystal (located at RO element exit) during a single filtration period of up to 20 min, as per the diffusional growth model (Eq. (5-5)), for SBRO operation in which the level of gypsum saturation at the beginning of the flushing period was set as  $(SI_{g,m})_{exit}^o = 0.73, 0.86,$  and  $0.99$ , corresponding to conditions of test run #1a, 1b, and 1c, respectively (Table 5-2) with (a) raw feed water saturation of  $SI_g = 0.4$  (Table 5-1), and  $(SI_{g,m})_{exit}^o = 0.25$  (with corresponding raw feed  $SI_g$  of 0.18, indicated with dotted line), and (b) Variation of  $(SI_{g,m})_{exit}$  during the filtration period, obtained as per the approach described in Section 5.3.4, and Section 5.4.1. The analysis assumed complete membrane solute rejection,  $Y_{SP}$  of 9.5%, gypsum ion diffusivity ( $D$ ) of  $9.23 \times 10^{-6} \text{ cm}^2/\text{s}$  [62], effective crystal density ( $\rho_s$ ) of  $2.7 \text{ g/cm}^3$  [87], and membrane 15 cm/s channel cross-flow velocity.

As shown in **Fig. 5-12**, once a stable nucleus is formed, crystal growth can reach sizes (in terms of an equivalent diameter) of ~14  $\mu\text{m}$ , 16  $\mu\text{m}$ , and 19  $\mu\text{m}$  for the condition of concentrate supersturation, at the membrane exit, in the beginning of the filtration period of  $(SI_{g,m})_{exit}^o = 0.73$ , 0.86 and 0.99, respectively. As suggested by the analysis in **Section 5.4.4.2**, crystals of such sizes would not be completely removed by dissolution over the flushing period of 100 s employed in the present study.

#### 5.4.4.2 Gypsum Crystal Dissolution

SBRO operation is in the single-pass mode during the flushing period. Mitigation of any mineral scale crystals that may have formed during the filtration period would depend on the efficacy of crystal dissolution which will depend in turn on the level of raw feed saturation and flushing duration. In order to gain insight as to the level of achievable dissolution, the same simple model of a hemispherical gypsum crystal can be adapted for the early crystal growth period during RO filtration. Although more complex geometries can be used, the above simple approximation should suffice as a means of obtaining an estimate of the time for dissolution. Accordingly, the dissolution rate can be described by  $d(d_{eq})/dt = 2[k_C/\rho_s] \cdot MW_g \cdot (C_o - C_s)$ , in which  $C_o$  is the bulk solution concentration at the membrane surface at the crystal position. The temporal change in crystal diameter upon dissolution (during SBRO flushing) is shown in **Fig. 5-13** for crystals of different initial gypsum crystal diameters and for different levels of feed saturation, for the same crossflow condition as in **Fig. 5-12**.

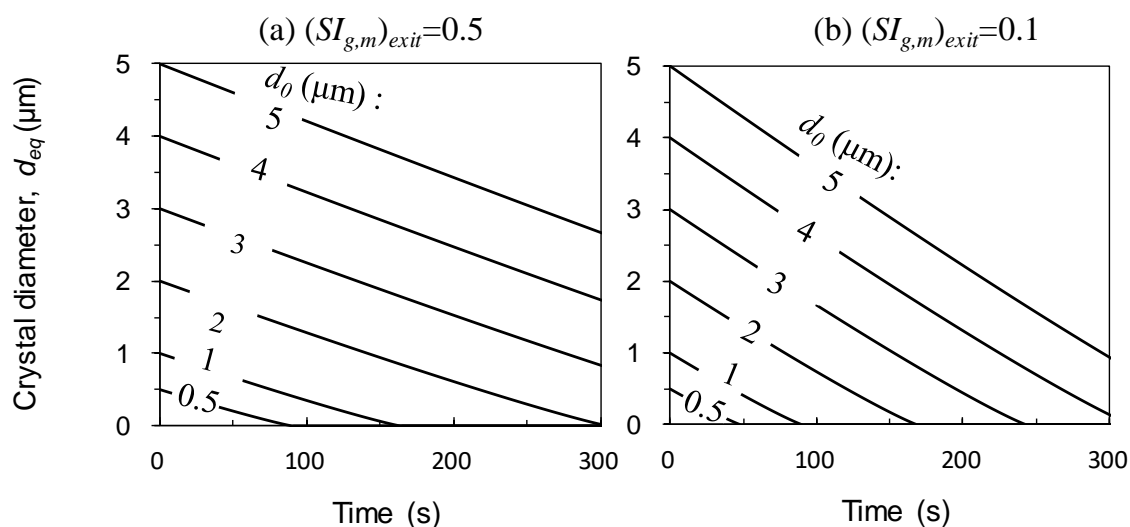


**Fig. 5-13.** Gypsum crystal (located at RO element exit) diameter (of initial size  $d_0=0.5 - 5 \mu\text{m}$ ) decrease due to dissolution during flushing period for a gypsum supersaturation index at the membrane surface at the element exit,  $(SI_{g,m})_{exit}$ , of (a) 0.5 and (b) 0.1. It is noted that crystals of the size formed by the end of a filtration period, as illustrated in **Fig. 5-12**, would not dissolve to any significant degree over a flushing time greater by even a factor of about three greater than the 100 s flushing time employed in the current study.

## 5.5 Summary

An experimental investigation was undertaken in a spiral-wound RO system to assess the mineral scaling propensity, using gypsum as a model scalant, in the modes of semi-batch RO (SBRO) and single-pass steady-state RO with partial recycle (SSRO-PR). The progression and severity of membrane surface mineral scaling, over a range of gypsum supersaturation at the membrane surface ( $SI_{g,m}=1.2 - 1.9$ ), was monitored in real-time by a membrane surface monitoring (MeSuM) system interfaced with the RO system. Mineral scaling in SSRO-PR for the condition of gypsum saturation at the membrane surface at the RO element exit,  $(SI_{g,m})_{exit}$ , was compared to scaling in SBRO at the equivalent time-average value. Mineral scaling in both RO systems was also assessed for operation at the same overall recovery. Comparison of mineral scaling at both equivalent recovery and at the same solution supersaturation indicated a greater scaling propensity in SBRO relative to SSRO-PR. In SBRO, the rate of appearance

of surface crystals was higher and the observed crystallization induction time was shorter relative to SBRO based comparison at the above conditions. The above results suggest that the nucleation rate was higher in SBRO when operating at either the same recovery or at the time-average supersaturation equivalent to the saturation level in SSRO-PR. This assertion is consistent with the higher level of supersaturation reached in the SBRO filtration period relative to SSRO-PR when the two system are compared at either the same overall recovery or equivalent mineral scalant saturation. It is noted, however, that in both SBRO and SSRO-PR growth rates of surface crystals, which followed diffusional growth, were similar at the same level of solution supersaturation.

Reduction of the extent of mineral scaling in SBRO, at a given target recovery, could potentially be achieved by a sufficiently long flushing period for complete scale removal (i.e., dissolution of gypsum crystals), provided that the raw feed is reasonably undersaturated. However, longer flushing period would necessitate increasing the filtration period to maintain the target recovery; this in turn would raise the supersaturation level in the membrane element over the course of the filtration period. Flushing at the early stage of scale formation could provide more effective scale removal as smaller crystals would require a shorter period for complete dissolution. It is expected that there will be a tradeoff in SBRO operation with respect to scale mitigation that requires optimization of flushing duration and frequency with the need for meeting the overall target recovery objective and reduced energy consumption. Here we note that permeate flush in SSRO-PR, as well as in SSRO-SP systems can also be used to partially mitigate the progression of mineral scaling. The benefit of such an approach will depend on the duration, frequency and volume of permeate flush and thus will impact the overall attainable recovery and the specific energy consumption.



## Appendix A. Flexible RO pilot membrane system platforms

### A.1 Flexible RO (FLERO) system components

The FLERO system (Fig. A.1 and Fig. A.2) consisted of a single 2.5” x 40” spiral wound membrane element having permeate production capacity of up to 1.5 m<sup>3</sup>/d (400 gpd) for brackish water of salinity up to 5000 mg/L TDS and up to 1.36 m<sup>3</sup>/d (360 gal/day) capacity for seawater desalination. Prior to be supplied to the RO system, the raw-feed water was pretreated with cartridge filters of sizes 20, 5 μm (cellulose pleated 2-1/2”x10”, Ocean Link Inc., Portsmouth, RI; F1 and F2, respectively on Fig. A.1) using a low-pressure booster pump, P1 (Model DRIVE D5 Strong, Laing Pumps, Medford, OR). The pre-treated source water (S2) was then combined (at M1) with the recycled concentrate stream (S8) from the membrane module (Fig. A.1).

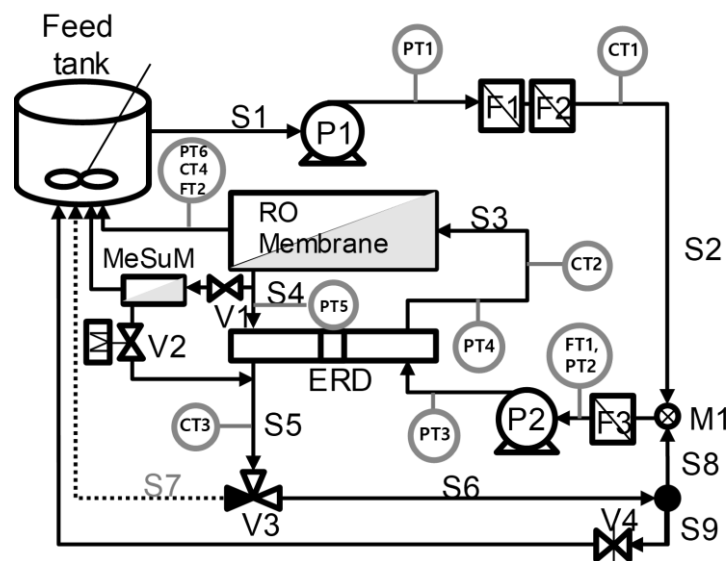


**Fig. A.1** Process flow diagram of FLERO RO system. Streams S1 and S2 are the raw feed streams before and after filtration pretreatment, respectively, and S3 and S4 represent the RO element feed and concentrate streams, respectively. Streams S6 and S7 are those of the concentrate recycle and discharge, respectively, and S9 is the discharged flow portion of the concentrate stream S6. Pressure, flow rate, and conductivity transmitters are indicated with PT, FT and CT, respectively.

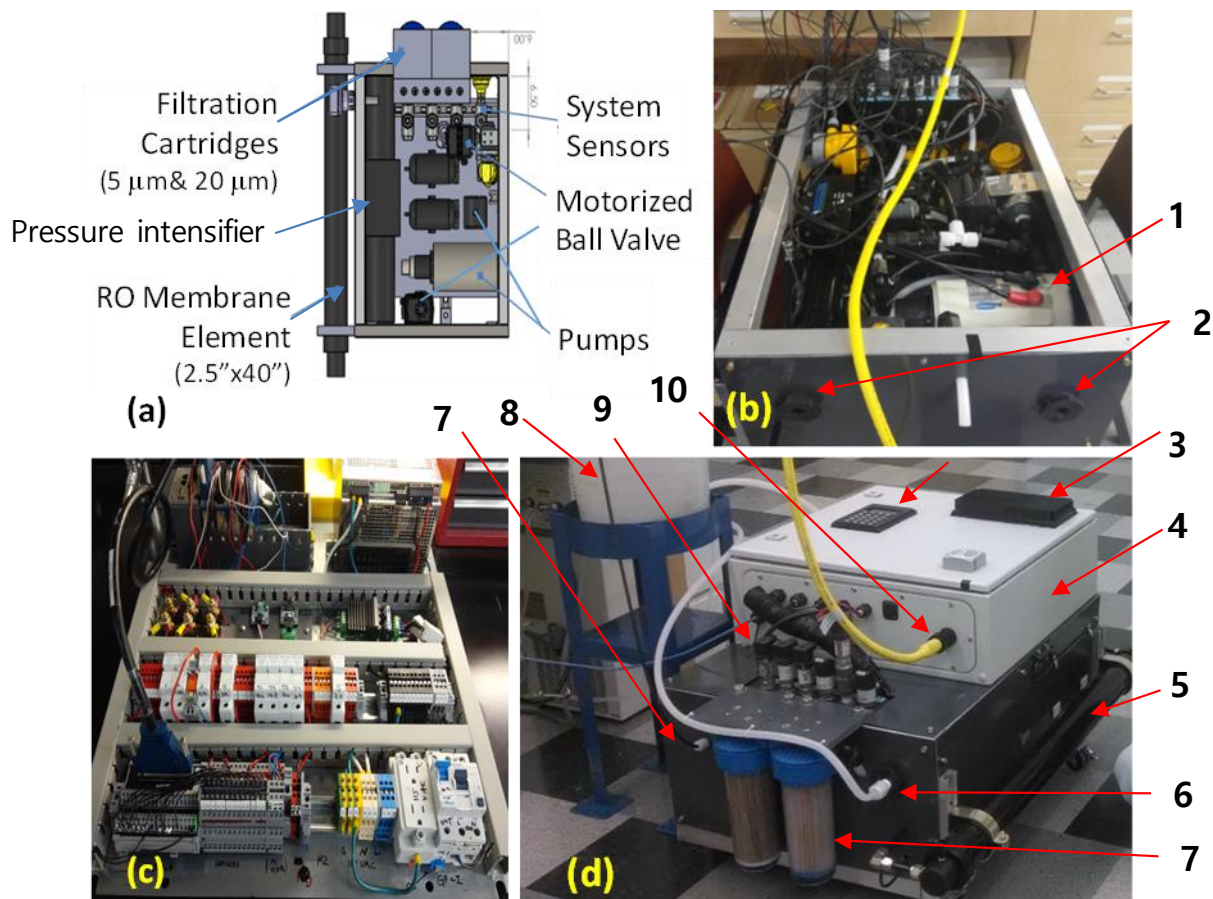


**Fig. A.2.** FLERO system showing: (a) physical design with components layout, (b) system body construction, (c) electrical circuit box, and (d) assembled spiral wound RO system with permeate production capacity of ~400 gallons/day at various water recoveries up to 90% where 1) DC motor for the main pump, 2) the port for feed and the concentrate streams 3) aluminum cooling block for electrical box, 4) electrical box with a computer and input/output module 5) pressure vessel for a single 2.4 in x 40 in RO membrane element, 6) port for the raw feed stream 7) cartridge filters in pretreatment module, 8) feed tank, 9) pressure transmitters, 10) power cord (110V AC).

The combined feed stream (S2+S8, **Fig. A.1**) was further treated with 0.2 μm plastic filter (F3) before it was pressurized and delivered to the RO element using a positive displacement vane pump, **P2** (Mag Drive, PROCON Products, Smyrna, TN), with a magnet motor operating at 24V DC voltage (Model C4D20FC2B DC motor, Leeson Electric Corporation, Grafton, WI), in addition to a pressure intensifier (or energy recovery device, i.e., ERD on **Fig. A.5**, Clark Pump, Spectra Watermakers, San Rafael, CA). The volumetric feed flow rate to the RO

element (S3) was controlled by the pump’s DC speed controller (Model NEMA 4X, DART Controls, Zionsville, IN), while the concentrate discharge was adjustable by an in-line flow control valve (ARO 1/2" 104104-N03, Bryan, Ohio).

## A.2. RO process monitoring

**Table A-1** In-line sensor positions and measurement ranges.

Sensors	Measurement Range
Pressure Transducer (PT) 1	0-50 psig
Pressure Transducer (PT) 2	0-150 psig
Pressure Transducer (PT) 3	0-150 psig
Pressure Transducer (PT) 4	0-1000 psig
Pressure Transducer (PT) 5	0-1000 psig
Pressure Transducer (PT) 6	0-50 psig
Conductivity Transmitter (CT) 1	0-200 mS/cm
Conductivity Transmitter (CT) 2	0-200 mS/cm
Conductivity Transmitter (CT) 3	0-200 mS/cm
Conductivity Transmitter (CT) 4	0-1000 $\mu$ S/cm
Flow Transmitter (FT) 1	0-5 gpm
Flow Transmitter (FT) 2	0-0.5 gpm
Current Transducer 1	0-5 A
Current Transducer 2	0-10 A

The required specific energy consumption was calculated from measurement of the pressures of the feed entering the membrane array. The RO element feed and exit (i.e., concentrate) pressures were monitored using in-line pressure transducers, (Type S-20 4-20 mA, Wika, Klingenberg, Germany, PT1 – PT4 on **Fig. A.1**). The permeate and feed flow rates were monitored with in-line flow transmitters, FT1 and FT2 (Signet 8550, George Fischer Signet, Inc. El Monte, CA). Electrical conductivities (*EC*) of the raw feed, membrane element feed,

RO concentrate, and permeate streams were monitored with in-line conductivity sensors (Signet 2850, George Fischer Signet, Inc. El Monte, CA). The measurement range for aforementioned sensors is summarized in **Table A-1**.

The measured conductivities were converted to NaCl concentrations in terms of total dissolved solids (TDS) using the correlation  $TDS = 460 \cdot EC^{1.1}$  (mg/L; applicable over a TDS range of 1,000 – 40,000 mg/L), derived based on simulation results from a multi-electrolyte thermodynamic simulator (OLI Analyzer, Version Studio, Morris Plains, NJ), in which TDS is the salt concentration in terms of total dissolved solids, and  $EC$  is the solution conductivity (mS/cm). The osmotic pressure (in units of bar), for a given TDS level for the NaCl solutions, was also calculated using the following simple correlation  $\pi = B \cdot [TDS]$ , in which  $B = 7.8 \times 10^{-4}$  (L/mg) derived based on results from the multi-electrolyte thermodynamic simulator for NaCl solution, and is consistent with previous results reported in [47]. Sensor measurements were acquired and recorded in real time via an embedded system computer.

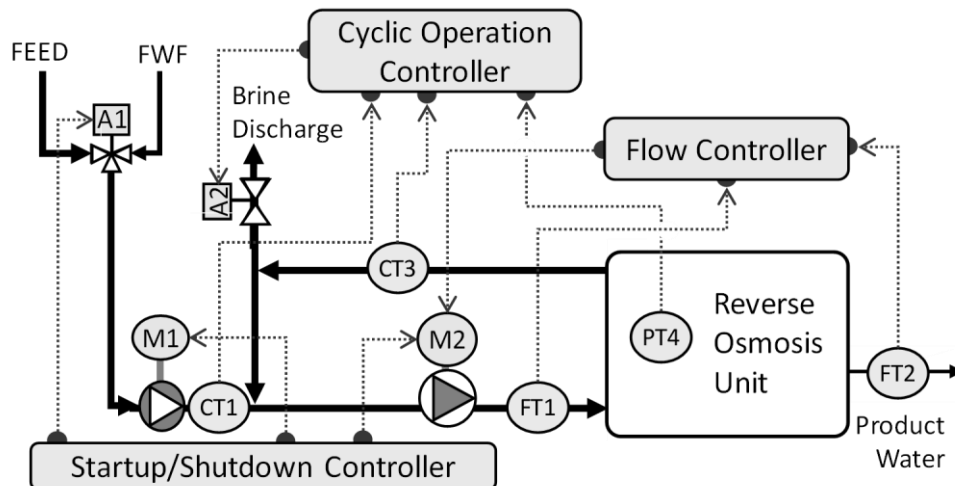


**Fig. A.3.** Flexible RO process control strategy. Black solid arrows indicate the direction of water flow, and dotted arrows indicate the signal toward the actuators and controllers.

## A.2 Implementation of RO Process Control

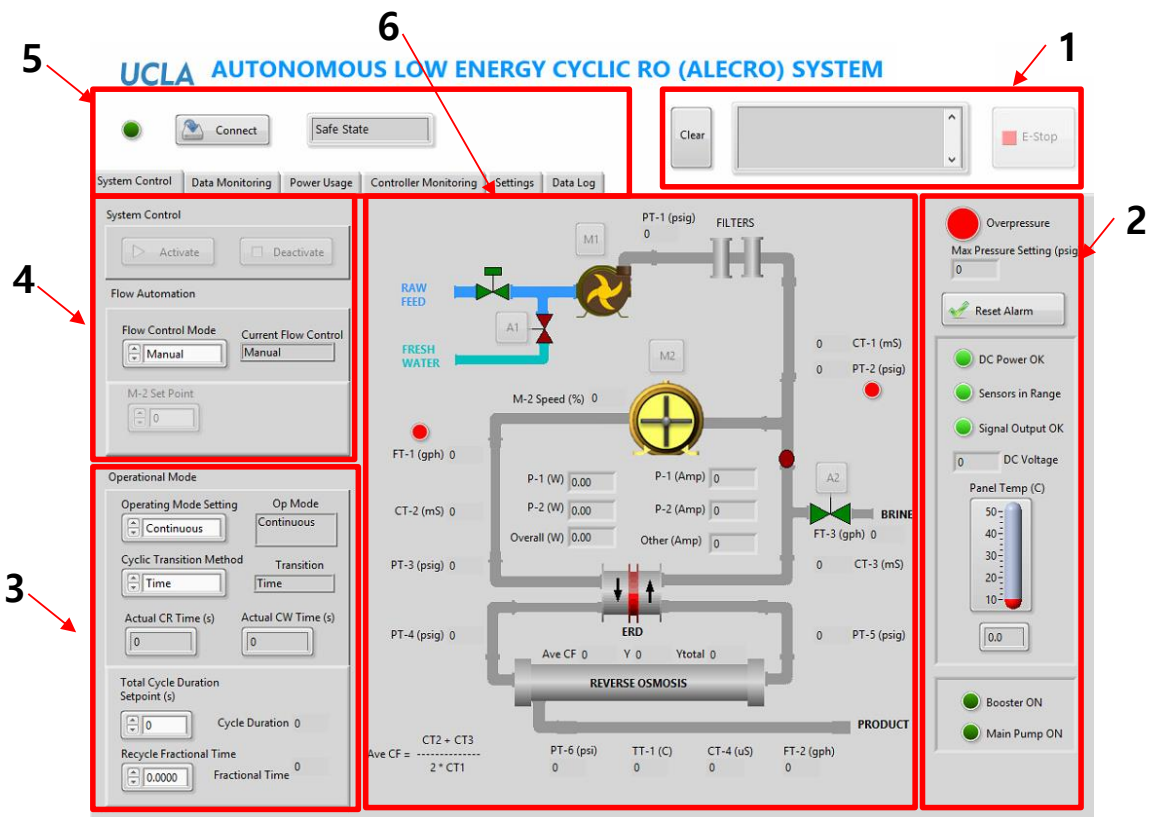


**Fig. A.4.** Graphical user interface of the pilot FLERO system with 1) system status/warning message box, 2) system status indicators for power, pressure, and temperature, 3) process control box for operating modes (i.e., semi-batch, continuous, etc.), operation time, and overall water recovery, 4) control box for flow automation, 5) features for data monitoring and storage, 6) real-time graphical report of fluid configuration and sensor measurements.

A model-based controller was developed for the FLERO system based on the control architecture described in **Fig. A.3**. A system startup-shutdown controller was implemented to enable sequence startup/shutdown of the feed booster pump motor (M1) and main pump motor (M2). A proportional-integral (PI) controller enabled control of the main pump motor (M2) in order to maintain the RO unit feed flow rate (FT1) and/or product flow rate (FT2) at the prescribed setpoint. The model-based semi-batch operation control was implemented for estimating the appropriate filtration and flushing durations based on the overall water recovery

set point (Section 4.2.1, Chapter 4). In order to avoid system damage, cyclic operation controller was implemented to continuously monitor the RO concentrate salt concentration and the RO unit pressure, and trigger emergency shutdown in the event that the feed pressure exceeds recommended operating limits set by membrane manufacturer. A graphical user interface was developed (Fig. A.4) using LabVIEW software (National Instrument, Austin, TX) to allow intuitive system operation by providing real-time visual feedback about the system status, fluid configuration, sensor measurements simultaneously.

### A.3 System start-up and operation

It is critical to verify prior system start-up that all tube connections are secured and that the brine discharge and the permeate streams are directed to the feed tank, which should be filled with DI water to conduct the system start-up procedure.

#### A.3.1 System start-up procedure

1. Power up the system by turning on the circuit breaker located on top of the electrical box.
2. The pressure relief valve located on the side of the pressure intensifier (Fig. A.5) to 1/2 turn

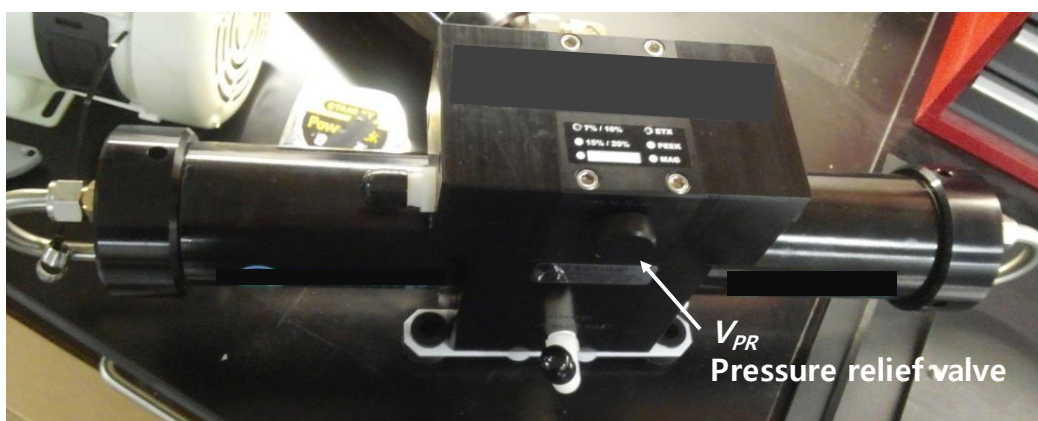


**Fig. A.5.** Pressure relief valve on the pressure intensifier (Clark Pump, Spectra Watermakers, San Rafael, CA).

3. Turn on the booster pump (P1, **Fig. A.1**), and ensure that pressure builds as monitored by pressure transducer, PT1 (**Fig. A.1**).
4. Set the flow control mode to “Manual”, then set the high-pressure pump (M2) setpoint to “30%” (Box 4, **Fig. A.4**).
5. Turn on the high-pressure pump (P2 on **Fig. A.1**). Check pressure transducers, PT1-5 (**Fig. A.1**) to ensure stable operation.
6. Slowly ramp-up the pressure by increasing the M2 setpoint to 100%.
7. Run the system for 20 minutes to purge the system of chemicals for at least twenty minutes.
8. Close the pressure relief valve (**Fig. A.5**). Increase in the RO element feed pressure should be observed from PT4 (**Fig. A.1**). Accordingly, the permeate flux monitored flow transmitter, FT2 (**Fig. A.1**) should also increase.
9. Carefully inspect for leaks over the entire system.
10. System is now ready for operation under high pressure.
11. Note: if repair is needed due to detected leakage, shut down the system by pressing M2, and then M1 buttons (**Fig. A.4**). Open the pressure relief valve,  $V_{PR}$ , (**Fig. A.5**) to depressurize the system.

Note: System cleaning protocol is provided in **Appendix C**.

## **Appendix B. Field evaluation of flexible RO (FLERO) system for nitrate removal from impaired small community well water**

### **B.1 Overview**

The feasibility of nitrate removal and salinity reduction from impaired community well water via RO treatment using a flexible RO system (**Appendix A**) with partial concentrate recycle was assessed via onsite field tests. RO treatment can be integrated into existing community small water systems to provide effective water purification, as well as salinity reduction if needed, over wide range of nitrate and salinity levels, while meeting the community water demand. RO treatment results in the generation of RO concentrate (i.e. residual) stream that requires appropriate management. In remote small communities that rely on septic systems for residential wastewater treatment, discharge of the RO residual stream (containing nitrate) to the community septic tank can be a feasible option. The existing literature suggests that nitrate entering the septic tank at is anoxic condition is likely to undergo measurable denitrification under its anoxic conditions. However, RO treatment should be carried out at the highest feasible recovery in order to minimize the volume of generated concentrate, comply with the septic tank capacity and required retention time, as well as minimize the amount of nitrate discharge (from the septic tank) to the leach field. Accordingly, the feasibility of nitrate removal and salinity reduction via RO treatment in small community water systems was evaluated using RO operation with concentrate recycle. Laboratory and field testing in a selected number of small communities were carried out to assess the expected level of water treatment performance for brackish water RO membranes of high level of nitrate rejection.



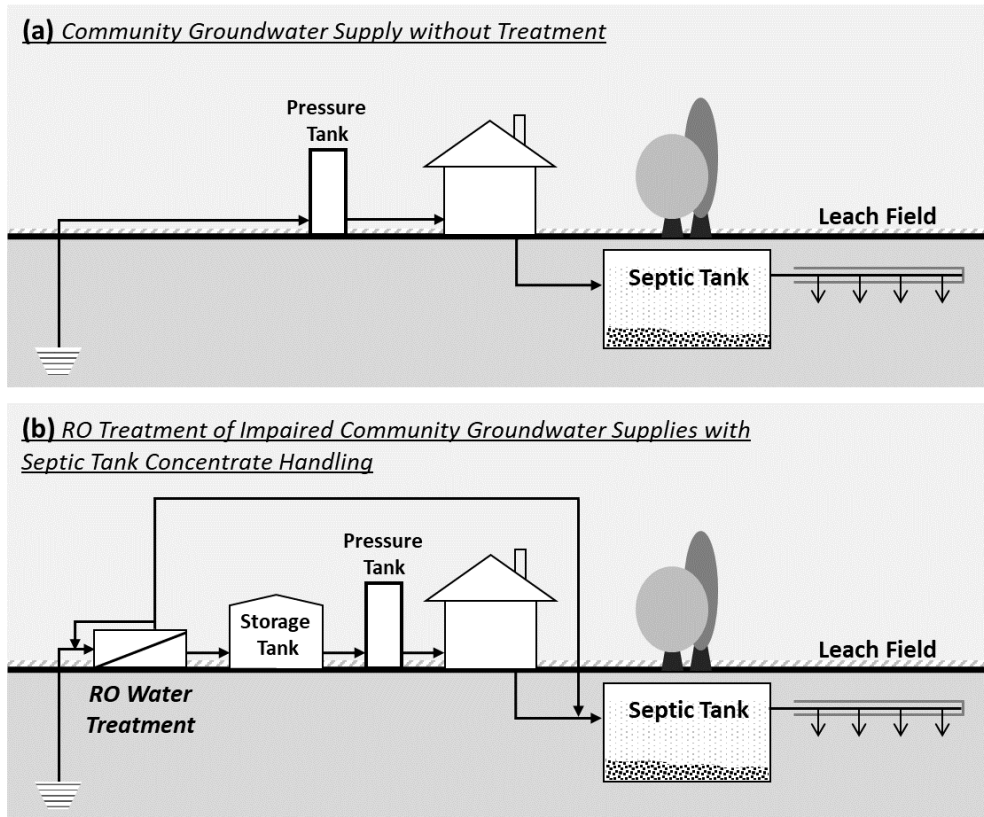


**Fig. B.1.** Water system in a small remote community without (a) and with (b) RO water treatment with concentrate recycle.

## B.2 RO treatment approach

Small and remote community water systems that rely on local groundwater for their domestic supply of potable water and are not connected to centralized sewer system utilize septic systems for handling their domestic wastewater (**Fig. B.1a**). Such communities whose water supplies have been impaired due to nitrate contamination and often also excessive salinity, could in principle utilize RO treatment of their well water to effectively upgrade their source water to produce safe drinking water (**Fig. B.1b**). Water consumption is expected to vary temporally. Therefore, a product water storage tank can be used as a buffer from which water is pumped to the community pressure tank which would then feed the community water

distribution system. With such an arrangement (**Fig. B.1b**), the RO system can be operated continuously for only part of the day while meeting the daily product water demand even during days of peak water consumption.

### **B.3 Experimental field studies**

Field testing of salinity reduction and nitrate removal was conducted with a low-energy spiral-wound element (XLE-2540, DOW FilmTec, hereinafter M-1) having a manufacturer reported membrane area of 2.6 m<sup>2</sup>, water permeability of 4.6 L/m<sup>2</sup>·h·bar, and salt rejection of 99% (measured at 10 bar and 500 ppm NaCl solution). Laboratory tests demonstrated nitrate rejection of 90%. An alternate high nitrate rejection membrane (CSM RE-2540 BE, Toray USA, hereinafter labeled M-2) of membrane area of 2.5 m<sup>2</sup>, water permeability of 3.2 L/m<sup>2</sup>·h·bar (at 15.5 bar and 2,000 mg/L NaCl solution), showed nitrate and salt rejections of 96% and 99.7%, respectively. Field tests with M-2 at Community Site D demonstrated nitrate and salt rejection of 97% and 99.4%, respectively.

The RO system operation in steady-state with partial concentrate recycle (SSRO-PR) allowed high recovery of up to 90% at RO element crossflow velocity of 0.23 m/s which was maintained for all field and laboratory tests and with permeate flux of  $5.8 \times 10^2$  L/m<sup>2</sup>·d (within the recommended range for the RO elements). Nitrate concentrations in the feed and permeate streams were monitored on-site using an optical UV nitrate sensor (Model CAS51D, Endress+Hauser, Netherland) housed in a mobile platform. A slip stream from the RO system (feed or permeate) at a flow rate of 100-300 mL/min was first passed through a filtration unit (R series; cartridge filter of 20 and 5  $\mu$ m cellulose pleated 2-1/2"x10", Penair Inc., USA) with the aid of auxiliary pump (medium duty peristaltic pump, Hydrobuilder Inc. Chico, CA) and

then directed to the optical flow UV cell. The nitrate sensor was calibrated against synthetic nitrate model solutions prepared by dissolving reagent grade sodium nitrate ( $\text{NaNO}_3$ ) and sodium chloride ( $\text{NaCl}$ ) (Fisher Scientific, Pittsburgh, PA) in deionized water. Water grab samples were also collected (**Table B-2**) from the community water well (i.e., raw source water feed to the RO unit) and from residential water taps, following State of California approved protocols, and delivered on the same day to a State Certified Laboratory for water quality analysis.

#### **B.4 Characteristics of study communities**

The feasibility of deploying small scale FLERO system to remote communities that utilize local groundwater for their potable water use was evaluated for four typical small communities located in central California. These communities (**Table B-1**), located in the midst of agricultural fields in the San Joaquin Valley, have 8-77 residential units (16-308 residents) with their household wastewater discharged to existing septic systems except of Community Site D.

Water quality analysis (**Table B-2**) revealed that the local potable water sources (i.e., local groundwater wells) of three of the study communities (A-C) were impaired, with respect to nitrate contamination, exceeding the nitrate MCL (10 mg/L as N) by a factor of 1.03-4.06. The source water salinity of communities A, B and D was about 80%- 304 % and in community C about 18% above the recommended level of 500 mg/L TDS for drinking water [206]). In communities A-C there were no contaminants (organic or inorganic) other than nitrate above the MCL, while in community D chromium (VI) was at a level of 12  $\mu\text{g/L}$  which was above the MCL of 10  $\mu\text{g/L}$  [207]. Tap water sampling revealed that lead and copper concentrations were below the action levels indicating the suitability of the existing water distribution system for delivering drinking water.

**Table B-1.** Study sites

Community	No. Residential Units	Population	Community Area	Proximity to nearest centralized water delivery and sewer infrastructure (km)	Septic Tank Capacity (m <sup>3</sup> )
A	11	16	70 x 60 m <sup>2</sup>	2.2 km <sup>(a)</sup>	17.0
B	8	36	160 x 50 m <sup>2</sup>	4.4 km <sup>(b)</sup>	18.9
C	10	34	143 x 80 m <sup>2</sup>	4.1 km <sup>(b)</sup>	18.9
D	77	308 <sup>(c)</sup>	400 x 200 m <sup>2</sup>	24 km <sup>(d)</sup>	Wastewater lagoon

<sup>(a)</sup> distance from Ecowater Water treatment plant, and <sup>(b)</sup> distance from Soledad sewage treatment plant; <sup>(c)</sup> assuming an average of four persons per home; <sup>(d)</sup> distance from the nearest wastewater treatment plant in Porterville CA.

**Table B-2.** Summary of water quality analysis

	Sampling/ Analytical Method	Well Source Water			
		Site A	Site B	Site C	Site D <sup>(d)</sup>
<b>Turbidity</b> (NTU)	EPA180.1	0.15	0.15	0.82	0.1
<b>Total dissolved solids</b> (mg/L)	SM2540C	1126 - 1500	1091- 2020	554 - 594	900 - 938
<b>Nitrate</b> (mg/L as N)	EPA 300.0	27.1 – 40.6	20.7 – 21.9	10.3 – 11.0	8.7 – 9.5
<b>pH</b>	SM4500-H+B	7.3	7.6	7.4	8.2
<b>Alkalinity</b> (mg/L as CaCO <sub>3</sub> )	SM2320B	348	244	112	130
<b>SI<sub>Calcite</sub></b>		4.33	4.76	0.84	2.41
<b>SI<sub>Gypsum</sub></b>		0.11	0.09	0.01	0.006
	Sampling/ Analytical Method	Tap Water <sup>(a)</sup>			
		Site A	Site B	Site C	Site D
<b>Lead</b> (µg/L)	EPA200.8	ND	ND	ND	N/A
<b>Copper</b> (µg/L)	EPA200.8	75.1	624	21.8	

<sup>(a)</sup> kitchen tap water was collected based on the “Lead and Copper Rule” [208]; <sup>(c)</sup> Total organic carbon (TOC) for all four sites was below  $\leq 1$  mg/L; N/A: not available; <sup>(d)</sup> Site D was evaluated for comparative analysis, but was excluded from the final analysis since it did not qualify as a Small Water System as defined by the State of California [207].

## B.5 Results and discussions

Field testing of the feasibility of RO desalting with concentrate recycle was conducted with membrane M-1 (**Appendix B.2**) at recovery of 90%. Product water quality was well below the MCL of nitrate by 23%, 41% and 75% for Site A, B, C, and D, respectively (**Fig. B.2**). Salinity reduction was also effective with the treated product water salinity being in the range of 46-300 mg/L, well below the recommended upper limit of 500 mg/L TDS for all sites. Nitrate rejection, however, was in the range of 83%-87% which could prove to be insufficient with membrane M-1 to meet the MCL for nitrate removal of feed water in excess of 17.3 mg/L nitrate as N and salinity SMCL in excess of 2100 mg/L TDS.

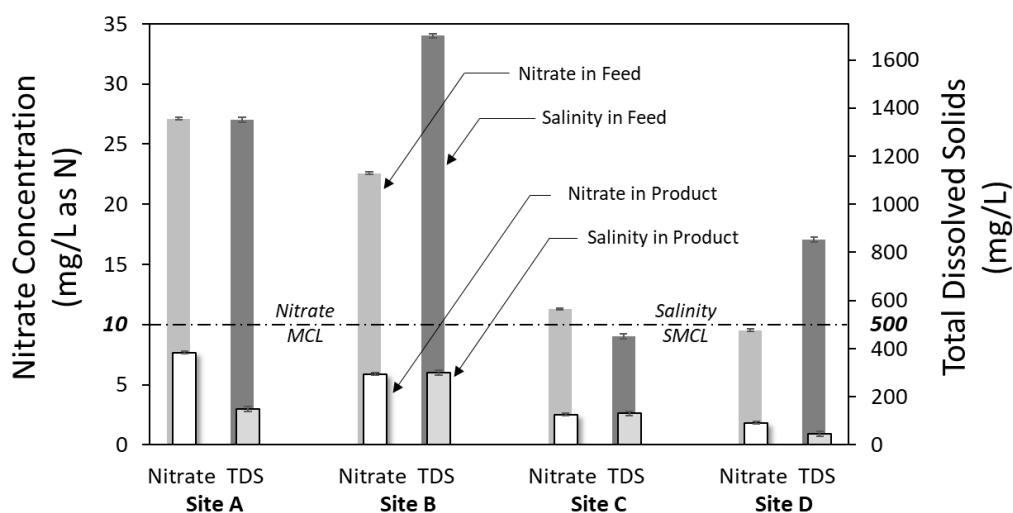


**Fig. B.2.** Onsite testing of RO well water treatment for the study communities. The RO test system (**Appendix A**) was operated at water recovery of 90% in SSRO-PR. The dashed line denotes the nitrate MCL (10 mg/L as N) and the recommended upper salinity level (500 mg/L TDS) for drinking water. The error bar indicates the salinity and nitrate range of measurement uncertainty.

In order to accommodate the potential for upward temporal fluctuations in source water quality (particularly with respect to nitrate in groundwater adjacent to agricultural areas [209]) the use of higher nitrate and salt rejection membrane was considered. Accordingly, a membrane

having nitrate and salt rejection of 96% and 99.7%, respectively was evaluated (i.e., membrane M-2, **Appendix B.2**) for treatment of source water of nitrate concentration in the range of 13-40 mg/L as N and salinity of 1000 mg/L TDS. Laboratory tests of the product water nitrate concentration dependence on the treatment system recovery (**Fig. B.3**) matched predictions from **Equations (3-16)** and **(3-17)** (**Section 3.2.3**).

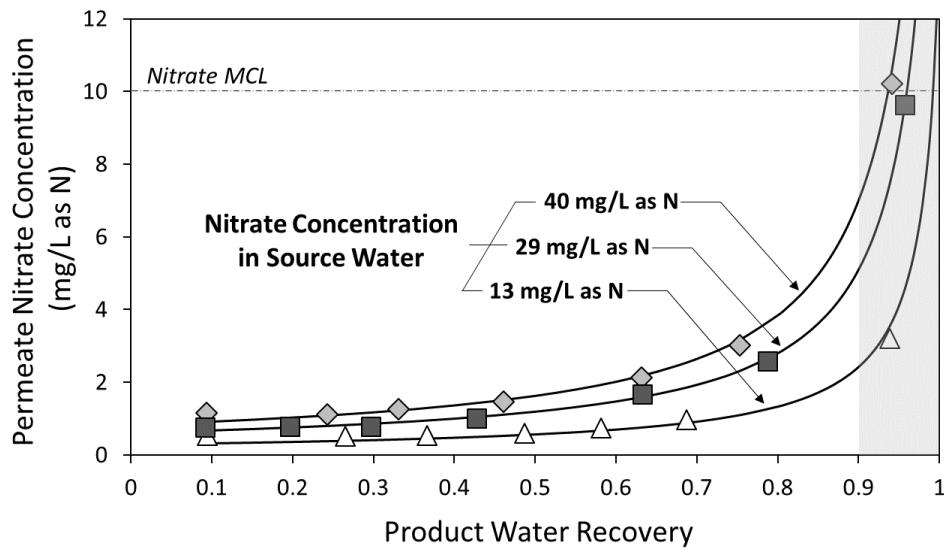


**Fig. B.3.** Nitrate concentration in the RO product water for treatment using a high nitrate rejection membrane (M-2) over a range of product water recovery for initial feed nitrate concentration of 13-40 mg/L as N. The solid curves are prediction of  $C_p = C_0 \cdot (1 - R_s)(1 - Y_{SP}) / [1 - R_s Y - Y_{SP}(1 - R_s)]$  (as per **Equations (3-16)** and **(3-17)**, **Section 3.2.3**). (Note: RO recovery must be maintained below 94%-99% in order to ensure that the product water meets both the MCL and SMCL with respect to nitrate and salinity, respectively, and that the feed pressure remains below the maximum allowed pressure for the RO element).

Water treatment can produce product water of concentration below the MCL for RO recovery of up to 94%-99% for the corresponding feed nitrate concentration range of 13-40 mg/L as N. Clearly, predictions as per **Equations (3-16)** and **(3-17)** (**Fig. B.3**) indicate that for operation at 90% recovery with membrane M-2 one could treat source water of up to a nitrate level of 19 mg/L as N and salinity of up to 9400 mg/L TDS and produce safe drinking water

that is at least 1/3 of the MCL in nitrate and  $\sim 1/2$  below the SMCL for salinity (similar level to 275 mg/L TDS of California State Water Project Deliveries [210]). The above study suggests that RO treatment can handle a wide range of nitrate levels at high recovery operation to provide safe drinking water for remote and often disadvantaged communities.

## Appendix C. Membrane Surface Monitor Operation

The membrane surface monitor (MeSuM) (Section 5.3.3) was operated through the graphical user interface, GUI (Fig. 5-3), which records sensor readings and sets the pressure and crossflow velocity.

### C.1 Membrane coupon preparation

1. Cut membrane coupons from a larger sheet of membrane to a size that would overlap the flow channel of the membrane cell (Fig. 5-2a,  $\sim 10 \text{ cm} \times 5 \text{ cm}$ ).
2. Gently rinse the membranes with de-ionized (DI) water for  $\sim 3$  minutes.
3. Place the membrane coupons in a 600 mL beaker of DI water, cover the beaker with parafilm and place in refrigerator for at least  $\sim 2$  hours and up to 3 days. **Note:** If stored for extended periods, the membrane should be stored in a preservative solution of 0.5 – 1 wt.% sodium meta-bisulfite in sealed plastic bags.

### C.2 Model solution preparation

The following is a procedure to prepare for the model solution (Table 5-1) for evaluation of gypsum scaling in Chapter 5.

1. Fill two 4L Erlenmeyer flasks with DI water to accommodate  $\text{CaCl}_2 \cdot 2\text{H}_2\text{O}$  and  $\text{Na}_2\text{SO}_4$
2. Prepare for 890g  $\text{CaCl}_2 \cdot 2\text{H}_2\text{O}$  and 860g  $\text{Na}_2\text{SO}_4$  by using weight balance.
3. Dissolve  $\text{CaCl}_2 \cdot 2\text{H}_2\text{O}$  and  $\text{Na}_2\text{SO}_4$  in DI water in separate Erlenmeyer flasks using a magnetic stir bar and a stir plate. **Note:** Cover each beaker with parafilm to prevent contamination.
4. Slowly transfer the prepared solution in the flasks to the large RO feed tank, which is filled with DI water using a peristaltic pump.



### C.3 System operating procedure

1. Lightly rinse the feed channel of the membrane cell before inserting the membrane coupon.
2. Place the membrane coupon flat inside the MeSuM cell.
3. Carefully check the o-ring gasket for any damage that may lead to water leakage or membrane damage. Note: It is recommended to periodically re-lubricate the o-ring gasket with a compatible lubricant.
4. Clamp the cell by tightening threaded nuts onto the studs. **Attention:** Use a pre-calibrated torque wrench to equally fasten each nut. Start with low torque setting, then tighten each of the four studs following the crisscross sequence to avoid cell damage from overtightening.
5. Connect the MeSuM with the RO system (as per **Fig. 5-1**), in order to provide the feed flow of a standard sodium chloride solution or other test solution (e.g., a partial salt scaling solution of  $\text{Na}_2\text{SO}_4$ ). **Note:** the hydraulic valve for MeSuM concentrate stream should be 100% opened (V2, **Fig. 5-1**).
6. Gradually increase the pressure upto 200 psig. Check for leakage.
7. Open the image acquisition software to examine membrane surface.
8. Adjust camera focus and light arrangement to verify that the membrane appears clean (i.e., free from air bubbles, contaminants, membrane damage, etc.). **Note:** The system may require extended water flushing to ensure that the membrane and system are clean and free of air bubbles.
9. For membrane compaction, operate the system using DI water under the applied pressure of 200 psig for at least 24 hours. Before each experiment, verify constant water permeability and salt rejection have stabilized (i.e., time-invariant).

## **Appendix D. System cleaning procedure**

### **Light Cleaning –DI Water**

**Note:** If the system has been operated for a period of 1-2 weeks, then light cleaning is sufficient, unless a solution containing significant amounts of organic or biological material was used, such as a wastewater solution.

1. Fill the RO feed tank with 20L of DI water.
2. Place a membrane coupon in the membrane cell and securely tighten the cell studs.
3. Follow the start-up procedure in **Section A.3.1** to start the system
4. Recirculate the DI water through the system for 24 hours at 5-10 bar and 30-50 L/hr.
5. Turn off the pump.

### **Heavy Cleaning – EDTA + NaOH**

**Note:** Chemical cleaning is necessary when the system has not been used for more than several weeks or the system was determined to be contaminated.

1. Remove the microfilter cartridges and re-tighten the filter housing.
2. Remove the spiral wound RO element and membrane coupon from MeSuM cell and securely tighten the cell studs.
3. Fill the feed tank with DI water containing EDTA dissolved in 1 g/L and NaOH at 4 g/L (final pH ~ 13).
4. Start the system following the start-up procedure in **Section A.3.1**, and circulate the solution at 5-10 bar and 30-50 L/hr for 30 minutes.
5. Drain the system.

6. Rinse the feed tank with DI water and recirculate DI water through the system until the discharge water pH reaches the DI water pH value.
7. Dissolve sodium meta-bisulfite in the RO feed tank containing 1 wt.% in 20L DI water.
8. Start the system following the start-up procedure in **Section A.3.1**, and circulate the solution at 5-10 bar and 30-50 L/hr for 45 minutes.
9. Turn off the system by pressing M2, and then M1 buttons (**Fig. A.4**).
10. Open the pressure relief valve,  $V_{PR}$ , (**Fig. A.5**) to depressurize the system.
11. Close the concentrate discharge valve, V4 (**Fig. A.1**).
12. To preserve the system for an extended period, leave the sodium meta-bisulfite solution in the system

## References

- [1] American Society of Civil Engineers, 2009 Report Card for America's Infrastructure, [www.asce.org/reportcard](http://www.asce.org/reportcard), in, ASCE, Washington, D.C., 2009.
- [2] B.I. Cook, T.R. Ault, J.E. Smerdon, Unprecedented 21st century drought risk in the American Southwest and Central Plains, *Science Advances*, 1 (2015).
- [3] Committee on Future Options for Management in the Nation's Subsurface Remediation Effort, National Research Council, Alternatives for Managing the Nation's Complex Contaminated Groundwater Sites, National Academies Press, Washington, D.C., 2013.
- [4] E.M. Biggs, E. Bruce, B. Boruff, J.M.A. Duncan, J. Horsley, N. Pauli, K. McNeill, A. Neef, F. Van Ogtrop, J. Curnow, B. Haworth, S. Duce, Y. Imanari, Sustainable development and the water–energy–food nexus: A perspective on livelihoods, *Environmental Science & Policy*, 54 (2015) 389-397.
- [5] D.C. DiGiulio, R.B. Jackson, Impact to Underground Sources of Drinking Water and Domestic Wells from Production Well Stimulation and Completion Practices in the Pavillion, Wyoming, *Field, Environmental Science & Technology*, 50 (2016) 4524-4536.
- [6] J. Schewe, J. Heinke, D. Gerten, I. Haddeland, N.W. Arnell, D.B. Clark, R. Dankers, S. Eisner, B.M. Fekete, F.J. Colón-González, S.N. Gosling, H. Kim, X. Liu, Y. Masaki, F.T. Portmann, Y. Satoh, T. Stacke, Q. Tang, Y. Wada, D. Wisser, T. Albrecht, K. Frieler, F. Piontek, L. Warszawski, P. Kabat, Multimodel assessment of water scarcity under climate change, *Proceedings of the National Academy of Sciences of the United States of America*, 111 (2014) 3245-3250.
- [7] Reverse osmosis elements for Carlsbad desalination plant, *Filtration + Separation*, 52 (2015) 14.
- [8] V.G. Gude, Desalination and sustainability – An appraisal and current perspective, *Water Research*, 89 (2016) 87-106.
- [9] M. Wilf, Design consequences of recent improvements in membrane performance, *Desalination*, 113 (1997) 157-163.
- [10] V.G. Gude, Energy consumption and recovery in reverse osmosis, *Desalin Water Treat*, 36 (2011) 239-260.
- [11] R. Semiat, D. Hasson, Seawater and Brackish-Water Desalination with Membrane Operations, in: *Membrane Technology*, Wiley-VCH Verlag GmbH & Co. KGaA, 2010, pp. 147-168.
- [12] S. Gray, R. Semiat, M. Duke, A. Rahardianto, Y. Cohen, Seawater Use and Desalination Technology, *Treatise on Water Science, Vol 4: Water-Quality Engineering*, (2011) 73-109.

- [13] R. Semiat, Desalination - Present and Future, *Water International*, 25 (2000) 54-65.
- [14] S.S. Shenvi, A.M. Isloor, A.F. Ismail, A review on RO membrane technology: Developments and challenges, *Desalination*, 368 (2015) 10-26.
- [15] G. Amy, N. Ghaffour, Z. Li, L. Francis, R. Valladares Linares, T. Missimer, S. Lattemann, Membrane-based seawater desalination : Present and future prospects, *Desalination*, 401 (2017) 16-21.
- [16] L. Camacho, L. Dumée, J. Zhang, J.-d. Li, M. Duke, J. Gomez, S. Gray, Advances in Membrane Distillation for Water Desalination and Purification Applications, *water*, 5 (2013) 94-196.
- [17] D. Shaffer, J. Werber, H. Jaramillo, S. Lin, M. Elimelech, Forward osmosis: Where are we now?, 2014.
- [18] OCWD, OCSD, Groundwater Replenishment System Technical Brochure, Orange County Water District and Orange County Sanitation District, in, Fountain Valley, California, 2016.
- [19] L.X. Gao, A. Rahardianto, H. Gu, P.D. Christofides, Y. Cohen, Novel design and operational control of integrated ultrafiltration — Reverse osmosis system with RO concentrate backwash, *Desalination*, 382 (2016) 43-52.
- [20] L. Gao, A. Rahardianto, H. Gu, P.D. Christofides, Y. Cohen, Energy-Optimal Control of RO Desalination, *Industrial & Engineering Chemistry Research*, 53 (2014) 7409-7420.
- [21] F. Virgili, T. Pankratz, J. Gasson, IDA Desalination Yearbook 2015-2016, *Global Water Intelligence*, 2016.
- [22] Y. Cohen, R. Semiat, A. Rahardianto, A perspective on reverse osmosis water desalination: Quest for sustainability, *Aiche J*, 63 (2017) 1771-1784.
- [23] E. Jones, M. Qadir, M.T.H. van Vliet, V. Smakhtin, S.-m. Kang, The state of desalination and brine production: A global outlook, *Science of The Total Environment*, 657 (2019) 1343-1356.
- [24] M. Faigon, Success behind advanced SWRO desalination plant, *Filtration + Separation*, 53 (2016) 29-31.
- [25] B. Sauvet-Goichon, Ashkelon desalination plant — A successful challenge, *Desalination*, 203 (2007) 75-81.
- [26] M. Shahzad, K. Ng, Sustainable desalination using ocean thermocline energy, 2018.
- [27] T.D. Qiu, Philip A. , Comparison of Configurations for High-Recovery Inland Desalination Systems *Water*, 2012 (2012) 690-706.
- [28] L. Song, Z. Ma, X. Liao, P.B. Kosaraju, J.R. Irish, K.K. Sirkar, Pilot plant studies of novel

membranes and devices for direct contact membrane distillation-based desalination, *Journal of Membrane Science*, 323 (2008) 257-270.

[29] T. Qiu, D. P.A., Comparison of Configurations for High-Recovery Inland Desalination Systems, *water*, 2012 (2012) 690-706.

[30] R.I. Bratt, Fluid treatment by reverse osmosis - using high pressure loop including reverse osmosis membrane vessel, for treating sea water or well water, in, U.S., 1989.

[31] A. Efraty, Closed circuit desalination series no-3: high recovery low energy desalination of brackish water by a new two-mode consecutive sequential method, *Desalin Water Treat*, 42 (2012) 256-261.

[32] F. Vince, F. Marechal, E. Aoustin, P. Bréant, Multi-objective optimization of RO desalination plants, *Desalination*, 222 (2008) 96-118.

[33] H.M. Laborde, K.B. França, H. Neff, A.M.N. Lima, Optimization strategy for a small-scale reverse osmosis water desalination system based on solar energy, *Desalination*, 133 (2001) 1-12.

[34] M. Wilf, C. Bartels, Optimization of seawater RO systems design, *Desalination*, 173 (2005) 1-12.

[35] A. Zhu, P.D. Christofides, Y. Cohen, Energy Consumption Optimization of Reverse Osmosis Membrane Water Desalination Subject to Feed Salinity Fluctuation, *Industrial & Engineering Chemistry Research*, 48 (2009) 9581-9589.

[36] A. Giwa, V. Dufour, F. Al Marzooqi, M. Al Kaabi, S.W. Hasan, Brine management methods: Recent innovations and current status, *Desalination*, 407 (2017) 1-23.

[37] S.G. Yiantsios, D. Sioutopoulos, A.J. Karabelas, Colloidal fouling of RO membranes: an overview of key issues and efforts to develop improved prediction techniques, *Desalination*, 183 (2005).

[38] S. Lee, J. Cho, M. Elimelech, Influence of colloidal fouling and feed water recovery on salt rejection of RO and NF membranes, *Desalination*, 160 (2004) 1-12.

[39] X. Zhu, M. Elimelech, Colloidal Fouling of Reverse Osmosis Membranes: Measurements and Fouling Mechanisms, *Environmental Science & Technology*, 31 (1997) 3654-3662.

[40] S.S. Bucs, N. Farhat, J.C. Kruithof, C. Picioreanu, M.C.M. van Loosdrecht, J.S. Vrouwenvelder, Review on strategies for biofouling mitigation in spiral wound membrane systems, *Desalination*, 434 (2018) 189-197.

[41] M.A. Alghoul, P. Poovanaesvaran, K. Sopian, M.Y. Sulaiman, Review of brackish water reverse osmosis (BWRO) system designs, *Renewable and Sustainable Energy Reviews*, 13 (2009) 2661-2667.

- [42] S. Lin, M. Elimelech, Staged reverse osmosis operation: Configurations, energy efficiency, and application potential, *Desalination*, 366 (2015) 9-14.
- [43] J.R. Werber, A. Deshmukh, M. Elimelech, Can batch or semi-batch processes save energy in reverse-osmosis desalination?, *Desalination*, 402 (2017) 109-122.
- [44] T.Y. Qiu, P.A. Davies, Longitudinal dispersion in spiral wound RO modules and its effect on the performance of batch mode RO operations, *Desalination*, 288 (2012) 1-7.
- [45] Q. Yang, A. Drak, D. Hasson, R. Serniat, RO module RTD analyses based on directly processing conductivity signals, *Journal of Membrane Science*, 306 (2007) 355-364.
- [46] E. Lyster, J. Au, R. Rallo, F. Giralt, Y. Cohen, Coupled 3-D hydrodynamics and mass transfer analysis of mineral scaling-induced flux decline in a laboratory plate-and-frame reverse osmosis membrane module, *Journal of Membrane Science*, 339 (2009) 39-48.
- [47] E. Lyster, Y. Cohen, Numerical study of concentration polarization in a rectangular reverse osmosis membrane channel: Permeate flux variation and hydrodynamic end effects, *Journal of Membrane Science*, 303 (2007) 140-153.
- [48] D.M. Warsinger, E.W. Tow, L.A. Maswadeh, G.B. Connors, J. Swaminathan, J.H. Lienhard V, Inorganic fouling mitigation by salinity cycling in batch reverse osmosis, *Water Research*, 137 (2018) 384-394.
- [49] S.M. Riley, D.C. Ahoor, K. Oetjen, T.Y. Cath, Closed circuit desalination of O&G produced water: An evaluation of NF/RO performance and integrity, *Desalination*, 442 (2018) 51-61.
- [50] A. Efraty, R.N. Barak, Z. Gal, Closed circuit desalination series no-2: new affordable technology for sea water desalination of low energy and high flux using short modules without need of energy recovery, *Desalin Water Treat*, 42 (2011) 189-196.
- [51] M. Uchymiak, A. Rahardianto, E. Lyster, J. Glater, Y. Cohen, A novel RO ex situ scale observation detector (EXSOD) for mineral scale characterization and early detection, *Journal of Membrane Science*, 291 (2007) 86-95.
- [52] N. Pomerantz, Y. Ladizhansky, E. Korin, M. Waisman, N. Daltrophe, J. Gilron, Prevention of Scaling of Reverse Osmosis Membranes by “Zeroing” the Elapsed Nucleation Time. Part I. Calcium Sulfate, *Industrial & Engineering Chemistry Research*, 45 (2006) 2008-2016.
- [53] D. Li, Y. Yan, H. Wang, Recent advances in polymer and polymer composite membranes for reverse and forward osmosis processes, *Progress in Polymer Science*, 61 (2016) 104-155.
- [54] L. Malaeb, G.M. Ayoub, Reverse osmosis technology for water treatment: State of the art review, *Desalination*, 267 (2011) 1-8.
- [55] L.F. Greenlee, D.F. Lawler, B.D. Freeman, B. Marrot, P. Moulin, Reverse osmosis desalination: Water sources, technology, and today's challenges, *Water Research*, 43 (2009)

2317-2348.

[56] M.A. Al Mamun, S. Bhattacharjee, D. Pernitsky, M. Sadrzadeh, Colloidal Fouling of Nanofiltration Membranes: Development of a Standard Operating Procedure, *Membranes*, 7 (2017).

[57] W. Mulder, *Basic Principles of Membrane Technology*, 2nd ed., Kluwer Academic Publishers, Boston, 1997.

[58] Zhu, A, P.D. Christofides, Y. Cohen, Effect of Thermodynamic Restriction on Energy Cost Optimization of RO Membrane Water Desalination, *Ind. Eng. Chem. Res.*, 48 (2009) 6010-6021.

[59] M. Kargol, A. Kargol, Investigation of reverse osmosis on the basis of the Kedem-Katchalsky equations and mechanistic transport equations, *Desalination*, 190 (2006) 267-276.

[60] K.S. Spiegel, O. Kedem, Thermodynamics of hyperfiltration (reverse osmosis): criteria for efficient membranes, *Desalination*, 1 (1966) 311-326.

[61] M. Mulder, *Basic Principles of Membrane Technology*, Kluwer Academic Publishers, Boston, (1997).

[62] E.L. Cussler, *Diffusion: Mass Transfer in Fluid Systems*, Second ed., Cambridge University Press, New York, 1997.

[63] A. Zhu, Energy and Cost Optimization of Reverse Osmosis Desalination (Doctoral dissertation) in: *Chemical and Biomolecular Engineering University of California Los Angeles* 2012.

[64] J. Thompson, A. Rahardianto, S. Kim, M. Bilal, R. Breckenridge, Y. Cohen, Real-time direct detection of silica scaling on RO membranes, *Journal of Membrane Science*, 528 (2017) 346-358.

[65] S. Loeb, S. Sourirajan, Sea Water Demineralization by Means of an Osmotic Membrane, in: *Saline Water Conversion—II*, AMERICAN CHEMICAL SOCIETY, 1963, pp. 117-132.

[66] P.S. Singh, P. Ray, P. Kallem, S. Maurya, G.S. Trivedi, Structure and performance of nanofiltration membrane prepared in a large-scale at CSIR-CSMCRI using indigenous coating unit, *Desalination*, 288 (2012) 8-15.

[67] C. Bartels, M. Hirose, H. Fujioka, Performance advancement in the spiral wound RO/NF element design, *Desalination*, 221 (2008) 207-214.

[68] P.L. Riley, C.E. Milstead, A.L. Lloyd, M.W. Seroy, M. Tagami, Spiral-wound thin-film composite membrane systems for brackish and seawater desalination by reverse osmosis, *Desalination*, 23 (1966) 331-355.

[69] J. Schwinge, P.R. Neal, D.E. Wiley, D.F. Fletcher, A.G. Fane, *Spiral wound modules and*



spacers: Review and analysis, *Journal of Membrane Science*, 242 (2004) 129-153.

[70] G. Han, Demonstration of Rapid Membrane Characterization and Real-Time Membrane Module performance Analysis Using an Automated Reverse Osmosis Desalination Pilot Plant, (2010).

[71] A.L. Zydney, Stagnant film model for concentration polarization in membrane systems, *Journal of Membrane Science*, 130 (1997) 275-281.

[72] S.S. Sablani, M.F.A. Goosen, R. Al-Belushi, M. Wilf, Concentration polarization in ultrafiltration and reverse osmosis: a critical review, *Desalination*, 141 (2001) 269-289.

[73] M. Uchymiak, E. Lyster, J. Glater, Y. Cohen, Kinetics of gypsum crystal growth on a reverse osmosis membrane, *Journal of Membrane Science*, 314 (2008) 163-172.

[74] M. Uchymiak, A.R. Bartman, N. Daltrophe, M. Weissman, J. Gilron, P.D. Christofides, W.J. Kaiser, Y. Cohen, Brackish water reverse osmosis (BWRO) operation in feed flow reversal mode using an ex situ scale observation detector (EXSOD), *Journal of Membrane Science*, 341 (2009) 60-66.

[75] A.R. Bartman, E. Lyster, R. Rallo, P.D. Christofides, Y. Cohen, Mineral scale monitoring for reverse osmosis desalination via real-time membrane surface image analysis, *Desalination*, 273 (2011) 64-71.

[76] S.F.E. Boerlage, M.D. Kennedy, I. Bremere, G.J. Witkamp, J.P. Van der Hoek, J.C. Schippers, The scaling potential of barium sulphate in reverse osmosis systems, *Journal of Membrane Science*, 197 (2002) 251-268.

[77] B.C. McCool, A. Rahardianto, J. Faria, K. Kovac, D. Lara, Y. Cohen, Feasibility of reverse osmosis desalination of brackish agricultural drainage water in the San Joaquin Valley, *Desalination*, 261 (2010) 240-250.

[78] J. Wang, L. Wang, R. Miao, Y. Lv, X. Wang, X. Meng, R. Yang, X. Zhang, Enhanced gypsum scaling by organic fouling layer on nanofiltration membrane: Characteristics and mechanisms, *Water Research*, 91 (2016) 203-213.

[79] M.A. Rotter, S. Kwong, R.W. Briehl, F.A. Ferrone, Heterogeneous Nucleation in Sickle Hemoglobin: Experimental Validation of a Structural Mechanism, *Biophysical Journal*, 89 (2005) 2677-2684.

[80] J. Thompson, N. Lin, E. Lyster, R. Arbel, T. Knoell, J. Gilron, Y. Cohen, RO membrane mineral scaling in the presence of a biofilm, *Journal of Membrane Science*, 415-416 (2012) 181-191.

[81] D. Hasson, A. Drak, R. Semiat, Inception of CaSO<sub>4</sub> scaling on RO membranes at various water recovery levels, *Desalination*, 139 (2001) 73-81.

[82] R. Semiat, I. Sutzkover, D. Hasson, Technique for evaluating silica scaling and its

inhibition in RO desalting, *Desalination*, 140 (2001) 181-193.

[83] W.-Y. Shih, K. Albrecht, J. Glater, Y. Cohen, A dual-probe approach for evaluation of gypsum crystallization in response to antiscalant treatment, *Desalination*, 169 (2004) 213-221.

[84] A.J. Karabelas, A. Karanasiou, S.T. Mitrouli, Incipient membrane scaling by calcium sulfate during desalination in narrow spacer-filled channels, *Desalination*, 345 (2014) 146-157.

[85] W.-Y. Shih, A. Rahardianto, R.-W. Lee, Y. Cohen, Morphometric characterization of calcium sulfate dihydrate (gypsum) scale on reverse osmosis membranes, *Journal of Membrane Science*, 252 (2005) 253-263.

[86] S. Lee, C.-H. Lee, Effect of operating conditions on CaSO<sub>4</sub> scale formation mechanism in nanofiltration for water softening, *Water Research*, 34 (2000) 3854-3866.

[87] M. Brusilovsky, J. Borden, D. Hasson, Flux decline due to gypsum precipitation on RO membranes, *Desalination*, 86 (1992) 187-222.

[88] H. Shemer, D. Hasson, R. Semiat, Review of the State of the Art of Antiscalant Selection, *Mineral Scales in Biological and Industrial Systems*, CRC Press, (2013) 227-256, doi: 210.1201/b15606-15616.

[89] J.W. Mullin, *Crystallization*, 3rd ed., Butterworth-Heinemann, Oxford, 1997.

[90] A.E. Nielsen, *Kinetics of Precipitation*, Pergamon Press (distributed in the Western Hemisphere by Macmillan, New York), Oxford, New York, 1964.

[91] P. Dydo, M. Turek, J. Ciba, K. Wandachowicz, J. Misztal, The nucleation kinetic aspects of gypsum nanofiltration membrane scaling, *Desalination*, 164 (2004) 41-52.

[92] O. Söhnel, J.W. Mullin, Interpretation of crystallization induction periods, *Journal of Colloid and Interface Science*, 123 (1988) 43-50.

[93] A. Milchev, I. Krastev, Two-dimensional progressive and instantaneous nucleation with overlap: The case of multi-step electrochemical reactions, *Electrochimica Acta*, 56 (2011) 2399-2403.

[94] O. Söhnel, J.W. Mullin, Precipitation of calcium carbonate, *Journal of Crystal Growth*, 60 (1982) 239-250.

[95] S. He, J.E. Oddo, M.B. Tomson, The Nucleation Kinetics of Calcium Sulfate Dihydrate in NaCl Solutions up to 6 m and 90°C, *Journal of Colloid and Interface Science*, 162 (1994) 297-303.

[96] D. Hasson, A. Drak, R. Semiat, Induction times induced in an RO system by antiscalants delaying CaSO<sub>4</sub> precipitation, *Desalination*, 157 (2003) 193-207.

[97] S. He, A.T. Kan, M.B. Tomson, Inhibition of calcium carbonate precipitation in NaCl

brines from 25 to 90°C, *Applied Geochemistry*, 14 (1999) 17-25.

[98] X. Li, D. Hasson, H. Shemer, Flow conditions affecting the induction period of CaSO<sub>4</sub> scaling on RO membranes, *Desalination*, 431 (2018) 119-125.

[99] Y. Cohen, M. Uchymiak, Method and System for Monitoring Reverse Osmosis Membranes, in, 2011.

[100] H. Gu, A.R. Bartman, M. Uchymiak, P.D. Christofides, Y. Cohen, Self-adaptive feed flow reversal operation of reverse osmosis desalination, *Desalination*, 308 (2013) 63-72.

[101] J. Thompson, A. Rahardianto, H. Gu, M. Uchymiak, A. Bartman, M. Hedrick, D. Lara, J. Cooper, J. Faria, P.D. Christofides, Y. Cohen, Rapid field assessment of RO desalination of brackish agricultural drainage water, *Water Research*, 47 (2013) 2649-2660.

[102] E. Lyster, M.-m. Kim, J. Au, Y. Cohen, A method for evaluating antiscalant retardation of crystal nucleation and growth on RO membranes, *Journal of Membrane Science*, 364 (2010) 122-131.

[103] A. Packter, The precipitation of calcium sulphate dihydrate from aqueous solution: Induction periods, crystal numbers and final size, *Journal of Crystal Growth*, 21 (1974) 191-194.

[104] S. Oren, L. Birnhack, O. Lehmann, O. Lahav, A different approach for brackish-water desalination, comprising acidification of the feed-water and CO<sub>2</sub>(aq) reuse for alkalinity, Ca<sup>2+</sup> and Mg<sup>2+</sup> supply in the post treatment stage, *Separation and Purification Technology*, 89 (2012) 252-260.

[105] B.T. Croll, Membrane Technology - the Way Forward, *J Inst Water Env Man*, 6 (1992) 121-129.

[106] A. Venkatesan, P.C. Wankat, Simulation of ion exchange water softening pretreatment for reverse osmosis desalination of brackish water, *Desalination*, 271 (2011) 122-131.

[107] M.M. Kim, J. Au, A. Rahardianto, J. Glater, Y. Cohen, F.W. Geringer, C.J. Gabelich, Impact of Conventional Water Treatment Coagulants on Mineral Scaling in RO Desalting of Brackish Water, *Industrial & Engineering Chemistry Research*, 48 (2009) 3126-3135.

[108] J. Benecke, J. Rozova, M. Ernst, Anti-scale effects of select organic macromolecules on gypsum bulk and surface crystallization during reverse osmosis desalination, *Separation and Purification Technology*, 198 (2018) 68-78.

[109] M. Malki, Case Study: Optimizing Scale Inhibition Costs in Reverse Osmosis Desalination Plants American Water Chemicals, Inc., (2009) 1-8.

[110] B. McCool, A. Rahardianto, J. Faria, K. Kovac, D. Lara, Y. Cohen, Feasibility of reverse osmosis desalination of brackish agricultural drainage water in the San Joaquin Valley, *Desalination*, 261 (2010) 240-250.

- [111] R. de Abreu Domingos, F.V. da Fonseca, Evaluation of adsorbent and ion exchange resins for removal of organic matter from petroleum refinery wastewaters aiming to increase water reuse, *Journal of Environmental Management*, 214 (2018) 362-369.
- [112] J.R. Stahlbush, R.M. Strom, A decomposition mechanism for cation exchange resins, *Reactive Polymers*, 13 (1990) 233-240.
- [113] J. Lipnizki, B. Adams, M. Okazaki, A. Sharpe, Water treatment: Combining reverse osmosis and ion exchange, *Filtration + Separation*, 49 (2012) 30-33.
- [114] H.-J. Oh, Y.-K. Choung, S. Lee, J.-S. Choi, T.-M. Hwang, J.H. Kim, Scale formation in reverse osmosis desalination: model development, *Desalination*, 238 (2009) 333-346.
- [115] W.S. Ang, S.Y. Lee, M. Elimelech, Chemical and physical aspects of cleaning of organic-fouled reverse osmosis membranes, *Journal of Membrane Science*, 272 (2006) 198-210.
- [116] C. Ma, L. Wang, S. Li, S.G.J. Heijman, L.C. Rietveld, X.B. Su, Practical experience of backwashing with RO permeate for UF fouling control treating surface water at low temperatures, *Separation and Purification Technology*, 119 (2013) 136-142.
- [117] J. Gilron, M. Waisman, N. Daltrophe, N. Pomerantz, M. Milman, I. Ladizhansky, E. Korin, Prevention of precipitation fouling in NF/RO by reverse flow operation, *Desalination*, 199 (2006) 29-30.
- [118] H. Wang, M. Gao, Y. Guo, Y. Yang, R. Hu, A natural extract of tobacco rob as scale and corrosion inhibitor in artificial seawater, *Desalination*, 398 (2016) 198-207.
- [119] A.I. Schäfer, A.G. Fane, T.D. Waite, *Nanofiltration: principles and applications*, Elsevier Science, 2005.
- [120] B.A.M. Al-Rashdi, D.J. Johnson, N. Hilal, Removal of heavy metal ions by nanofiltration, *Desalination*, 315 (2013) 2-17.
- [121] E. Steinle-Darling, M. Reinhard, Nanofiltration for Trace Organic Contaminant Removal: Structure, Solution, and Membrane Fouling Effects on the Rejection of Perfluorochemicals, *Environmental Science & Technology*, 42 (2008) 5292-5297.
- [122] B. Van der Bruggen, K. Everaert, D. Wilms, C. Vandecasteele, Application of nanofiltration for removal of pesticides, nitrate and hardness from ground water: rejection properties and economic evaluation, *Journal of Membrane Science*, 193 (2001) 239-248.
- [123] U.S. National Archives and Records Administration, Secondary maximum contaminant levels, Code of Federal Regulations, Title 40, Section § 143.3 (2016).
- [124] I.C. Watson, O.J. Morin Jr., L. Henthorne, *Desalting Handbook for Planners*, Third Edition, in: *Desalination and Water Purification Research and Development Program Report No. 72*, U.S. Bureau of Reclamation, Denver, CO, 2003.

- [125] M. Pontie, S. Rapenne, A. Thekkedath, J. Duchesne, V. Jacquemet, J. Leparc, H. Suty, Tools for membrane autopsies and antifouling strategies in seawater feeds: a review, *Desalination*, 181 (2005) 75-90.
- [126] N. Voutchkov, Considerations for selection of seawater filtration pretreatment system, *Desalination*, 261 (2010) 354-364.
- [127] N. Ghaffour, T.M. Missimer, G.L. Amy, Technical review and evaluation of the economics of water desalination: current and future challenges for better water supply sustainability, *Desalination*, 309 (2013) 197-207.
- [128] T. Manth, M. Gabor, E. Oklejas Jr, Minimizing RO energy consumption under variable conditions of operation, *Desalination*, 157 (2003) 9-21.
- [129] A.M. Farooque, A.T.M. Jamaluddin, A.R. Al-Reweli, P.A.M. Jalaluddin, S.M. Al-Marwani, A.A. Al-Mobayed, A.H. Qasim, Parametric analyses of energy consumption and losses in SWCC SWRO plants utilizing energy recovery devices, *Desalination*, 219 (2008) 137-159.
- [130] R. Semiat, Energy Issues in Desalination Processes, *Environmental Science & Technology*, 42 (2008) 8193-8201.
- [131] M. Li, Minimization of Energy in Reverse Osmosis Water Desalination Using Constrained Nonlinear Optimization, *Industrial & Engineering Chemistry Research*, 49 (2010) 1822-1831.
- [132] A.H. Zhu, P.D. Christofides, Y. Cohen, Minimization of energy consumption for a two-pass membrane desalination: Effect of energy recovery, membrane rejection and retentate recycling, *Journal of Membrane Science*, 339 (2009) 126-137.
- [133] S.H. Fathi, A. Shabani, Optimization of Energy Consumption and Load Management In Industries, 2005.
- [134] L. Song, J.Y. Hu, S.L. Ong, W.J. Ng, M. Elimelech, M. Wilf, Emergence of thermodynamic restriction and its implications for full-scale reverse osmosis processes, *Desalination*, 155 (2003) 213-228.
- [135] L. Song, J.Y. Hu, S.L. Ong, W.J. Ng, M. Elimelech, M. Wilf, Performance limitation of the full-scale reverse osmosis process, *Journal of Membrane Science*, 214 (2003) 239-244.
- [136] A. Zhu, P.D. Christofides, Y. Cohen, Effect of Thermodynamic Restriction on Energy Cost Optimization of RO Membrane Water Desalination, *Industrial & Engineering Chemistry Research*, 48 (2009) 6010-6021.
- [137] E. Cardona, A. Piacentino, F. Marchese, Energy saving in two-stage reverse osmosis systems coupled with ultrafiltration processes, *Desalination*, 184 (2005) 125-137.
- [138] S. Kremen, M. Wilf, P. Lange, Operating results and economics of single stage and two

stage large size sea water RO systems, *Desalination*, 82 (1991) 3-13.

[139] A.S.a.T. BERMUDEZ-CONTRERAS, M., Energy recovery for reverse osmosis desalination in Mexico, Proceedings of the 1st IWA Mexico National Young Water Professionals Conference, (2008).

[140] M.J. Guirguis, Energy Recovery Devices in Seawater Reverse Osmosis Desalination Plants with Emphasis on Efficiency and Economical Analysis of Isobaric versus Centrifugal Devices, Master of Science Thesis University of South Florida (2011).

[141] R. Huehmer, S. Alt, J. Lozier, A. Kupp, T. Nading, K. Egrican, B. Emerson, Evaluation and Optimization of Emerging and Existing Energy Recovery Devices for Desalination and Wastewater Membrane Treatment Plants, WateReuse Research Foundation, Alexandria, VA, 2013.

[142] R. Huehmer, S. Alt, J. Lozier, A. Kupp, T. Nading, K. Egrican, B. Emerson, Evaluation and Optimization of Emerging and Existing Energy Recovery Devices for Desalination and Wastewater Membrane Treatment Plants, WateReuse Research Foundation Project No. WRF-08-14, (2014).

[143] N.M. Mazlan, D. Peshev, A.G. Livingston, Energy consumption for desalination — A comparison of forward osmosis with reverse osmosis, and the potential for perfect membranes, *Desalination*, 377 (2016) 138-151.

[144] C. Fritzmann, J. Löwenberg, T. Wintgens, T. Melin, State-of-the-art of reverse osmosis desalination, *Desalination*, 216 (2007) 1-76.

[145] M. Elimelech, W.A. Phillip, The Future of Seawater Desalination: Energy, Technology, and the Environment, *Science*, 333 (2011) 712.

[146] S. Miller, H. Shemer, R. Semiat, Energy and environmental issues in desalination, *Desalination*, 366 (2015) 2-8.

[147] A. Efraty, CCD series no-19: The lowest energy prospects for SWRO through single-element modules under plug-flow and closed-circuit desalination conditions, *Desalin Water Treat*, (2016).

[148] CSM, Technical Manual Reverse Osmosis Membrane Woongjin Chemical, (2010) 143-145.

[149] M.A. Al-Obaidi, C. Kara- Zaïtri, I.M. Mujtaba, Optimum design of a multi-stage reverse osmosis process for the production of highly concentrated apple juice, *Journal of Food Engineering*, 214 (2017) 47-59.

[150] N. Voutchkov, Chapter 1 - Membrane Desalination—Process Selection, Design, and Implementation, in: V.G. Gude (Ed.) *Sustainable Desalination Handbook*, Butterworth-Heinemann, 2018, pp. 3-24.

- [151] A.-M. Georgescu, C. Coşoiu, P. Sorin, S.-C. Georgescu, H. Liviu Valer, A. Anton, Estimation of the Efficiency for Variable Speed Pumps in EPANET Compared with Experimental Data, 2014.
- [152] B. Stoffel, Chapter 4 - Physical and Technical Background of the Efficiency of Pumps, in: B. Stoffel (Ed.) Assessing the Energy Efficiency of Pumps and Pump Units, Elsevier, Boston, 2015, pp. 45-61.
- [153] G. Bombar, D. Dolgen, M.N. Alpaslan, Environmental impacts and impact mitigation plans for desalination facilities, *Desalin Water Treat*, 57 (2016) 11528-11539.
- [154] N. Afrasiabi, E. Shahbazali, RO brine treatment and disposal methods, *Desalin Water Treat*, 35 (2011) 39-53.
- [155] A.H. Zhu, A. Rahardianto, P.D. Christofides, Y. Cohen, Reverse osmosis desalination with high permeability membranes - Cost optimization and research needs, *Desalin Water Treat*, 15 (2010) 256-266.
- [156] R.I. Bratt, Method and apparatus for fluid treatment by reverse osmosis, US Patent No. 4,814,086 A, (1989).
- [157] A. Efraty, Continuous closed-circuit desalination apparatus without containers, US Patent No. 7,695,614 B2, (2010).
- [158] R. Stover, CCD starts a new generation for RO, 2011.
- [159] A. Efraty, Closed circuit desalination series no-6: conventional RO compared with the conceptually different new closed circuit desalination technology, *Desalin Water Treat*, 41 (2012) 279-295.
- [160] R.L. Stover, N. Efraty, Low-Energy Consumption With Closed-Circuit Desalination, *IDA Journal of Desalination and Water Reuse*, 4 (2012) 12-19.
- [161] D.M. Warsinger, E.W. Tow, K.G. Nayar, L.A. Maswadeh, V.J. Lienhard, Energy efficiency of batch and semi-batch (CCRO) reverse osmosis desalination, *Water Research*, 106 (2016) 272-282.
- [162] A. Efraty, Closed circuit desalination series no-4: high recovery low energy desalination of brackish water by a new single stage method without any loss of brine energy, *Desalin Water Treat*, 42 (2012) 262-268.
- [163] A. Drak, M. Kerstholt, G. Houwelingen, T. Efrat, Reverse osmosis system with high recovery for industrial water treatment applications The international Desalination Association World Congress, (2017).
- [164] R.L. Stover, CCD starts a new generation for RO, *Desalination & Water Reuse*, 6 (2011) 34-35.

- [165] L. Song, B. Schuetze, K. Rainwater, Demonstration of a High Recovery and Energy Efficient RO System for Small-Scale Brackish Water Desalination, in, Texas Water Development Board, 2012.
- [166] B. Schuetze, K. Rainwater, L. Song, Closed-Concentrate Circulation for High Recovery and Energy Efficiency in Small-Scale Brackish Reverse Osmosis, *Journal of Environmental Engineering*, 140 (2014) 04014012.
- [167] J. Swaminathan, E. W. Tow, D. Warsinger, J. H Lienhard, Effect of practical losses on optimal design of batch RO systems. In: IDA 2017 World Congress on Water Reuse and Desalination, in: IDA, Sao Paulo, Brazil, 2017.
- [168] A. Efraty, R. Natanel Barak, Z. Gal, Closed circuit desalination — A new low energy high recovery technology without energy recovery, 2011.
- [169] D. Hasson, A. Drak, C. Komlos, Q. Yang, R. Semiat, Detection of fouling on RO modules by residence time distribution analyses, *Desalination*, 204 (2007) 132-144.
- [170] D. VanGauwbergen, J. Baeyens, Macroscopic fluid flow conditions in spiral-wound membrane elements, *Desalination*, 110 (1997) 287-299.
- [171] D.M. Warsinger, E.W. Tow, K.G. Nayar, L.A. Maswadeh, J.H. Lienhard V, Energy efficiency of batch and semi-batch (CCRO) reverse osmosis desalination, *Water Research*, 106 (2016) 272-282.
- [172] A. Rahardianto, W.Y. Shih, R.W. Lee, Y. Cohen, Diagnostic characterization of gypsum scale formation and control in RO membrane desalination of brackish water, *Journal of Membrane Science*, 279 (2006) 655-668.
- [173] L. Szucz, A. Szucs, Method and apparatus for treating fluids containing foreign materials by membrane filter equipment, US Patent No. 4,983,301 A, (1991).
- [174] E. Oklejas Jr, Method and apparatus for membrane recirculation and concentrate energy recovery in a reverse osmosis system, US Patent No. 6797173 B1, (2004).
- [175] A. Efraty, R.N. Barak, Z. Gal, Apparatus for continuous closed circuit desalination under variable pressure with a single container, US Patent No. 7,628,921 B2, (2009).
- [176] A. Efraty, Continuous closed-circuit desalination method without containers, US Patent No. 8,025,804 B2, (2011).
- [177] A. Efraty, J. Septon, Closed circuit desalination series no-5: high recovery, reduced fouling and low energy nitrate decontamination by a cost-effective BWRO-CCD method, *Desalin Water Treat*, 49 (2012) 384-389.
- [178] A. Efraty, CCD Series No-14: SWRO-CCD under fixed-pressure and variable flow compared with fixed-flow and variable pressure conditions, *Desalin Water Treat*, 56 (2015) 875-893.



- [179] Z. Gal, A. Efraty, CCD series no. 18: record low energy in closed-circuit desalination of Ocean seawater with nanoH<sub>2</sub>O elements without ERD, *Desalin Water Treat*, 57 (2016) 9180-9189.
- [180] Z. Gal, J. Septon, A. Efraty, A.-M. Lee, CCD series no-20: high-flux low-energy upgrade of municipal water supplies with 96% recovery for boiler-feed and related applications, *Desalin Water Treat*, 57 (2016) 20219-20227.
- [181] V. Sonera, J. Septon, A. Efraty, CCD series no-21: illustration of high recovery (93.8%) of a silica containing (57 ppm) source by a powerful technology of volume reduction prospects, *Desalin Water Treat*, 57 (2016) 20228-20236.
- [182] A. Efraty, Apparatus for continuous closed circuit desalination under variable pressure with a single container, US Patent No. 7,628,921 B2, (2009).
- [183] M. Barello, D. Manca, R. Patel, I.M. Mujtaba, Operation and modeling of RO desalination process in batch mode, *Computers & Chemical Engineering*, 83 (2015) 139-156.
- [184] C. Liu, K. Rainwater, L. Song, Energy analysis and efficiency assessment of reverse osmosis desalination process, *Desalination*, 276 (2011) 352-358.
- [185] M. Hamdan, A. Sharif, G. Derwish, S. Alaibi, A. Altaee, Draw solutions for Forward Osmosis Process: Osmotic Pressure of Binary and Ternary Aqueous solutions of Magnesium Chloride, Sodium Chloride, Sucrose and Maltose, *Journal of Food Engineering*, Volume 155 (2015) 10-15.
- [186] L. Song, Concentration polarization in a narrow reverse osmosis membrane channel, *Aiche J*, 56 (2009) 143-149.
- [187] DOW, FILMTEC™ Reverse Osmosis Membranes Technical Manual, in.
- [188] OLI Systems, OLI Analyzer, Morris Plains, NJ, (2005).
- [189] R.L. Stover, High recovery, low fouling, and low energy reverse osmosis, *Desalin Water Treat*, 57 (2016) 26501-26506.
- [190] T. Lee, C. Jinyoung, Y. Cohen, Gypsum Scaling Propensity in Semi-Batch RO and Steady-State RO with Partial Recycle (SSRO-PR), *Journal of Membrane Science*, (2019) (In Review).
- [191] H.S. Fogler, *Elements of chemical reaction engineering*, Third edition. Upper Saddle River, N.J. : Prentice Hall PTR, [1999] ©1999, 1999.
- [192] M.C. Porter, Concentration Polarization with Membrane Ultrafiltration, *Ind. Eng. Chem. Prod. Res. Dev.*, 11 (1972) 234-248.
- [193] V. Gekas, B. Hallström, Mass transfer in the membrane concentration polarization layer under turbulent cross flow : I. Critical literature review and adaptation of existing sherwood

correlations to membrane operations, *Journal of Membrane Science*, 30 (1987) 153-170.

[194] J. Park, K.S. Lee, A two-dimensional model for the spiral wound reverse osmosis membrane module, *Desalination*, 416 (2017) 157-165.

[195] E. Dimitriou, E.S. Mohamed, C. Karavas, G. Papadakis, Experimental comparison of the performance of two reverse osmosis desalination units equipped with different energy recovery devices, *Desalin Water Treat*, 55 (2015) 3019-3026.

[196] Y.-N. Wang, R. Wang, Chapter 1 - Reverse Osmosis Membrane Separation Technology, in: A.F. Ismail, M.A. Rahman, M.H.D. Othman, T. Matsuura (Eds.) *Membrane Separation Principles and Applications*, Elsevier, 2019, pp. 1-45.

[197] R. Stover, Evaluation of closed circuit reverse osmosis for water reuse, in: 27th Annual Water Reuse Symposium, Water Reuse Association, FL, USA, 2012, pp. B4-2.

[198] C. Whittaker, H. Ridgway, B.H. Olson, Evaluation of Cleaning Strategies for Removal of Biofilms from Reverse-Osmosis Membranes, *Applied and Environmental Microbiology*, 48 (1984) 395-403.

[199] A. Al-Amoudi, R.W. Lovitt, Fouling strategies and the cleaning system of NF membranes and factors affecting cleaning efficiency, *Journal of Membrane Science*, 303 (2007) 4-28.

[200] A.S. Al-Amoudi, Factors affecting natural organic matter (NOM) and scaling fouling in NF membranes: A review, *Desalination*, 259 (2010) 1-10.

[201] I.J. Reznik, J. Ganor, C. Gruber, I. Gavrieli, Towards the establishment of a general rate law for gypsum nucleation, *Geochimica et Cosmochimica Acta*, 85 (2012) 75-87.

[202] J. Thompson, A. Rahardianto, H. Gu, M. Uchymiak, A. Bartman, M. Hedrick, D. Lara, J. Cooper, J. Faria, P.D. Christofides, Y. Cohen, Rapid field assessment of RO desalination of brackish agricultural drainage water, *Water Research*, 47 (2013) 2649-2660.

[203] S. Jiang, J.H. ter Horst, Crystal Nucleation Rates from Probability Distributions of Induction Times, *Crystal Growth & Design*, 11 (2011) 256-261.

[204] G.H. Nancollas, Kinetics of crystal growth from solution, *Journal of Crystal Growth*, 3-4 (1968) 335-339.

[205] J. Benecke, M. Haas, F. Baur, M. Ernst, Investigating the development and reproducibility of heterogeneous gypsum scaling on reverse osmosis membranes using real-time membrane surface imaging, *Desalination*, 428 (2018) 161-171.

[206] USEPA, National Primary Drinking Water Regulations, in, USEPA, 2009.

[207] SWRCB, Titles 17 and 22 California Code of Regulations California Regulations Related to Drinking Water, in, 2016.

[208] SWRCB, Lead and Copper Rule Sampling Guidance, in, 2018.

[209] H. Amano, K. Nakagawa, R. Berndtsson, Groundwater geochemistry of a nitrate-contaminated agricultural site, *Environmental Earth Sciences*, 75 (2016) 1145.

[210] SWRCB, Groundwater Information Sheet Salinity, in, California State Water Resources Control Board, 2017.